P-type thermoelectric Sr-doped LaCrO3 epitaxial films

Dong Han

N°d'ordre NNT : 2020LYSEC28

THESE de DOCTORAT DE L'UNIVERSITE DE LYON
opérée au sein de l'Ecole Centrale de Lyon

Ecole Doctorale N° 160
Electronique, Electrotechnique et Automatique

Spécialité de doctorat : Science des matériaux

Préparée à l'Institut des Nanotechnologies de Lyon (INL)

Soutenue publiquement le 06 novembre 2020, par :

Dong HAN

P-type thermoelectric Sr-doped $LaCrO_3$ epitaxial films

Devant le jury composé de :

Mme. Sylvie HEBERT	Directrice de recherche (CNRS), CRISMAT, Caen	Présidente
Mme. Nathalie VIART	Professeure, Université de Strasbourg, IPCMS	Rapporteure
Mme. Ulrike LÜDERS	Directrice de recherche (CNRS), CRISMAT, Caen	Rapporteure
M. Stéphane PAILHES	Chargé de recherche (CNRS), ILM, Lyon	Examinateur
M. Guillaume SAINT-GIRONS	Directeur de recherche (CNRS), INL, Lyon	Directeur de thèse
M. Romain BACHELET	Chargé de recherche (CNRS), INL, Lyon	Encadrant de thèse

Acknowledgments

This thesis is carried out within the Institut des Nanotechnologies de Lyon (INL) of the Université de Lyon (site of the Ecole Centrale de Lyon), and thanks to the financial support of the French Ministry of Higher Education and Scientific Research as well as the China Scholarship Council.

This Ph.D. work is completed under the careful guidance of my supervisor Dr. Romain BACHELET, Chargé de Recherche of the Centre National de la Recherche Scientifique (CNRS). From the topic selection, the design of the experimental scheme, the discussion of the experimental conditions, to the analysis of the results and the writing of the manuscript, Romain has concentrated a lot of effort and energy. I am deeply grateful to him for welcoming me to the team, providing me with a scientific research platform and a good academic atmosphere, and being available when I needed to discuss new challenges in my work. His rigorous academic attitude, meticulous logical thinking, and keen academic insight have given me a lot of inspiration. Honestly, I have learned a lot from him over the past three years. His tolerant and humble style and noble personality made me unforgettable.

I would like to thank my thesis supervisor Dr. Guillaume SAINT-GIRONS, Directeur de Recherche of CNRS, who put a lot of effort into my thesis and study. His patient guidance has benefited me a lot, and his conscientiousness is a role model for me. I am sincerely grateful to him for the constant attention to my work, wise advice, and listening, which were, without a doubt, important for the success and the good progress of my thesis.

I am very grateful to the members of my dissertation committee: Dr. Sylvie HEBERT, Prof. Nathalie VIART, Dr. Ulrike LÜDERS, and Dr. Stéphane PAILHES, for the time and effort in reading my thesis and invaluable feedback/evaluation, and also for their relevant questions and remarks as well as the fruitful discussion during the defense.

I also give my best thanks to all the people who helped me during my research. Mr. Claude BOTELLA helped me complete a large number of analysis tests in this

thesis. Thanks to Claude for all the practical help with the software. I extend my heartfelt thanks to Mr. Jean-Baptiste GOURE for all the technical support. And sincere thanks to Dr. Philippe REGRENY and the other technicians in the cleanroom of INL for fixing our setups. I would like to thank Mr. Aziz BENAMROUCHE, Dr. Bruno CANUT, Dr. Geneviève GRENET, Dr. Alexandre DANESCU, Dr. Valentina GIORDANO, and Dr. Régis DEBORD for their help in the characterization, analysis, and discussion.

I would also like to thank the directors of INL: Dr. Catherine BRU-CHEVALIER and Dr. Christian SEASSAL, for welcoming me to the laboratory. Also, thanks to Mme. Sylvie GONCALVES and Mme. Patricia DUFAUT for all the administrative supports. Thanks to Mr. Raphaël LOPEZ and Dr. Laurent CARREL for the informative help.

I appreciate all Ph.D. students/doctors and post doctors who accompanied me in my research in these three years. I would like to thank Dr. Mohamed BOURAS whom I followed for all the experiments at the beginning of my Ph.D. career. Thanks to Dr. Rahma MOALLA for the cooperation in the project. We worked together for two years. Their help and support made my scientific life more smooth. Also, thanks to Dr. ZHANG Jian, Dr. GUAN Xin, Dr. LI Muchen, Dr. MA Yue, and Dr. ZHANG Yu for the discussion on scientific research and help in life. Besides, thanks to those colleagues who have shared the office with me: Dr. Louise FOUQUAT, Dr. Marco VETTORI, Dr. Ali JAFFAL, Thomas DURSAP, Marc D'ESPERONNAT, Henri-Gabriel GLORIES, and Masoumeh RAZAGHI-PEY-GHALEH.

I will never forget my dear friend RUAN Yucang who helped me adapt myself to the new research work and to enjoy the abroad life in this tranquil French downtown. Then, LI Shiwei, ZHU Minglei, and DING Shuoliang, we graduated from the same class and came to France for Ph.D. research. We worked hard in our respective research fields and spent a wonderful time together. I am truly grateful for all of their encouragement over the last few years.

Finally, I owe my deepest gratitude to the love, support, and encouragement I have received from my parents, grandparents, and all family members.

Contents

General introduction

With increasing global energy demand, renewable energies have attracted much attention in the past several decades. Thermal management has become of major importance in microelectronic devices. Either the temperature of the device needs to be well controlled to obtain a high work efficiency, or the residual heat can be harvested and converted into useful electricity to build autonomous devices. Thermoelectric material is a kind of functional material that can achieve the reversible conversion between thermal energy and electrical energy. However, nowadays, the main thermoelectric materials working around room temperature are alloy semiconductors based on tellurides which are toxic, chemically unstable, scarce, and expensive. Therefore, it is necessary to develop alternative thermoelectric materials that can overcome these disadvantages. Oxide-based materials are good candidates, especially doped $SrTiO_3$ of perovskite structure, because of its good chemical stability and flexibility, large thermoelectric power factor, and possible integration in single-crystalline films on silicon, which is still the most used microelectronic platform in the world.

Perovskite oxides of chemical structure ABO_3 have a variety of functional properties (thermoelectricity, ferroelectricity, ferromagnetism...), as well as many advantages such as chemical stability, flexibility, tunable conductivity, and the possibility of integration on silicon by epitaxy, that make them extremely attractive for many applications, especially in the fields of cooling or thermal energy harvesting. Indeed, *n*-type thermoelectric perovskite oxides such as transparent La-doped $SrTiO_3$ can reach large conductivity ($\sim 10^4$ $S \cdot cm^{-1}$) and large power factor (~ 40 $\mu W \cdot cm^{-1} \cdot K^{-2}$) at room temperature. However, efficient *p*-type thermoelectric perovskite oxides remain challenging. *P*-type transparent conducting Sr-doped $LaCrO_3$ is appealing in this context.

In this Ph.D. thesis, we aimed to epitaxially grow *p*-type thermoelectric Sr-doped $LaCrO_3$ films of perovskite structure on perovskite-oxide substrates using molecular beam epitaxy (MBE). The manuscript is divided into six chapters, as follows:

Chapter I. As a general introduction, this chapter presents the context of the study, the scientific background of thermoelectricity as well as the main thermoelectric materials, and the main researches in this field carried out during the last decades. Finally, the motivations for developing epitaxial thermoelectric perovskite oxide films (especially *p*-type) as well as the main parameters studied in this Ph.D. thesis are introduced.

Chapter II. This chapter presents the main experimental techniques employed during this thesis. The basic scientific background of these techniques is introduced.

Chapter III. This chapter is devoted to present first the stoichiometry calibrations series of $La_{1+\delta}CrO_3$ ($|\delta| \leq 0.25$) and $Sr_{1+\delta}CrO_3$ ($|\delta| \leq 0.14$) epitaxial films. Based on these calibrations, the effects of the Sr substitution ratio (x) in stoichiometric epitaxial $La_{1-x}Sr_xCrO_3$ solid-solution films on its structural, electronic, and thermoelectric properties are presented. The substitution range investigated is $0 \leq x \leq 0.4$. As the outcome of this study, the composition yielding the largest power factor ($0.33\ \mu W \cdot cm^{-1} \cdot K^{-2}$ at $x = 0.25$) is then set for the next studies.

Chapter IV. This chapter is devoted to the study of the effects of epitaxial strain on structural, electronic, and thermoelectric properties of high-quality epitaxially-strained $La_{0.75}Sr_{0.25}CrO_3$ and $LaCrO_3$ thin films grown on four different perovskite-oxide substrates, leading to a wide in-plane strain value ($-2.1\% \leq \varepsilon_{xx} \leq +1.8\%$). The Poisson ratio as well as the bulk lattice constant of $La_{0.75}Sr_{0.25}CrO_3$ is extracted for the first time. This study shows also that its electronic and thermoelectric properties can be tuned by strain, and that a slight in-plane tensile strain provides the largest thermoelectric power factor to most relaxed films.

Chapter V. This chapter is devoted to present the effects of the deviation from cationic stoichiometry in epitaxially strained $(La_{0.75}Sr_{0.25})_{1+\delta}CrO_3$ thin films ($-0.3 \leq \delta \leq 0.3$) on the structural, electronic, and thermoelectric properties. This study shows that deviation from cationic stoichiometry strongly alters the properties and that slight B-site Cr-deficiency ($\delta \sim 0.15$) can enhance the thermoelectric power factor by around 70% as compared to stoichiometric

films.

Chapter VI. As a conclusion and perspectives, this chapter presents the main conclusion of the Ph.D. thesis, as well as the works in progress and some perspectives for this thematic at INL. For instance, it briefly mentions the thermal conductivity measurements started using the 3ω method, the contact resistance study in progress by C-TLM methods, and targeted microfabrication of a planar perovskite-oxide thermoelectric module. In particular, this chapter presents the epitaxial integration and structural properties of $La_{0.75}Sr_{0.25}CrO_3$ film on silicon for the first time.

Chapter I Introduction

1.1. Context

1.1.1. “More than Moore” vision in the microelectronic industry

The microelectronic industry witnessed its growth in agreement with the empirical Moore’s law from decades guiding by a miniaturization strategy: the number of transistors on integrated circuits has doubled every two years until recently [1]. Nowadays, coming to physical limits [1, 2], different new strategies have been developed by the International Technology Roadmap for Semiconductors (ITRS) [3, 4] allowing to maintain market growth. In particular, the “More-than-Moore” vision has emerged as an important development towards diversification and heterogeneous integration of new functionalities beyond information processing (Figure 1. 1). Especially, the interaction with the environment, smart sensors, actuators, RF wireless communications or energy harvesters, has emerged as an important part of this vision, even more with the rapid growth of the internet of things (IoT) market.

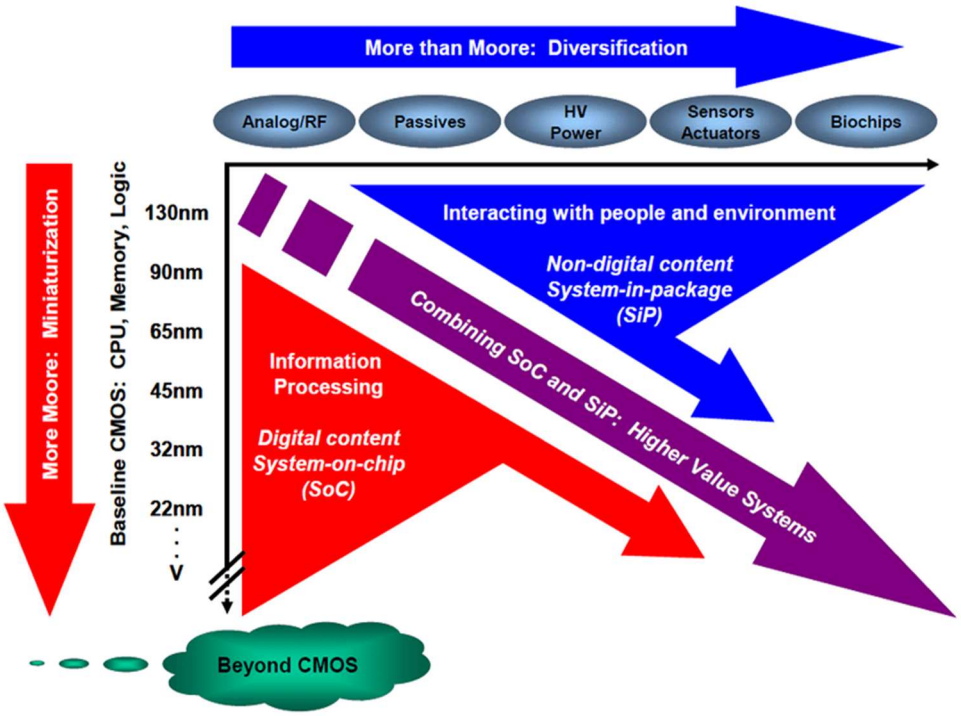

Figure 1. 1 Sketch of strategic trends of the microelectronic industry from the ITRS. Taken from Ref. 5.

1.1.2. Internet of things and energy harvesting

The number of small devices interconnected by wireless communication, composing the internet of things, is estimated to be around 50 billion around the world in 2020 (more than 6

devices/person on average), representing a rising market of around 500 billion US$ [6] (Figure 1. 2). This huge rising market is sometimes described as the new industrial revolution. The numerous wireless sensors, composing the interconnected networks, often need only a few microjoules of energy as maximum to transmit the information from one sensor to another by RF transceiver, paving the way to the micro-energy field, energy harvesting for powering autonomous wireless sensor networks (WSN) of the IoT without batteries [7, 8, 9, 10].

Figure 1. 2 Sketch representing the internet of things. Taken from Ref. 11.

1.1.3. Efficient on-chip cooling of optoelectronic devices

Being even more miniaturized, compact with 3D stacks, the optoelectronic devices of the microelectronic platforms (Figure 1. 3a) need an even more efficient cooling or thermal management to avoid damaging hot spots or to permit precise regulation of the working temperature for optimal device operations [12]. The integration of additional thermal management layers on microelectronic boards at the wafer-scale close to the warming devices is of high interest and is actively developed. For instance, it was the goal of a collaborative European project (H2020 TIPS 2014-2018) in which the team at INL was involved [6].

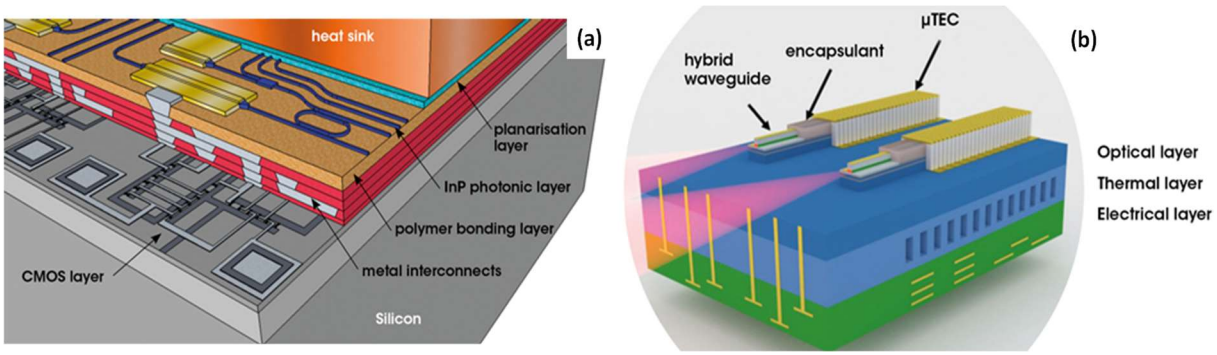

Figure 1. 3 Sketches representing (a) an optoelectronic platform and (b) with an additional active thermal management layer. Taken from Ref. 12 and 6, respectively.

1.1.4. Thermoelectricity interests

Thermoelectric materials allow a reversible conversion between thermal energy (thermal difference) and electric energy (electric potential). They can thus be used either for energy harvesting and powering applications (through Seebeck effect), or either for thermal management and cooling applications (through Peltier effect) [13, 14, 15]. They are considered with a rising interest in the scientific community for these important applications at different scales [16]. As the energy and the environmental crisis continues to intensify, the thermoelectric materials adapted to the theme of green environmental protection in the 21st century are of great significance in condensed matter physics, materials science, energy and environmental science, and industrial technology applications. Therefore, many scientists have been newly attracted to explore their synthesis and properties. As we will see in the following, the optimizations of the thermoelectric properties and devices are challenging. International and national scientific community networks have emerged in this field, as the international thermoelectric society (ITS) [17], European thermoelectric society (ETS) [18], as well as French research networks on thermoelectricity from 2007 (GDR TE and GIS TE) [19], organizing international and national conferences, meetings and schools to globally speed up the developments in this field and applications.

1.2. Insights into thermoelectricity

1.2.1. A brief history

Thermoelectricity has been discovered two hundred years ago. In the first hundred years, the research on this phenomenon was mainly focused on metallic materials. In the meantime, people have been continuously exploring and developing possible industrial applications. However, the thermoelectric conversion efficiency of the materials obtained at that time was very low. At the same time, conventional power generation and compression refrigeration technologies have developed rapidly due to their relatively high efficiency, which has somehow hindered the research on thermoelectric materials. Around the 1950s, some high-efficiency thermoelectric alloys (*e.g.* Bi_2Te_3 [20, 21, 22]) were successively discovered, which greatly promoted the extensive development of thermoelectric materials.

In 1909, the German physicist E. Altenkirch established the principles of thermoelectricity based on previous work and summarized that thermoelectric performance is

closely related to three parameters: thermoelectric potential (Seebeck coefficient), electrical conductivity, and thermal conductivity. These three physical parameters can be directly measured, and are directly related to the energy band structure and microstructure of the material. A good thermoelectric material must have a high thermoelectric potential to ensure that a significant thermoelectric effect can be produced. At the same time, high electrical conductivity is required, so that the Joule heat generated is small and the output power is large. Besides, it is also required that the thermal conductivity is small so that a large temperature difference can be maintained at both ends of the material.

At that time, people's attention was focused on metallic materials, due to their good electrical conductivity. However, these materials have low Seebeck coefficients (*i.e.* ~10 $\mu V \cdot K^{-1}$), and the resulting thermoelectric power generation device is very inefficient. With the development of solid-state physics, especially semiconductor physics, it has been found that the Seebeck coefficient of some semiconductors can be higher than 100 $\mu V \cdot K^{-1}$. Therefore, the research on semiconductor thermoelectric materials has begun to develop. In 1949, the former Soviet Union academician A. F. Ioffe proposed the thermoelectric theory of semiconductors. Ioffe and colleagues proved theoretically and experimentally that using two or more semiconductors to form a solid solution can effectively increase σ/κ, thus demonstrating the prospect of improving thermoelectric performance through research and development of new materials [23, 24] (see section 1.2.3).

In the last few decades, due to the diversification and progress of elaboration processes, analysis methods and theoretical predictions, the possibility of designing and preparing high-performance complex thermoelectric materials has greatly increased [16, 25, 26, 27, 28, 29, 30, 31, 32]. The emergence of high performant thermoelectric materials has made people see the broad prospects for the development of real thermoelectric devices and firmly believe that the research and development on thermoelectric materials will have a huge breakthrough in the next few years.

1.2.2. Fundamental thermoelectric effects

A thermoelectric device is a solid energy conversion device capable of a direct conversion between thermal energy (thermal difference) and electrical energy (current of potential difference). Its essence is the transport and interaction of electronic charge carriers (electrons or holes) and thermal carriers (electronic, and phononic from lattice vibration). The

transport of carriers in the crystal lattice and the accompanying transfer of energy is the source of the thermoelectric conversion. The reversible thermoelectric conversion can yield a temperature difference caused by a flowing current (Peltier effect) or an electrical current caused by a temperature difference (Seebeck effect). More completely, it includes three interrelated effects: Seebeck effect, Peltier effect, and Thomson effect corresponding to three thermoelectric coefficients: Seebeck coefficient, Peltier coefficient, and Thomson coefficient (Seebeck coefficient being the main reported). Only a brief introduction to these effects is presented, but a more exhaustive treatment can be found elsewhere [33, 34].

1.2.2.1. Seebeck effect

Seebeck effect is the theoretical basis for directly converting thermal energy into electrical energy to achieve power generation. In 1821, the German physicist T. J. Seebeck discovered the Seebeck effect when studying the electromagnetic effects in Bi-Cu and Bi-Te based circuits. It shows that when the two nodes of a closed-loop composed of two different conductors have different temperatures, a thermal current is generated in the loop. When the circuit is open, a potential difference appears between the two ends of the open circuit, which is called the Seebeck potential. The ratio between the developed electric potential difference (ΔV) and the applied temperature difference (ΔT) is given by the Seebeck coefficient, or so-called thermopower ($S = \Delta V/\Delta T$).

The micro-physical mechanism of the Seebeck effect can be explained by the change in the distribution of carriers in a semiconductor under a temperature gradient. For an isolated semiconductor, the carriers inside are uniformly distributed. When a temperature gradient is established inside the semiconductor, the carriers at the hot end have larger kinetic energy, tend to diffuse and accumulate at the cold end, so that the number of carriers at the cold end is greater than the hot end. This accumulation of charge unbalance the electrical neutrality inside the semiconductor and causes a self-built electric field. In this case, when the system reaches equilibrium, there is no directional movement of the net charge. The potential difference formed at both ends is the thermoelectromotive force (emf).

1.2.2.2. Peltier effect

Peltier effect was discovered by French physicist C. A. Peltier in 1834. When an electric

current (I) passes through a junction of two different conductors, the temperature near the junction will change. The heat is evolved or absorbed at each side of the junction. The Peltier coefficient (Π) is given by the ratio between the rate of heat evolution/absorption (dQ) and the current ($\Pi = dQ/I$). The reason for the Peltier effect is that the carrier concentration and the Fermi level of the two materials are different. When a current passes through the junction, carriers move from one conductor to another. To maintain energy and charge conservation, energy must be exchanged with the environment.

1.2.2.3. Thomson effect

In 1854, the British physicist W. Thomson analyzed the thermoelectric phenomenon using the energy conservation law and predicted the Thomson effect: when an electric current (I) passes through a uniform conductor with a temperature difference/gradient (ΔT), the original temperature distribution in the conductor is changed. To maintain the original temperature distribution, the conductor absorbs or releases heat (dQ). Thomson coefficient (τ) is given by $dQ = -\tau I \Delta T$.

Also, it is worth noting that the Seebeck effect, the Peltier effect, and the Thomson effect are reversible, cross-coupling effects between thermal conduction and electrical conduction. Based on these three effects, the mutual conversion between thermal energy and electrical energy can be achieved. However, the Joule effect and the Fourier effect are irreversible thermal effects, which do not belong to the thermoelectric effect. The application of thermoelectric conversion is mainly based on two aspects: (*i*) temperature difference power generation using the Seebeck effect and (*ii*) thermoelectric cooling/heating using the Peltier effect.

1.2.3. Evaluation of thermoelectric material performances

1.2.3.1. Thermoelectric figure-of-merit

The efficiency of thermoelectricity relies on three material-dependent parameters: the Seebeck coefficient (S), the electrical conductivity ($\sigma = \rho^{-1}$), and the thermal conductivity (κ), summarized in the thermoelectric figure-of-merit (Z), developed by A. F. Ioffe in 1949, which evaluates the performance of the thermoelectric properties:

$$Z = \frac{S^2\sigma}{\kappa} \tag{1.1}$$

The thermal conductivity contains both the phononic contribution (vibrations from the atomic lattice) and the electronic contribution (electrons and holes transporting heat) [14, 25]. The thermoelectric conversion performance ($S^2\sigma$) is called the thermoelectric power factor. Due to the different figure of merit values of materials at different temperatures, it is customary to use the product of Z and absolute temperature (T, in Kelvin), which is the dimensionless index ZT to describe the quality of thermoelectric performance. The larger the ZT value, the higher the thermoelectric performance of the material, and the higher the thermoelectric conversion efficiency. The best performant thermoelectric materials have rather complex structures (Clathrate, Skutterudite, half-Heusler phases, Zintl phases, two-dimensional layered materials, etc…) of low lattice thermal conductivity [25]. Their ZT values can be as high as 1 to 3 [16, 25, 26, 27, 28, 35, 36], and even up to 6 as recently reported in a metastable Half-Heusler phase [37], even though the very high ZT (> 2) reports are subjected to controversy as seen in Ref. 38 and 39.

1.2.3.2. Seebeck coefficient

For metals and degenerate semiconductors, the Seebeck coefficient can be expressed by the Pisarenko relation [40]:

$$S = \frac{8\pi^2 k_B^2}{3eh^2} m^* T \left(\frac{\pi}{3n}\right)^{2/3} \tag{1.2}$$

where k_B is the Boltzmann constant (1.381×10^{-23} kg·m^2·s^{-2}·K^{-1}), e is the elemental charge (1.6×10^{-19} C), h is the Planck constant (6.626×10^{-34} kg·m^2·s^{-1}), n is the charge carrier concentration, and m^* is the charge carriers effective mass.

Theoretically, a low charge carrier concentration with a high effective mass can ensure a high Seebeck coefficient value. Also, there should only be one type of carrier. Mixed *n*-type and *p*-type conduction leads to both charge carriers moving to the cold end, canceling out the induced Seebeck voltages.

1.2.3.3. Electrical conductivity

Similarly, the electrical conductivity is dependent on charge carrier concentration and effective mass.

$$\sigma = ne\mu \tag{1.3}$$

$$\mu \propto \frac{1}{m^*} \tag{1.4}$$

where μ is the charge carrier mobility.

The electrical conductivity and the Seebeck coefficient evolve contrariwise concerning those parameters. Therefore, in pursuance of a better thermoelectric conversion rate, it is more reasonable to work on the power factor (PF = $S^2\sigma$) which balances the contradiction between these two important thermoelectric parameters.

1.2.3.4. Thermal conductivity

According to equation (1.1), the thermal conductivity of the material should be controlled as low as possible. That is to maintain a maximal temperature difference/gradient between the junction, thereby guaranteeing the generation of a strong potential difference.

The total thermal conductivity (κ) of a material has a lattice thermal conductivity (κ_L) component and an electronic thermal conductivity (κ_e) component:

$$\kappa = \kappa_L + \kappa_e \tag{1.5}$$

The lattice thermal conductivity can be expressed by the relation [41]:

$$\kappa_L = \frac{v_s C_p L_{ph}}{3} \tag{1.6}$$

where v_s is the sound velocity, C_p is the lattice specific heat, and L_{ph} is the phonon mean free path.

The electronic thermal conductivity is related to electrical conductivity through

Wiedemann-Franz's law [42]:

$$\kappa_e = \sigma LT = ne\mu LT \tag{1.7}$$

where L is the Lorenz factor (2.45×10^{-8} $J^2\cdot K^{-2}\cdot C^{-2}$ for free electrons). However, the Lorenz factor is dependent on the diffusion process of the charge carriers at the Fermi level. Therefore, the compounds used in thermoelectricity present a lower value, *e.g.* 1.5×10^{-8} $J^2\cdot K^{-2}\cdot C^{-2}$ [43].

1.2.4. Optimization of thermoelectric performances

Thermoelectric parameters are to be tuned when possible to optimize the *ZT* value. Beyond this parameters compromise, the researches have focused on two main strategies to optimize the properties: (*i*) by tuning the band structure and increasing the power factor (the numerator of the *ZT*) and/or (*ii*) by phononic engineering to decrease the lattice thermal conductivity (κ_L, part of the denominator of the *ZT*) [16, 25, 26, 44, 45, 46].

Quality factor (β) is proposed by Wang *et al.* [47] to demonstrate that thermoelectric performance is related to fundamental properties.

$$\beta \propto m^{*3/2}\frac{\mu}{\kappa_L} \tag{1.8}$$

Some approaches to improve the quality factor are described as follows. However, optimization is susceptible to have a positive or negative impact on different parameters. Therefore, the research groups try to find compromises to obtain a fully optimized *ZT*. Additionally, the potential of each strategy is strongly correlated to the nature of the material as well as to the control of the synthesis conditions and its consequent microstructure properties.

1.2.4.1. Tuning the band structure

(a) Adjusting the charge carrier concentration/bandgap

Under constant temperature, the *ZT* of a semiconductor can be optimized by changing

the charge carrier concentration. All three main parameters of thermoelectric materials (electrical conductivity, Seebeck coefficient, and thermal conductivity) can be effectively tuned by changing the charge carrier concentration, as shown in Figure 1. 4. That indicates the variation of the three parameters of thermoelectric materials as a function of carrier concentration. With increasing carrier concentration, both the electrical and thermal conductivities increase but the Seebeck coefficient decreases. A compromise has to be encountered and the *ZT* optimum typically occurs at carrier concentrations around 10^{19} and 10^{20} cm^{-3} (depending on the materials), which falls in the category of heavily-doped or degenerated semiconductors [25].

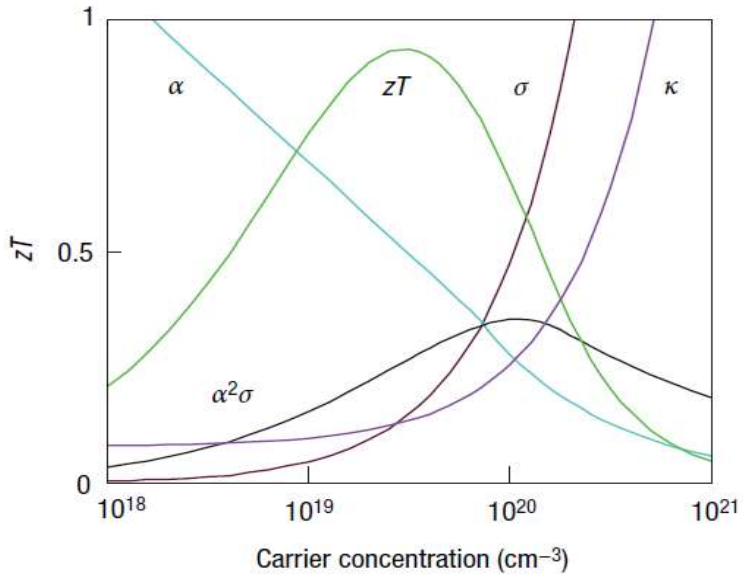

Figure 1. 4 *ZT* value involves a compromise of electrical conductivity σ, Seebeck coefficient α, and thermal conductivity κ as a function of carrier concentration. The thermoelectric power factor $\alpha^2\sigma$ maximizes at a higher carrier concentration than *ZT*. Taken from Ref. 25.

(b) Increase the effective mass

According to equation (1.2), the Seebeck coefficient can be enlarged by increasing the effective mass of the charge carriers. The principle of increasing effective mass via doping is to increase the band effective mass of a single valley (m_b^*) as shown in Refs. 48, 49, 50, 51, 52, 53, 54, 55, 56, 57, 58, and 59.

$$m^* = N_v^{2/3} m_b^* \tag{1.9}$$

where N_v is the band degeneracy. However, increasing m_b^* will reduce μ since [60, 48]:

$$\mu \propto 1/m_b^{*5/2} \tag{1.10}$$

A high m^* does not always lead to an overall high *ZT*. To practically enhance the σ of thermoelectric materials, it is important to tune m^* to compromise with μ to obtain the optimized $S^2\sigma$.

(c) Quantum confinement and resonant states

Because of the generation of abrupt discontinuities in the density of states (DOS), quantum confinement in low-dimensional structures allows to increase the Seebeck coefficient, and consequently, the thermoelectric power factor preserving electrical conductivity [26, 45].

Low-dimensional materials offer a possibility of significantly increasing the *ZT* value [36, 45, 61]. Reducing the dimension can improve the thermoelectric properties for the following reasons [62, 63]. Due to the confinement effect, the density of states near the Fermi level is increased, thereby increasing the thermoelectric potential. However, in low-dimensional thermoelectric materials, the thermoelectric properties are far more difficult to determine than in bulk materials, especially the determination of thermal conductivity and thermoelectric potential (see Chapter II). Other emergent low-dimensional thermoelectric materials are 2D structured materials with possible topological effects, as chalcogenides like MoS_2 for instance [64], or graphene, black phosphorous, silicene… [65]. These 2D layered materials can have very low lattice thermal conductivity in the cross-plane direction, as in WSe_2 [66] or SnSe [67] crystals.

Superlattices (SLs) are periodic layered structures. If the period thickness is low enough (in the few nanometers range: short-period SLs), they can be viewed as 2D layered structures. These short-period SLs can be used for enhanced thermoelectricity for two reasons: (*i*) to enlarge the power factor via increased Seebeck coefficient through quantum confinement effects (see sections 1.2.4.1 and 1.3.2.3) [26], and (*ii*) to study the phononic transport and decrease the lattice thermal conductivity by adjusting the periodicity and interface density [76, 79, 80, 81]. Ohta *et al.* [68] found that the Seebeck coefficient of short-period SLs made of electron-doped and undoped $SrTiO_3$ layers increases significantly with decreasing the thickness of the electron-doped layer. Maintaining constant the thickness of the undoped layer,

when the thickness of the electron-doped layer is reduced to the order of 1-unit cell layer (~0.4 nm) similarly to a 2D electron gas, the Seebeck coefficient of the SLs increases dramatically. If the thermal conductivity of $SrTiO_3$ is used to estimate the thermoelectric properties of the 2D electron gas, the room-temperature *ZT* can reach 2.4. However, this article is subject to controversy, in particular, because Seebeck can follow simply the one on electron-doped "bulk" $SrTiO_3$ without confinement effects [69, 70, 71].

Besides, such a low-dimensional structure would decrease the lattice thermal conductivity by phonon scattering through the numerous interfaces, as a benefit for global *ZT* (see section 1.2.4.2).

Also, some "resonant" states due to distortions can be created on the host band of the energy level of dopants (so-called resonant doping) [50, 56, 57, 72, 73, 74]. When the Fermi level moves close to the resonant state, m^* becomes significantly increased due to the increased DOS [72, 74] thus, *S* increases according to equation (1.2) without changing *n*.

1.2.4.2. Decrease of thermal conductivity

Reducing the lattice thermal conductivity is one of the most effective ways to improve the thermoelectric efficiency of materials and is widely studied. Phonon scattering at different length scales from punctual defects (atomic vacancies/substitutions, inclusions…) to two/three-dimensional nanometric defects/inclusions (grain boundaries, dislocations, interfaces, nanoparticles, nanowires) allows decreasing the lattice thermal conductivity of the material as schematically shown in Figure 1. 5. Theoretically, for a given composition, the material has the lowest lattice thermal conductivity in the amorphous state like glasses [75]. Some emerging thermoelectric materials are mainly designed with full consideration of phononic engineering by intentionally reducing lattice thermal conductivity through nanostructurations, atomic substitutions, punctual defects introduction, etc [16, 26, 30, 76, 77, 78]. The propagation of phonons can also be tuned by periodic structures, as short-period superlattices because of the wave nature of phonons at these length scales [79, 80, 81, 82, 83]. It compromises the required good electronic properties (high electric conductivity, large thermoelectric power factor), and a low lattice thermal conductivity as much as possible to effectively enhance the *ZT* [16, 36]. Naturally, low lattice thermal conductivities are found in complex structures with large lattice volume [25, 43] (as shown in Figure 1. 7).

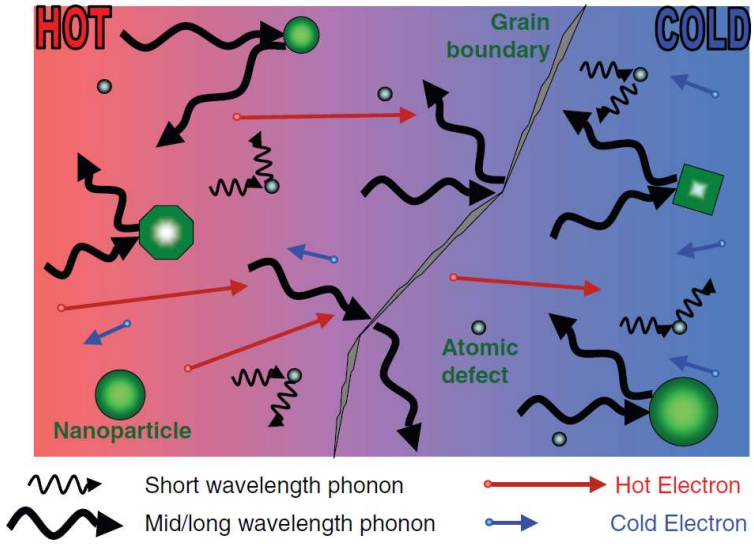

Figure 1. 5 Diagram illustrating various phonon scattering mechanisms within a thermoelectric material, along with electronic transport of hot and cold electrons. Atomic defects are effective at scattering short wavelength phonons, but larger embedded nanoparticles are required to scatter mid- and long-wavelength phonons effectively. Grain boundaries can also play an effective role in scattering these longer-wavelength phonons. Taken from Ref. 26.

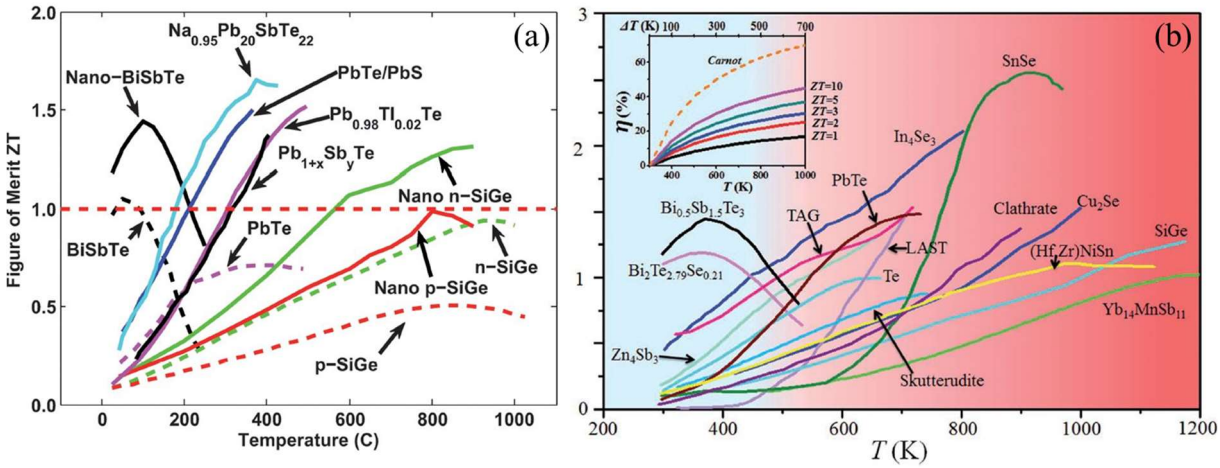

Figure 1. 6 (a) *ZT* of thermoelectric materials versus temperature summarized in 2009. The dashed lines show the maximum *ZT* values for bulk materials, and the solid lines show the *ZT* values of bulk nanostructured materials. Taken from Ref. 36. (b) Currently reported *ZT* as a function of temperature for typical high-efficiency thermoelectric materials summarized in 2018. Taken from Ref. 16.

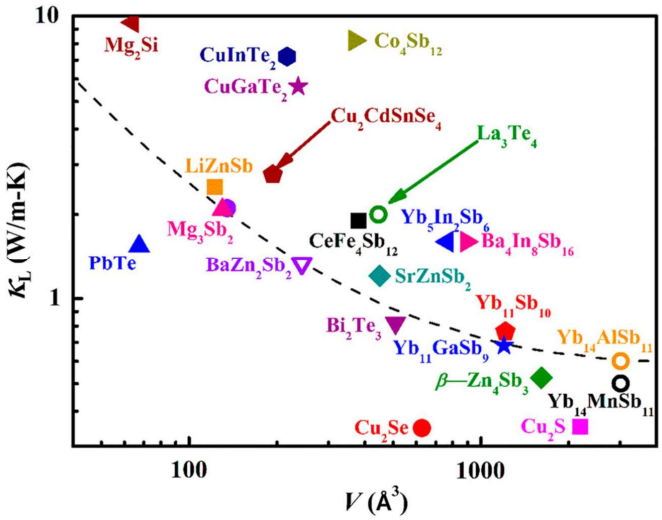

Figure 1. 7 Lattice thermal conductivity at 300 K for a variety of thermoelectric materials. The dashed line shows an inverse dependence on the primitive cell volume, revealing low lattice thermal conductivity in compounds having large unit cell volumes. Taken from Ref. 43.

1.3. State-of-the-art thermoelectric materials

Since the middle of the last century, the development of the condensed matter physics, especially semiconductor physics, has promoted the studies of semiconductor thermoelectric materials. Today, the development of elaboration and characterization methods, as well as modeling tools, has brought unprecedented breakthroughs in the research of thermoelectric materials. The research activities on thermoelectric materials are broads from chemistry, physics, and engineering, and thus presents a complementary multi-polar development trend. The state-of-the-art representative and promising thermoelectric materials will be introduced as follows.

1.3.1. State-of-the-art traditional thermoelectric materials

Broadly speaking, almost all heavily doped semiconductor materials have different degrees of thermoelectric performance. However, currently, only a few alloys and semiconductor compounds have high thermoelectric performance. Previous researches have well summarized the typical high-performance thermoelectric materials, as shown in Figure 1. 8. According to applicable temperature, there are mainly few fundamental systems of high-performance thermoelectric materials that have been widely used at present: two tellurides systems [$(Bi, Sb)_2Te_3$ alloys suitable for the room-temperature region, and PbTe alloys suitable for the medium-temperature region], and SiGe alloys suitable for the

high-temperature region. These thermoelectric alloys, especially the $(Bi, Sb)_2Te_3$ alloys, are currently widely used in commercial macroscopic thermoelectric power generation and refrigeration (Peltier) devices, which have to contain both *n*-type and *p*-type thermoelectric materials.

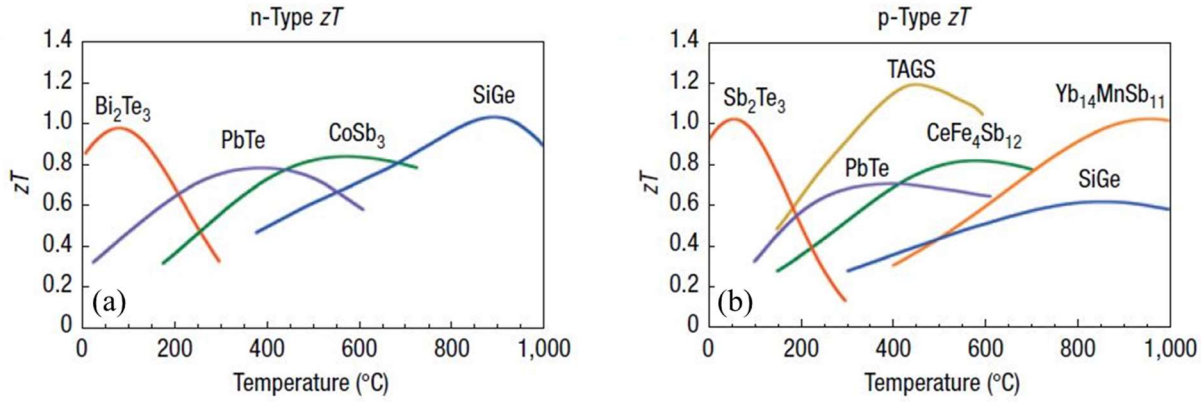

Figure 1. 8 *ZT* of commercial materials for thermoelectric power generation summarized in 2008, (a) *n*-type and (b) *p*-type. Taken from Ref. 25.

$(Bi, Sb)_2Te_3$ based alloy system is still currently the semiconductor thermoelectric material with the greatest *ZT* value near room temperature [84, 85, 86], and plays a very important role in thermoelectric devices [87]. This alloy was first investigated as a material of great thermoelectric performance in the 1950s [20, 21, 22, 88, 89, 90]. Dominantly, Bi_2Te_3 is an *n*-type thermoelectric material whereas Sb_2Te_3 is *p*-type [25]. The stability and the performance of this alloy can be improved by partial substation, as Se in the Te site [39]. The electronic transport properties and detailed defect chemistry of these alloys are now well-understood thanks to extensive studies of single crystal and polycrystalline material [91, 92]. BiTe-based alloys have made a pioneering contribution and an epoch-making significance. On this basis, people have carried out extensive research on thermoelectric materials, and have discovered some new high-performance alloy thermoelectric materials. However, these alloys still lack chemical stability under air with temperature cycling above room temperature (oxidation), besides that they contain scarce and toxic telluride elements in each developed alloy.

Meanwhile, PbTe is also usually used as a thermoelectric material, especially in the middle-temperature range (from 300 to 900 K) [93] because of good chemical stability. By appropriate doping, an *n*-type or *p*-type material can be formed, thereby preparing a thermoelectric device. NASA's early space exploration often used doped PbTe alloys to make thermoelectric power generators. Until today many researchers continue to improve its thermoelectric performance in various ways. However, as $(Bi, Sb)_2Te_3$ alloys, these PbTe

alloys still lack strong chemical stability under air with medium-range temperature cycling (oxidation), in addition to the fact that they contain scarce and toxic telluride elements in each developed alloys.

Si and Ge have high thermoelectric power factors, but their thermal conductivities are also large, at the detriment of their overall thermoelectric performance. However, when Si and Ge form an alloy, the thermal conductivity decreases drastically, as is the case for other alloys. Currently, SiGe-based alloys are mature high-temperature thermoelectric materials. For example, the *ZT* of *n*-type $Si_{0.7}Ge_{0.3}$ above 1000 K can exceed 1 [36, 94]. Vining *et al*. [95] have found that the Seebeck coefficient of the SiGe alloy reached a maximum value near the composition with Si ratio around 0.15. This is because the density of the state of the system and the effective mass of electrons are the largest. However, in applications, alloys with higher Si content are often used to obtain higher *ZT* value and more stable performance. As the Si content increases, the thermal conductivity of the material can be significantly decreased. Besides, the alloy system has a larger bandgap and a higher melting point, which can be effectively suitable for working at high temperatures. SiGe-based alloys are suitable for thermoelectric power generations provided by radioisotopes and have been widely used. As a remarkable example, the thermoelectric power generation device used by the Voyager space probe launched by the United States in 1977 is based on SiGe alloy material.

1.3.2. State-of-the-art of new complex thermoelectric materials

In recent years, with the development of elaboration methods and characterization techniques, the enhancement of thermoelectric materials has made rapid progress. In addition to further research on traditional thermoelectric materials, various new types of thermoelectric materials are emerging.

1.3.2.1. Intermetallics

In 1995, the phonon glass-electron crystal (PGEC) was first introduced by G. A. Slack [96]. The new kind of material possesses a structure that limits phonon propagation while having a negligible influence on charge carrier mobility [78].

(a) Clathrates and skutterudites

The Clathrate [97, 98, 99] and skutterudite [62, 97, 100] structures contain an atom or molecule in a weakly bound state in a cage-like super-large void composed of covalently bonded atoms. This kind of atom or molecule presents a localized non-simple resonance in the gap, and this kind of vibration is completely independent of other atoms in the crystal [101]. Since this vibration only reduces the lattice part of the thermal conductivity and has little effect on the electrical transport of the material, this type of material can achieve a high thermoelectric figure of merit. Their typical structures are shown in Figure 1. 9.

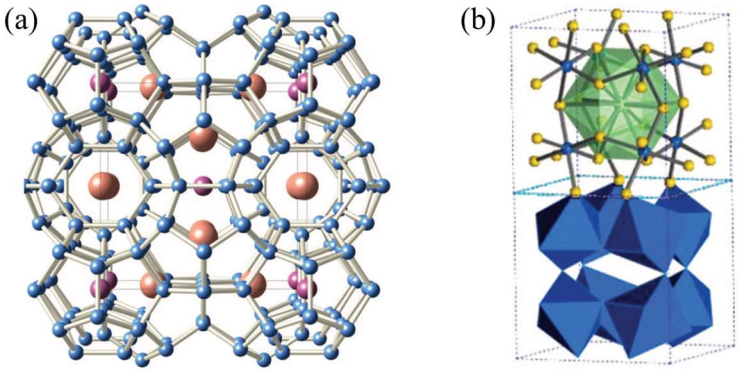

Figure 1. 9 (a) Crystal structure of one type of clathrate. Framework atoms are shown in blue, guest atoms inside the tetrakaidecahedra are orange, and guest atoms inside the pentagonal dodecahedra are purple. (b) Schematic illustration of a skutterudite crystal, where the guest atom is inside a 12-coordinated "cage" (green) surrounded by yellow pnicogen atoms. The metal sites are depicted in blue. The octahedral environment surrounding the metal sites is shown in the lower portion of the figure, also in blue. Taken from Ref. 97.

(b) Half-Heusler alloys

The structural formula of the Half-Heusler alloy can be written as MNiSn or MCoSb (M: Zr, Hf, Ti). The structure consists of two face-centered cubes interspersed with each other and a simple cube at the center, as shown in Figure 1. 10.

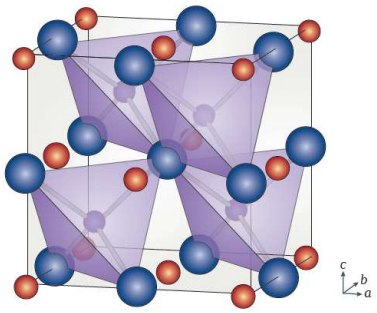

Figure 1. 10 Schematic representation of the half-Heusler structure XYZ, consisting of a covalent, diamond-like (or ZnS) substructure of the $(YZ)^{n-}$ Zintl chemistry framework (purple tetrahedra) formed by the tetrahedral coordination of Y atoms (purple) and Z atoms (blue). The electropositive X^{n+} (red) fills the octahedral voids around the tetrahedral framework. Taken from Ref. 102.

Half-Heusler alloy systems have excellent electrical properties due to the narrow bandgap, which is about 0.1-0.5 eV. The room-temperature Seebeck coefficient is as high as 400 $\mu V \cdot K^{-1}$ [103]. To obtain Half-Heusler alloys with better thermoelectric properties, some groups have conducted research on MCoSb-type alloys with large bandgaps. For example, Xia *et al.* [104] found that the Seebeck coefficient of TiCoSb at room temperature can reach -500 $\mu V \cdot K^{-1}$. Both the Seebeck coefficient and the resistance were decreased after doping. The lowest thermal conductivity is obtained at the same time. Moreover, Xing *et al.* [105] fabricated the *n*-type $Zr_{0.5}Hf_{0.5}NiSn_{0.985}Sb_{0.015}$ and *p*-type $Zr_{0.5}Hf_{0.5}CoSb_{0.8}Sn_{0.2}$ half-Heusler alloys. Dense dislocation arrays were introduced in both *n*-type and *p*-type materials, which greatly depressed their lattice thermal conductivities. At present, research on the optimal composition and the optimal doping amount of Half-Heusler alloy is still in progress. More recently, Zeier *et al.* [102] provided an overview of the electronic properties of half-Heusler compounds, which explained the basic structural chemistry and physical properties.

1.3.2.2. Oxide thermoelectric materials

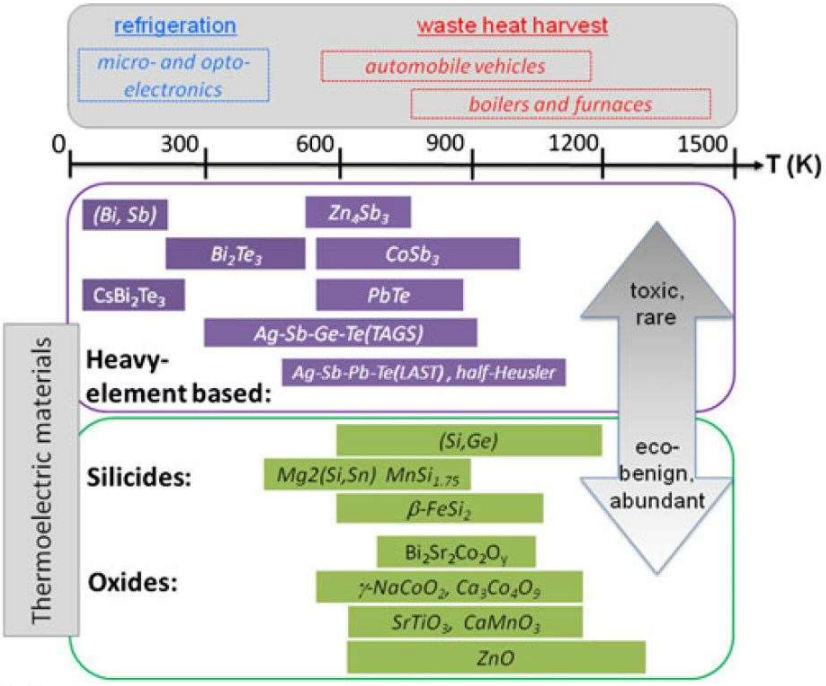

Figure 1. 11 Schematic comparison of various thermoelectric materials for applications of waste heat harvest and refrigeration, in terms of the temperature range of operation and the abundance and environmental friendliness of constituent elements. Taken from Ref. 106.

As mentioned earlier, currently, most of the thermoelectric materials with good

performance generally belong to heavy elements metallic alloys, such as $(Bi, Sb)_2Te_3$, PbTe, $CoSb_3$, SiGe, etc. Although their *ZT* values are high, they still have the disadvantages of chemical instability, high cost, and containing toxic heavy elements (such as Te), which have to be limited in their applications. In contrast, oxides have obvious advantages due to their good thermal and chemical stability and are considered for potential thermoelectric materials [27, 32, 106, 107].

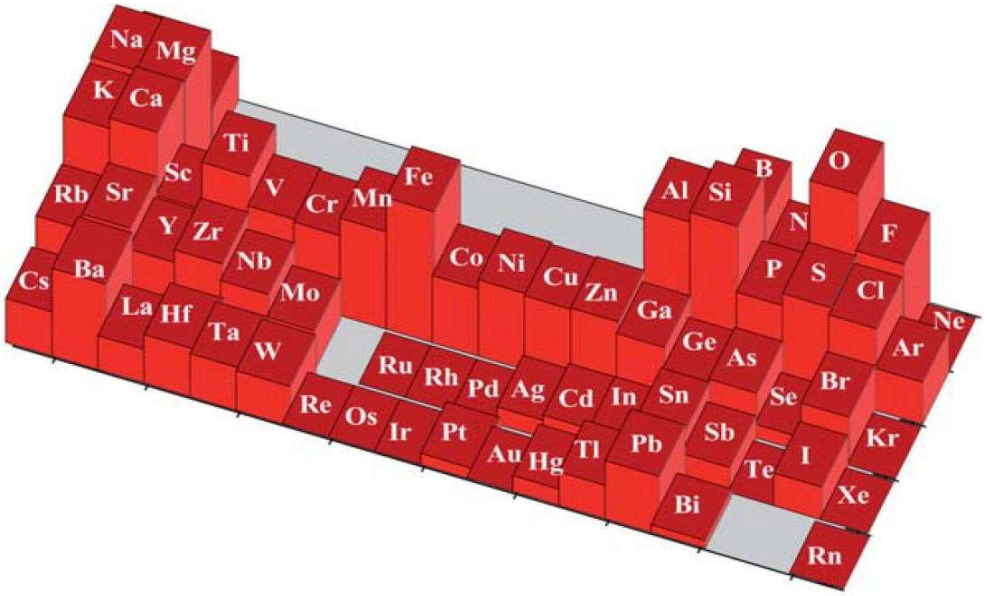

Figure 1. 12 The relative abundance of the principal elements in the earth's crust, presented using a logarithmic scale. Taken from Ref. 108.

In recent years, oxide thermoelectric materials are considered to be a promising type of thermoelectric material due to their thermal and chemical stability (oxidation resistance) and can contain elements with low toxicity, abundance, and low cost, as shown in Figure 1. 11 and Figure 1. 12. Research on oxide thermoelectric materials began in the 1950s. However, it has long been thought that oxides could not be used as high-performance thermoelectric materials, as the metal-oxygen bonds characteristic of such materials promote heat conduction. Oxides have hence larger lattice thermal conductivities than other alloys. Researchers changed their view on oxide thermoelectric materials until the report of thermoelectric Na_xCoO_2 layered single crystals (like Figure 1. 13) with a high thermoelectric power factor [109, 110, 111].

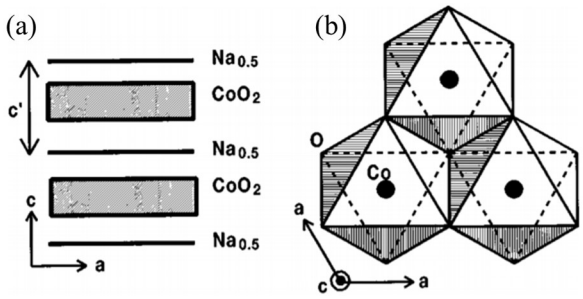

Figure 1. 13 Schematic picture of the crystal structure of $NaCo_2O_4$. (a) Layered structure and (b) CoO_2 layer. Taken from Ref. 109.

Since then, layered Co-based oxide thermoelectric materials have been reported successively, and the *ZT* has been continuously improved [112, 113], in which spin and orbital degree of freedoms can play a major role [114, 115]. With the continuous research on various oxide thermoelectric materials, it is believed that not only their thermoelectric properties will be further improved, but also their physical nature will be deeply understood allowing to open the door to other (layered) thermoelectric oxides of different compositions and structures, as doped TiO_2, $KNbO_3$, $ZnNb_2O_6$, for instance, Figure 1. 14. Then, high-performance oxide thermoelectric materials have also been studied as an important material in thermoelectric power generation and refrigeration. As one of many oxide thermoelectric materials, perovskite oxide of general formula ABO_3 has attracted much attention with its unique advantages.

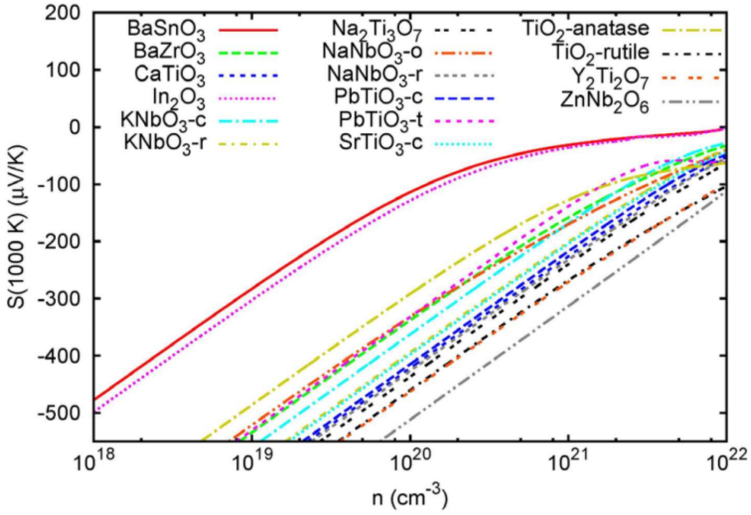

Figure 1. 14 Seebeck (at 1000 K) as a function of doping level on a log scale. Taken from Ref. 116.

1.4. State-of-the-art thermoelectric perovskite oxides

Perovskite structure originally refers to the calcium titanium oxide ($CaTiO_3$), which was discovered by German geologist G. Rose in 1830 and named after Russian geologist C. L.

Perovski. Perovskite is the most abundant mineral on our planet. It is estimated that more than 50% of the components in the crust are perovskite-type compounds.

The general chemical formula for perovskite crystal is ABO_3, which has a cubic structure and belongs to the space group O_h-*Pm*3*m*. A is an alkaline earth metal or lanthanide cation, coordinated with 12 O, and is located in the center of the cube. B is a 3*d* transition metal cation, coordinated with 6 O, and located at the center of an octahedron composed of 6 O, as shown in Figure 1. 15.

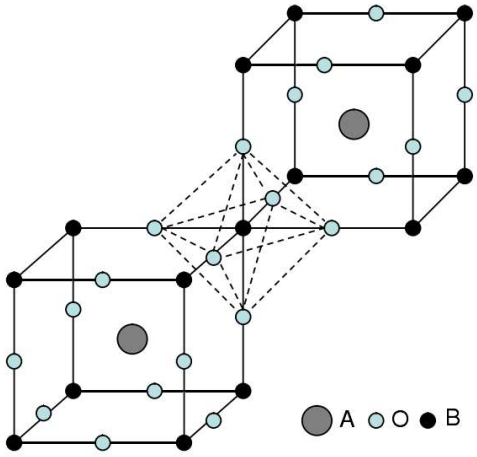

Figure 1. 15 Crystalline structure of perovskite oxides ABO_3.

A tolerance factor (t) is defined as:

$$t = \frac{r_A + r_O}{\sqrt{2}\left(r_B + r_O\right)} \tag{1.11}$$

where r_A, r_B, and r_O are the empirical radii of the corresponding ions. The material can be defined as a perovskite crystal for $0.7 < t < 1.1$ although the perovskite structure is predicted nearly cubic and stable only when t is between 0.8 and 1.0 [117]. The structure is orthorhombic for $t < 0.8$, and hexagonal for $t > 1$. An octahedral factor (μ) is also proposed: $\mu = r_B/r_O$, and it has to be in between 0.44 and 0.9 for ideal crystal structure [118]. Recently, Bartel *et al.* [119] developed an accurate, physically interpretable, and one-dimensional tolerance factor, which correctly predicts 92% of compounds as perovskite or nonperovskite.

$$t = \frac{r_X}{r_B} - n_A\left(n_A - \frac{r_A / r_B}{\ln\left(r_A / r_B\right)}\right) \tag{1.12}$$

where n_A is the oxidation state of A, r_i is the ionic radius of ion i, $r_A > r_B$ by definition, and $t <$ 4.18 indicates perovskite.

1.4.1. Advantages of perovskite oxides

Compared to the state-of-the-art metallic alloys like tellurides, which have been mentioned before, perovskite-type compounds have a lot of advantages, beyond high chemical stability and elemental abundance, chemical flexibility. The structure can host an impressive variety of cations. The set of elements that can occupy the A-site and B-site of the structure are given in Figure 1. 16.

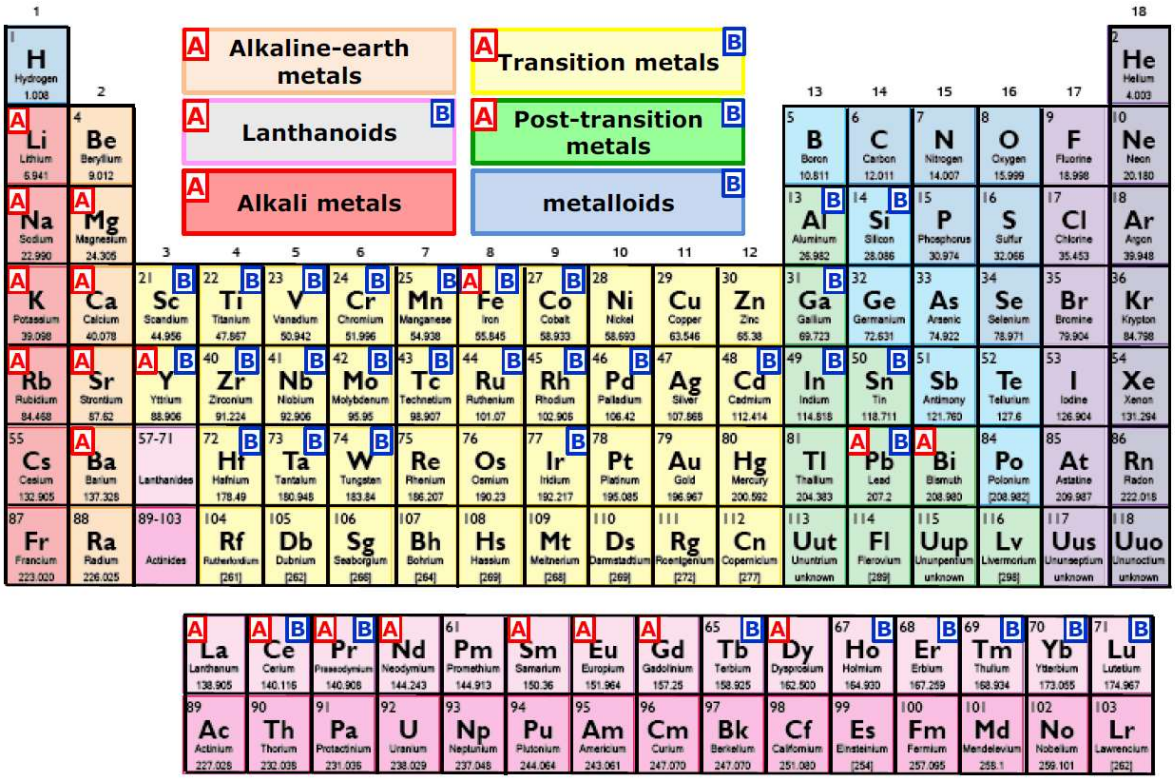

Figure 1. 16 Periodic table of atoms that can be accommodated on the A-site and B-site of the perovskite oxide. Taken from Ref. 120.

As can be seen from Figure 1. 16, there are many different possibilities for the cations at A-site and B-site. Therefore, the functional properties of perovskite oxides can be easily controlled and tuned by doping and partial cationic substitutions. This chemical flexibility, which is extremely attractive for many applications, offers the perovskite-oxide family a variety of functional properties, such as thermoelectricity, piezoelectricity, ferroelectricity, ferromagnetism, etc. Based on these special physical and chemical properties, perovskite-oxide materials can be used for a large number of applications, such as sensors [121, 122], bio-detectors [123], fuel cells [124], catalysis [125], non-volatile memories [126], photonic components [127], solar cells [128], recovery of thermal energy [129], and so on.

It has been reported that some tunable conducting perovskite oxides can present a large thermopower, as in the case of electron-doped $SrTiO_3$ [69]. As mentioned in section 1.2.4, two main methods have been utilized to enhance the *ZT* value of thermoelectric materials. The one is tuning the electrical part and enhanced the thermoelectric power factor. The other one is the engineering of structure to decrease thermal conductivity while maintaining acceptable electronic transport properties.

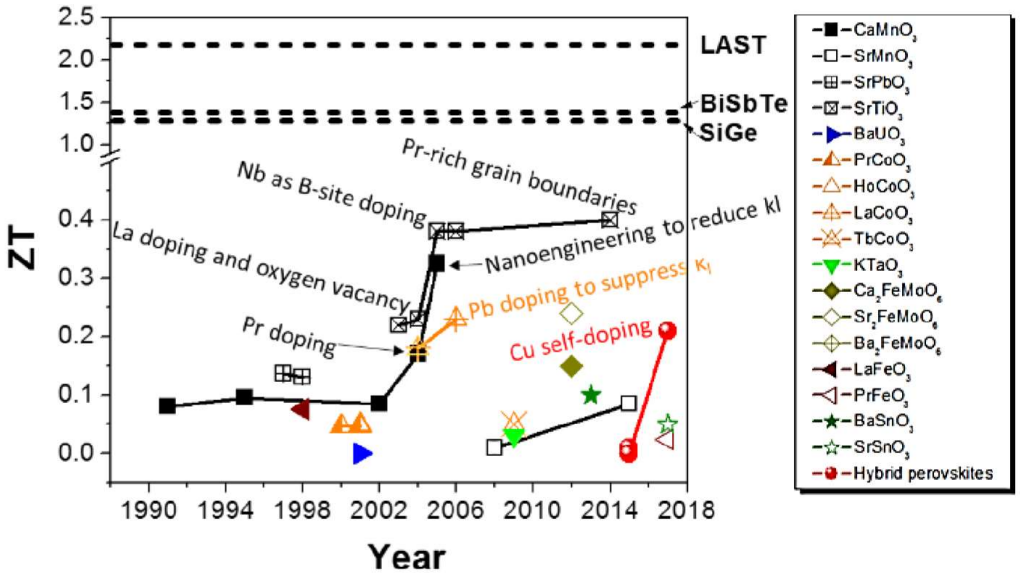

Figure 1. 17 Summary of *ZT* values of perovskite oxides by year. The thermoelectric *ZT* values of all materials were extracted from literature at its optimum working temperature. The three dashed lines are the *ZT* values of BiSbTe [85], $AgPb_{18}SbTe_{20}$ (LAST) [130], and SiGe [131], having a different optimum working temperature. Taken from Ref. 132.

Perovskite oxides can thus be applied as alternative thermoelectric materials. According to the literature, their highest *ZT* value obtained experimentally is nearly 0.4 [132], as shown in Figure 1. 17 along with other relatively good thermoelectric perovskite oxides so far. In general, the *n*-type thin-film perovskite oxides (*i.e.* La-doped $SrTiO_3$, Nb-doped $SrTiO_3$) show a better thermoelectric performance than *p*-type. Moreover, inducing a small amount of oxygen vacancy can lead to a positive effect on electrical conductivity for *n*-type perovskite oxides. Therefore, the thermoelectric properties of *p*-type need to be developed and investigated in many details.

In the following parts, the different perovskite-oxide materials are classified as *n*-type and *p*-type, and their thermoelectric properties are discussed. An overview of the reported thermoelectric data for perovskite oxides is shown in the tables below.

Table 1. 1 Literature data about thermoelectric properties of *n*-type perovskite oxides.

Reference		Material		Elaboration method	σ	S	PF	κ	ZT	T
					$S \cdot cm^{-1}$	$\mu V \cdot K^{-1}$	$\mu W \cdot cm^{-1} \cdot K^{-2}$	$W \cdot m \cdot K^{-1}$		K
		$Tb_{0.1}Ca_{0.9}MnO_3$							0.13	
[160]	1991	$Ho_{0.1}Ca_{0.9}MnO_3$	powders						0.08	1000
		$Y_{0.1}Ca_{0.9}MnO_3$							0.15	
[165]	1997								0.13	
		$Ba_xSr_{1-x}PbO_3$ (0 < x < 1)	ceramics		from 20 to 1585					673
[166]	2003								(max)	
[69]	2001	$La_xSr_{1-x}TiO_3$ (0 < x < 0.1)	bulk single crystal	floating-zone			from 28 to 36			343
[133]	2001	$BaNb_xTi_{1-x}O_3$ ($0.01 \leq x \leq 0.05$)	ceramics			from -50 to -650				300
[161]	2002	$Bi_{0.04}Ca_{0.96}MnO_3$	polycrystalline						0.086	1000
[146]	2003	$Sr_{0.9}Dy_{0.1}TiO_3$	polycrystalline						0.22	573
[134]	2003	$CaMn_{0.96}Mo_{0.04}O_3$	ceramics		154				0.012	270
[152]	2004	$Ba_{0.3}Sr_{0.6}La_{0.1}TiO_3$	polycrystalline						0.126	420
[162]	2004	$Pr_{0.15}Ca_{0.85}MnO_{2.98}$	powders						0.17	1100
[135]	2004	$CaMn_{0.96}Ta_{0.04}O_3$	polycrystalline		29				0.05	1000
		$La_xSr_{1-x}TiO_3$			54	-420	9.5	12	0.02	253
					1000	-150	23	9.1	0.08	320
[153]	2005		bulk single crystal	conventional verneuil						
					95	-330	10	11	0.03	322
		$SrNb_xTi_{1-x}O_3$								
					353	-240	20	9.6	0.06	288
[154]	2005	$La_{0.05}Sr_{0.95}TiO_3$	bulk single crystal		150	-260	10	5.5	0.14	773

[159]	2005	$SrNb_{0.2}Ti_{0.8}O$	film	pulsed laser deposition						0.37	1000
[136]	2006	$Yb_{0.1}Ca_{0.9}MnO_3$	polycrystalline		167					0.16	1000
[137]	2008	$SrMn_{0.7}Ru_{0.3}O_3$	polycrystalline		67					0.01	370
[163]	2008	$CaMn_{0.98}Nb_{0.02}O_3$	polycrystalline		31	-240	1.78	0.8		0.32	1070
[147]	2009	$SrTiO_{2.97}$	polycrystalline				10				300
[138]	2009	$La_{0.1}Sr_{0.9}TiO_{3-\delta}$	ceramics							0.21	750
[149]	2009	$BaTiO_{3-\delta}$	polycrystalline		11	-280					300
[139]	2009	$SrTi_{0.9}Ta_{0.1}O_3$	polycrystalline		300	-175	9.2	4		0.17	752
[155]	2010	$La_{0.15}Sr_{0.85}TiO_{3-\delta}$	film	pulsed laser deposition						0.28	873
[158]	2010	$La_xSr_{1-x}TiO_3$	film	molecular beam epitaxy	from 0.2 to 2000	from -100 to -1000	39 (max)				300
[148]	2011	$SrTiO_{3-\delta/2}$ ($0.0046 < \delta < 0.06$)	polycrystalline		5-1000		20				300
[167]	2013	$La_{0.002}Ba_{0.998}SnO_3$	polycrystalline							0.1	1073
[140]	2014	$Pr_{0.125}Sr_{0.875}TiO_3$	polycrystalline					1.3		0.4	773
[156]	2015	$La_xSr_{1-x}TiO_{3-\delta}$	film	pulsed laser deposition		from -120 to -260					
[164]	2015	$Sr_{0.7}Pr_{0.3}MnO_3$	polycrystalline							0.085	1073
[168]	2017	$La_{0.01}Sr_{0.99}SnO_3$	polycrystalline							0.05	1073

Table 1. 2 Literature data about thermoelectric properties of *p*-type perovskite oxides.

Reference		Material		Elaboration method	σ	S	PF	κ	ZT	T
					$S \cdot cm^{-1}$	$\mu V \cdot K^{-1}$	$\mu W \cdot cm^{-1} \cdot K^{-2}$	$W \cdot m \cdot K^{-1}$		K
[141]	1988	$La_{0.9}Ca_{0.1}MnO_3$	single crystal	arc-image floating zone	1	300	0.09			220
		$La_{0.7}Ca_{0.3}MnO_3$			100	10	0.01			
		$La_{0.8}Sr_{0.2}MnO_3$			100	4	0.0016			150
		$La_{0.6}Sr_{0.4}MnO_3$			630	1	0.0006			
[169]	2000	$Gd_{0.9}Ca_{0.1}CoO_3$	ceramics		21					
		$Pr_{0.9}Ca_{0.1}CoO_3$			210	108	2.4		0.047	358
[170]	2001	$Pr_{0.9}Ca_{0.1}CoO_3$	ceramics		350					
		$Pr_{0.9}Ba_{0.1}CoO_3$			420					
[171]	2001	$Ho_{0.9}Ca_{0.1}CoO_3$	ceramics		2	210	0.088	0.75	0.051	573
[172]	2004	$La_{0.95}Sr_{0.05}CoO_3$	polycrystalline			710		3.7	0.18	300
[173]	2006	$La_{0.9}Sr_{0.1}CoO_3$	polycrystalline		108	120	2.5	1.45	0.046	300
		$La_{0.8}Sr_{0.2}CoO_3$			296					
[142]	2006	$La_{0.875}Sr_{0.125}CoO_3$	single crystal						0.035	225
[174]	2008	$La_{0.9}Pb_{0.1}CoO_3$	polycrystalline		250	110	3	1.55	0.23	575
		$La_{0.9}Na_{0.1}CoO_3$	polycrystalline		33			0.9		575
[143]	2012	$La_{0.67}Sr_{0.33}MnO_3$/LMO	film	pulsed laser deposition	2.2			0.89		300
[144]	2013	$La_{0.67}Sr_{0.33}MnO_3$/LMO	film	pulsed laser deposition	0.007	2560	0.04			300
						16640	0.95		0.037	360

[187]	2014	$La_{0.96}Sr_{0.04}CrO_3$	film	molecular beam epitaxy	1.5	321	0.15		300
		$La_{0.88}Sr_{0.12}CrO_3$			3	281	0.24		
		$La_{0.75}Sr_{0.25}CrO_3$			15	180	0.49		
		$La_{0.5}Sr_{0.5}CrO_3$			50	80	0.32		

1.4.2. *N*-type thermoelectric perovskite oxides

To enhance the electrical conductivity, chemical doping by partial aliovalent cationic substitution is commonly applied. For *n*-type (electron-doped) thermoelectric perovskite oxides, oxygen vacancy, doping/substitution at A-site, and/or B-site cations are effective ways. The main studies are divided into the titanates and manganates.

1.4.2.1. Titanates

The reported *ZT* as a function of temperature is shown in Figure 1. 18. All the materials presented here are *n*-type thermoelectric materials.

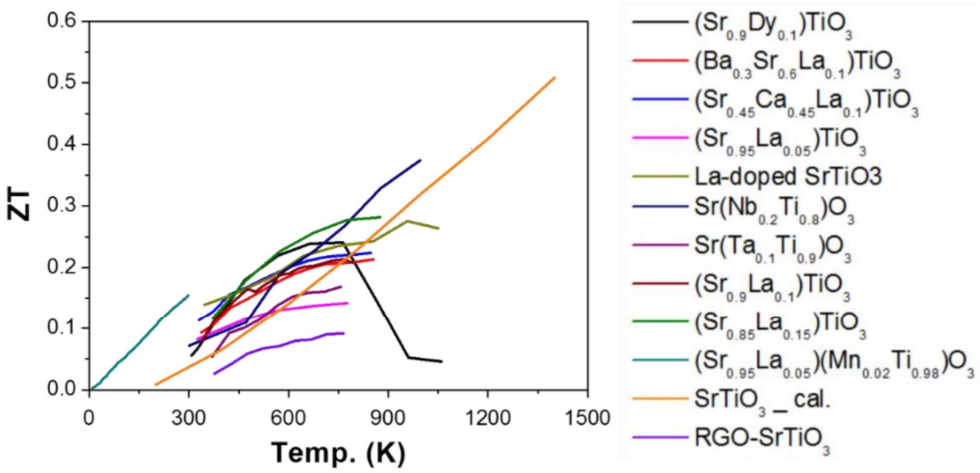

Figure 1. 18 *ZT* value of $ATiO_3$ based oxide perovskite materials, all the materials are *n*-type semiconductors. The symbol "cal." means the results come from the calculation. Taken from Ref. 132.

(a) Polycrystalline

One of the archetypal titanates is the band insulator $SrTiO_3$. $SrTiO_3$ can become conducting and thermoelectric when doped with partial aliovalent cationic substitution or oxygen vacancy [145]. *N*-type is obtained with partial substitution with higher valence cations (Nb^{5+} on Ti^{4+}, or La^{3+} on Sr^{2+} for instance), and/or with oxygen vacancies.

Almost twenty years ago, Muta *et al*. studied [146] the thermoelectric properties of polycrystalline $R_{0.1}Sr_{0.9}TiO_3$ (R: Y, La, Sm, Gd, Dy). They found that $Sr_{0.9}Dy_{0.1}TiO_3$ showed the highest *ZT*, reaching 0.22 at 573 K. Onoda and Goto [147] investigated the structural and electronic properties in the metal-band-insulator crossover of polycrystalline $SrTiO_{3-\delta/2}$. A thermoelectric power factor over 10 $\mu W \cdot cm^{-1} \cdot K^{-2}$ was obtained for $SrTiO_{2.97}$ at 300 K. After

two years, Onoda and Tsukahara [148] studied the polycrystalline $SrTiO_{3-\delta/2}$ with $0.0046 \leq \delta < 0.06$. The electrical conductivity was enhanced from 5 to 1000 $S \cdot cm^{-1}$ when δ increased from 0.0046 to 0.06. An upper limit of 20 $\mu W \cdot cm^{-1} \cdot K^{-2}$ was obtained for the thermoelectric power factor with a carrier concentration of 2×10^{20} cm^{-3}. Moreover, Lee *et al.* [149] fabricated polycrystalline $BaTiO_3$ inducing oxygen vacancies by using a specific process [150]. The electrical conductivity reached 11 $S \cdot cm^{-1}$ at 300 K with a carrier concentration of 3×10^{20} cm^{-3}, while the single crystal $BaTiO_3$ shows electrical conductivity of only 0.05 $S \cdot cm^{-1}$ at 300 K [151]. However, the Seebeck coefficient decreased from -550 (single crystal [151]) to -280 $\mu V \cdot K^{-1}$ (polycrystalline [149]) at 300 K.

Furthermore, two cations can be doped/substituted at the same time to improve the overall thermoelectric performance. For example, Muta *et al.* [152] reported that the electrical conductivity of La-doped $BaTiO_3$-$SrTiO_3$ solid solutions increased from 200 to 2500 $S \cdot cm^{-1}$ when x increased from 0 to 0.9 at 420 K. The highest *ZT* value of $Ba_{0.3}Sr_{0.6}La_{0.1}TiO_3$ achieved is 0.126 at 420 K.

(b) Bulk single crystal

Okuda *et al.* [69] investigated the single crystals of $La_xSr_{1-x}TiO_3$ ($0 < x < 0.1$). They have found a large thermoelectric power factor 28-36 $\mu W \cdot cm^{-1} \cdot K^{-2}$ at room temperature with a carrier concentration of $0.2\text{-}2 \times 10^{21}$ cm^{-3}. This work constitutes an important reference for this material in this field (as shown in Figure 1. 19). Moreover, Ohta *et al.* [153] studied the electron and thermal transport properties of heavily La- or Nb-doped $SrTiO_3$ bulk single crystals at high temperatures. They have found that the density-of-states effective mass of Nb-doped $SrTiO_3$ was larger than that of La-doped $SrTiO_3$. The thermal conductivity of the samples was similar to that of undoped $SrTiO_3$ single crystal, namely about 11 $W \cdot m^{-1} \cdot K^{-1}$. In the same year, Muta *et al.* [154] indicated that La doping of single-crystalline $SrTiO_3$ is probably attributed to the decrease of the mean free path of the phonons caused by lattice defects. The *ZT* value achieved for $La_{0.05}Sr_{0.95}TiO_3$ was 0.14 at 773 K for a carrier concentration of about 8×10^{20} cm^{-3} and an electrical conductivity of 150 $S \cdot cm^{-1}$.

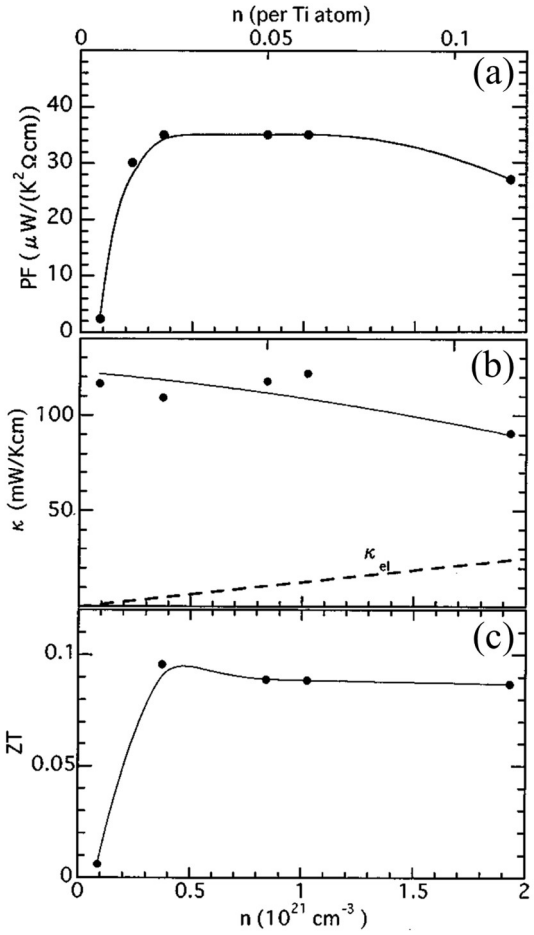

Figure 1. 19 Carrier doping dependence of power factor, thermal conductivity, and the *ZT* value at room temperature in $La_xSr_{1-x}TiO_3$. Solid lines are guides to the eye and a dashed line represents the electronic thermal conductivity (κ_e) estimated by the Wiedemann-Franz law. Taken from Ref. 69.

(c) Thin film

Thin-film materials have also attracted widespread attention for application purposes. Ravichandran *et al*. [155] grow $SrTiO_3$ epitaxial thin films doped with both La and oxygen vacancies by pulsed laser deposition. They reported that a high *ZT* value of 0.28 was achieved for the $La_{0.15}Sr_{0.85}TiO_3$ film at 873 K (shown in Figure 1. 20a and b) at a carrier concentration of 2.5×10^{21} cm^{-3}.

Similarly, Choi *et al*. [156] investigated La-doped $SrTiO_3$ thin films with controlled elemental vacancies by varying the oxygen partial pressure $P(O_2)$ via pulsed laser deposition. The carrier concentration was tuned from 4.3×10^{20} to 1.15×10^{21} cm^{-3} when $P(O_2)$ decreased from 10^{-2} to 10^{-6} Torr. The Seebeck coefficient of thin films can be largely modulated from -120 to -260 $\mu V\cdot K^{-1}$. The oxygen vacancy can increase the carrier concentration of the *n*-type perovskite oxides, thus improving the electrical conductivity.

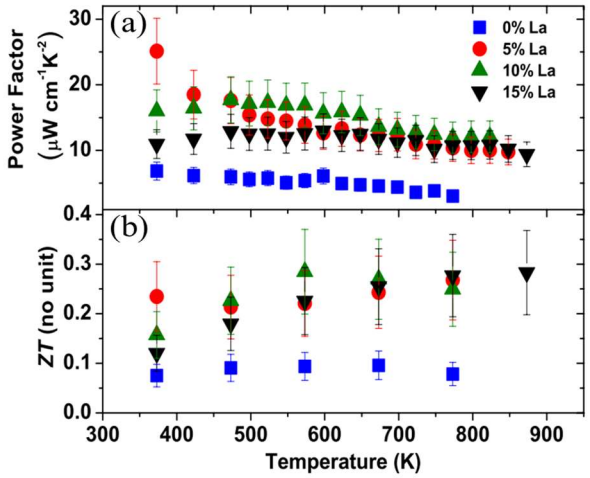

Figure 1. 20 (a) and (b) Thermoelectric power factor and *ZT* of $SrTiO_3$ epitaxial thin films doped with both La and oxygen vacancies as a function of temperature. Taken from Ref. 155.

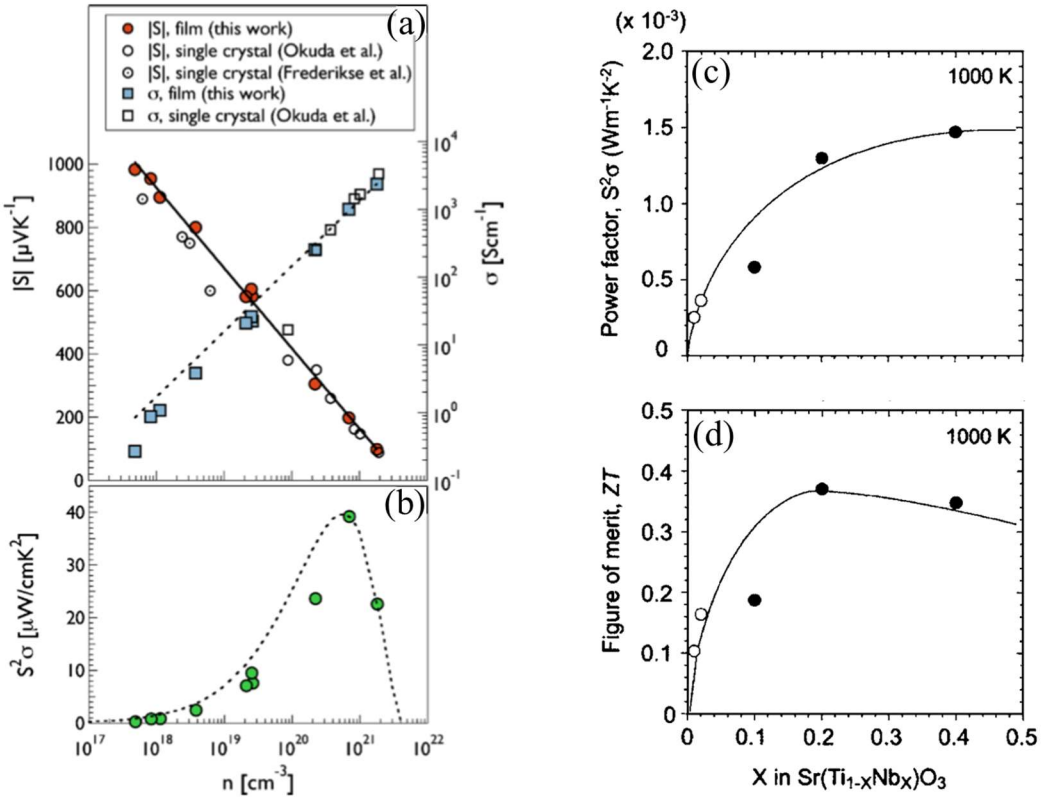

Figure 1. 21 (a) Seebeck coefficient (circles) and electrical conductivity (squares) as a function of carrier concentration for the La-doped $SrTiO_3$ films and single crystals in the literature (open symbols). The literature data is from Refs. 157 and 69. (b) The power factor of La-doped $SrTiO_3$ films as a function of carrier concentration. Taken from Ref. 158. Nb concentration dependence of (c) thermoelectric power factor and (d) *ZT* for Nb-doped $SrTiO_3$ epitaxial films at 1000 K. Open circles are for the single crystals and solid circles are for the films. Taken from Ref. 159.

It is worth noting that Jalan and Stemmer prepared $La_xSr_{1-x}TiO_3$ thin films [158]. They found the films showing very high Seebeck coefficients up to 980 $\mu V \cdot K^{-1}$ at low carrier

concentrations. Confirming the work of Okuda *et al.* on bulk single-crystals [69], a large room-temperature thermoelectric power factor about 39 $\mu W \cdot cm^{-1} \cdot K^{-2}$ was obtained, with a carrier concentration of 3×10^{20} cm^{-3} as shown in Figure 1. 21a and b, which can be compared with that of $(Bi, Sb)_2Te_3$ based alloy.

Additionally, Ohta *et al.* [159] studied the B-site doping/substitution of titanate. They grew the $SrNb_xTi_{1-x}O_3$ ($0.01 < x < 0.4$) epitaxial films by pulsed-laser deposition, in which substituted Nb^{5+} at Ti^{4+} site generates carrier electrons. The highest *ZT* value of 0.37 was obtained for the $SrNb_{0.2}Ti_{0.8}O_3$ film at 1000 K shown in Figure 1. 21c and d.

Finally, recent theoretical work shows that different *n*-type dopants in $SrTiO_3$ globally yield similar thermoelectric properties, in agreement with experimental results [70].

1.4.2.2. Manganates

Manganates are another widely-studied thermoelectric perovskite oxide. The *ZT* values as a function of temperature are shown in Figure 1. 22, where all the materials here are *n*-type semiconductors.

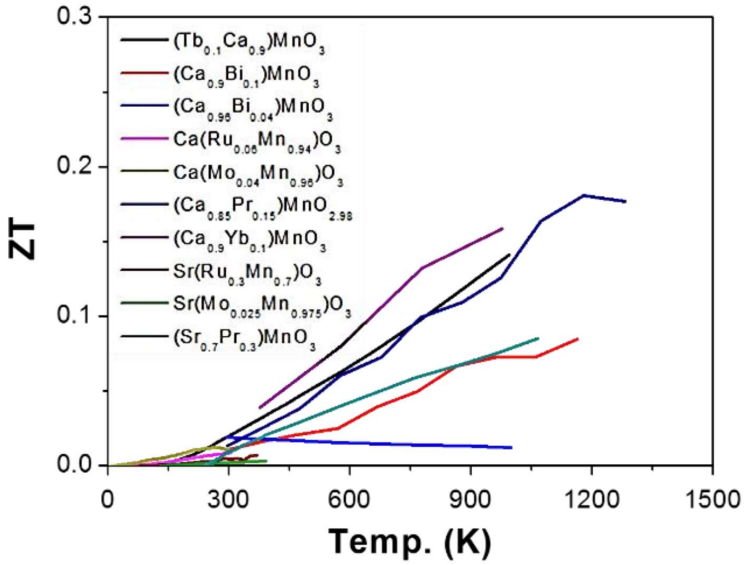

Figure 1. 22 *ZT* value of $AMnO_3$ based oxide perovskite materials. All the materials are *n*-type semiconductors. Taken from Ref. 132.

Since a few decades ago, Kobayashi *et al.* [160] have investigated the electrical conductivity of $R_xCa_{1-x}MnO_3$ (R: Tb, Ho, Y) powders, which increased with x value from 0.1 to 0.3 (*e.g.*, from 100 to 182 $S \cdot cm^{-1}$ for $Tb_xCa_{1-x}MnO_3$, from 91 to 250 $S \cdot cm^{-1}$ for

$Ho_xCa_{1-x}MnO_3$), and the highest *ZT* value was achieved at x = 0.13, 0.08, and 0.15, for $Tb_{0.1}Ca_{0.9}MnO_3$, $Ho_{0.1}Ca_{0.9}MnO_3$, and $Y_{0.1}Ca_{0.9}MnO_3$, respectively. Similarly, Xu *et al.* [161] reported that the electrical conductivity of polycrystalline $Bi_xCa_{1-x}MnO_3$ increased from 32 to 222 $S \cdot cm^{-1}$ when x changed from 0.02 to 0.2. A *ZT* value of 0.086 was obtained at 1000 K for x = 0.04. Moreover, Cong *et al.* [162] combined the Pr-A-site doping and oxygen vacancy then fabricated $Pr_xCa_{1-x}MnO_{3-\delta}$ ($0 < x < 0.15$) powders. The electrical conductivity increased from 40 to 125 $S \cdot cm^{-1}$ at 1100 K when x changed from 0 to 0.15, leading to the highest *ZT* value of 0.17 at 1100 K for $Pr_{0.15}Ca_{0.85}MnO_{2.98}$. Furthermore, Bocher *et al.* [163] have synthesized polycrystalline $CaMn_{0.98}Nb_{0.02}O_3$ compounds, which have an electrical conductivity of 31 $S \cdot cm^{-1}$, Seebeck coefficient of -240 $\mu V \cdot K^{-1}$, and thermal conductivity of 0.8 $W \cdot m^{-1} \cdot K^{-1}$ at 1070 K, leading a *ZT* value of 0.32. This significant enhancement of *ZT* value to 0.32 was mainly attributed to low thermal conductivity, caused by phonon scattering from the nanosized twinned domains or the porous morphology.

Additionally, Nakatsugawa *et al.* [164] synthesized polycrystalline $Sr_xPr_{1-x}MnO_3$ ($0.1 \leq x \leq 0.7$), which can form both *n*-type and *p*-type semiconductors. They found that all the samples showed a negative Seebeck coefficient at a high temperature. The largest *ZT* was 0.085 at 1073 K for x = 0.7. Also, they obtained the largest *ZT* in the *p*-type specimens for x = 0.1, thus, attaining a maximum value of 0.0035 at 468 K.

1.4.2.3. Other perovskite systems

Furthermore, there are still other *n*-type perovskite oxides showing relatively good thermoelectric performance. For example, Yasukawa and Murayama [165, 166] studied the bulk $Ba_xSr_{1-x}PbO_3$ ($0 < x < 1$) since the last century. The electrical conductivity increased from 20 to 1585 $S \cdot cm^{-1}$ when x changed from 0 to 1. A *ZT* of 0.13 was achieved at 673 K when x = 0.4. Besides, Yasukawa *et al.* [167] studied the polycrystalline La-doped $BaSnO_3$. They prepared $La_xBa_{1-x}SnO_3$ with x = 0.002, 0.005, 0.008, and 0.010. The electrical conductivity increased from 120 to 350 $S \cdot cm^{-1}$ when x changed from 0.002 to 0.01. A *ZT* value reached 0.1 at 1073 K for $La_{0.002}Ba_{0.998}SnO_3$. More recently, they also studied the $La_xSr_{1-x}SnO_3$ ceramics with x from 0.01 to 0.05. The electrical conductivity increased from 4 to 120 $S \cdot cm^{-1}$ when x changed from 0.01 to 0.03. A *ZT* value of 0.05 was achieved at 1073 K for $La_{0.01}Sr_{0.99}SnO_3$ [168].

1.4.3. *P*-type thermoelectric perovskite oxides

A complete thermoelectric device requires two types of semiconductors, *n*-type and *p*-type (see section 1.5). For further applications, their thermoelectric properties must be matched with each other. However, the *p*-type thermoelectric perovskite oxides are currently relatively scarcer and less studied than *n*-types. Also, their thermoelectric properties are not as good as those of *n*-type. We can mention the main following *p*-type thermoelectric oxides of perovskite structures: cobaltates, chromates, and manganates.

1.4.3.1. Cobaltates

Cobaltates are the first *p*-type thermoelectric perovskite oxides that have been studied, following the works on $NaCo_2O_4$ [109]. The reported *ZT* as a function of temperature when Co is used as B-site perovskite oxide is presented in Figure 1. 23. All the materials here are *p*-type semiconductors.

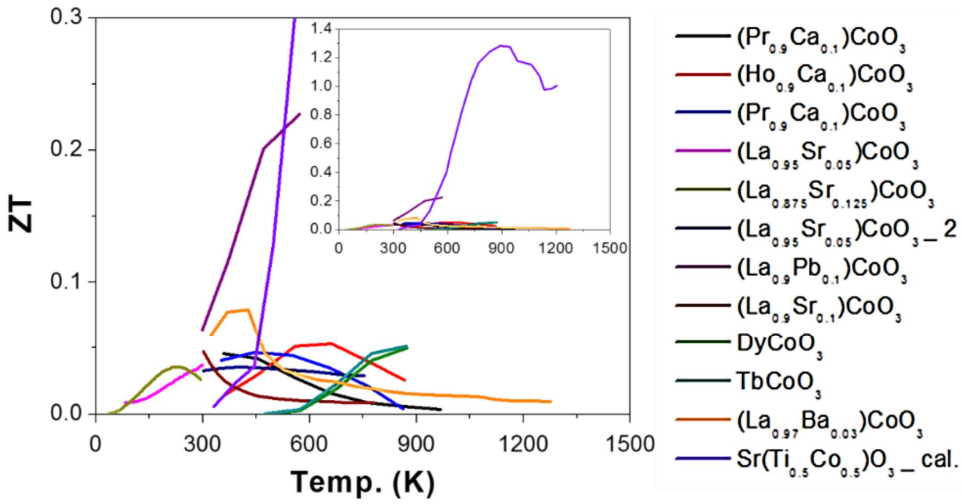

Figure 1. 23 *ZT* value of $ACoO_3$ based oxide perovskite materials. All the materials are *p*-type semiconductors. The symbol "cal." means the results come from the calculation. Taken from Ref. 132.

Moon *et al.* [169] presented the thermoelectric properties of ceramics $R_{0.9}Ca_{0.1}CoO_3$ (R: Gd, Sm, Nd, Pr) twenty years ago. The results showed that the electrical conductivity, which increased sharply with increasing the ionic radius of the rare-earth element (Pr > Nd > Sm > Gd), changed from 23 to 210 $S \cdot cm^{-1}$ when the samples changed from $Gd_{0.9}Ca_{0.1}CoO_3$ to $Pr_{0.9}Ca_{0.1}CoO_3$. A relatively high *ZT* value of 0.047 was achieved at 358 K for $Pr_{0.9}Ca_{0.1}CoO_3$. Later, they observed that when the ionic radius of dopants ($Ca^{2+} < Sr^{2+} < Ba^{2+}$) increased for

$Pr_{0.9}M_{0.1}CoO_3$ (M: Ca, Sr, Ba), the electrical conductivity increased from 350 to 420 $S \cdot cm^{-1}$ when varied from $Pr_{0.9}Ca_{0.1}CoO_3$ to $Pr_{0.9}Ba_{0.1}CoO_3$ [170]. Also, they investigated the thermoelectric properties of $Ho_{1-x}Ca_xCoO_3$. The electrical conductivity was enhanced from 1×10^{-4} to 2 $S \cdot cm^{-1}$ when x changed from 0 to 0.1 at 573 K. The highest *ZT* value obtained was 0.051 at 573 K for $Ho_{0.9}Ca_{0.1}CoO_3$ with Seebeck coefficient of 210 $\mu V \cdot K^{-1}$ and thermal conductivity of 0.75 $W \cdot m^{-1} \cdot K^{-1}$ [171].

Moreover, Androulakis *et al*. [172] found that the polycrystalline $La_{0.95}Sr_{0.05}CoO_3$ exhibits a very respectable room-temperature *ZT* value of 0.18 with a Seebeck coefficient of 710 $\mu V \cdot K^{-1}$ and thermal conductivity of 3.7 $W \cdot m^{-1} \cdot K^{-1}$. Similarly, Zhou *et al*. [173] prepared polycrystalline $La_{1-x}Sr_xCoO_3$ ($0 \leq x \leq 0.2$). The electrical conductivity was enhanced from 2 to 296 $S \cdot cm^{-1}$ when x changed from 0 to 0.2 at 300 K. A *ZT* value of $La_{0.9}Sr_{0.1}CoO_3$ obtained was 0.046 at 300 K with electrical conductivity of 180 $S \cdot cm^{-1}$, Seebeck coefficient of 120 $\mu V \cdot K^{-1}$, and thermal conductivity of 1.45 $W \cdot m^{-1} \cdot K^{-1}$. Additionally, He *et al*. [174] used lead and sodium as an A-site dopant for $LaCoO_3$ with composition $La_{0.9}R_{0.1}CoO_3$ (R: Pb, Na). The electrical conductivity for undoped polycrystalline $LaCoO_3$ was 25 $S \cdot cm^{-1}$ and was enhanced to 250 and 33 $S \cdot cm^{-1}$ at 575 K when doped with Pb ($La_{0.9}Pb_{0.1}CoO_3$) and Na ($La_{0.9}Na_{0.1}CoO_3$), respectively. The thermal conductivity of $LaCoO_3$, $La_{0.9}Pb_{0.1}CoO_3$, and $La_{0.9}Na_{0.1}CoO_3$ were 1.83, 1.55, and 0.9 $W \cdot m^{-1} \cdot K^{-1}$, respectively. A *ZT* value of 0.23 was achieved at 575 K for $La_{0.9}Pb_{0.1}CoO_3$, which was attributed to both increasing the electrical conductivity and suppressing the lattice thermal conductivity.

Although $LaCoO_3$ has been studied for more than thirty years for its magnetic properties [175, 176, 177, 178, 179, 180, 181], its thermoelectric properties are much less studied and mainly based on polycrystalline ceramics. At the same time, some thermoelectric properties in polycrystalline samples are reduced in single crystals. Berggold *et al*. [142] found that, at 225 K, $La_{1-x}Sr_xCoO_3$ ($0 \leq x \leq 0.3$) single crystal had the highest *ZT* value of 0.035 (when x = 0.125), which was much lower than that of polycrystalline materials. Therefore, it is important to develop other *p*-type thin-film thermoelectric perovskite oxides.

1.4.3.2. Chromates

As one of the interesting perovskite-type oxide, $LaCrO_3$ has attracted strong attention and motivated an increasing number of studies in the past few years due to its remarkable physical properties. $LaCrO_3$ is an antiferromagnetic insulator at room temperature [182, 183] and

can become a *p*-type transparent conductor with partial substitution with divalent strontium on A-site for instance [184, 185]. Substituting Sr^{2+} for La^{3+} in $LaCrO_3$ effectively dopes holes into the top of the valence band and results in *p*-type conductivity [186].

Zhang *et al*. [187, 186] investigated the transport properties of $La_{1-x}Sr_xCrO_3$ thin films. They first achieved the films and found that $La_{1-x}Sr_xCrO_3$ is also thermoelectric, the property which is tunable by the substitution ratio x (highest thermoelectric power factor nearly 0.5 $\mu W \cdot cm^{-1} \cdot K^{-2}$ at room temperature when x = 0.25), as shown in Figure 1. 24.

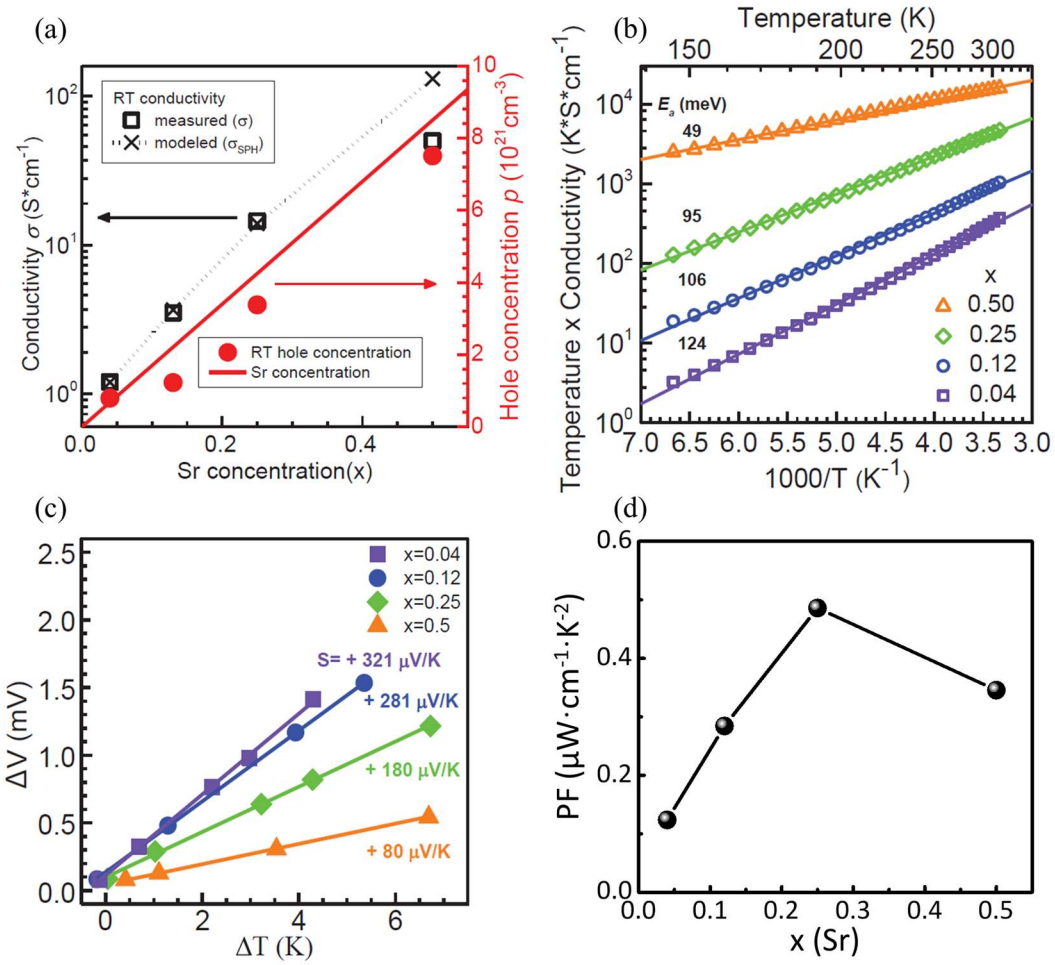

Figure 1. 24 (a) Room-temperature conductivity and hole concentration of $La_{1-x}Sr_xCrO_3$ films versus x. The $La_{0.5}Sr_{0.5}CrO_3$ film is deposited on the $LaAlO_3$ substrate, all others are deposited on the STO substrate. (b) Temperature dependence of the conductivity. (c) Seebeck coefficients as well as hole concentration as a function of Sr doping concentration. Taken from Ref. 187. (d) Room-temperature thermoelectric power factor extracted from (a) and (c). Not shown in reference but extracted by us.

In addition to the Pisarenko relation (see section 1.2.3.2), some authors tried to analyze the relationship between the hole concentration (*p*) and the Seebeck coefficient (*S*) [186].

Following the study from Farrell *et al*. [188], they determined *p* from *S* using a small polaron hopping model, which is appropriate for materials with extremely low mobilities.

$$S(c) = \frac{k_B}{e} \ln\left(\frac{2(1-c)}{c}\right) \tag{1.13}$$

where k_B is Boltzmann's constant, *e* is the electronic charge, and *c* is the fraction of hopping sites occupied with holes. Hole creation by Sr doping at a La site thus corresponds to activation of an adjacent Cr site for hole hopping [186].

$$p(c) = cN_{Cr} \tag{1.14}$$

where N_{Cr} is the Cr number density, 1.7×10^{22} cm^{-3}. Based on the equations (1.13) and (1.14), they determined the *p* value to range from 7.9×10^{20} to 7.5×10^{21} cm^{-3} with the corresponding mobilities [from equation (1.3) in section 1.2.3.3] of 0.009 to 0.04 $cm^2\cdot V^{-1}\cdot s^{-1}$ for x = 0.04 to 0.5. Although the mobility is low, the carrier concentration can easily be made high by Sr substitution for La. Therefore, the electrical conductivity can still be made high (up to 50 $S\cdot cm^{-1}$ in Figure 1. 24a).

Experimental measures show that the transport is due to small polaron hopping for x < 0.65 [186]. In the metallic state, all Cr-O bond lengths lie between 1.97 and 2 Å, and there is no significant difference between the four Cr atoms. In the polaronic state, the bond lengths decrease for one of the Cr atoms, while all other Cr atoms have longer Cr-O bonds: the O atoms are more localized around one of the Cr atoms [189]. Figure 1. 25 [189] represents the band structures of the metallic and polaronic systems calculated by the *ab-initio* method. A single state appears in the forbidden band. This state is the consequence of the localization of the hole around one of the Cr atoms due to the crystal structure obtained with the tetrahedron method. It lies 0.29 eV above the valence band, and its bandwidth is 0.17 eV. Other than that, the two band structures have only a few differences. The metallic material has many degenerated (or close to being degenerated) states, while in the polaronic one these are well separated [189]. Based on spectroscopic measurements (XPS and XAS) combined with density functional theory (DFT) calculations, hole introduction from Sr substitution for La is explained from chemical potential shifts towards the valence band and the creation of split-off empty Cr 3*d* t_{2g} / O 2*p* hybridized orbitals (Figure 1. 26) [187].

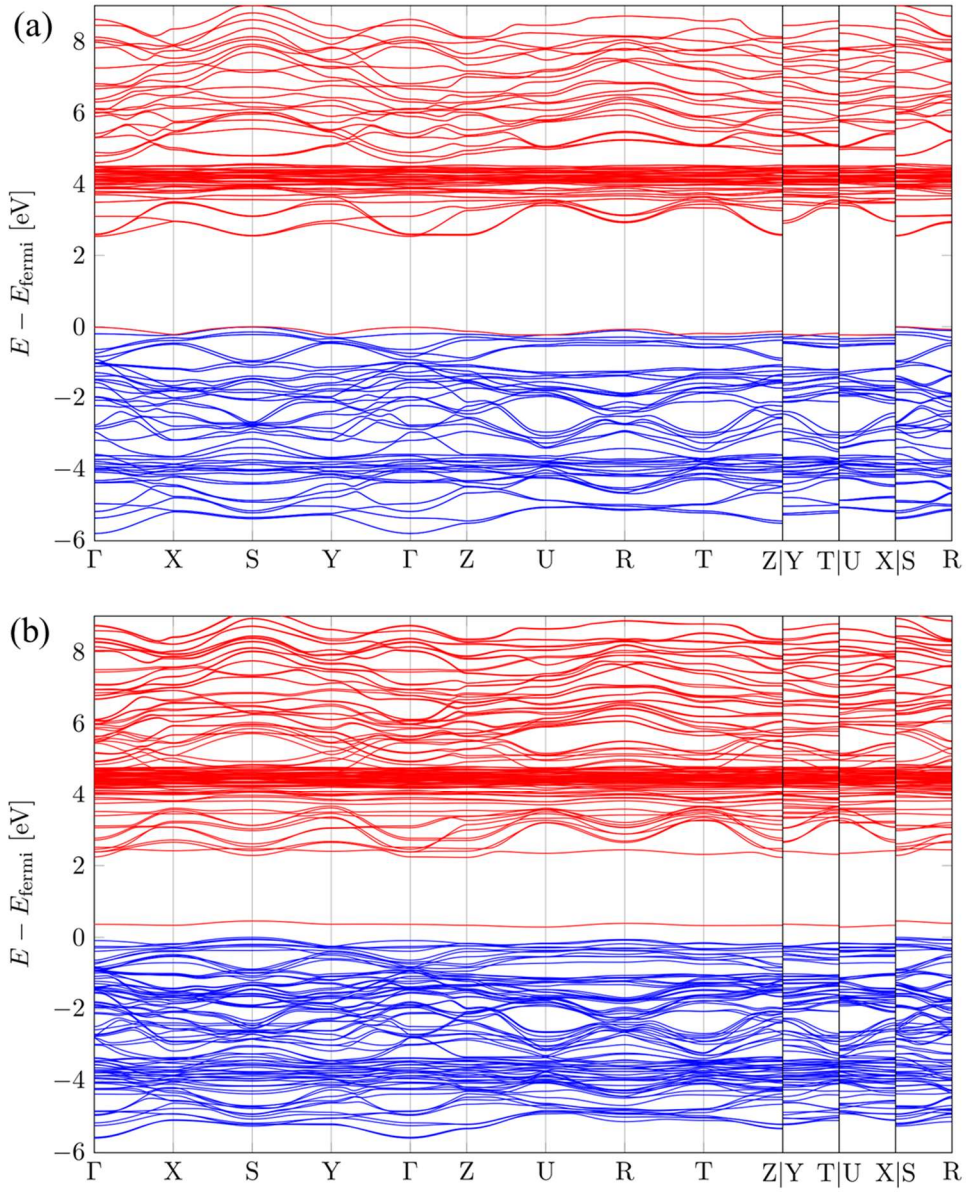

Figure 1. 25 Band structure of (a) metallic and (b) polaronic $La_{0.75}Sr_{0.25}CrO_3$ computed with a smearing of 0.01 Ha. Blue states are occupied at $T = 0$ K, and red ones are not. Taken from Ref. 189.

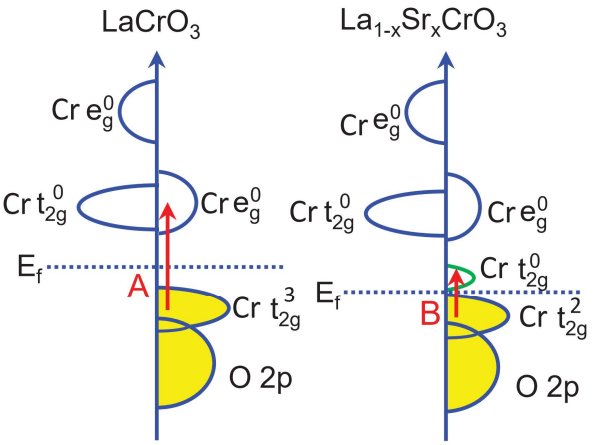

Figure 1. 26 Sketch of the band diagram of $LaCrO_3$ and $La_{1-x}Sr_xCrO_3$. Taken from Ref. 187.

1.4.3.3. Manganates

As mentioned in section 1.4.2.2, manganites can be both *n*-type and *p*-type semiconductors (*e.g.* $Pr_{1-x}Sr_xMnO_3$ [164]). Decades ago, Hashimoto *et al*. [141] studied the temperature dependence of the electrical resistivity and Seebeck coefficient on single crystals of $La_{1-x}Ca_xMnO_3$ ($0 \leq x \leq 0.3$) and $La_{1-x}Sr_xMnO_3$ ($0 \leq x \leq 0.4$). All $La_{1-x}Ca_xMnO_3$ are *p*-type. The electrical conductivity increased from 1 to 100 $S \cdot cm^{-1}$, however, the Seebeck coefficient dropped from 300 to 5 $\mu V \cdot K^{-1}$ at 200 K when increasing x from 0.1 to 0.3. Meanwhile, the Seebeck coefficients are 2 to 4 $\mu V \cdot K^{-1}$ in $La_{1-x}Sr_xMnO_3$, which are as small as those of metals. These values change their sign at about room temperature and the absolute values increase with temperature. A similar tendency was also reported by Volger [190] and could be explained by the phonon drag effect occurring at relatively high temperatures.

Additionally, Jha *et al*. [143] investigated the $La_{0.67}Sr_{0.33}MnO_3/LaMnO_3$ perovskite oxide metal/semiconductor superlattices as a potential *p*-type thermoelectric material. The superlattices exhibited a room temperature cross-plane thermal conductivity (0.89 $W \cdot m^{-1} \cdot K^{-1}$) that is significantly lower than the thermal conductivity of individual thin films of either $La_{0.67}Sr_{0.33}MnO_3$ (1.60 $W \cdot m^{-1} \cdot K^{-1}$) or $LaMnO_3$ (1.29 $W \cdot m^{-1} \cdot K^{-1}$). That may help overcome one of the major limitations of oxides as thermoelectrics. After one year, the authors [144] showed the cross-plane $La_{0.67}Sr_{0.33}MnO_3/LaMnO_3$ superlattices a giant Seebeck coefficient of 2560 $\mu V \cdot K^{-1}$ at 300 K that increases to 16640 $\mu V \cdot K^{-1}$ at 360 K. The low resistance oxide superlattices exhibited a room temperature cross-plane thermal conductivity of 0.92 $W \cdot m^{-1} \cdot K^{-1}$. However, the corresponding *ZT* values only rose from 0.001 to 0.037 in the same temperature range, due to the high electrical conductivity.

1.4.3.4. Other perovskite systems

There are still some other reported *p*-type thermoelectric perovskite oxides, for example, Sr-doped $LaFeO_3$, which has been studied for several decades. The *ZT* value of $La_{1-x}Sr_xFeO_3$ powders was 0.076 at 1273 K when x = 0.05 ($La_{0.95}Sr_{0.05}FeO_3$) with electrical conductivity of 21 $S \cdot cm^{-1}$, Seebeck coefficient of 228 $\mu V \cdot K^{-1}$, and thermal conductivity of 1.85 $W \cdot m^{-1} \cdot K^{-1}$ [191, 192]. And more recently, the thermoelectric power factor of $LaFeO_3$ based compounds has been further improved. It is 3.73 $\mu W \cdot cm^{-1} \cdot K^{-2}$ for $La_{0.9}Ba_{0.1}FeO_3$ compound, and 1.61 $\mu W \cdot cm^{-1} \cdot K^{-2}$ for $La_{0.9}Ca_{0.1}FeO_3$ compound at 650 K [193].

1.5. Thermoelectric devices

1.5.1. Introduction

Thermoelectric applications (power generation and heating/cooling) are achieved utilizing the thermoelectric device or so-called thermoelectric module. The basic unit of a thermoelectric module is composed of two different types of thermoelectric materials (*n*-type and *p*-type), so-called "legs", which are electrically connected through a conducting contact material. Thermoelectric devices are made of such basic units in parallel thermally or in series electrically. The same module can be used for power generation or cooling/heating applications, as shown in Figure 1. 27. For power generation, when there is a temperature difference between the two ends of the semiconductors, a potential difference will occur according to the Seebeck effect between the two poles of the device (Figure 1. 27a). However, in thermoelectric refrigeration shown in Figure 1. 27b, when a current flows through the circuit, according to the Peltier effect, the top of the device absorbs heat for cooling.

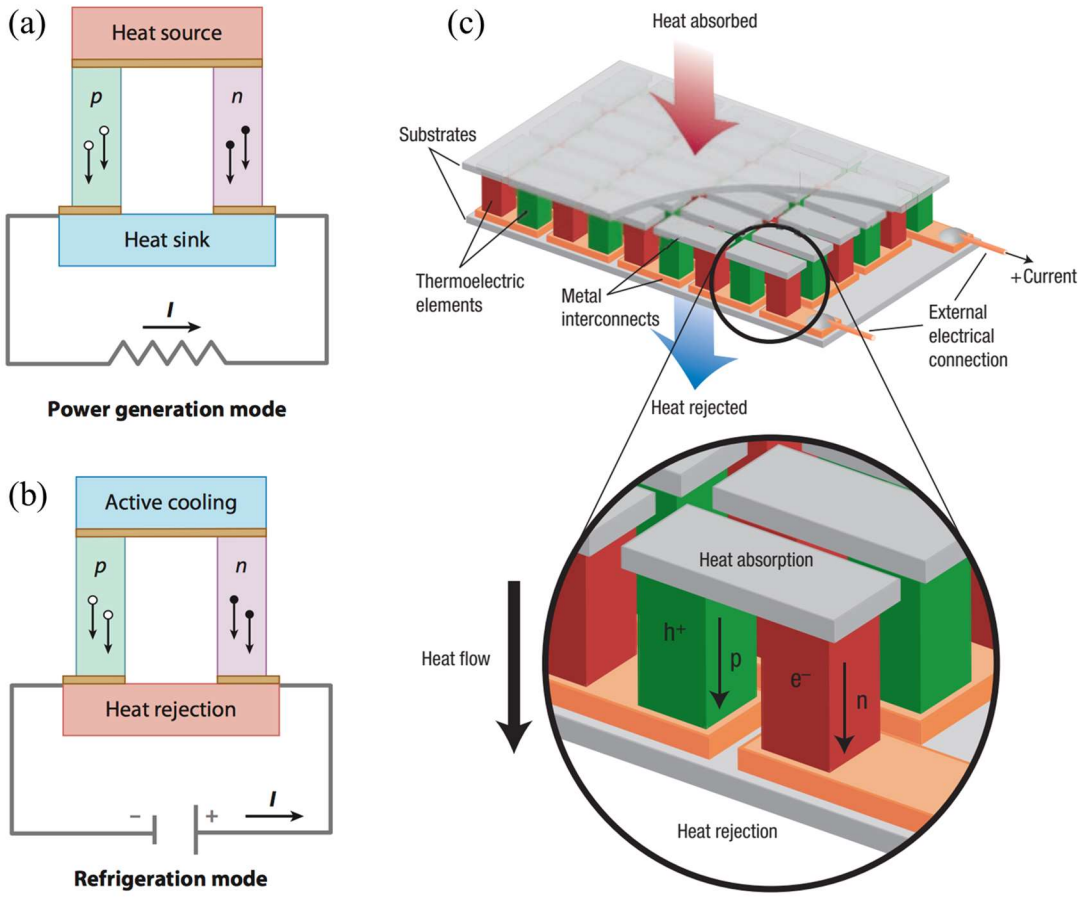

Figure 1. 27 Diagram of (a) thermoelectric power generator and (b) refrigeration. Taken from Ref. 15. (c) Thermoelectric module showing the direction of charge flow on both cooling and power generation. Taken from Ref. 25.

The thermoelectric device ZT, given a finite temperature difference $\Delta T = T_h - T_c$ is defined from the maximum efficiency (η) of a single thermoelectric leg and equation [194]:

$$ZT = \left(\frac{T_h - T_c(1-\eta)}{T_h(1-\eta) - T_c} \right)^2 - 1 \tag{1.15}$$

where the η is calculated from the temperature-dependent properties $S(T)$, $\rho(T)$, and $\kappa(T)$ between hot side temperature T_h and cold side temperature T_c. The η of a thermoelectric generation device is also traditionally characterized by the equation [194]:

$$\eta = \frac{\Delta T}{T_h} = \frac{\sqrt{1+ZT} - 1}{\sqrt{1+ZT} + T_c / T_h} \tag{1.16}$$

Thus, maximizing the number of *p*-*n* leg pairs ($N_{p\text{-}n}$), in an open circuit the generated output voltage can be calculated:

$$\Delta V = \Delta T \times S \times N_{p\text{-}n} \tag{1.17}$$

And thus, minimizing also contact resistance (R_c) between thermoelectric material and metallic electrode to max efficiency. R_c should be $< 10^{-10}$ $\Omega \cdot m^2$, otherwise, heating by Joule effect instead of cooling (for cooling applications) [195].

1.5.2. Micro-modules

Whereas thermoelectric modules are commercially available at the macroscale, micro thermoelectric modules are still under investigation or in development although a need is rising for the wide microelectronic applications. The challenge resides in the microfabrication process of such a module structured in 3D, with at least 3 or 4 different materials (thermoelectric *n*- and *p*-types, metallic electrodes, and support/substrate). Besides, maintaining a sufficient temperature difference at the microscale represents an additional challenge and pushes ever the enhancement of thermoelectric materials, especially in terms of low thermal conductivity limits.

Different groups have reported the fabrications of micro thermoelectric modules (μ-TEG) with different geometries [196]. According to structure, the devices can be classified into three different types: vertical structure, lateral structure, and hybrid structure.

Table 1. 3 Classification of micro thermoelectric devices.

Structure type	Advantage	Drawback
Vertical structure μ-TEG with both vertical heat and current flow, as shown in Figure 1. 28a	Simple design Large output power High conversion efficiency	Difficulty in fabrication High requirement of technology
Lateral structure μ-TEG with both lateral heat and current flow, as shown in Figure 1. 28b	Easily realized for its compatibility with IC planar technology	Comparatively poor performance owing to high parasitic heat flux through the membrane Difficulty in the package
Hybrid structure μ-TEG with vertical heat flow and lateral current flow as shown in Figure 1. 28c	Convenient package like vertical structure In-planar thermopile can be fabricated by the IC-compatible technology like lateral structure	Output power to be improved (optimization of the heat flux path [197])

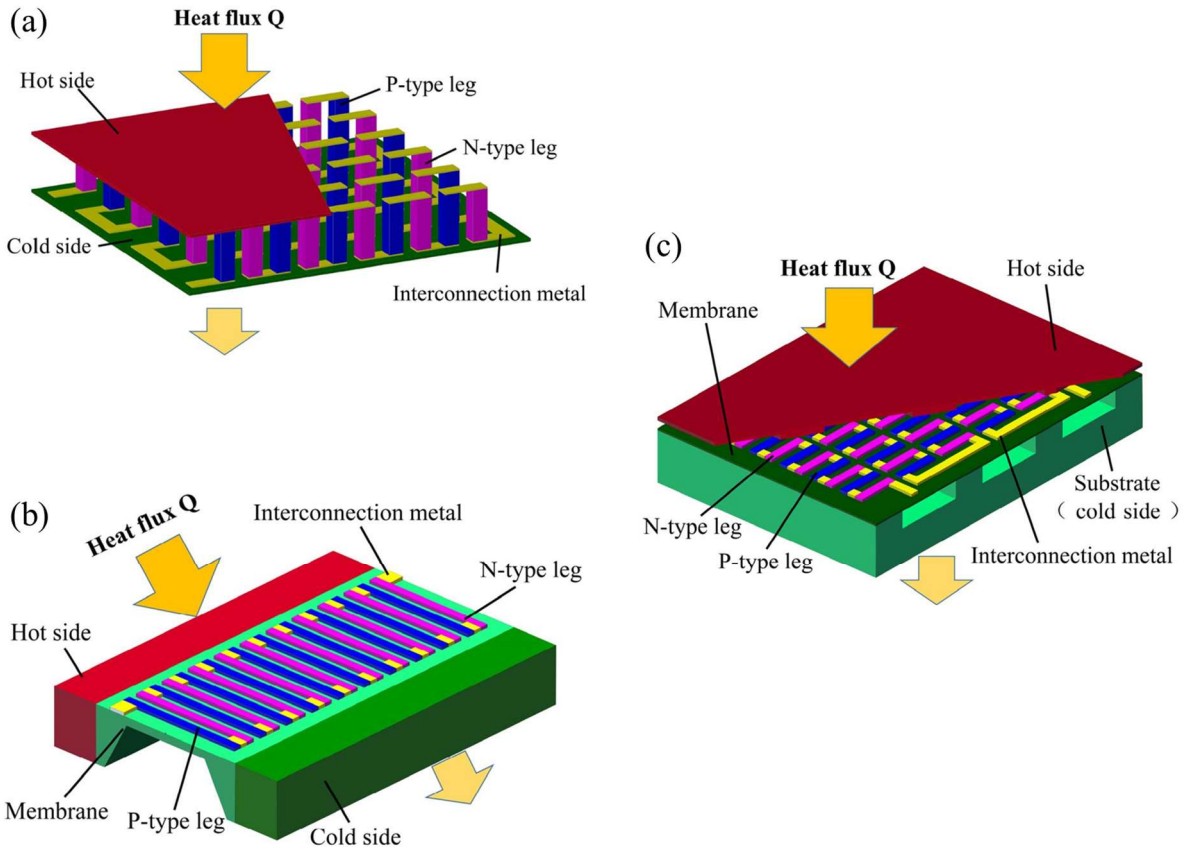

Figure 1. 28 Schematic overviews of (a) typical vertical structure, (b) lateral structure, and (c) hybrid structure μ-TEG. Taken from Ref. 196.

Commercially, Micropelt proposes miniaturized standard modules based on (Bi, Sb)$_2$Te$_3$ structured films that are finally assembled by flip-chip bonding. But the micro modules need a large heat sink to maintain the temperature differences [198]. Similarly, academic works on miniaturized standard modules based on (Bi, Sb)$_2$Te$_3$ films electrodeposited on different supports containing the electrodes and finally assembled by flip-chip bonding [199]. Additionally, planar modules based on doped silicon membranes were studied by researchers [200, 201]. Planar modules with silicon membranes as support with deposited (Bi, Sb)$_2$Te$_3$ thermoelectric films are leading to start-up developments [202, 203]. However, no report on micro thermoelectric oxide modules up to now, and this is the purpose of the project ANR MITO (first MIcro-Thermoelectric module based on Oxides) in which this thesis is involved.

1.6. Objective and significance of my subject

This Ph.D. thesis focuses on the *p*-type thermoelectric perovskite oxide Sr-doped $LaCrO_3$ films, which is a part of the project MITO aiming to integrate promising thermoelectric materials based on oxides into micrometric thermoelectric modules for thermal management onto micro-optoelectronic platforms. The thin films fabricated during this thesis are devoted to building a micrometric thermoelectric module as a demonstrator, composed of electrically connected *p*-*n* leg pairs.

At the beginning of this work, the calibrations of $LaCrO_3$ and $SrCrO_3$ epitaxial thin films grown by molecular beam epitaxy were studied respectively. In order to prepare high-quality Sr-doped $LaCrO_3$ films, $La_{1+\delta}CrO_3$ ($|\delta| \leq 0.25$) and $Sr_{1+\delta}CrO_3$ ($|\delta| \leq 0.14$) thin films were grown on $SrTiO_3$(001) substrates. Then the impact of large cationic-stoichiometry deviation (δ) on structural properties has been thoroughly investigated via various characterization methods. Particularly, the surface structure, morphology, lattice cell parameters, and crystalline quality of the thin films are shown and discussed (see Chapter III).

Having the good calibrations of undoped films, stoichiometric single-crystalline $La_{1-x}Sr_xCrO_3$ films in the Sr doping range between 0 and 0.4 were fabricated. The structural and room-temperature thermoelectric properties (electrical conductivity, carrier concentration, and Seebeck coefficient) were also measured and studied. Then the film with the highest thermoelectric power factor has been found and confirmed (see Chapter III).

Moreover, high-quality strained epitaxial $La_{0.75}Sr_{0.25}CrO_3$ and $LaCrO_3$ thin films were

grown on four different perovskite-oxide substrates, leading various lattice mismatch strain values. The epitaxial strain effect on the in- and out-of-plane lattice parameters of the thin layers have been investigated, and the Poisson ratio, as well as the bulk lattice constant of $La_{0.75}Sr_{0.25}CrO_3$, has been extracted for the first time. The parameters significantly differ from those measured for $LaCrO_3$. Besides, the electrical conductivity, carrier concentration, and Seebeck coefficient as a function of strain have been traced. The influence of strain effect on in-plane room temperature thermoelectric properties has been discussed (see Chapter IV).

Furthermore, stoichiometry-deviation was induced to decrease the thermal conductivity of our thin films. Epitaxially-strained $(La_{0.75}Sr_{0.25})_{1+\delta}CrO_3$ films ($|\delta| \leq 0.3$) were grown $SrTiO_3$(001) substrate. The films with different compositions were prepared by adjusting the Sr/Cr and La/Cr flux ratios of the effusion cells. The effect of stoichiometry-deviation on the structural and thermoelectric properties has been investigated (see Chapter V).

Finally, we move to do the integration of Sr-doped $LaCrO_3$ film on silicon. Firstly, a layer of $SrTiO_3$ as a pseudo-substrate was achieved. Then the stoichiometric $La_{0.75}Sr_{0.25}CrO_3$ epitaxial film was deposed on the $SrTiO_3$/Si(001) template for the first time. The structural properties were obtained and the thermoelectric performance needs to be achieved and optimized for its further application (see Chapter VI).

1.7. References

[1] M. M. Waldrop. The chips are down for Moore's law. Nature News, 2016, 530(7589): 144.

[2] Moore's deviation. Nature Nanotechnology, 2017, 12, 1105.

[3] Official site of world-wide distribution of ITRS documents in accordance with the MOU signed by the WSC members on July 10, 2000. Retrieved from: http://www.itrs2.net/.

[4] Resources of 2015 International Technology Roadmap for Semiconductors (ITRS) published on June 5, 2015, by Semiconductor Industry Association. Retrieved from: https://www.semiconductors.org/resources/2015-international-technology-roadmap-for-semiconductors-itrs/.

[5] W. Arden, M. Brillouët, P. Cogez, M. Graef, B. Huizing, and R. Mahnkopf. More-than-Moore white paper. Version 2010, 2: 14. Retrieved from: http://www.itrs2.net/uploads/4/9/7/7/49775221/irc-itrs-mtm-v2_3.pdf.

[6] The TIPS project consortium of industry and academic research organisations aims to develop and demonstrate a smart and scalable, thermally-enabled, integrated optoelectronic platform. Retrieved from: http://www.tips2020.eu/.

[7] Energy harvesting to power the rise of the Internet of Things. Retrieved from: https://ec.europa.eu/growth/ tools-databases/dem/monitor/sites/default/files/DTM_Energy%20harvesting%20v1_0.pdf.

[8] When the Internet of Things grabs energy. Retrieved from: https://lejournal.cnrs.fr/ articles/quand-linternet -des-objets-grappille-de-lenergie.

[9] J. P. Feser and J. Ravichandran. More power to pyroelectrics. Nature Materials, 2018, 17(5): 385-386.

[10] G. Sebald, E. Lefeuvre, and D. Guyomar. Pyroelectric energy conversion: Optimization principles. IEEE transactions on ultrasonics, ferroelectrics, and frequency control, 2008, 55(3): 538-551.

[11] The challenges of the Internet of Things. Retrieved from: https://lejournal.cnrs.fr/articles/les-defis-de -linternet-des-objets.

[12] Taking the heat off PICs. Retrieved from: https://www.electrooptics.com/feature/taking-heat-pics.

[13] G. Mahan and B. Sales. Thermoelectric materials: New approaches to an old problem. Physics Today, 1997, 50(3): 42-47.

[14] G. D. Mahan. *Solid state physics: Advances in research and applications*, Chapter 1: Good thermoelectrics, vol. 51, edited by H. Ehrenreich and F. Spaepen, Academic Press, New York, 1998.

[15] F. J. DiSalvo. Thermoelectric cooling and power generation. Science, 1999, 285(5428): 703-706.

[16] L. Yang, Z. G. Chen, M. S. Dargusch, and J. Zou. High performance thermoelectric materials: Progress and their applications. Advanced Energy Materials, 2018, 8(6): 1701797.

[17] Official site of International Thermoelectric Society (ITS). Retrieved from: http://www.its.org/.

[18] Official site of European Thermoelectric Society. Retrieved from: http://www.thermoelectricity.eu/.

[19] Official sites of French research networks on thermoelectricity. Retrieved from: http://gdr-thermoelectricite. cnrs.fr/ and http://gis-te.univ-lyon1.fr/.

[20] H. J. Goldsmid and R. W. Douglas. The use of semiconductors in thermoelectric refrigeration. British Journal of Applied Physics, 1954, 5(11): 386.

[21] F. D. Rosi, E. F. Hockings, and N. E. Lindenblad. Semiconducting materials for thermoelectric power generation. RCA (Radio Corporation of America) Review, 1961, 22, 82-121.

[22] F. D. Rosi. Thermoelectricity and thermoelectric power generation. Solid-State Electronics, 1968, 11(9): 833-868.

[23] A. F. Ioffe, S. V. Airapetyants, A. V. Ioffe, N. V. Kolomoets, and L. S. Stil'bans. On improving the efficiency of semiconductor thermoelements. Dokl. Akad. Nauk SSSR. 1956, 106: 981.

[24] A. F. Ioffe. Semiconductor thermoelements and thermoelectric refrigeration. Infosearch, London, 1957: 39.

[25] G. J. Snyder and E. S. Toberer. Complex thermoelectric materials. Nature Materials, 2008, 7: 105-114.

[26] C. J. Vineis, A. Shakouri, A. Majumdar, and M. G. Kanatzidis. Nanostructured thermoelectrics: big efficiency gains from small features. Advanced Materials, 2010, 22(36): 3970-3980.

[27] J. He and T. M. Tritt. Advances in thermoelectric materials research: Looking back and moving forward. Science, 2017, 357(6358).

[28] Z. Lu, H. Zhang, W. Lei, D. C. Sinclair, and I. M. Reaney. High-figure-of-merit thermoelectric La-doped A-site-deficient $SrTiO_3$ ceramics. Chemistry of Materials, 2016, 28(3): 925-935.

[29] T. Zhu, Y. Liu, C. Fu, J. P. Heremans, J. G. Snyder, and X. Zhao. Compromise and synergy in high-efficiency thermoelectric materials. Advanced Materials, 2017, 29(14): 1605884.

[30] J. He, M. G. Kanatzidis, and V. P. Dravid. High performance bulk thermoelectrics via a panoscopic approach. Materials Today, 2013, 16(5): 166-176.

[31] W. Liu, J. Hu, S. Zhang, M. Deng C. G. Han, and Y. Liu. New trends, strategies and opportunities in thermoelectric materials: A perspective. Materials Today Physics, 2017, 1: 50-60.

[32] Y. Lin, J. Lan, and C. Nan. *Oxide thermoelectric materials: From basic principles to applications*. Wiley-VCH, 2019.

[33] D. M. Rowe. *Handbook of thermoelectrics*. CRC Press, 1995.

[34] D. M. Rowe. *Thermoelectrics handbook: Macro to nano*. CRC Press, 2006.

[35] L. E. Bell. Cooling, heating, generating power, and recovering waste heat with thermoelectric systems. Science, 2008, 321: 1457-1461.

[36] A. J. Minnich, M. S. Dresselhaus, Z. F. Ren, and G. Chen. Bulk nanostructured thermoelectric materials: current research and future prospects. Energy & Environmental Science, 2009, 2: 466-479.

[37] B. Hinterleitner, I. Knapp, M. Poneder, Yongpeng Shi, H. Müller, G. Eguchi, C. Eisenmenger-Sittner, M. Stöger-Pollach, Y. Kakefuda, N. Kawamoto, Q. Guo, T. Baba, T. Mori, Sami Ullah, Xing-Qiu Chen, and E. Bauer. Thermoelectric performance of a metastable thin-film Heusler alloy. Nature, 2019, 576(7785): 85-90.

[38] E. Alleno. ZT = 6 dans un film mince de $Fe_2V_{0.8}W_{0.2}Al$: Mythe ou réalité. Journées nationales de thermoélectricité (JNTE), Metz, France, 2020.

[39] B. Zhu, X. Liu, Q. Wang, Y. Qiu, Z. Shu, Z. Guo, Y. Tong, J. Cui, M. Gu, and J. He. Realizing record high performance in n-type Bi_2Te_3-based thermoelectric materials. Energy & Environmental Science, 2020, 13(7): 2106-2114.

[40] Characteristics and properties of new semiconductor materials. Retrieved from: http://www.ioffe.ru/SVA/.

[41] G. S. Nolas, J. Sharp, and J. Goldsmid. *Thermoelectrics: Basic principles and new materials developments*. Springer Science & Business Media, 2013.

[42] R. Franz and G. Wiedemann. Ueber die Wärme-Leitungsfähigkeit der Metalle. Annalen der Physik, 1853, 165(8): 497-531.

[43] X. Shi, L. Chen, and C. Uher. Recent advances in high-performance bulk thermoelectric materials. International Materials Reviews, 2016, 61(6): 379-415.

[44] Y. G. Gurevich and G. N. Logvinov. Physics of thermoelectric cooling. Semiconductor Science and Technology, 2005, 20: 57-64.

[45] M. S. Dresselhaus, G Chen, M. Y. Tang, R. G. Yang, H. Lee, D. Z. Wang, Z. F. Ren, J. P. Fleurial, and P. Gogna. New directions for low-dimensional thermoelectric materials. Advanced Materials, 2007, 19: 1043-1053.

[46] M. Dutta, T. Ghosh, and K. Biswas. Electronic structure modulation strategies in high-performance thermoelectrics. APL Materials, 2020, 8(4): 040910.

[47] H. Wang, Y. Pei, A. D. LaLonde, and G. J. Snyder. Material design considerations based on thermoelectric quality factor. Thermoelectric Nanomaterials. Springer, Berlin, Heidelberg, 2013: 3-32.

[48] Y. Z. Pei, X. Y. Shi, A. LaLonde, H. Wang, L. D. Chen, and G. J. Snyder. Convergence of electronic bands for high performance bulk thermoelectrics. Nature, 2011, 473(7345): 66-69.

[49] G. Tan, F. Shi, S. Hao, H. Chi, L. D. Zhao, C. Uher, C. Wolverton, V. P. Dravid, and M. G. Kanatzidis. Codoping in SnTe: Enhancement of thermoelectric performance through synergy of resonance levels and band convergence. Journal of the American Chemical Society, 2015, 137(15): 5100-5112.

[50] J. P. Heremans, V. Jovovic, E. S. Toberer, A. Saramat, K. Kurosaki, A. Charoenphakdee, S. Yamanaka, and G. J. Snyder. Enhancement of thermoelectric efficiency in PbTe by distortion of the electronic density of states. Science, 2008, 321(5888): 554-557.

[51] N. Boukhris, H. Meradji, S. Ghemid, S. Drablia, and F. E. Hassan. Ab initio study of the structural, electronic and thermodynamic properties of $PbSe_{1-x}S_x$, $PbSe_{1-x}Te_x$ and $PbS_{1-x}Te_x$ ternary alloys. Physica Scripta, 2011, 83(6): 065701.

[52] K. Hoang, S. D. Mahanti, and M. G. Kanatzidis. Impurity clustering and impurity-induced bands in PbTe-, SnTe-, and GeTe-based bulk thermoelectrics. Physical Review B, 2010, 81(11): 115106.

[53] J. H. Bahk and A. Shakouri. Enhancing the thermoelectric figure of merit through the reduction of bipolar thermal conductivity with heterostructure barriers. Applied Physics Letters, 2014, 105(5): 052106.

[54] S. Wang, J. Yang, T. Toll, J. Yang, W. Zhang, and X. Tang. Conductivity-limiting bipolar thermal conductivity in semiconductors. Scientific Reports, 2015, 5: 10136.

[55] M. Hong, Z. G. Chen, L. Yang, and J. Zou. Enhancing thermoelectric performance of Bi_2Te_3-based nanostructures through rational structure design. Nanoscale, 2016, 8(16): 8681-8686.

[56] G. D. Mahan and J. O. Sofo. The best thermoelectric. Proceedings of the National Academy of Sciences, 1996, 93(15): 7436-7439.

[57] A. Popescu and L. M. Woods. Enhanced thermoelectricity in composites by electronic structure modifications and nanostructuring. Applied Physics Letters, 2010, 97(5): 052102.

[58] Q. Zhang, H. Wang, W. Liu, H. Wang, B. Yu, Q. Zhang, Z. Tian, G. Ni, S. Lee, K. Esfarjani, G. Chen, and Z. Ren. Enhancement of thermoelectric figure-of-merit by resonant states of aluminium doping in lead selenide. Energy & Environmental Science, 2012, 5(1): 5246-5251.

[59] Q. Zhang, B. Liao, Y. Lan, K. Lukas, W. Liu, K. Esfarjani, C. Opeil, D. Broido, G. Chen, and Z. Ren. High thermoelectric performance by resonant dopant indium in nanostructured SnTe. Proceedings of the National Academy of Sciences, 2013, 110(33): 13261-13266.

[60] Y. Pei, H. Wang, and G. J. Snyder. Band engineering of thermoelectric materials. Advanced Materials, 2012, 24(46): 6125-6135.

[61] L. D. Hicks and M. S. Dresselhaus. Effect of quantum-well structures on the thermoelectric figure of merit. Physical Review B, 1993, 47(19): 12727.

[62] J. W. Sharp, E. C. Jones, and R. K. Williams. Thermoelectric properties of $CoSb_3$ and related alloys. Journal of Applied Physics, 1995, 78: 1013-1018.

[63] D. A. Broido and T. L. Reinecke. Thermoelectric transport in quantum-well superlattices. Applied Physics Letters, 1997, 70: 2834-2836.

[64] C. A. Adessi, S. Pecorario, S. Thébaud, and G. Bouzerar. First principle investigation of the influence of sulfur vacancies on the thermoelectric properties of single layered MoS_2. Physical Chemistry Chemical Physics, 2020, 22: 15048-15057.

[65] D. Li, Y. Gong, Y. Chen, J. Lin, Q. Khan, Y. Zhang, Y. Li, H. Zhang, and H. Xie. Recent progress of two-dimensional thermoelectric materials. Nano-Micro Letters, 2020, 12(1): 36.

[66] C. Chiritescu, D. G. Cahill, N. Nguyen, D. Johnson, A. Bodapati, P. Keblinski, and P. Zschack. Ultralow thermal conductivity in disordered, layered WSe_2 crystals. Science, 2007, 315(5810): 351-353.

[67] L. Zhao, S. Lo, Y. Zhang, H. Sun, G. Tan, C. Uher, C. Wolverton, V. P. Dravid, and M. G. Kanatzidis. Ultralow thermal conductivity and high thermoelectric figure of merit in SnSe crystals. Nature, 2014, 508(7496): 373-377.

[68] H. Ohta, S. Kim, Y. Mune, T. Mizoguchi, K. Nomura, S. Ohta, T. Nomura, Y. Nakanishi, Y. Ikuhara, M. hirano, H. Hosono, and K. Koumoto. Giant thermoelectric Seebeck coefficient of a two-dimensional electron gas in $SrTiO_3$. Nature Materials, 2007, 6(2): 129-134

[69] T. Okuda, K. Nakanishi, S. Miyasaka, and Y. Tokura. Large thermoelectric response of metallic perovskites: $Sr_{1-x}La_xTiO_3$ ($0 < x < 0.1$). Physical Review B, 2001, 63(11): 113104.

[70] G. Bouzerar, S. Thébaud, C. Adessi, R. Debord, M. Apreutesei, R. Bachelet, and S. Pailhès. Unified modelling of the thermoelectric properties in $SrTiO_3$. EPL Europhysics Letters, 2017, 118(6): 67004.

[71] G. Bouzerar, S. Thébaud, R. Bouzerar, S. Pailhès, and C. Adessi. Absence of confinement in $(SrTiO_3)/(SrTi_{0.8}Nb_{0.2}O_3)$ superlattices. Physical Review Materials, 2018, 2(3): 035402.

[72] J. P. Heremans, B. Wiendlocha, and A. M. Chamoire. Resonant levels in bulk thermoelectric semiconductors. Energy & Environmental Science, 2012, 5(2): 5510-5530.

[73] D. Bilc, S. D. Mahanti, E. Quarez, K. F. Hsu, R. Pcionek, and M. G. Kanatzidis. Resonant states in the electronic structure of the high performance thermoelectrics $AgPb_mSbTe_{2+m}$: The role of Ag-Sb microstructures. Physical Review Letters, 2004, 93(14): 146403.

[74] S. Thébaud, C. Adessi, S. Pailhès, and G. Bouzerar. Boosting the power factor with resonant states: A model study. Physical Review B, 2017, 96(7): 075201.

[75] G. A. Slack. *Solid state physics*. Academic press, New York, 1979.

[76] K. Biswas, J. He, I. D. Blum, C. Wu, T. P. Hogan, D. N. Seidman, V. P. Dravid, and M. G. Kanatzidis. High-performance bulk thermoelectrics with all-scale hierarchical architectures. Nature, 2012, 489(7416): 414-418.

[77] A. I. Abutaha, S. R. S. Kumar, K. Li, A. M. Dehkordi, T. M. Tritt, and H. N. Alshareef. Enhanced thermoelectric figure-of-merit in thermally robust, nanostructured superlattices based on $SrTiO_3$. Chemistry of Materials, 2015, 27(6): 2165-2171.

[78] G. A. Slack. New materials and performance limits for thermoelectric cooling. CRC handbook of thermoelectrics, 1995: 407-440.

[79] K. J. M. Bishop. Acoustic metamaterials: Living bandgaps. Nature Materials, 2017, 16(8): 786-787.

[80] M. N. Luckyanova, J. Garg, K. Esfarjani, A. Jandl, M. T. Bulsara, A. J. Schmidt, A. J. Minnich, S. Chen, M. S. Dresselhaus, Z. Ren, E. A. Fitzgerald, and G. Chen. Coherent phonon heat conduction in superlattices. Science, 2012, 338(6109): 936-939.

[81] J. Ravichandran, A. K. Yadav, R. Cheaito, P. B. Rossen, A. Soukiassian, S. J. Suresha, J. C. Duda, B. M. Foley, C. Lee, Y. Zhu, A. W. Lichtenberger, J. E. Moore, D. A. Muller, D. G. Schlom, P. E. Hopkins, A. Majumdar, R. Ramesh, and M. A. Zurbuchen. Crossover from incoherent to coherent phonon scattering in epitaxial oxide superlattices. Nature Materials, 2014, 13(2): 168-172.

[82] M. Maldovan. Phonon wave interference and thermal bandgap materials. Nature Materials, 2015, 14(7): 667-674.

[83] M. Maldovan. Sound and heat revolutions in phononics. Nature, 2013, 503(7475): 209-217.

[84] D. Y. Chung, T. Hogan, P. Brazis, M. Rocci-Lane, C. Kannewurf, M. Bastea, C. Uher, and M. G. Kanatzidis. A high-performance thermoelectric material for low-temperature applications. Science, 2000, 287(5455): 1024-1027.

[85] B. Poudel, Q. Hao, Y. Ma, Y. C. Lan, A. Minnich, B. Yu, X. Yan, D. Z. Wang, A. Muto, D. Vashaee, X. Y. Chen, J. M. Liu, M. S. Dresselhaus, G. Chen, and Z. Ren. High-thermoelectric performance of nanostructured bismuth antimony telluride bulk alloys. Science, 2008, 320(5876): 634-638.

[86] J. Wei, L. Yang, Z. Ma, P. Song, M. Zhang, J. Ma, F. Yang, and X. Wang. Review of current high-ZT thermoelectric materials. Journal of Materials Science, 2020: 1-63.

[87] R. Venkatasubramanian, E. Siivola, T. Colpitts, and B. O'Quinn. Thin-film thermoelectric devices with high room-temperature figures of merit. Nature, 2001, 413(6856): 597.

[88] R. R. Heikes and R. W. Ure. *Thermoelectricity: Science and engineering*. Interscience, New York, 1961.

[89] H. J. Goldsmid, A. R. Sheard, and D. A. Wright. The performance of bismuth telluride thermojunctions. British Journal of Applied Physics, 1958, 9(9): 365.

[90] C. Wood. Materials for thermoelectric energy-conversion. Reports on Progress in Physics, 1988, 51(4): 459.

[91] H. Scherrer and S. Scherrer. *Thermoelectrics handbook macro to nano*, Chapter 27, edited by D. M. Rowe, CRC press, Boca Raton, 2006.

[92] V. A. Kutasov, L. N. Lukyanova, and M. V. Vedernikov. *Thermoelectrics handbook macro to nano*, Chapter 37, edited by D. M. Rowe, CRC press, Boca Raton, 2006.

[93] R. W. Fritts. *Thermoelectric materials and devices*, page 143-162, edited by I. B. Cadoff and E. Miller, Reinhold press, New York, 1960.

[94] F. A. Trumbore and A. Tartaglia. Resistivities and hole mobilities in very heavility doped germanium. Journal of Applied Physics, 1958, 29: 1511-1514.

[95] C. B. Vining, W. Laskow, J. O. Hanson, R. R. Vanderbeck, and P. D. Gorsuch. Thermoelectric properties of pressure-sintered $Si_{0.8}Ge_{0.2}$ thermoelectric alloys. Journal of Applied Physics, 1991, 69(8): 4333-4340.

[96] G. A. Slack and D. M. Rowe. *Handbook of thermoelectrics*, page 407-440. CRC Press Book, 1995.

[97] G. S. Nolas, J. Poon, and M. Kanatzidis. Recent developments in bulk thermoelectric materials. MRS bulletin, 2006, 31(3): 199-205.

[98] A. Saramat, G. Svensson, A. E. C. Palmqvist, C. Stiewe, E. Mueller, D. Platzek, S. G. K. Williams, D. M. Rowe, J. D. Bryan, and G. D. Stucky. Large thermoelectric figure of merit at high temperature in Czochralski-grown clathrate $Ba_8Ga_{16}Ge_{30}$. Journal of Applied Physics, 2006, 99(2): 023708.

[99] E. S. Toberer, M. Christensen, B. B. Iversen, and G. J. Snyder. High temperature thermoelectric efficiency in $Ba_8Ga_{16}Ge_{30}$. Physical Review B, 2008, 77(7): 075203.

[100] B. C. Sales, D. Mandrus, and R. K. Williams. Filled skutterudite antimonides: A new class of thermoeletric materials. Science, 1996, 272(5266): 1325-1328.

[101] D. G. Cahill and P. Avouris. Si ejection and regrouth during the initial stages of Si(001) oxidation. Applied Physics Letters, 1992, 60: 326-328.

[102] W. G. Zeier, J. Schmitt, G. Hautier, U. Aydemir, Z. M. Gibbs, C. Felser, and G. J. Snyder. Engineering half-Heusler thermoelectric materials using Zintl chemistry. Nature Reviews Materials, 2016, 1(6): 16032.

[103] C. Uher, J. Yang, S. Hu. D. T. Morelli, and G. P. Melsuer, Transport properties of pure and doped MNiSn (M= Zr, Hf). Physical Review B, 1999, 59(13): 8615.

[104] Y. Xia, S Bhattacharya, and V Ponnambalam. Thermoelectric properties of semimetallic (Zr,Hf)CoSb half-Heusler phases. Journal of Applied Physics, 2000, 88(4): 1952-1955.

[105] Y. Xing, R. Liu, J. Liao, Q. Zhang, X. Xia, C. Wang, H. Huang, J. Chu, M. Gu, T. Zhu, C. Zhu, F. Xu, D. Yao, Y. Zeng, S. Bai, and L. Chen. High-efficiency half-Heusler thermoelectric modules enabled by self-propagating synthesis and topologic structure optimization. Energy & Environmental Science, 2019, 12(11): 3390-3399.

[106] J. He, Y. Liu, and R. Funahashi. Oxide thermoelectrics: The challenges, progress, and outlook. Journal of Materials Research, 2011, 26(15): 1762-1772.

[107] J. Ravichandran. Thermoelectric and thermal transport properties of complex oxide thin films, heterostructures and superlattices. Journal of Materials Research, 2017, 32(1): 183-203.

[108] P. Vaqueiro and A. V. Powell. Recent developments in nanostructured materials for high-performance thermoelectrics. Journal of Materials Chemistry, 2010, 20(43): 9577-9584.

[109] I. Terasaki, Y. Sasago, and K. Uchinokura. Large thermoelectric power in $NaCo_2O_4$ single crystals. Physical Review B, 1997, 56(20): R12685.

[110] K. Takahata, Y. Iguchi, D. Tanaka, T. Itoh, and I. Terasaki. Low thermal conductivity of the layered oxide (Na, Ca)Co_2O_4: Another example of a phonon glass and an electron crystal. Physical Review B, 2000, 61(19): 12551.

[111] W. Koshibae, K. Tsutsui, and S. Maekawa. Thermopower in cobalt oxides. Physical Review B, 2000, 62(11): 6869.

[112] M. Ito and D. Furumoto. Effects of noble metal addition on microstructure and thermoelectric properties of $NaxCo_2O_4$. Journal of Alloys and Compounds, 2008, 450(1-2): 494-498.

[113] K Fujita, T. Mochida, and K. Nakamura. High-temperature thermoelectric properties of $NaxCoO_{2-\delta}$ single crystals. Japanese Journal of Applied Physics, 2001, 40(7R): 4644.

[114] Y. Wang, N. S. Rogado, R. J. Cava, and N. P. Ong. Spin entropy as the likely source of enhanced thermopower in $NaxCo_2O_4$. Nature, 2003, 423(6938): 425-428.

[115] W. Koshibae and S. Maekawa. Effects of spin and orbital degeneracy on the thermopower of strongly correlated systems. Physical Review Letters, 2001, 87(23): 236603.

[116] G. Xing, J. Sun, K. P. Ong, X. Fan, W. Zheng, and D. J. Singh. Perspective: N-type oxide thermoelectrics via visual search strategies. APL Materials, 2016, 4(5): 053201.

[117] H. D. Megaw. Crystal structure of double oxide of the perovskite type. Proceedings of the Physical Society, 1946, 58: 133-141.

[118] S. S. Jerpoth, J. Iannello, E. A. Aboagye, and K. M. Yenkie. Computer-aided synthesis of cost-effective perovskite crystals: An emerging alternative to silicon solar cells. Clean Technologies and Environmental Policy, 2020, 22, 1187-1198.

[119] C. J. Bartel, C. Sutton, B. R. Goldsmith, R. Ouyang, C. B. Musgrave, L. M. Ghiringhelli, and M. Scheffler. New tolerance factor to predict the stability of perovskite oxides and halides. Science Advances, 2019, 5, 1-9.

[120] M. E. Bouras. Ingénierie des propriétés diélectriques d'oxydes pérovskites par nanostructuration jusqu'à l'échelle de la monocouche (Thesis). Institut des Nanotechnologies de Lyon, Ecole Centrale de Lyon, Lyon, France, 2019.

[121] M. Ghasdi and H. Alamdari. CO sensitive nanocrystalline $LaCoO_3$ perovskite sensor prepared by high energy ball milling. Sensors and Actuators B: Chemical, 2010, 148, 478-485.

[122] J. W. Fergus. Perovskite oxides for semiconductor-based gas sensors. Sensors and Actuators B: Chemical, 2007, 123: 1169-1179.

[123] F. Jia, H. Zhong, W. Zhang, X.Li, G. Wang, J. Song, Z. Cheng, J. Yin, and L. Guo. A novel nonenzymatic ECL glucose sensor based on perovskite $LaTiO_3$-$Ag_{0.1}$ nanomaterials. Sensors and Actuators B: Chemical, 2015, 212: 174-182.

[124] K. W. Song and K. T. Lee. Characterization of $Ba_{0.5}Sr_{0.5}M_{1-x}Fe_xO_{3-\delta}$ (M = Co and Cu) perovskite oxide cathode materials for intermediate temperature solid oxide fuel cells. Ceramics International, 2012, 38: 5123-5131.

[125] A. Galal, N. F. Atta, and S. M. Ali. Investigation of the catalytic activity of $LaBO_3$ (B = Ni, Co, Fe or Mn) prepared by the microwave-assisted method for hydrogen evolution in acidic medium. Electrochimica Acta, 2011, 56: 5722-5730.

[126] Y. Watanabe, J. G. Bednorz, A. Bietsch, Ch. Gerber, D. Widmer, and A. Beck. Current-driven insulator-conductor transition and nonvolatile memory in chromium-doped $SrTiO_3$ single crystals. Applied Physics Letters, 2001, 78: 3738-3740.

[127] C. Xiong, W. H. P. Pernice, J. H. Ngai, J. W. Reiner, D. Kumah, F. J. Walker, C. H. Ahn, and H. X. Tang. Active silicon integrated nanophotonics: ferroelectric $BaTiO_3$ devices. Nano Letters, 2014, 14: 1419-1425.

[128] H. Zhou, Q. Chen, G. Li, S. Luo, T. B. Song, H. S. Duan, Z. Hong, J. You, Y. Liu, and Y. Yang. Interface engineering of highly efficient perovskite solar cells. Science, 2014, 345: 542-546.

[129] K. Koumoto, R. Funahashi, E. Guilmeau, Y. Miyazaki, A. Weidenkaff, Y. Wang, and C. Wan. Thermoelectric ceramics for energy harvesting. Journal of the American Ceramic Society, 2013, 96: 1-23.

[130] K. F. Hsu, S. Loo, F. Guo, W. Chen, J. S. Dyck, C. Uher, T. Hogan, E. K. Polychroniadis, and M. G. Kanatzidis. Cubic $AgPb_mSbTe_{2+m}$: Bulk thermoelectric materials with high figure of merit. Science, 2004, 303(5659): 818-821.

[131] B. Yu, M. Zebarjadi, H. Wang, K. Lukas, H. Wang, D. Wang, C. Opeil, M. Dresselhaus, G. Chen, and Z. Ren. Enhancement of thermoelectric properties by modulation-doping in silicon germanium alloy nanocomposites. Nano Letters, 2012, 12(4): 2077-2082.

[132] T. Wu and P. Gao. Development of perovskite-type Materials for thermoelectric application. Materials, 2018, 11(6): 999.

[133] M. Nasir Khan, H. T. Kim, H. Minami, and H. Uwe. Thermoelectric properties of niobium doped hexagonal barium titanate. Materials Letters, 2001, 47(1-2): 95-101.

[134] L. Pi, S. Hébert, C. Martin, A. Maignan, and B. Raveau. Comparison of $CaMn_{1-x}Ru_xO_3$ and $CaMn_{1-y}Mo_yO_3$ perovskites. Physical Review B, 2003, 67(2): 024430.

[135] G. Xu, R. Funahashi, Q. Pu, B. Liu, R. Tao, G. Wang, and Z. Ding. High-temperature transport properties of Nb and Ta substituted $CaMnO_3$ system. Solid State Ionics, 2004, 171(1-2): 147-151.

[136] D. Flahaut, T. Mihara, R. Funahashi, N. Nabeshima, K. Lee, H. Ohta, and K. Koumoto. Thermoelectrical properties of A-site substituted $Ca_{1-x}Re_xMnO_3$ system. Journal of Applied Physics, 2006, 100(8): 084911.

[137] S. Kolesnik, B. Dabrowski, and O. Chmaissem. Structural and physical properties of $SrMn_{1-x}Ru_xO_3$ perovskites. Physical Review B, 2008, 78(21): 214425.

[138] J. Liu, C. L. Wang, W. B. Su, H. C. Wang, P. Zheng, J. C. Li, J. L. Zhang, and L. M. Mei. Enhancement of thermoelectric efficiency in oxygen-deficient $Sr_{1-x}La_xTiO_{3-\delta}$ ceramics. Applied Physics Letters, 2009, 95(16): 162110.

[139] Y. Cui, J. R. Salvador, J. Yang, H. Wang, G. Amow, and H. Kleinke. Thermoelectric properties of heavily doped n-type $SrTiO_3$ bulk materials. Journal of Electronic Materials, 2009, 38(7).

[140] A. Mehdizadeh Dehkordi, S. Bhattacharya, T. Darroudi, J. W. Graff, U. Schwingenschlögl, H. N. Alshareef, and T. M. Tritt. Large thermoelectric power factor in Pr-doped $SrTiO_{3-\delta}$ ceramics via grain-boundary-induced mobility enhancement. Chemistry of Materials, 2014, 26(7): 2478-2485.

[141] T. Hashimoto, N. Ishizawa, N. Mizutani, and M. Kato. Electrical resistivity and Seebeck coefficient of $La_{1-x}M_xMnO_3$ (M = Ca, Sr) single crystals. Journal of Materials Science, 1988, 23(3): 1102-1105.

[142] K. Berggold, M. Kriener, C. Zobel, A. Reichl, M. Reuther, R. Müller, A. Freimuth, and T. Lorenz. Thermal conductivity, thermopower, and figure of merit of $La_{1-x}Sr_xCoO_3$. Physical Review B, 2005, 72(15): 155116.

[143] P. Jha, T. D. Sands, L. Cassels, P. Jackson, T. Favaloro, B. Kirk, J. Zide, X. Xu, and A. Shakouri. Cross-plane electronic and thermal transport properties of p-type $La_{0.67}Sr_{0.33}MnO_3/LaMnO_3$ perovskite oxide metal/semiconductor superlattices. Journal of Applied Physics, 2012, 112(6): 063714.

[144] P. Jha, T. D. Sands, P. Jackson, C. Bomberger, T. Favaloro, S. Hodson, J. Zide, X. Xu, and A. Shakouri. Cross-plane thermoelectric transport in p-type $La_{0.67}Sr_{0.33}MnO_3/LaMnO_3$ oxide metal/semiconductor superlattices. Journal of Applied Physics, 2013, 113(19): 193702.

[145] J. Sun and D. J. Singh. Thermoelectric properties of n-type $SrTiO_3$. APL Materials, 2016, 4(10): 104803.

[146] H. Muta, K. Kurosaki, and S. Yamanaka. Thermoelectric properties of rare earth doped $SrTiO_3$. Journal of Alloys and Compounds, 2003, 350(1-2): 292-295.

[147] M. Onoda and I. Goto. Correlation and phonon effects for the electronic transport and thermoelectric power factors in the metal–band-insulator crossover of perovskite-type titanates. Journal of Physics: Condensed Matter, 2009, 21(43): 435603.

[148] M. Onoda and S. Tsukahara. The upper limit of thermoelectric power factors in the metal-band-insulator crossover of the perovskite-type oxygen deficient system $SrTiO_{3-\delta/2}$. Journal of Physics: Condensed Matter, 2011, 23: 045604.

[149] S. Lee, G. Yang, R. H. T. Wilke, S. Trolier-Mckinstry, and C.A. Randall. Thermopower in highly reduced n-type ferroelectric and related perovskite oxides and the role of heterogeneous nonstoichiometry. Physical Review B, 2009, 79(13): 134110.

[150] S. Lee, C. A. Randall, and Z. K. Liu. Factors limiting equilibrium in fabricating a simple ferroelectric oxide: $BaTiO_3$. Journal of the American Ceramic Society, 2009, 92(1): 222-228.

[151] T. Kolodiazhnyi, A. Petric, M. Niewczas, C. Bridges, A. Safa-Sefat, and J. E. Greedan. Thermoelectric power, Hall effect, and mobility of n-type $BaTiO_3$. Physical Review B, 2003, 68(8): 085205.

[152] H. Muta, K. Kurosaki, and S. Yamanaka. Thermoelectric properties of doped $BaTiO_3$-$SrTiO_3$ solid solution. Journal of Alloys and Compounds, 2004, 368(1-2): 22-24.

[153] S. Ohta, T. Nomura, H. Ohta, and K. Koumoto. High-temperature carrier transport and thermoelectric properties of heavily La- or Nb-doped $SrTiO_3$ single crystals. Journal of Applied Physics, 2005, 97(3): 034106.

[154] H. Muta, K. Kurosaki, and S. Yamanaka. Thermoelectric properties of reduced and La-doped single-crystalline $SrTiO_3$. Journal of alloys and compounds, 2005, 392(1-2): 306-309.

[155] J. Ravichandran, W. Siemons, D. W. Oh, J. T. Kardel, A. Chari, H. Heijmerikx, M. L. Scullin, A. Majumdar, R. Ramesh, and D.G. Cahill. High-temperature thermoelectric response of double-doped $SrTiO_3$ epitaxial films. Physical Review B, 2010, 82(16): 165126.

[156] W. S. Choi, H. K. Yoo, and H. Ohta. Polaron transport and thermoelectric behavior in la-doped $SrTiO_3$ thin films with elemental vacancies. Advanced Functional Materials, 2015, 25(5): 799-804.

[157] H. P. R. Frederikse, W. R. Thurber, and W. R. Hosler. Electronic transport in strontium titanate. Physical Review, 1964, 134(2A): A442.

[158] B. Jalan and S. Stemmer. Large Seebeck coefficients and thermoelectric power factor of La-doped $SrTiO_3$ thin films. Applied Physics Letters, 2010, 97: 042106.

[159] S. Ohta, T. Nomura, H. Ohta, M. Hirano, H. Hosono, and K. Koumoto. Large thermoelectric performance of heavily Nb-doped $SrTiO_3$ epitaxial film at high temperature. Applied Physics Letters, 2005, 87(9): 092108.

[160] T. Kobayashi, H. Takizawa, T. Endo, T. Sato, M. Shimada, H. Taguchi, and M. Nagao. Metal-insulator transition and thermoelectric properties in the system $(R_{1-x}Ca_x)MnO_{3-\delta}$ (R: Tb, Ho, Y). Journal of Solid State Chemistry, 1991, 92(1): 116-129.

[161] G. Xu, R. Funahashi, I. Matsubara, M. Shikano, and Y. Zhou. High-temperature thermoelectric properties of the $Ca_{1-x}Bi_xMnO_3$ system. Journal of Materials Research, 2002, 17(5): 1092-1095.

[162] B. T. Cong, T. Tsuji, P. X. Thao, P. Q. Thanh, and Y. Yamamura. High-temperature thermoelectric properties of $Ca_{1-x}Pr_xMnO_{3-\delta}$ ($0 < x < 1$). Physica B: Condensed Matter, 2004, 352(1-4): 18-23.

[163] L. Bocher, M. H. Aguirre, D. Logvinovich, A. Shkabko, R. Robert, M. Trottmann, and A. Weidenkaff. $CaMn_{1-x}Nb_xO_3$ ($x \leq 0.08$) perovskite-type phases as promising new high-temperature n-type thermoelectric materials. Inorganic Chemistry, 2008, 47(18): 8077-8085.

[164] H. Nakatsugawa, M. Kubota, and M. Saito. Thermoelectric and magnetic properties of $Pr_{1-x}Sr_xMnO_3$ ($0.1 \leq x \leq 0.7$). Materials Transactions, 2015, 56(6): 864-871.

[165] M. Yasukawa and N. Murayama. High-temperature thermoelectric properties of the oxide material: $Ba_{1-x}Sr_xPbO_3$ (x = 0-0.6). Journal of Materials Science Letters, 1997, 16(21): 1731-1734.

[166] M. Yasukawa and N. Murayama. A promising oxide material for high-temperature thermoelectric energy conversion: $Ba_{1-x}Sr_xPbO_3$ solid solution system. Materials Science and Engineering: B, 1998, 54(1-2): 64-69.

[167] M. Yasukawa, T. Kono, K. Ueda, H. Yanagi, S. Wng Kim, and H. Hosono. Thermoelectric properties and figure of merit of perovskite-type $Ba_{1-x}La_xSnO_3$ with x = 0.002-0.008. Solid State Communications, 2013, 172: 49-53.

[168] M. Yasukawa, K. Ueda, S. Fujitsu, and H. Hosono. Thermoelectric properties and figure of merit of perovskite-type $Sr_{1-x}La_xSnO_3$ ceramics. Ceramics International, 2017, 43(13): 9653-9657.

[169] J. W. Moon, W. S. Seo, H. Okabe, T. Okawa, and K. Koumoto. Ca-doped $RCoO_3$ (R = Gd, Sm, Nd, Pr) as thermoelectric materials. Journal of Materials Chemistry, 2000, 10(9): 2007-2009.

[170] J. W. Moon, Y. Masuda, W. S. Seo, and K. Koumoto. Influence of ionic size of rare-earth site on the thermoelectric properties of $RCoO_3$-type perovskite cobalt oxides. Materials Science and Engineering: B, 2001, 85(1): 70-75.

[171] J. W. Moon, Y. Masuda, W. S. Seo, and K. Koumoto. Ca-doped $HoCoO_3$ as p-type oxide thermoelectric material. Materials Letters, 2001, 48(3-4): 225-229.

[172] J. Androulakis, P. Migiakis, and J. Giapintzakis. $La_{0.95}Sr_{0.05}CoO_3$: an efficient room-temperature thermoelectric oxide. Applied Physics Letters, 2004, 84(7): 1099-1101.

[173] A. J. Zhou, T. J. Zhu, and X. B. Zhao. Thermoelectric properties of perovskite oxides $La_{1-x}Sr_xCoO_3$ prepared by polymerlized complex method. Journal of Materials Science, 2008, 43(5): 1520-1524.

[174] T. He, J. Chen, T. G. Calvarese, and M. A. Subramanian. Thermoelectric properties of $La_{1-x}A_xCoO_3$ (A = Pb, Na). Solid State Sciences, 2006, 8(5): 467-469.

[175] E. Guo, R. D. Desautels, D. Keavney, A. Herklotz, T. Z. Ward, M. R. Fitzsimmons, and H. N. Lee. Switchable orbital polarization and magnetization in strained $LaCoO_3$ films. Physical Review Materials, 2019, 3(1): 014407.

[176] G. M. Kaminsky, D. P. Belanger, F. Ye, J. A. Fernandez-Baca, J. Wang, M. Matsuda, and J. Q. Yan. Origin of the net magnetic moment in $LaCoO_3$. Physical Review B, 2018, 97(2): 024418.

[177] A. O. Fumega and V. Pardo. Ferromagnetic and insulating behavior of $LaCoO_3$ films grown on a (001) $SrTiO_3$ substrate: A simple ionic picture explained ab initio. Physical Review Materials, 2017, 1(5): 054403.

[178] Kapil Gupta and Priya Mahadevan. Strain-driven magnetism in $LaCoO_3$ thin films. Physical Review B, 2009, 79(2): 020406.

[179] J. Q. Yan, J. S. Zhou, and J. B. Goodenough. Ferromagnetism in $LaCoO_3$. Physical Review B, 2004, 70(1): 014402.

[180] G. Maris, Y. Ren, V. Volotchaev, C. Zobel, T. Lorenz, and T. T. M. Palstra. Evidence for orbital ordering in $LaCoO_3$. Physical Review B, 2003, 67(22): 224423.

[181] K. Asai, P. Gehring, H. Chou, and G. Shirane. Temperature-induced magnetism in $LaCoO_3$. Physical Review B, 1989, 40(16): 10982.

[182] I. Weinberg and P. Larssen. Electron paramagnetic resonance and antiferromagnetism in $LaCrO_3$. Nature, 1961, 192(4801): 445-446.

[183] T. Arima, Y. Tokura, and J. B. Torrance. Variation of optical gaps in perovskite-type 3d transition-metal oxides. Physical Review B, 1993, 48(23): 17006.

[184] J. B. Webb, M. Sayer, and A. Mansingh. Polaronic conduction in lanthanum strontium chromite. Canadian Journal of Physics, 1977, 55(19): 1725-1731.

[185] D. P. Karim and A. T. Aldred, Localized level hopping transport in $La(Sr)CrO_3$. Physical Review B, 1979, 20(6): 2255.

[186] K. H. L. Zhang, Y. Du, P. V. Sushko, M. E. Bowden, V. Shutthanandan, S. Sallis, L. F. J. Piper, and S. A. Chambers. Hole-induced insulator-to-metal transition in $La_{1-x}Sr_xCrO_3$ epitaxial films. Physical Review B, 2015, 91(15): 155129.

[187] K. H. L. Zhang, Y. Du, A. Papadogianni, O. Bierwagen, S. Sallis, L. F. J. Piper, M. E. Bowden, V. Shutthanandan, P. V. Sushko, and S. A. Chambers. Perovskite Sr-doped $LaCrO_3$ as a new p-type transparent conducting oxide. Advanced Materials, 2015, 27(35): 5191-5195.

[188] L. Farrell, K. Fleischer, D. Caffrey, D. Mullarkey, E. Norton, and I. V. Shvets. Conducting mechanism in the epitaxial p-type transparent conducting oxide Cr_2O_3: Mg. Physical Review B, 2015, 91(12): 125202.

[189] G. Brunin. Perovskite Sr-doped $LaCrO_3$: An ab initio study (Thesis). Ecole polytechnique de Louvain, Université catholique de Louvain, Louvain-la-Neuve, Belgium, 2016.

[190] J. Volger. Further experimental investigations on some ferromagnetic oxidic compounds of manganese with perovskite structure. Physica, 1954, 20(1-6): 49-66.

[191] J. Mizusaki, T. Sasamoto, W. R. Cannon, and H. K. Bowen. Electronic conductivity, Seebeck coefficient, and defect structure of $La_{1-x}Sr_xFeO_3$ (x = 0.l, 0.25). Journal of the American Ceramic Society, 1983, 66(4): 247-252.

[192] M. Iijima and N. Murayama. High temperature thermoelectric properties of $La_{1-x}Sr_xFeO_3$ ($0 < x < 1$). In Proceedings ICT98 of the 17th International Conference on Thermoelectrics, Nagoya, Japan, 28 May 1998.

[193] N. Karthikeyan, R. R. Kumar, G. Jaiganesh, and K. Sivakumara. Thermoelectric power factor of $La_{0.9}M_{0.1}FeO_3$ (M = Ca and Ba) system: structural, band gap and electrical transport evaluations. Physica B: Condensed Matter, 2018, 529: 1-8.

[194] G. J. Snyder and A. H. Snyder. Figure of merit ZT of a thermoelectric device defined from materials properties. Energy & Environmental Science, 2017, 10(11): 2280-2283.

[195] R. Enright, S. Lei, G. Cunningham, I. Mathews, R. Frizzell, and A. Shen. Integrated thermoelectric cooling for silicon photonics. ECS Journal of Solid State Science and Technology, 2017, 6(3): N3103.

[196] J. Yan, X. Liao, D. Yan, and Y. Chen. Review of micro thermoelectric generator. Journal of Microelectromechanical Systems, 2018, 27(1): 1-18.

[197] J. Xie, C. Lee, and H. Feng. Design, fabrication, and characterization of CMOS MEMS-based thermoelectric power generators. Journal of Microelectromechanical Systems, 2010, 19(2): 317-324.

[198] Homepage of embedded design engineer for smart heating control and IoT applications. Retrieved from: http://www.micropelt.com/en.html.

[199] Commercial website of the thermoelectric generator. Retrieved from: https://www.tyndall.ie/thermo electric-generator.

[200] Z. Yuan. Etude et réalisation de microgénérateurs thermoélectriques planaires en technologie silicium. Université de Lille, Lille, France, 2012.

[201] A. P. Perez-Marín, A. F. Lopeandía Ll. Abad, P. Ferrando-Villaba, G. Garcia, A. M. Lopez, F. X. Muñoz-Pascual, and J. Rodríguez-Viejo. Micropower thermoelectric generator from thin Si membranes. Nano Energy, 2014, 4: 73-80.

[202] Modulo: a new technology for recovering ambient energy to power connected objects. Retrieved from: http://www.cnrs.fr/cnrsinnovation-lalettre/actus.php?numero=417.

[203] Homepage of MOÏZ devices use a silicon micro-chip to convert heat flux, created by temperature differences, in electricity (thermoelectric Seebeck effect). Retrieved from: https://moiz-eh.com/.

Chapter II Experimental techniques

2.1. Introduction

This chapter is dedicated to the presentation of the main experimental techniques used during my Ph.D. studies. They are classified into three main categories: elaboration (epitaxial growth of oxide thin films), structural characterizations, and physical property measurements.

2.2. Elaboration method: molecular beam epitaxy

2.2.1. Introduction

Main applications in the microelectronic industry require the use of thin films rather than bulk materials. Besides, epitaxial thin films are often desired rather than polycrystalline thin films to optimize or better control their properties [1, 2, 3]. Epitaxy is an oriented growth, both in the out-of-plane and in-plane directions, on a single-crystalline substrate. The main epitaxial growth techniques that are used for oxide thin films are listed in the following. Chemical routes: chemical vapor deposition (CVD), atomic layer deposition (ALD), chemical solution deposition (CSD) with the so-called sol-gel process with dip or spin coating… Physical routes: pulsed laser deposition (PLD), sputtering, molecular beam epitaxy (MBE)… Among these techniques, the MBE technique used in this thesis is not so mature for oxides but presents many advantages which will be described below.

Molecular beam epitaxy, which was used for the first time in the 1970s by A. Y. Cho and J. R. Arthur from Bell labs [4, 5], is an atomic layer by atomic layer crystal growth technique, based on the reaction of molecular or atomic beams with a heated crystalline substrate, performed in an ultra-high vacuum (UHV) environment [6]. MBE is capable of producing extremely high-quality crystalline heterostructures with precise control of chemical compositions and interfaces in the fraction of the atomic layer [7, 8, 9]. MBE has been used to successfully synthesize a variety of materials from semiconductors to metals, although the elaboration of semiconductor compounds has been the most common due to the rising demands from the micro/optoelectronic industry. Engineers continue to develop this technique to expand the range of materials and thus the scope of MBE applications. MBE has been developed for functional oxides only a few decades ago (from the ’90s), in particular for the growth of high Tc superconductors and the first epitaxial oxide buffer layers on semiconductors [3, 10, 11, 12, 13, 14]. In this context, INL benefits from a collaboration with RIBER Company (international

leader of MBE providers) through a common laboratory to further enhance the MBE tools for oxide growth.

The main advantages of MBE are the following. Because of elemental sources, MBE offers strong chemical flexibility, allowing the elaboration of full range solid-solutions with tunable doping for instance [15, 16]. Also, it provides the opportunity to control the growth at the monoatomic layer range (half perovskite oxide unit cell), allowing the elaboration of original superlattices or crystalline phases such as the Ruddlesden-Popper (RP) phases for instance [17]. Besides, because of the UHV environment (base pressure ≤ 10^{-10} Torr) and low oxygen partial pressure controlled in the 10^{-8} Torr range, MBE can ensure high purity of the deposited material and make it possible to manage very reactive surfaces of semiconductors such as that of silicon, paving the way to the monolithic integration by epitaxy of functional oxides on semiconductors [3, 10, 18, 19]. Finally, MBE growth is always associated with an *in-situ* reflection high-energy electron diffraction (RHEED) surface analysis providing important growth monitoring (see next section).

The main challenges of oxide MBE reside in the precise tiny-flux measurements, as well as the flux stability (or monitoring) during growth under oxygen partial pressure (preservation of the metallic source against oxidation), and thus the final control of the chemical composition of the growing film [20, 21]. Good oxidation of the oxide films at low oxygen partial pressure represents another challenge that can be critical for some oxides with targeted dielectric properties for instance since oxygen vacancy induces *n*-type doping. Post-deposition oxidation annealing is then often required.

2.2.2. Presentation of the oxide MBE chamber used at INL

During my thesis, all samples were fabricated in a RIBER Compact 21 chamber. The main structure/environment of this equipment is schematically presented in Figure 2. 1. The main oxide MBE growth chamber is connected to a transfer tube maintained in UHV (~10^{-8} Torr) by ionic pumps. This transfer tube is connected under UHV to a modutrac equipped with an outgazing furnace, an introduction chamber equipped with a turbomolecular pump allowing to quickly reach UHV pressures in the 10^{-8} Torr range, a III-V dedicated MBE chamber (RIBER 32), and an X-ray photoemission spectrometer (XPS). These UHV elements are separated from each other by gate valves. Each main element of the growth chamber will be briefly described in the following.

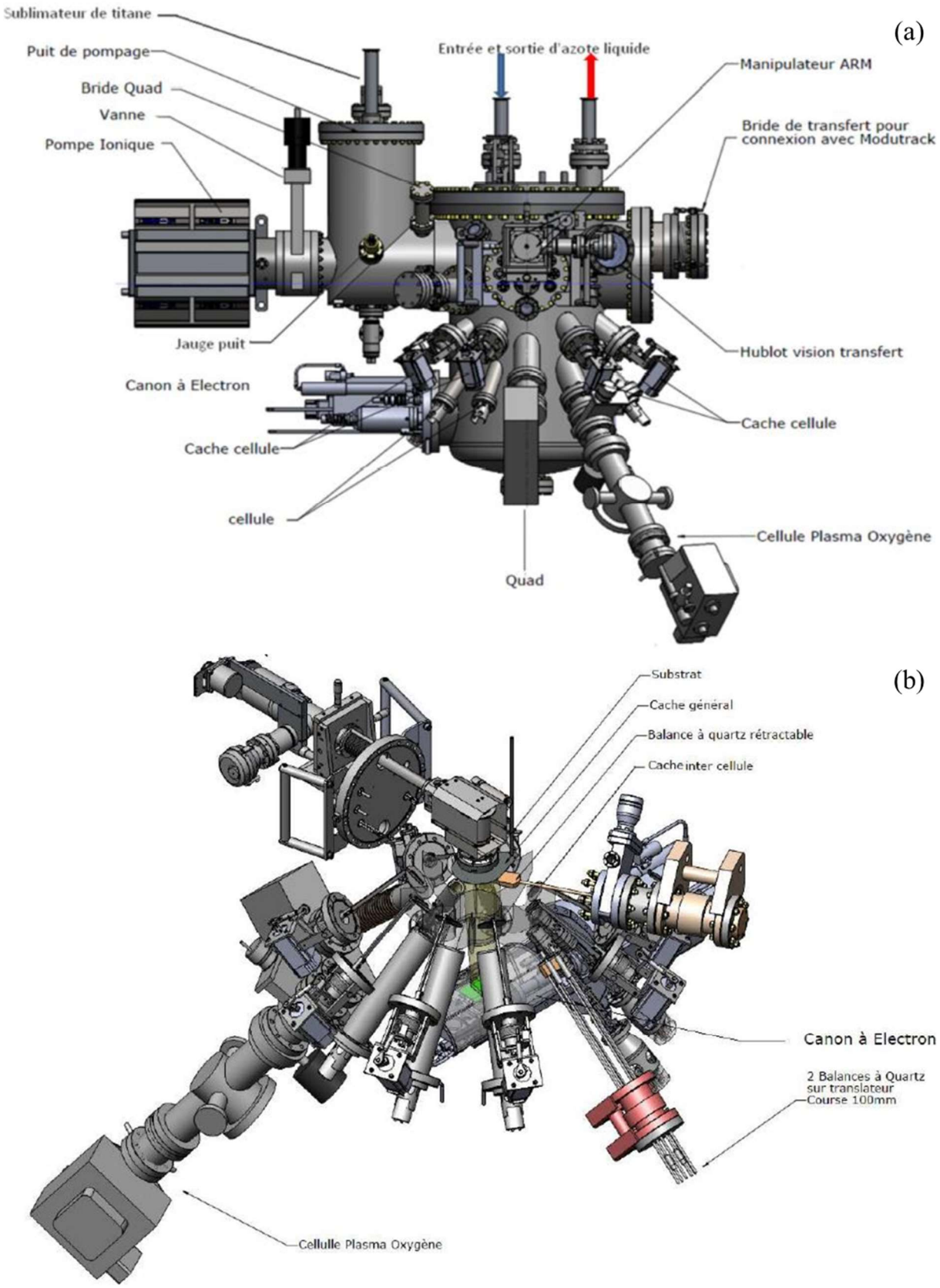

Figure 2. 1 (a) Side view and (b) exploded view of the epitaxy reactor for oxides at INL. Taken from Ref. 22.

2.2.2.1. Pumping elements

The main chamber is equipped with a turbomolecular pump, a cryogenic pumping (liquid nitrogen cooling in a cryogenic panel inside the chamber), and a titanium sublimation pumping, achieving an ultimate UHV base pressure down to 10^{-10} Torr.

2.2.2.2. Elemental sources

Knudsen effusion cells are mainly used to evaporate the elements thanks to heating filaments by Joule effect, of medium temperature (up to 1400 °C) for Sr, Cr, Ba, In, Ge, and Al, and of high temperature (up to 2000 °C) for La and Ti, with adapted crucibles made of refractory materials (pyrolytic boron nitride PBN, Tantalum…). The logarithm of the elemental flux is proportional to the inverse of the cell temperature in agreement with an Arrhenius law [8, 9]. I used these different Knudsen effusion cells during my thesis to grow $La_{1-x}Sr_xCrO_3$ and $SrTiO_3$ (see next chapters).

An electron gun with four crucibles is also available in the lower part of this chamber. It is mainly used to evaporate refractory materials and has been filled with Si, Ti, HfO_2, $LaAlO_3$, or Gd_2O_3.

The oxygen source is made of molecular oxygen introduced in a pre-chamber via a mass flow and a pressure regulation (in the mTorr range) with differential pumping. There is the possibility to produce atomic oxygen with an RF plasma box inside this pre-chamber, but I used only molecular oxygen during my thesis. The oxygen partial pressure inside the growth chamber is regulated through a regulation loop with the Bayard-Alpert ionization gauge and a butterfly valve (with gradual apertures positions) which is located in-between the oxygen pre-chamber and the growth chamber.

2.2.2.3. Flux measurement tools

Before growth, the targeted fluxes from the effusion cells [beam equivalent pressure (BEP)] have been accurately measured using a Bayard-Alpert (BA) ionization gauge located at the sample position, after subtraction of the background pressure. The growth rate of the material/element is proportional to its flux. The details will be presented in Chapter III. Moreover, a cross-check can be made by measuring the flux with a quartz crystal microbalance

(QCM) which gives an absolute growth rate measurement, although the measurement is very noisy due to the high sensitivity of the QCM to temperature (see Chapter III). Other flux measurement tools such as a mass spectrometer or an electron impact emission spectrometer (EIES) are also available in the chamber, but they are dedicated to the measurements of the flux coming from the electron gun, and thus they were not used in my thesis. They are not exempt from challenges and lack of accuracy either [20].

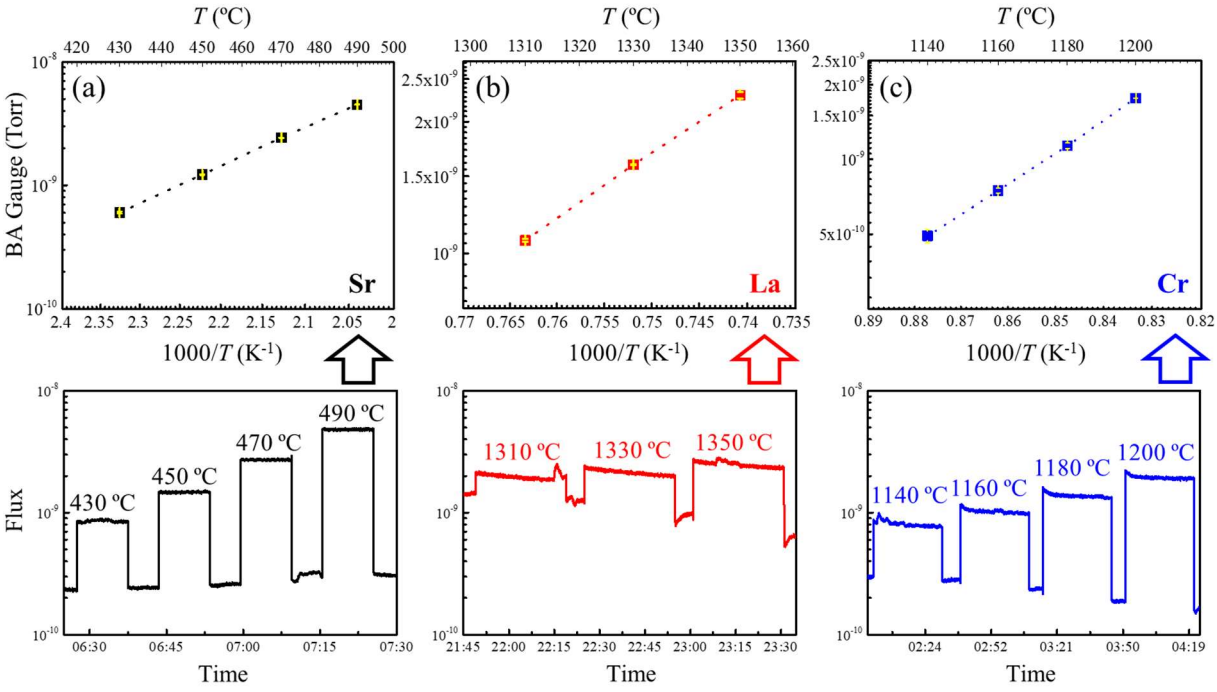

Figure 2. 2 An example of the beam equivalent pressures (BEP) of (a) Sr, (b) La, and (c) Cr fluxes, respectively, measured by Bayard-Alpert (BA) ionization gauge at different effusion cell temperatures, and the corresponding raw flux values measured before growth.

In Figure 2. 2, the MBE elemental fluxes, BEP measured by BA ionization gauge at different temperatures, have linear trends (even there are little errors) with $1/T$ as expected. The films were grown successively in the same period, after proper calibration series. A tolerable uncertainty of chemical composition within 4.4% is generated by this kind of measurement.

2.2.2.4. Sample holder

The sample holder mainly consists of a tantalum heating filament, protected by a PBN slab which also increases heating homogeneity. Theoretically, the temperature of the substrate can be set up to ~900 °C. It is measured from the backside of the sample using a thermocouple and

from its front side using a pyrometer (for T > 450-500 °C). The sample holder is made of molybdenum (low reactivity, refractory material). During the growth, the sample holder rotates with a constant angular velocity (~3 rpm) around the axis perpendicular to the substrate to enhance uniformity. Different sample sizes can be loaded on the 2-inch diameter holder: 1×1 cm^2 substrate, 2.5×3 cm^2 and 2-inch diameter substrates.

2.3. Structural characterization methods

The structural properties of thin films were mainly characterized after growth, even if some characterizations could be done *in-situ* during growth. The different *in-situ* and *ex-situ* characterization tools employed in this thesis to reveal the structural properties of the films (surface smoothness, thickness, crystalline quality, lattice parameters, chemical composition, etc.) are presented in the following.

2.3.1. Reflection high energy electron diffraction

Reflection high-energy electron diffraction (RHEED) is an *in-situ* non-destructive surface diffraction technique to characterize the surface of the substrates and films. This is the first characterization tool giving important information before, during, and after the growth (morphology, crystalline quality, in-plane lattice parameter, growth rate…).

2.3.1.1. Basic principle

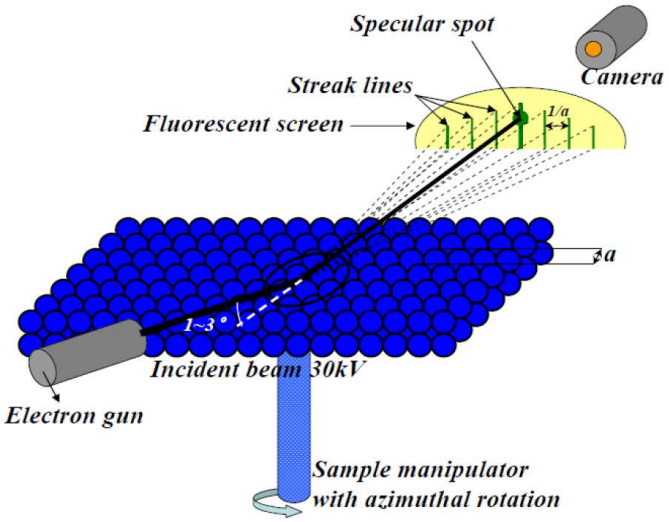

Figure 2. 3 Schematic diagram of the principle of RHEED. Taken from Ref. 23.

Figure 2. 3 illustrates the basic principle of RHEED. An electron beam [accelerated by a high voltage of 30 kV (for our equipment)], is reflected at grazing incidence (1-3°) by the sample surface and diffracted, as the surface is crystalline. The diffraction patterns are formed on a phosphorus screen. It gives information on the surface structure. Due to this special surface diffraction geometry, the RHEED gathers information only from the near-surface atomic layers of the sample.

2.3.1.2. Crystalline quality and surface morphology

The RHEED pattern analysis is very sensitive to crystalline surface quality and surface morphology. In Figure 2. 4, five different cases are illustrated depending on the surface quality.

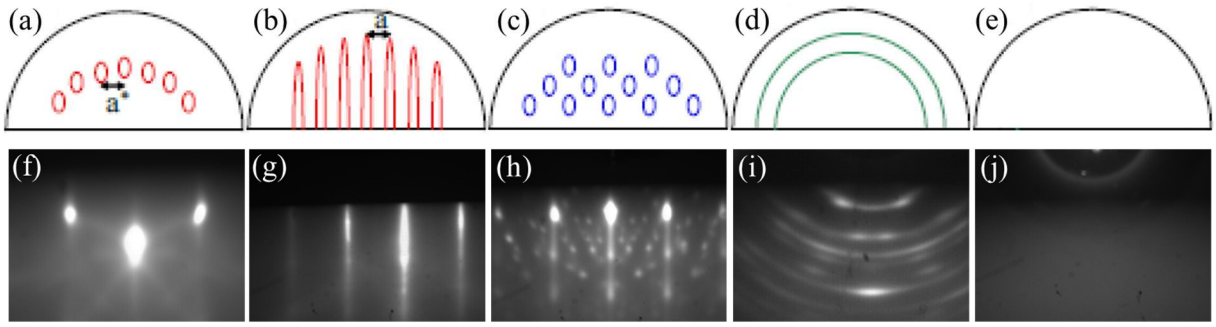

Figure 2. 4 RHEED patterns obtained as a function of surface quality (this work). (a) and (f) Perfectly smooth single-crystalline $SrTiO_3$ surface. (b) and (g) Smooth single-crystalline surface with a little disorder (micro-strain or crystalline mosaicity), *e.g.* stoichiometric epitaxial $LaCrO_3$ film. (c) and (h) Rough oriented surface, *e.g.* non-stoichiometric $SrCrO_3$ film. (d) and (i) Polycrystalline surface. (e) and (j) Amorphous surface, *e.g.* SiO_2.

If the sample has a perfectly smooth surface and an ideal monocrystalline quality, the reciprocal network corresponds to infinitely fine ordered rods normal to the surface. Consequently, the intersection of the network with the Ewald sphere gives fine diffraction spots on the Laue circle, as shown in Figure 2. 4a and f. When it is a smooth surface but with a little crystalline disorder (micro-strain or crystalline mosaicity), the reciprocal network consists of wider rods. Thus, the intersection of these rods with the Ewald sphere results in wider and elongated RHEED spots as shown in Figure 2. 4b and g. In the case where the surface of the sample is single-crystalline but rough, the presence of small 3D islands (from 3D growth) can be seen because of diffraction in transmission through those 3D surface crystals, the RHEED presents the pattern shown in Figure 2. 4c and h. In the case of a polycrystalline surface, which

possesses multiple crystalline orientations (multiple orientations of the corresponding truncation rods in the reciprocal space), Debye-Scherrer rings can be observed on the RHEED pattern, as shown in Figure 2. 4d and i. The RHEED pattern of a long-range orderless amorphous surface shows a diffuse halo (Figure 2. 4e and j).

2.3.1.3. Surface reconstruction, stoichiometry control, and in-plane lattice parameter

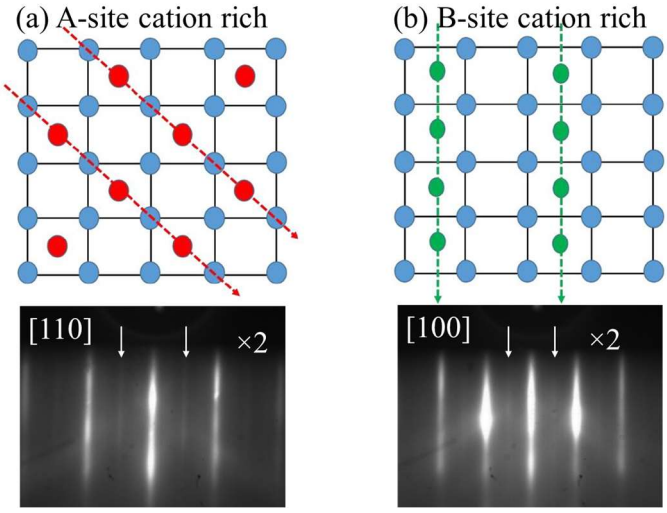

Figure 2. 5 Surface reconstructions as a function of composition for some perovskite oxide compounds and their corresponding RHEED images. (a) Excess in A-site cation. (b) Excess in B-site cation. Taken from Ref. 22.

In most crystalline materials, the arrangement of near-surface atoms is different from that of bulk. Atoms reorganize on the surface giving rise to surface reconstructions. In the study of perovskite-oxide structure, the homoepitaxial growth of $SrTiO_3$ on $SrTiO_3(001)$ has been taken as an example. In this oxide, the surface reconstruction depends on the surface composition with different chemical termination (SrO or TiO_2) and the excess cation type [24]. In the case of A-site (Sr cation) rich surfaces, the surface atoms present a double periodicity perpendicular to the azimuthal direction [110], compared to bulk periodicity (Figure 2. 5a). For the case of B-site (Ti cation) rich surfaces, the surface reconstructions generate a double crystalline periodicity perpendicular to the azimuthal direction [100] (Figure 2. 5b). On the corresponding RHEED patterns, the change in atomic periodicity due to these surface reconstructions results in the formation of half-order reflection streaks. Thus, during the growth of $SrTiO_3$ thin films, the stoichiometry can be monitored and corrected in real-time using RHEED. It should be noted that this type of reconstruction, clearly visible in the case of $SrTiO_3$, is not necessarily applicable to all other ABO_3 perovskite compounds.

Also, line profiles across the streaks can allow us to monitor *in-situ* the in-plane lattice parameters and lattice strain relaxation during growth [25, 26]. This can be useful to measure/confirm the critical thickness above which a film lattice is fully relaxed depending on the epitaxial lattice strain/mismatch.

2.3.1.4. Growth modes, growth rate, and atomic diffusion kinetics

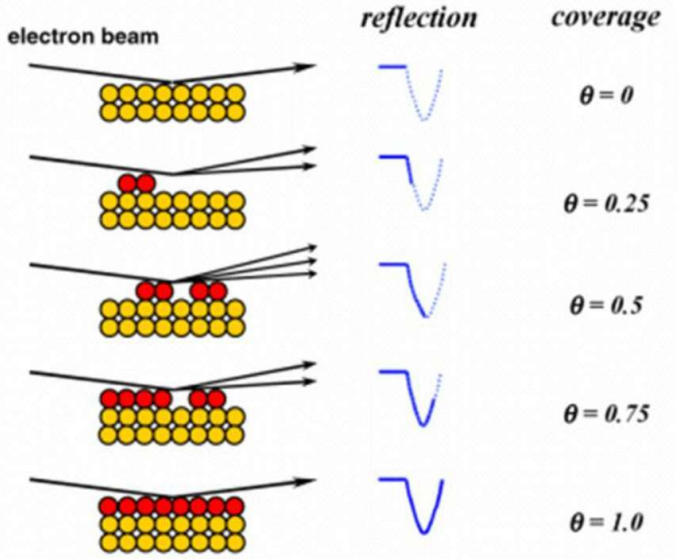

Figure 2. 6 RHEED intensity and atomic-scale surface roughness. Taken from Ref. 27.

As presented previously, the global RHEED pattern indicates if the growth is two-dimensional (spots or streaks aligned in the Laue circles) or 3D (arrays of transmission diffraction spots). In the case of 2D growth, monitoring the intensity of the specular spot gives information on the growth modes (atomic layer-by-layer or step-flow), and on the growth rate if the growth occurs in the layer-by-layer mode [28, 29]. The layer-by-layer mode occurs when the diffusion length of the adatoms is smaller than the mean terrace width whereas step-flow mode occurs when the diffusion length of the adatoms is larger than the mean terrace width [30].

In the 2D layer-by-layer growth, the intensity oscillation of the specular spot as shown in Figure 2. 6 can be observed. The intensity depends on the film's surface reflectivity, which is a function of the inverse of its surface roughness at the atomic scale.

In the initial state, the sample surface is atomically smooth with full coverage ($\theta = 0$) and the reflectivity of the specular beam is maximum. When a new atomic layer begins to be formed, the electrons also start to be diffused by the adatoms. The intensity of the specular beam decreases ($\theta = 0.25$). When the topmost atomic plane is half-covered ($\theta = 0.5$), its roughness

reaches the maximum, then the intensity a minimum. The growth continues, the surface atomic roughness decreases and the intensity recovers gradually (θ = 0.75). When the roughness continues to decrease with the growth up to a full new atomic layer, the reflectivity increases up to a maximum of the intensity. Thus, the growth of a fraction of complete monolayer can be monitored by RHEED in this growth mode and the corresponding growth rate can be determined by the oscillation periodicity. This growth rate can be cross-checked by *ex-situ* X-ray reflectivity measurements where the thickness of the grown film can be extracted (see the section below).

Also, the surface diffusion kinetics or coefficients of adatoms can be estimated by measuring the intensity recovery after stopping the growth (or after each laser pulse in the PLD growth technique) [31].

2.3.2. X-ray diffraction and reflectivity

X-ray diffraction (XRD) is a non-destructive technique allowing to investigate the structural properties of crystalline materials. In this section, after a summary of the basic XRD principle, various measurements such as X-ray reflectivity, rocking curve, reciprocal space map, and pole figure measurements will be introduced.

2.3.2.1. Principle

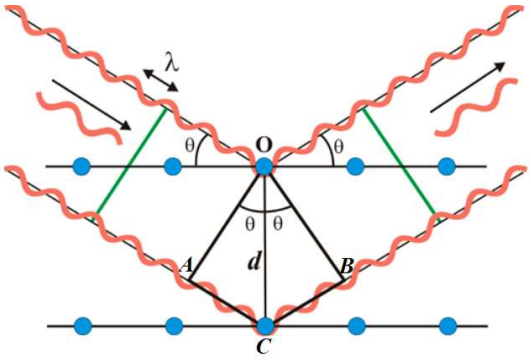

Figure 2. 7 Principle of X-ray diffraction by a crystal.

The principle of XRD consists in illuminating the material analyzed by monochromatic X-rays, such that the incident beam forms an angle θ with one of the reticular planes (*hkl*) of the crystal lattice (see Figure 2. 7). Thus, each atomic plane of this family (*hkl*) will reflect the

X-rays with the same angle of incidence θ. If the path difference traveled between two rays reflected on two successive reticular planes (*hkl*) is a multiple of the incident wavelength, the Bragg condition is satisfied and diffraction occurs (constructive interference) [32].

According to Bragg's law, the condition for (*hkl*) planes to diffract is given by the relation:

$$2d_{hkl}\sin\theta = n\lambda, \ (n = 1, 2, 3\ldots) \qquad (2.1)$$

where d_{hkl} is the inter-reticular distance of the (*hkl*) plane, θ is diffraction angle, and λ is X-ray wavelength.

The Bragg relation makes it possible to determine the interatomic distance d_{hkl} in the crystal direction perpendicular to the (*hkl*) planes by measuring the diffraction angle (with a constant X-ray wavelength).

2.3.2.2. Presentation of the diffractometer and the main measurements

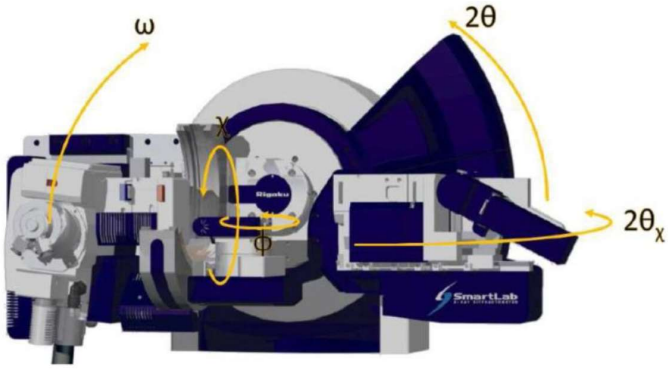

Figure 2. 8 The goniometer of the SmartLab diffractometer from Rigaku available at INL. Taken from Ref. 33.

The high-resolution "SmartLab" diffractometer from Rigaku has been used in my thesis. Incident parallel X-ray beam is generated by a high-power (45 kV × 200 mA = 9 kW) rotating anode, with monochromatic $Cu_{-k\alpha1}$ emission (λ = 1.54056 Å) thanks to two-bounces monochromator [double reflections Ge(004) or Ge(220) single-crystals] installed at the output of the X-ray source. With a goniometer allowing various rotational movements (shown in Figure 2. 8) for the X-ray source (ω), punctual detector (2θ and $2\theta_\chi$), and sample holder (ϕ, χ, and crossed cradles R_x and R_y), this diffractometer offers the degrees of freedom necessary to probe the crystal structure of single-crystals and epitaxial films in-plane and out-of-plane in

coplanar and non-coplanar (*e.g.* grazing incidence surface XRD) geometries with accurate positioning concerning crystallographic planes. In the following, the main measurements used with this diffractometer are presented.

– **X-ray reflectivity (XRR)** can be used to analyze film thickness, density, and roughness. In this case, the X-ray beam arrives on the sample surface at a glancing incident angle (0-4°) after the alignment of the mean surface. The reflectivity scan is then a $\theta/2\theta$ scan at low incidence angles (typically < 10°) with narrow slits (0.5 mm). The resulting profile enables analysis of the structural parameters of smooth thin films such as density, thickness, and root-mean-square (rms) roughness of the interfaces. Figure 2. 9 shows the resulting structural parameters that can be extracted from the fit of the reflectivity curve, here with an example of $LaCrO_3$ thin film grown on $SrTiO_3$(001). The XRR fits are mainly performed using the software "RCRefSimW" developed by P. Zaumseil from IHP, Frankfurt, Germany.

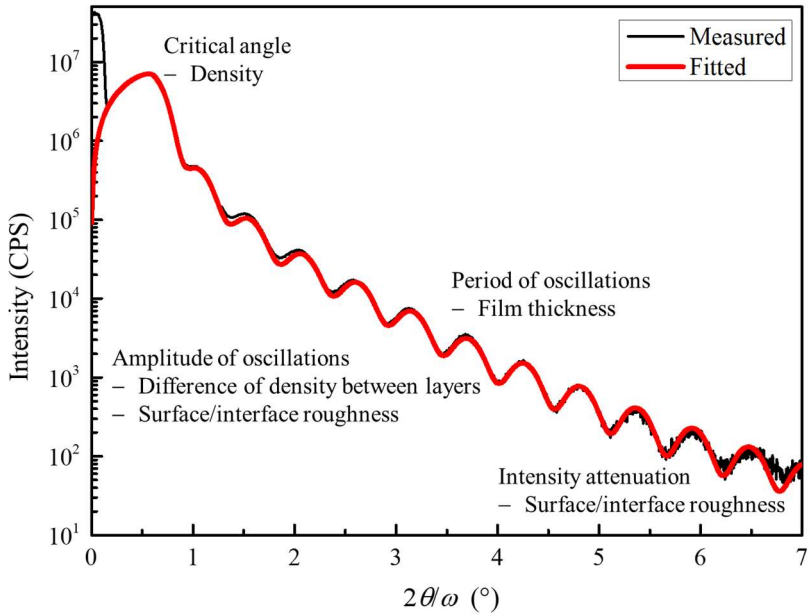

Figure 2. 9 Reflectivity curve (experimental data and fit) from a $LaCrO_3$ film on $SrTiO_3$(001) substrate (this work), allowing the extraction of structural parameters such as thickness, roughness, and density.

– **X-ray diffraction (XRD) $\theta/2\theta$ (or so-called $2\theta/\omega$) scan** is the first diffraction scan to be performed to have information on the crystallographic phase, the main out-of-plane crystalline orientations, and the out-of-plane lattice parameter of the crystal. In this case, the sample is aligned to the crystallographic plane of the substrate surface, and the scanned angle range can be large ($10° < 2\theta < \sim160°$) and is mainly restricted between 20° and 80° with a special focus on the intense (002) reflection of the perovskite oxides occurring between ~45° and 50° (as shown in Figure 2. 10).

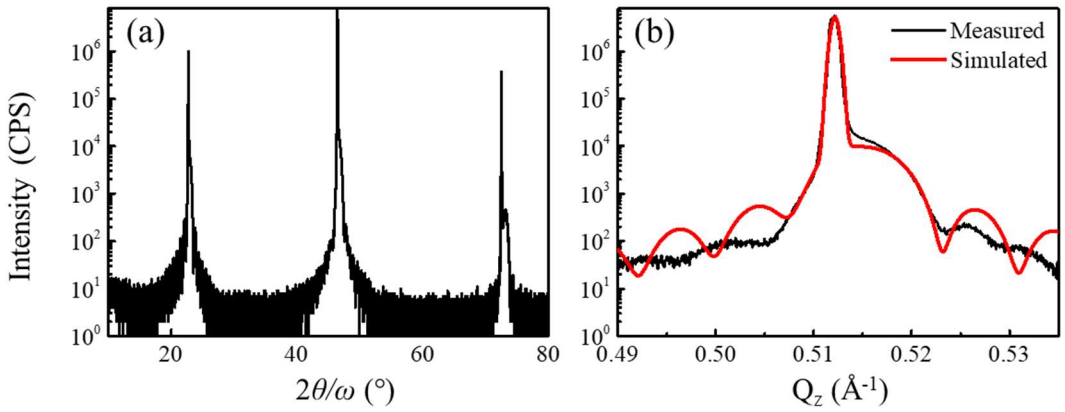

Figure 2. 10 (a) XRD $2\theta/\omega$ scan from 10° to 80° and (b) XRD scan near the (002) Bragg reflections on $LaCrO_3$ film grown on $SrTiO_3$(001) substrate (this work).

– **Rocking curve (RC) or the so-called *ω*-scan** allows measuring the distribution of the crystalline orientation which is called mosaicity (Figure 2. 11). For a given family (*hkl*), the atomic planes are not perfectly parallel. Maintaining $2\theta_{hkl}$ fixed at the maximum intensity Bragg position, the incident angle ω is scanned around the maximum intensity potion. This measurement reflects the crystalline quality of the sample. The full width at half maximum (FWHM) of this curve is the value of the mosaicity.

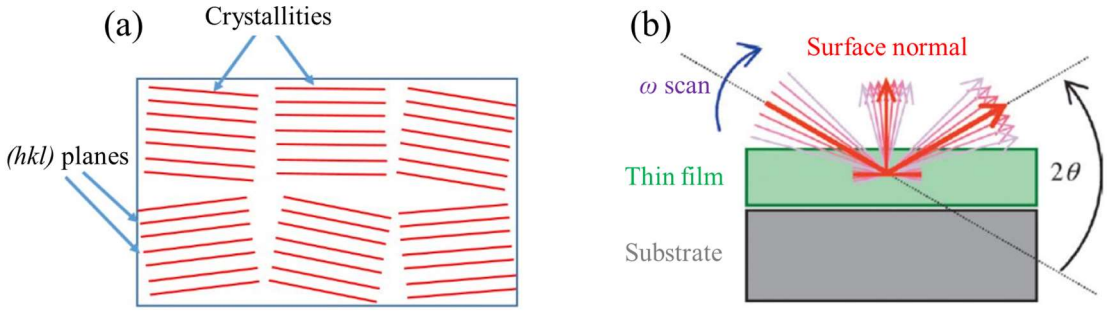

Figure 2. 11 (a) Mosaicity of textured crystalline materials. (b) Sketch of the XRD RC measurements on a thin film deposited on a substrate. Taken from Ref. 23.

– **Reciprocal space mapping (RSM)** is used to analyze the diffracted intensity in single-crystalline or epitaxial films both along the out-of-plane and in-plane directions. An RSM measurement acquires a two-dimensional intensity distribution by performing a series of $2\theta/\omega$ scans at stepped values of ω. In other words, it combines the two previous measurements, but it is rather done on asymmetric planes (not parallel to the substrate surface, to have in-plane information). Measuring such intensity distributions enables to analyze peak distributions and positions, such as the peaks spreading/position in the ω

direction (orientation distribution of the lattice, in-plane lattice parameter, and in-plane microstrain if asymmetric planes of different orders are used) and in the $2\theta/\omega$ direction (dispersion of the lattice constant, out-of-plane lattice parameter), as shown in Figure 2. 12. During the analysis of RSM, the coordinate (ω, 2θ) can be transformed into the reciprocal space unit (Q_x, Q_z) using the following relations:

$$Q_x = \frac{2\sin\theta\sin(\theta-\omega)}{\lambda} = \frac{h}{a} \tag{2.2}$$

$$Q_z = \frac{2\sin\theta\cos(\theta-\omega)}{\lambda} = \frac{l}{c} \tag{2.3}$$

where a and c represent the in-plane and out-of-plane lattice parameters respectively.

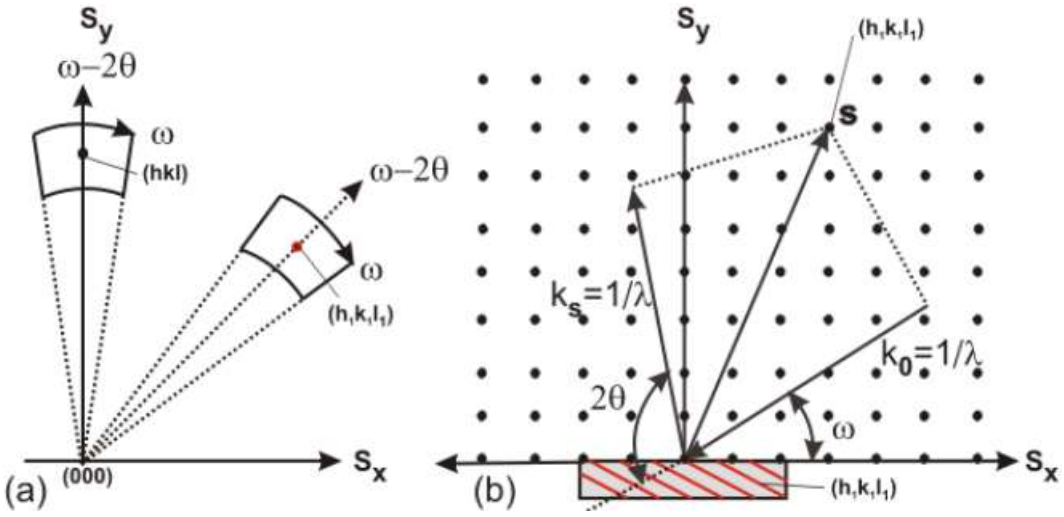

Figure 2. 12 (a) Scans in reciprocal space for two different reciprocal lattice points (hkl) (symmetric) and ($h_1k_1l_1$) (asymmetric). (b) Reciprocal space construction for the asymmetric reflection ($h_1k_1l_1$). $\boldsymbol{k}_s$ and $\boldsymbol{k}_0$ are the wave vectors for the diffracted and the incident X-rays, respectively. $\boldsymbol{S} = \boldsymbol{k}_0 + \boldsymbol{k}_s$ is the scattering vector. Taken from Ref. 34.

2.3.3. X-ray photoelectron spectroscopy

X-ray photoelectron spectroscopy (XPS) is a method to measure the chemical composition and the valence state of the elements of the material. The core-level electrons of the atoms of the near-surface of the sample (< 10 nm deep generally) can be excited by X-rays and emitted. The electrons are photo-emitted from the material with certain kinetic energies (KE), which can be measured by the spectrometer (detector).

At INL, the XPS is equipped with an Al rotating anode X-ray source with monochromatic Al Kα radiation ($h\nu_{\mathrm{Al\ K\alpha}}$ = 1486.6 eV), a UHV stainless steel chamber, an electron collection lens, an electron energy analyzer, a magnetic field shielding, and an electron detector system [35, 36, 37]. The XPS is directly connected to the oxide MBE providing *in-situ* measurements.

For instance, the excitation process of Sr^{2+} cation is illustrated in Figure 2. 13. The electron binding energy (*BE*) of each emitted electron can be determined:

$$KE = h\nu - BE - \phi_{spectrometer} \tag{2.4}$$

where h is the Planck constant, v is the frequency of photons, and $\phi_{spectrometer}$ is the minimum energy required for an electron to penetrate the analyzer.

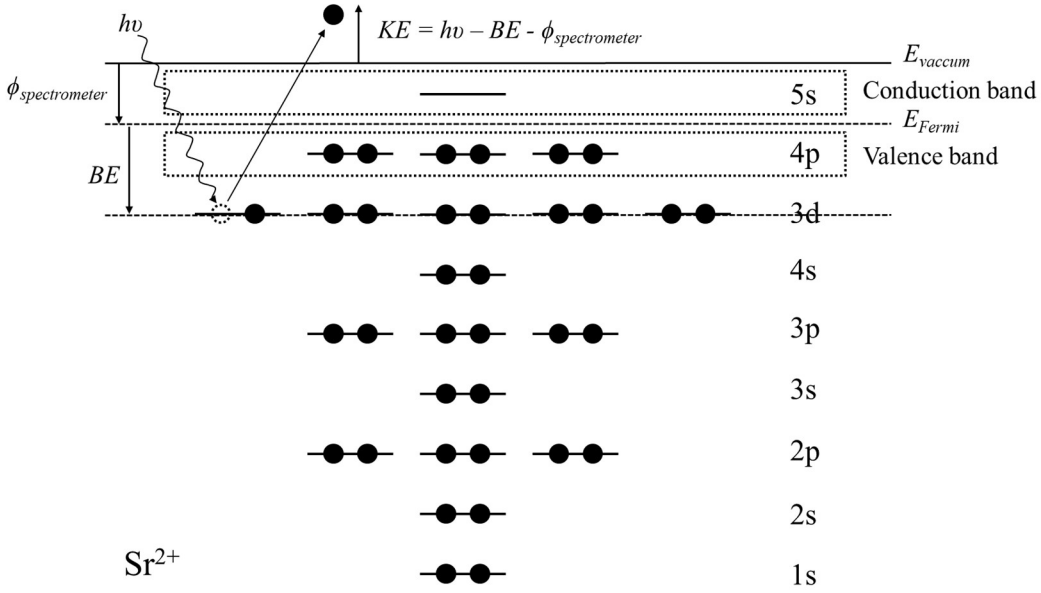

Figure 2. 13 An electron energy diagram for an Sr^{2+} cation showing the absorption of a photon and resultant expulsion of a 3*d* level photoelectron.

Each element composition (measured spectral intensity *I*) can be extracted using this equation:

$$I = \sigma\lambda N_{atom} \tag{2.5}$$

where σ is the photoionization cross-section of the considered element and core-level, λ is the mean free path, and N_{atom} is the number of considered atoms (within 5 nm of the film surface).

Our XPS equipment gives an error range of 5-15%, which is higher than that of flux measurement. In my following studies, I tend to adopt the more precise element composition given by flux measurement.

2.3.4. Rutherford backscattering spectrometry

Rutherford backscattering spectrometry (RBS) can also be used to determine the chemical composition of the films by analyzing the energy loss of light ions at high energies (0.5-4 MeV) passing through the material [38]. During an RBS analysis, high-energy He^{2+} ions (*i.e.* α particles) are directed onto the sample, then the energy distribution amount of the backscattered He^{2+} ions at a given angle is measured. Since the backscattering cross-section for each element is known, it is possible to obtain a quantitative compositional depth profile from the RBS spectrum obtained, for films that are less than 1 μm thick. In my thesis, the stoichiometric $LaCrO_3$ and $SrCrO_3$ calibrations were measured by RBS at Institut de Physique Nucléaire de Lyon (IPNL) with the help of B. Canut from INL. The results were in good agreement with that of XRD/RHEED, even with an uncertainty of 10%.

2.3.5. Atomic force microscope

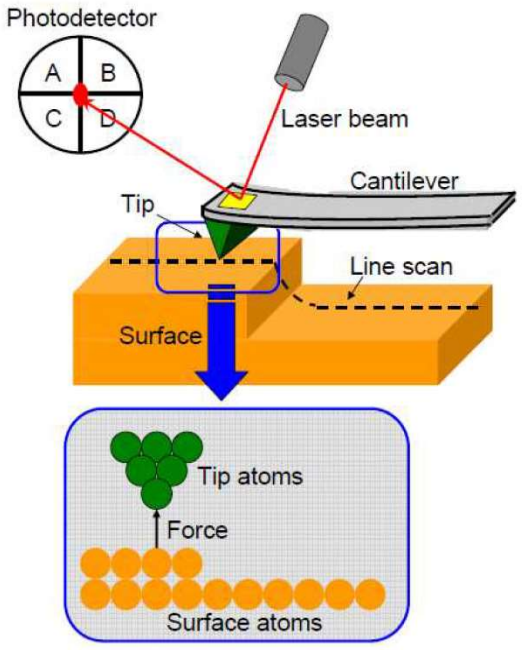

Figure 2. 14 Principles of AFM. A sample is probed by an ultrasharp stylus mounted on a cantilever, which scans over the surface. A reflected laser beam reports deflection of the cantilever to a split photodiode. Photoelectric circuitry then converts the deflections into height information recorded as a digital image. Taken from Ref. 39.

Atomic force microscopy (AFM), developed after the invention of the scanning tunneling microscopy (STM) in the ’80s [40], is a common near-field probe method for measuring and imaging the film surface at the nanoscale. Its main principle consists of lateral scanning a surface with a tip having a near-atomic radius. AFM can work with different modes, such as contact mode, non-contact mode (used for characterizing my samples). One of the most important elements of an AFM is the tip which should be extremely sharp for good lateral resolution. The corresponding stepper motors should be accurate as well for this lateral resolution. The tip is mounted at the end of a flexible cantilever as shown in Figure 2. 14.

As it approaches the surface, the tip and the investigated surface interact because of Van der Waals's force. By monitoring the deflection of the cantilever with a feedback loop, the downward or upward movement of the tip gives the topography of the scanned surface. This deflection is measured by an optical lever mode. A laser beam is reflected on the backside of the cantilever, and then collected by a photodetector, which consists of closely spaced photodiodes. The angular displacement of the cantilever leads to one photodiode collecting more light than the other photodiode, producing an output signal.

- As a new operation mode, the friction force microscopy (FFM) [41] measures the torsion of the cantilever when scanning, to obtain the chemical contrast at the sample surface. Along with other types of AFM measurements, FFM has established the AFM as an important tool in the emerging field of nanotribology.
- The phase shift-imaging in tapping mode (difference in sticking coefficient depending on the material) [42] can also give us the surface compositional contrast. Because any change of the phase shift is directly related to a local change in the energy dissipated in the sample and independent of the topography.

Many other derived modes have been developed for characterizing other properties, such as piezoelectric properties with piezoelectric force microscopy (PFM) for instance. The AFM images have been mainly treated using the open-source software WSxM [43].

2.4. Methods used to measure the functional properties

In this section, all transport measurements used in my thesis for characterizing the thermoelectric properties are introduced, in particular the electrical conductivity and Seebeck coefficient.

2.4.1. Electrical measurement

Resistivity (ρ) is the ability of a material to impede the flow of electrical charges under an applied electrical field. It is related to the electrical conductivity (σ) extracted by $\sigma = \rho^{-1}$.

2.4.1.1. Four-probe method

The four-probe method [44], which is illustrated in Figure 2. 15a, is a simple and effective way to measure the ρ of thin films. This equipment is available at INL.

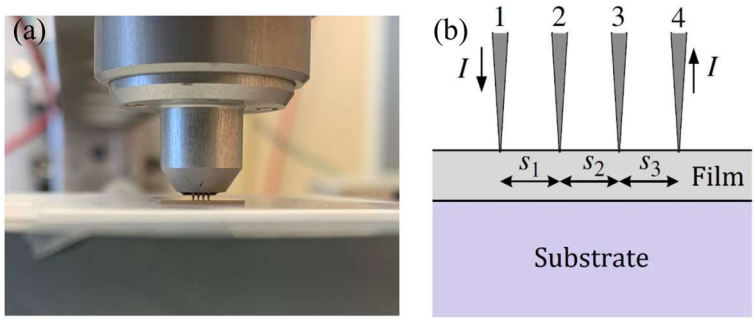

Figure 2. 15 (a) Four-probe measurement system at INL for in-plane σ of thin films. (b) Cross-sectional schematic sketch of the linear four probes on a film on a substrate.

The principle is to inject a current I on the surface at the external probes (1 and 4), and measure the induced voltage V on the internal probes (2 and 3). Then, an I-V curve can be plotted by sweeping the current. As shown in Figure 2. 15b, all four probes are placed on the surface of the thin film.

There are two types of measurements, the resistivity of a thin film deposited on a substrate and a solid material. Equations (2.6) and (2.7) give the resistivity for a solid material [45] and a film respectively. [46].

$$\rho = 2\pi s \frac{V}{I} \tag{2.6}$$

$$\rho = \frac{\pi d}{\ln 2} \frac{V}{I} \tag{2.7}$$

where V is the voltage between probes 2 and 3, I is the current flowing from points 1 to 4, s is the distance between probes, t is the thickness of the film. ρ can be extracted using the slope ($\Delta I/\Delta V$) of the I-V curve.

It is important to note that, to measure the intrinsic ρ of thin films, all samples should be annealed in the air to eliminate the possible impact of oxygen vacancy and conductivity from the substrate.

2.4.1.2. Hall effect measurement

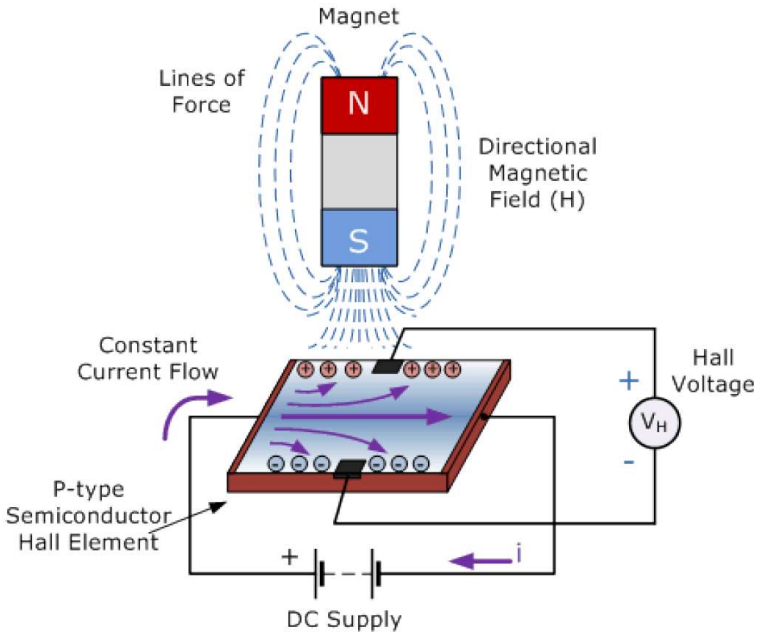

Figure 2. 16 Principle of the Hall effect measurement. Taken from Ref. 47.

Hall effect measurements are common to assess the electrical properties of conductive and semiconductor materials. A magnetic field is applied perpendicular to the direction of the applied current in the sample and the transverse voltage is measured in a direction perpendicular to both the current and magnetic field, as shown in Figure 2. 16.

The applied magnetic field induces a Lorentz force opposing the movement of the charge carriers, and separating the holes from the electrons. The created potential difference is called Hall voltage V_H, which can be related to the carrier concentration and the Hall constant R_H by the relation [48]:

$$V_H = \frac{BI}{net} = R_H \frac{BI}{t} \tag{2.8}$$

where B is the applied magnetic field, I is the applied current, n is the carrier concentration, e is the electronic charge, and t is the thickness of the thin film. The sign of the transverse voltage can be used to determine the sign of the charge carrier (electrons or holes) and hence the doping

type (*N* or *P*). It is also possible to estimate the mobility μ of the carriers [48]:

$$n = \frac{1}{eR_H} \tag{2.9}$$

$$\mu = |R_H|\sigma \tag{2.10}$$

$$\sigma = ne\mu \tag{2.11}$$

In my thesis, we prepared all the samples with squared shapes in the Van der Pauw geometry and ohmic metallic contacts in the four corners. The metallic contacts were Cr (~10 nm) followed by Au (~100 nm) and were deposited by e-beam evaporation using a shadow mask.

2.4.2. Seebeck measurement

2.4.2.1. Basic principle

As seen in Chapter I, the Seebeck coefficient (*S*) is a key thermoelectric parameter. When a thermoelectric sample is submitted to a temperature difference (ΔT), the ratio of the measured potential difference (ΔV), induced by ΔT, and this ΔT between any two points defines *S*:

$$S = \frac{\Delta V}{\Delta T} \tag{2.12}$$

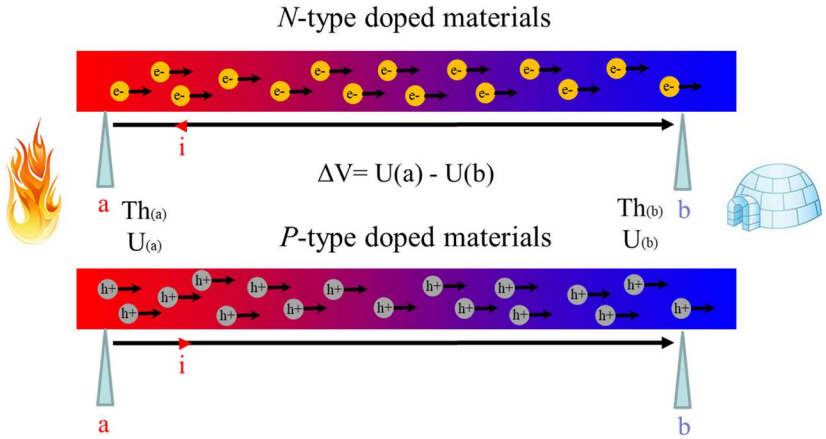

Figure 2. 17 Charge carrier migration of *n*-type (top) and *p*-type (bottom) thermoelectric materials during Seebeck measurement.

Figure 2. 16 represents the basic principle of S measurement. The ΔT between the two points (a and b) causes that the charge carriers in the thermoelectric material move from the hot side to the cold side, which creates a ΔV. The S of the thermoelectric material can be measured by precisely measure ΔV at each corresponding ΔT. In the case of n-type thermoelectrics (electron migration), S is negative, whereas, in the case of p-type thermoelectrics (hole migration), S is positive.

Conceptually, the measurement principle is quite simple. In practice, the measurement is relatively tricky because of the very low measured voltage (μV range) with low-temperature resolution (< 0.1 K). This is especially more tricky on thin films where the substrate can have a great impact on the measurement [49]. The removal of oxygen vacancy in the oxide substrates by post-deposition oxidation annealing is thus a prerequisite before the S measurements, to remove any contribution of the substrate to the electrical conductivity. Also, both the temperature and voltage measurements have to be measured exactly at the same points, and the contacts between the voltage leads and the sample should be ohmic [50]. The detailed description of different measuring methods has been explained by D. M. Rowe in the handbooks on thermoelectricity [51, 52].

2.4.2.2. Set-up built at INL and measurement

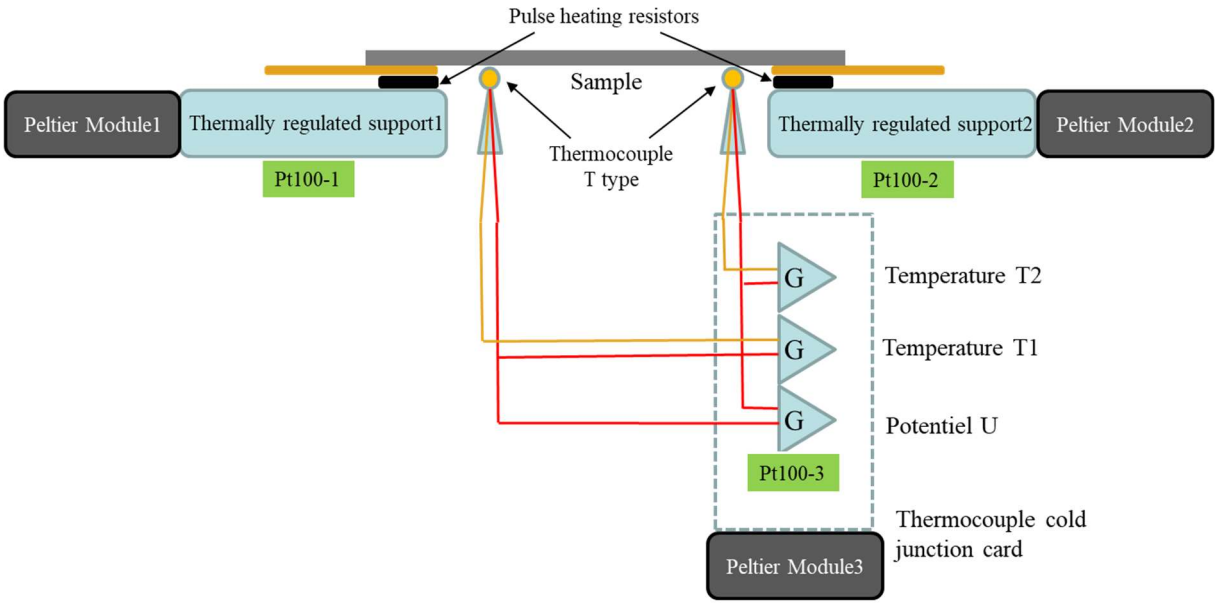

Figure 2. 18 Measurement architecture of the Seebeck set-up for films built at INL.

A Seebeck set-up, dedicated to the measurement of thin films or single-crystals, has been

built at INL by C. Botella during my Ph.D. thesis within the project ANR MITO. Figure 2. 18 presents the architecture of the measurement set-up. The set-up uses two Peltier modules (1 and 2) attached to two thermally regulated supports to create the ΔT inside the sample along the in-plane direction. One Peltier module is cooled and the other one is heated, and the reverse can be done (temperature difference can be induced in the two directions). Once the temperature difference on the sample is stabilized, the thermocouples in contact with the sample are used to measure both the temperature and voltage differences between the two points. The lead wires used to measure the voltage are copper and the thermocouples used are T type.

Figure 2. 19 shows the sample insertion area, inside a chamber in which a primary vacuum can be made. On the two sides, it can be seen that two arms thermally controlled by Peltier modules support the sample taped on Teflon support, which fits into the top of the thermocouples. Each arm can be regulated with a Pt100 thermometer. A third Peltier module (3) in Figure 2. 18 is used for the regulation of the electronic card at the same fixed T = 20 °C. As shown in Figure 2. 18c, the temperature resolution of the built equipment is less than 0.1 K and the voltage accuracy is about 5 µV.

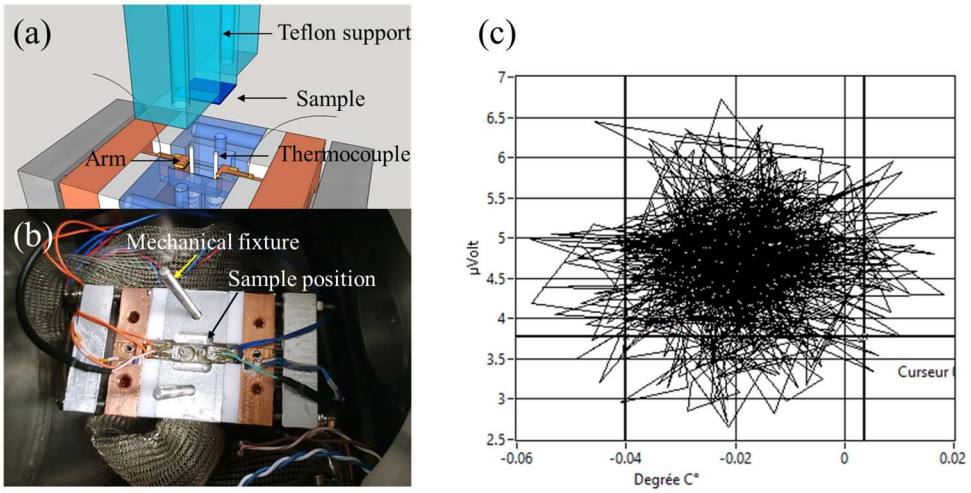

Figure 2. 19 (a) Schematic diagram of the measured sample, arms, and thermocouples. (b) Top view of the internal sample position. (c) Resolution (noise) both in voltage and temperature at static ΔT = 0 °C.

The measures have been calibrated at room temperature by using a 0.7 wt% Nb-doped $SrTiO_3$ (*n*-type, $n \approx 2.3\ 10^{20}$ cm^{-3}) substrate with an S = -300 µV·K^{-1} as a reference that has been measured a few years ago on the ILM set-up already calibrated and in agreement with the literature [53, 54, 55]. The voltage difference should be set to obtain 0 µV at ΔT = 0. Then, a sweep in T is induced and a created curve is obtained with a fixed slope ($\Delta V/\Delta T$) at 300 µV·K^{-1} (Figure 2. 20a). After such a calibration, measurement of *p*-type $La_{0.75}Sr_{0.25}CrO_3$ film epitaxially grown

on $SrTiO_3$(001) substrate gives a Seebeck coefficient of +180 $\mu V \cdot K^{-1}$, in perfect agreement with the literature [16]. The slope on *p*-type LSCO film is reversed with respect to *n*-type $SrTiO_3$:Nb substrate because of the different majority carrier type.

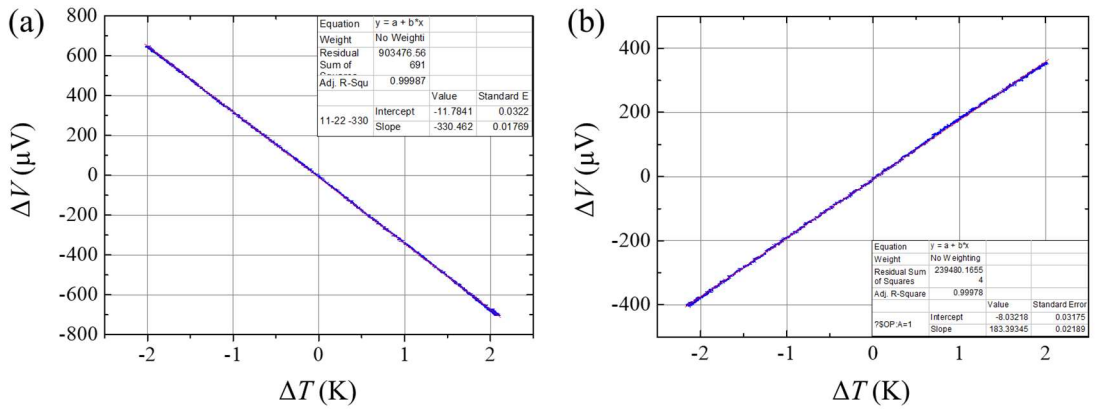

Figure 2. 20 Seebeck coefficient measurements at 300 K on (a) *n*-type 0.7 wt% $SrTiO_3$:Nb substrate used as calibration sample, and (b) *p*-type $La_{0.75}Sr_{0.25}CrO_3$ film epitaxially grown on $SrTiO_3$ (001) substrate, after set-up calibration with (a).

2.4.2.3. Set-up for high-temperature measurements at ILM

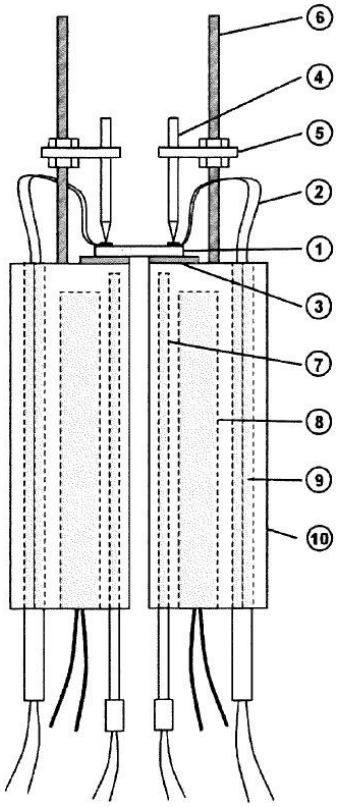

Figure 2. 21 Schematic representation of the *S* measurement. (1) Sample. (2) *N* type thermocouple. (3) Illumine strip. (4) Mullite rod. (5) Metallic support. (6) Threaded rod. (7) K type thermocouple. (8) Heating cartridge. (9) Ceramic sheath. (10) Refractory steel half-cylinder. Taken from Ref. 56.

In addition to the Seebeck measurement done at INL, some of my samples have been measured in collaboration with the group of S. Pailhès (and V. Giordano) at Institut Lumière Matière (ILM) to verify the results and to measure the temperature dependence $S(T)$ just above room temperature. The main components of the ILM set-up are sketched in Figure 2. 21. For each measurement, to have the most precise value, the average of four values has been calculated automatically.

Temperature differences in the sample, induced by the two different supporting blocs maintained at different temperatures, are measured using the measured voltages across the *N*-type thermocouples (2).

2.5. Conclusion

In this chapter, I presented the MBE technique as an elaboration method to grow epitaxial oxide films. I also introduced the structural characterization techniques used such as RHEED, XRD/XRR, XPS, RBS, and AFM. Finally, I presented the main techniques used for the characterization of the physical properties of the thermoelectric oxide films (electrical conductivity and Seebeck coefficient).

2.6. References

[1] S. B. Ogale. *Thin films and heterostructures for oxide electronics*. Springer Science & Business Media, New York, 2006.

[2] D. W. Bruce, D. O'Hare, and R. I. Walton. *Functional oxides*. Padstow, Wiley, 2010.

[3] A. A. Demkov and A. B. Posadas. *Integration of functional oxides with semiconductors*. Springer, New York, 2014.

[4] A. Y. Cho. Film deposition by molecular-beam techniques. Journal of Vacuum Science and Technology, 1971, 8(5): S31-S38.

[5] A. Y. Cho and J. R. Arthur. Molecular beam epitaxy. Progress in Solid State Chemistry, 1975, 10: 157.

[6] K. Alavi. *Encyclopedia of materials: Science and technology*, edited by K. H. J. Buschow, Amsterdam, New York, Elsevier, 2001.

[7] J. R. Arthur. Molecular beam epitaxy. Surface Science, 2002, 500(1-3): 189-217.

[8] H. Asahi and Y. Horikoshi. *Molecular beam epitaxy: Materials and applications for electronics and optoelectronics*. John Wiley & Sons, 2019.

[9] M. Henini. *Molecular beam epitaxy: From research to mass production*. Newnes, 2012.

[10] R. A. McKee, F. J. Walker, and M. F. Chisholm. Crystalline oxides on silicon: The first five monolayers. Physical Review Letters, 1998, 81(14): 3014.

[11] D. G. Schlom and J. S. Harris Jr. *MBE growth of high T_c superconductors*, pp. 505–622 in Molecular beam epitaxy: Applications to key materials, edited by R. F. C. Farrow. Park Ridge, Noyes, William Andrew Publishing, 1995.

[12] D. G. Schlom, L. Chen, X. Pan, A. Schmehl, and M. A. Zurbuchen. A thin film approach to engineering functionality into oxides. Journal of the American Ceramic Society, 2008, 91(8): 2429-2454.

[13] D. G. Schlom, J. H. Haeni, J. Lettieri, C. D. Theis, W. Tian, J. C. Jiang, and X. Q. Pan. Oxide nano-engineering using MBE. Materials Science and Engineering: B, 2001, 87(3): 282-291.

[14] D. G. Schlom. Perspective: Oxide molecular-beam epitaxy rocks!. APL Materials, 2015, 3(6): 062403.

[15] B. Jalan and S. Stemmer. Large Seebeck coefficients and thermoelectric power factor of La-doped $SrTiO_3$ thin films. Applied Physics Letters, 2010, 97: 042106.

[16] K. H. L. Zhang, Y. Du, A. Papadogianni, O. Bierwagen, S. Sallis, L. F. J. Piper, M. E. Bowden, V. Shutthanandan, P. V. Sushko, and S. A. Chambers. Perovskite Sr-doped $LaCrO_3$ as a new p-type transparent conducting oxide. Advanced Materials, 2015, 27(35): 5191-5195.

[17] J. H. Haeni, C. D. Theis, and D. G. Schlom. Epitaxial growth of the first five members of the $Sr_{n+1}Ti_nO_{3n+1}$ Ruddlesden-Popper homologous series. Applied Physics Letters, 2001, 78(21): 3292-3294.

[18] J. W. Reiner, A. M. Kolpak, Y. Segal, K. F. Garrity, S. Ismail-Beigi, C. H. Ahn, and F. J. Walker. Crystalline oxides on silicon. Advanced Materials, 2010, 22(26-27): 2919-2938.

[19] S. H. Baek and C. B. Eom. Epitaxial integration of perovskite-based multifunctional oxides on silicon. Acta Materialia, 2013, 61(8): 2734-2750.

[20] L. Louahadj. Développement de l'épitaxie par jets moléculaires pour la croissance d'oxydes fonctionnels sur semiconducteurs (Thesis). Institut des Nanotechnologies de Lyon, Ecole Centrale de Lyon, Lyon, France, 2014.

[21] Y. S. Kim. Sr flux stability against oxidation in oxide-molecular-beam-epitaxy environment: Flux, geometry, and pressure dependence. Journal of Vacuum Science & Technology A: Vacuum, Surfaces, and Films, 2010, 28(2): 271-276.

[22] M. E. Bouras. Ingénierie des propriétés diélectriques d'oxydes pérovskites par nanostructuration jusqu'à l'échelle de la monocouche (Thesis). Institut des Nanotechnologies de Lyon, Ecole Centrale de Lyon, Lyon, France, 2019.

[23] G. Niu. Epitaxy of crystalline oxides for functional materials integration on silicon (Thesis). Institut des Nanotechnologies de Lyon, Ecole Centrale de Lyon, Lyon, France, 2010.

[24] A. P. Kajdos and S. Stemmer. Surface reconstructions in molecular beam epitaxy of $SrTiO_3$. Applied Physics Letters, 2014, 105(19): 191901.

[25] N. Dix, I. Fina, R. Bachelet, L. Fàbrega, C. Kanamadi, J. Fontcuberta, and F. Sánchez. Large out-of-plane ferroelectric polarization in flat epitaxial $BaTiO_3$ on $CoFe_2O_4$ heterostructures. Applied Physics Letters, 2013, 102(17): 172907.

[26] R. Moalla. Couches minces d'oxydes pyroélectriques épitaxiées sur Si pour la récupération d'énergie thermique (Thesis). Institut des Nanotechnologies de Lyon, Ecole Centrale de Lyon, Lyon, France, 2016.

[27] Reflection High Energy Electron Diffraction. Graduate School of Engineering, Tohoku University. Retrieved from: http://www.material.tohoku.ac.jp/~kaimenb/B_RHEED.html.

[28] W. Braun. *Applied RHEED: Reflection high-energy electron diffraction during crystal growth*. Springer Science & Business Media, 1999.

[29] A. Ichimiya and P. I. Cohen. *Reflection high-energy electron diffraction*. Cambridge University Press, 2004.

[30] R. T. Longo. Mathematical modeling technique. AIP Advances, 2019, 9(12): 125211.

[31] X. D. Zhu. Reliable determination of kinetics parameters of adatoms in thin-film epitaxy. Physical Review B, 1998, 58(16): 10975.

[32] B. E. Warren. *X-ray Diffraction*. Courier Corporation, 1990.

[33] Commercial website of SmartLab (Rigaku). Retrieved from: https://www.rigaku.com/products/xrd/smartlab.

[34] High resolution X-ray diffraction. Retrieved from: http://www.geocities.ws/pranab_muduli/xrd.html.

[35] M. El Kazzi. Etude par photoemission (XPS & XPD) d'hétérostructures d'oxydes fonctionnels epitaxies sur silicium (Thesis). Institut des Nanotechnologies de Lyon, Ecole Centrale de Lyon, Lyon, France, 2007.

[36] D. Ferrah. Etude des propriétés physico-chimiques d'interfaces par photoémission (Thesis). Institut des Nanotechnologies de Lyon, Ecole Centrale de Lyon, Lyon, France, 2013.

[37] L. Fouquat. Etude par photoémission d'interfaces métal/oxyde et métal/semiconducteur élaborées par épitaxie par jets moléculaires (Thesis). Institut des Nanotechnologies de Lyon, Ecole Centrale de Lyon, Lyon, France, 2018.

[38] M. Mayer. Rutherford backscattering spectrometry (RBS). Workshop on Nuclear Data for Science and Technology: Materials Analysis. 2003, 34.

[39] G. Kada, F. Kienberger, and P. Hinterdorfer. Atomic force microscopy in bionanotechnology. Nano Today, 2008, 3(1-2): 12-19.

[40] G. Binnig, C. F. Quate, and C. Gerber. Atomic force microscope. Physical Review Letters, 1986, 56(9): 930.

[41] R. W. Carpick and M. Salmeron. Scratching the surface: Fundamental investigations of tribology with atomic force microscopy. Chemical Reviews, 1997, 97(4): 1163-1194.

[42] R. García, R. Magerle, and R. Perez. Nanoscale compositional mapping with gentle forces. Nature Materials, 2007, 6(6): 405-411.

[43] I. Horcas, R. Fernández, J. M. Gómez-Rodríguez, J. Gómez-Herrero, and A. M. Baro. WSXM: A software for scanning probe microscopy and a tool for nanotechnology. Review of Scientific Instruments, 2007, 78(1): 013705.

[44] D. K. Schroder. *Semiconductor material and device characterization*. John Wiley & Sons, 2015.

[45] F. M. Smits. Measurement of sheet resistivities with the four-point probe. Bell System Technical Journal, 1958, 37(3): 711-718.

[46] L. B. Valdes. Resistivity measurements on germanium for transistors. Proceedings of the IRE, 1954, 42(2): 420-427.

[47] T. Rachcha, S. Funde, K. Harihar, and N. Dhopare. Magnetically levitated solar powered DC machine with forward-reverse operation: Constructional design consideration. Second International Conference on Electrical, Computer and Communication Technologies (ICECCT). IEEE, 2017: 1-8.

[48] R. S. Popovic. *Hall effect devices*. CRC Press, 2003.

[49] M. L. Scullin, C. Yu, M. Huijben, S. Mukerjee, J. Seidel, Q. Zhan, J. Moore, A. Majumdar, and R. Ramesh. Anomalously large measured thermoelectric power factor in $Sr_{1-x}La_xTiO_3$ thin films due to $SrTiO_3$ substrate reduction. Applied Physics Letters, 2008, 92(20): 202113.

[50] J. Ravichandran. Thermal and electrical transport in oxide heterostructures (Thesis). UC Berkeley, California, United States, 2011.

[51] D. M. Rowe. *Handbook of thermoelectrics*. CRC Press, 1995.

[52] D. M. Rowe. *Thermoelectrics handbook: Macro to nano*. CRC Press, 2006.

[53] M. Apreutesei, R. Debord, M. Bouras, P. Regreny, C. Botella, A. Benamrouche, A. Carretero-Genevrier, J. Gazquez, G. Grenet, S. Pailhès, G. Saint-Girons, and R. Bachelet. Thermoelectric La-doped $SrTiO_3$ epitaxial layers with single-crystal quality: From nano to micrometers. Science and Technology of advanced Materials, 2017, 18(1): 430-435.

[54] S. Ohta and T. Nomura. High-temperature carrier transport and thermoelectric properties of heavily La-or Nb-doped $SrTiO_3$ single crystals. Journal of Applied Physics, 2005, 97(3): 034106.

[55] G. Bouzerar, S. Thébaud, C. Adessi, R. Debord, M. Apreutesei, R. Bachelet, and S. Pailhès. Unified modelling of the thermoelectric properties in $SrTiO_3$. Europhysics Letters (EPL), 2017, 118(6), 67004.

[56] A. Didier. Mesure du coefficient Seebeck à haute température (Stage de recherche). Institut Lumière Matière, Université Claude Bernard Lyon 1, Lyon, France, 2017.

Chapter III Effect of A-site Sr cationic substitution

3.1. Introduction

The purpose of this chapter is to present the structural, electrical, and thermoelectric properties of solid solutions $La_{1-x}Sr_xCrO_3$ (LSCO), with full composition range ($0 \leq x \leq 0.4$) from $LaCrO_3$ (LCO) to $SrCrO_3$ (SCO), grown on $SrTiO_3$(001) substrates. After a brief literature review concerning the structural and related physical properties of these compounds (section 3.2), the LCO and SCO calibration series, required to properly grow stoichiometric LSCO solid solutions, will be firstly presented (section 3.2). The results corresponding to LCO calibration are published in the reference [1]. Then, the effect of Sr-doping (or Sr substitution ratio for $x < 0.5$) on the structural and physical properties of stoichiometric LSCO epitaxial films will be presented (section 3.3). This chapter will in particular introduce the following chapters IV and V which concern the study of the effects of *i*) epitaxial strain (Chapter IV) and *ii*) the deviation from cationic stoichiometry (Chapter V) for $x = 0.25$ ($La_{0.75}Sr_{0.25}CrO_3$).

3.1.1. Lanthanum chromate $LaCrO_3$

3.1.1.1. Structural properties

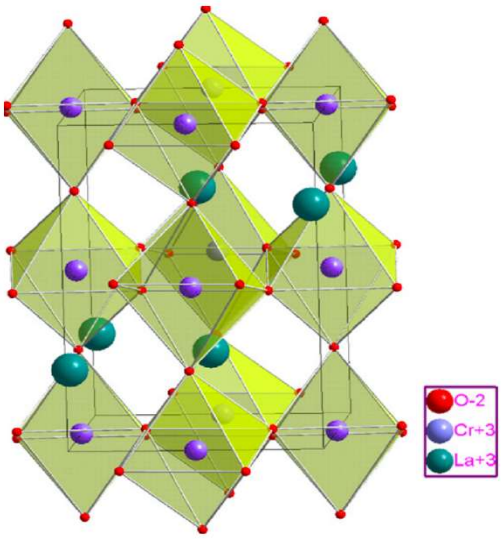

Figure 3. 1 The lattice unit cell structure of LCO at 295 K. Taken from Ref. 3.

The lanthanum chromate $LaCrO_3$ is a perovskite oxide with an orthorhombic structure at room temperature [2, 3, 4, 5, 6]. Its space group is *Pbnm* with lattice parameters $a = 5.513$ Å, $b = 5.473$ Å, and $c = 7.759$ Å at room temperature and ambient pressure [7, 8, 9, 10, 11]. However, it can be viewed as a pseudocubic lattice cell with lattice constant 3.885 Å [4, 7, 12], structurally

compatible with other functional perovskite oxides. The LCO unit cell simulated by Tseggai *et al*. [3] is represented in Figure 3. 1a and the octahedral coordination of the B cation with oxygen atoms is shown in Figure 3. 1b [13].

3.1.1.2. Physical properties

LCO is a G-type antiferromagnetic insulator with a charge transfer gap of 3.3 eV [14, 15]. However, its electronic bandgap of ~2.8 eV has also been measured by Maiti and Sarma via ultraviolet photoemission and Bremsstrahlung isochromatic spectroscopic measurements [16]. More recently, the different bandgaps have been studied in more details both experimentally and numerically by Sushko *et al*. [17] Different low-energy absorption levels are due to intra Cr *d-d* transitions (2.7 eV, 3.6 eV), while the O 2*p* to Cr 3*d* transitions happen for the energy of ~5 eV [17].

3.1.2. Strontium chromate $SrCrO_3$

Contrasting with $LaCrO_3$, strontium chromate $SrCrO_3$ has not been extensively described in the literature so far, probably because of difficult electro-neutrality from the main valence states ($Sr^{[2+]}Cr^{[3+]}O^{[2-]}_3$) which can induce structural instabilities [18].

3.1.2.1. Structural properties

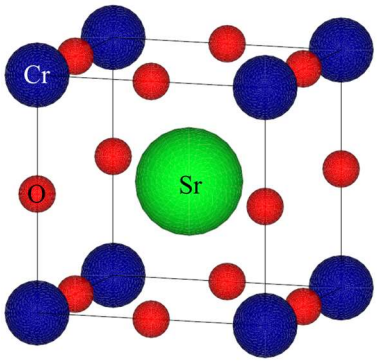

Figure 3. 2 Lattice unit-cell of cubic SCO at room temperature.

The bulk perovskite oxide SCO has mainly a cubic structure with a lattice parameter of 3.82 Å at room temperature [19], although a tetragonal phase can be induced by lattice strain [20], and a rhombohedral phase can be produced by reduction conditions at low temperature in thin

films [18]. The space group of the cubic compound is *Pm*3*m* [8, 9, 10]. The cubic lattice unit-cell at room temperature is represented in Figure 3. 2.

3.1.2.2. Physical properties

Unlike insulating LCO, SCO exhibits conducting properties with metallic behavior in its cubic phase, and semiconducting behavior in its rhombohedral phase with oxygen vacancies [18]. Also, the tetragonal phase is antiferromagnetic below 35-40 K, whereas the cubic phase remains paramagnetic at low temperatures. Figure 3. 3 [21] shows the evolution of the electrical resistivity (ρ) with temperature (T) ranging from 0 to 300 K for an epitaxial oxidized film grown on $LaAlO_3$(001) substrate with metallic transport behavior ($d\rho/dT > 0$). The room-temperature resistivity (ρ) is 1.3×10^{-3} Ω·cm, and it lowers to 5.2×10^{-4} Ω·cm at 50 K. Zhang *et al.* [21] fitted the $\rho(T)$ data using $\rho = \rho_0 + AT^2$ for 130-300 K (shown in the inset) with $\rho_0 = 4.6\times10^{-4}$ Ω·cm and $A = 1\times10^{-8}$ Ω·cm·K^{-2}, suggesting strong electron-electron scattering in metallic SCO. They also pointed out that the upturn at 50 K is common for many metallic transition metal oxides [22, 23] as well as for polar/nonpolar perovskite heterojunctions, such as the $LaAlO_3/SrTiO_3$(001) system [24, 25].

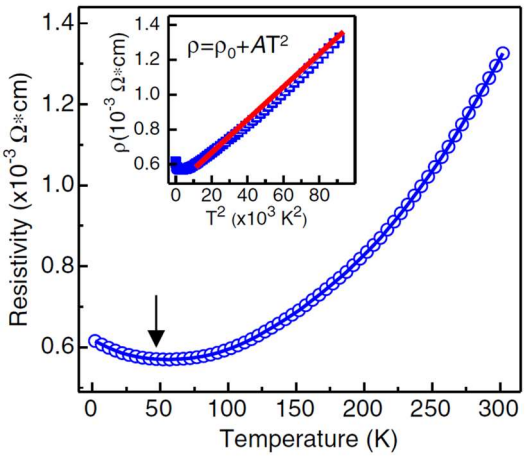

Figure 3. 3 Temperature-dependent electrical resistivity for a 50 nm SCO film grown on $LaAlO_3$(001) substrate. The inset shows resistivity versus T^2 and the best linearity occurs for temperature above 130 K. Taken from Ref. 21.

SCO thermoelectric properties are the object of some reports in the literature (none of these works report on the thermoelectric properties of epitaxial thin films). Zhou *et al.* [19] demonstrated a very small Seebeck coefficient (S) of polycrystalline SCO (~4 μV·K^{-1} shown in Figure 3. 4a), in agreement with high electronic conductivity. However, in this polycrystalline

compound, the temperature-dependence of the resistivity and Seebeck coefficient evoke that of a semiconductor probably because of grain boundary scattering [19]. More recently, Noor *et al.* [26] computed the thermoelectric properties of $XCrO_3$ (X = Ca, Sr, Ba) using the density functional theory. The temperature dependence of *S* is shown in Figure 3. 4b and appears coherent with a metallic electronic transport behavior. For SCO, at room temperature, the *S* value is 32.5 $\mu V \cdot K^{-1}$ and increases linearly with temperature (64.5 $\mu V \cdot K^{-1}$ at 800 K).

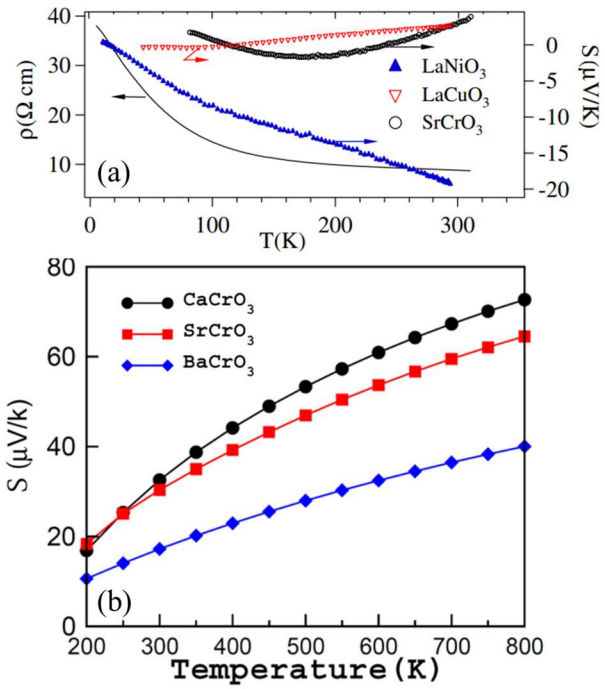

Figure 3. 4 (a) Temperature dependence of the resistivity and Seebeck coefficient of $SrCrO_3$, $LaNiO_3$, and $LaCuO_3$. Taken from Ref. 19. (b) Temperature-dependent calculated Seebeck coefficient for $XCrO_3$ (X = Ca, Sr, Ba) by using Boltztrap software. Taken from Ref. 26.

3.1.3. Strontium doped lanthanum chromate solid-solutions: $La_{1-x}Sr_xCrO_3$

The main structural, electrical, and thermoelectric properties of $La_{1-x}Sr_xCrO_3$ (LSCO) solid solutions reported in the literature are presented in this section [2, 27].

3.1.3.1. Structural properties

The unit-cell volume for different values of x in epitaxial LSCO films was measured by Zhang *et al.* [27] represented in Figure 3. 5 (red squares) where the blue and green lines represent the linear behavior between the two boundary values for two limiting cases: the green one stands for the case of bulk material, while the blue one supposes strained films and uses the

Poisson ratios of LCO and SCO (supposing the lattice parameter variation follows the Vegard's law) deposed on $LaAlO_3$ substrates.

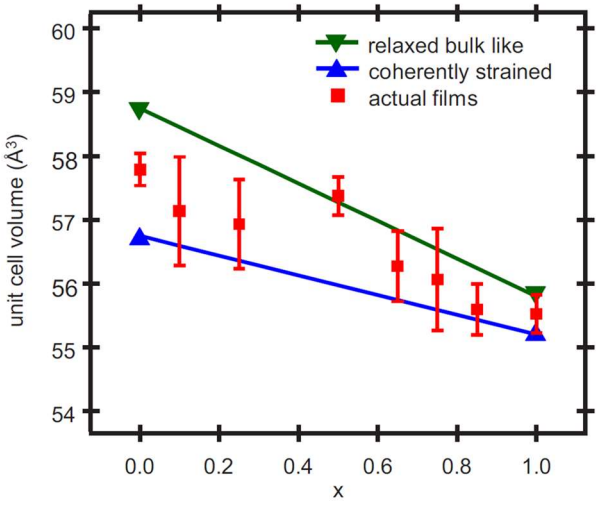

Figure 3. 5 Unit-cell volume of $La_{1-x}Sr_xCrO_3$ (LSCO) as a function of the Sr substitution ratio (x). The green and blue lines represent two limiting cases (the bulk volume, totally relaxed, and the volume of fully strained films). Taken from Ref. 27.

3.1.3.2. Physical properties

The effect of Sr doping in $LaCrO_3$ (A-site substitution of La^{3+} by Sr^{2+}) has been studied for more than 40 years [28]. Karim and Aldred have shown that increasing x in $La_{1-x}Sr_xCrO_3$ high-density sintered powder pellets (up to x = 0.4) induces a progressive increase of electrical conductivity, although a semiconductor-like transport behavior has been observed whatever x in this range ($x \leq 0.4$) [28]. The electrical conductivity increases over three decades at 300 K from ~10^{-2} $S \cdot cm^{-1}$ (x = 0) up to ~10 $S \cdot cm^{-1}$ (for x = 0.3-0.4). They also measure the corresponding Seebeck coefficient and show that it is positive and decreases accordingly with x from ~420 $\mu V \cdot K^{-1}$ (x = 0.02) to ~180 $\mu V \cdot K^{-1}$ (x = 0.2). They show that LSCO can be a relatively good *p*-type conducting oxide with transport properties described by small polaronic hopping. They also show that magnetic susceptibility follows a Curie-Weiss law between 600 and 1100 K, with an effective magnetic moment that decreases with an increase in Sr concentration. Later, the studies of Weber *et al.*, globally confirm these tendencies on the x-dependence of electrical conductivity and thermoelectric properties [29]. Later, Marsh and Parris predict that LSCO can become *n*-type at low temperature for x > 0.6 [30], while photoemission spectroscopy studies from Maiti and Sarma confirm that Sr substitution leads to hole doping and that a bandgap remains whatever the doping level in LSCO even if it decreases with x [16].

The most recent studies on epitaxial films from Zhang *et al*. (from the Chambers group) show that LSCO is *p*-type in the full composition range and becomes a metallic conductor for x ≥ 0.65 [27]. Interestingly, they also observed that this metallic behavior only happens when LSCO is deposited on $LaAlO_3$(001) substrate under slight compressive strain, revealing that lattice strain can have a great impact on the transport properties of LSCO (see Chapter IV). The curves for x ≤ 0.5 are characteristic of semiconducting material ($d\rho/dT < 0$), with increasing electrical conductivity and hole concentration with x [2]. The temperature dependence of electrical resistivity as well as the x-dependence of electrical conductivity (σ) and hole concentration (p) at room temperature from this latest work on epitaxial films grown by MBE are reported in Figure 3. 6.

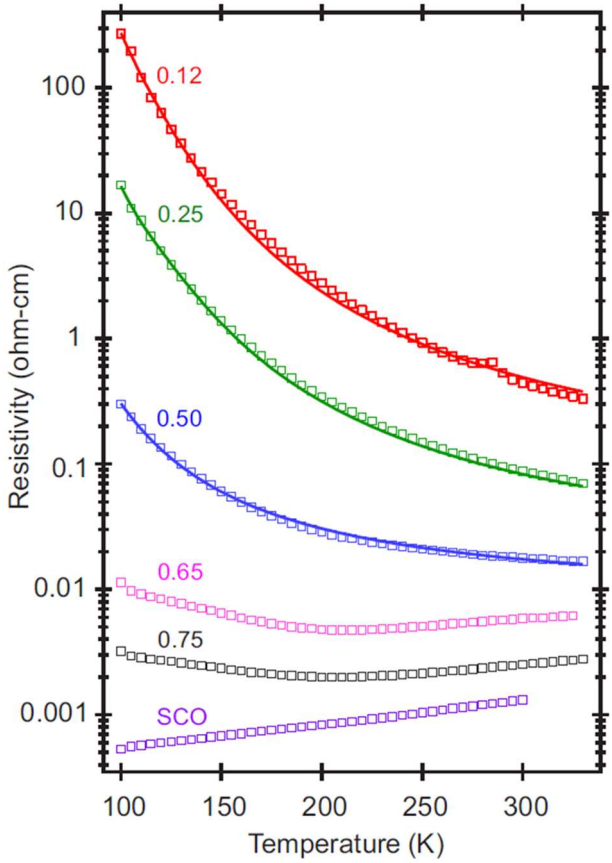

Figure 3. 6 Temperature dependence of the electrical resistivity of epitaxial LSCO films grown on $LaAlO_3$(001) substrates. Taken from Ref. 27.

It is worth noting that in the works of Zhang *et al*., hole concentration *p* was not directly measured (by Hall effect for instance). As mentioned in Chapter I section 1.4.3.2, following Farrell *et al*. [31] in their analysis of transport data for Mg-doped Cr_2O_3, Zhang *et al*. have determined the hole concentration *p* from *S* using a small polaron hopping model, which is appropriate for materials with extremely low charge carrier mobility (μ). Although the μ is low,

the *p* can easily be made relatively high by large Sr substitution for La. Therefore, the *σ* can be relatively high (up to 54 $S \cdot cm^{-1}$ with x = 0.5, $La_{0.5}Sr_{0.5}CrO_3$) for *p*-type thermoelectric films.

All the LSCO films exhibit positive *S* values, confirming *p*-type conductivity. According to the previous works, especially those of Karim *et al*. [28] and Zhang *et al*. [2], *S* decreases from 321 to 80 $\mu V \cdot K^{-1}$ from x = 0.04 to 0.5, while *σ* increases from 1.2 to 54 $S \cdot cm^{-1}$ at 300 K (See Chapter I, Figure 1. 24). The thermoelectric power factor extracted from these measurements gives a maximum of about 0.5 $\mu W\ cm^{-1}\ K^{-2}$ at x ~ 0.25 at room temperature (See Chapter I, Figure 1. 24). These values are summarized in Table 3. 1. The mobility values have been deduced from the equation $\mu = \sigma/ep$.

Table 3. 1 Room-temperature conductivity *σ*, hole concentration *p*, mobility *μ*, Seebeck coefficient *S*, and power factor PF of epitaxial LSCO films. Taken from Ref. 2.

x	*σ* $S \cdot cm^{-1}$	*p* $\times 10^{20}\ cm^{-3}$	*μ* $\times 10^{-2}\ cm^2 \cdot V^{-1} \cdot s^{-1}$	*S* $\mu V \cdot K^{-1}$	PF $\mu W \cdot cm \cdot K^{-2}$
0	-	-	-	-	-
0.04	1.2	7.9	0.95	321	0.124
0.12	3.6	12	1.8	281	0.284
0.25	15	34	2.7	180	0.486
0.5	54	75	4	80	0.346

3.2. $LaCrO_3$ and $SrCrO_3$ calibration series

During my thesis, we first studied the growth and structural properties of $La_{1+\delta}CrO_3$ (LCO) and $Sr_{1+\delta}CrO_3$ (SCO) epitaxial thin films before to grow epitaxial stoichiometric solid solutions $La_{1-x}Sr_xCrO_3$ (LSCO). The results corresponding to LCO calibration are published in Ref. 1. The next sections will present both the growth conditions as well as the structural properties of these LCO and SCO calibration films.

3.2.1. Growth conditions

For composition calibration purpose, about 15 nm thick epitaxial $La_{1+\delta}CrO_3$ ($-0.25 \leq \delta \leq$

0.25) and 60 nm thick epitaxial $Sr_{1+\delta}CrO_3$ ($-0.143 \leq \delta \leq 0.143$) thin films were grown on single-crystalline STO(001) substrates (MaTecK GmbH) by solid-source MBE in an ultra-high vacuum chamber with a base pressure less than 1×10^{-9} Torr (see Chapter II). Sr, La, and Cr were evaporated from effusion cells in co-deposition, with a growth rate of ~0.1 and ~0.67 nm per minute respectively. The fluxes were measured before the growth using a Bayard-Alpert (BA) ionization gauge (after subtraction of the background pressure) and checked using a quartz crystal microbalance (QCM), as shown in Figure 3. 7.

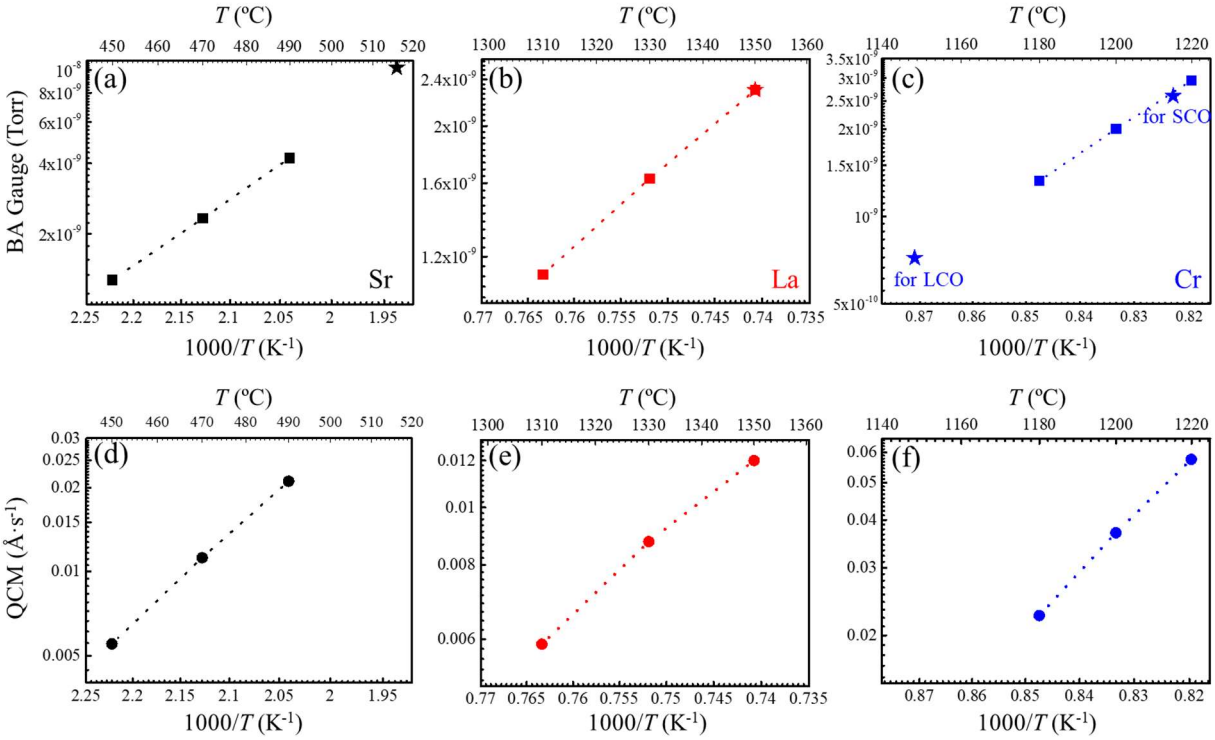

Figure 3. 7 The fluxes of Sr (a, d), La (b, e), and Cr (c, f) measured respectively by (a-c) BA ionization gauge, and (d-f) QCM at three different temperatures. These stars represent the corresponding temperatures used for stoichiometric LCO and SCO calibrations.

The molecular oxygen partial pressure $P(O_2)$ was kept constant at 1×10^{-7} Torr during the growth, and the growth temperature was set to 700 °C. The STO substrates were annealed for 15 minutes before starting the growth. All the calibration films are grown on as-received STO substrates, except for one additional stoichiometric LCO film ($\delta = 0$) grown on a TiO_2-terminated STO substrate. In general, the surfaces of commercial STO substrates consist of a mixture of TiO_2 and SrO that affects the quality of the epitaxial films deposited above [32, 33, 34]. To have a single TiO_2-termination substrate, a method was established by Kawasaki *et al.* [35] based on the hydrofluoric acid (HF) chemical etching which has become a standard treatment for $SrTiO_3$(001) substrates before the growth of thin oxide films. The etching selectivity was

then improved by Koster *et al.* [33] through the formation of basic Sr-hydroxyl groups in water before etching. Post-etching annealing can be done for the formation of well-defined unit-cell high steps and terraces. This latest etching procedure is commonly used to create an atomically-flat TiO_2-terminated $SrTiO_3$(001) substrate surface and was used for some growth in my Ph.D. thesis. The complete procedure consists of:

- 10 min of ultrasonic immersion in deionized water (on the SrO termination, to form basic hydroxide and carbon groups $Sr(OH)_2$ and $SrCO_3$ which increase the selectivity of the chemical attack).
- 20 seconds etching in buffered HF solution (15% NH_4F and 5.2% HF, which selectively attacks the $Sr(OH)_2$ and $SrCO_3$ groups to have only remaining TiO_2 termination).
- rinsing abundantly in deionized water (to avoid residual etchant yielding etching pits) and drying with nitrogen.
- annealing in air at 1000 °C for 1 hour (to remove residual impurities from previous treatments and to flatten the TiO_2-terminated terraces).

Figure 3. 8 shows the surface morphology of the STO substrate after the chemical and thermal treatment. A smooth surface terminated by TiO_2 planes with atomic steps of ~4 Å height corresponding to the size of a unit cell of single-crystalline STO(001) can be observed.

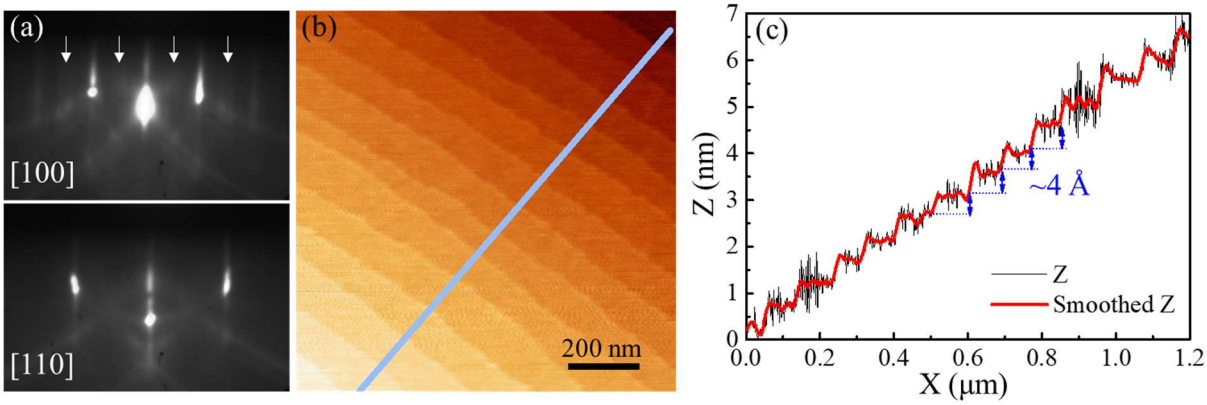

Figure 3. 8 (a) RHEED images along the azimuths [100] and [110] of STO substrate. Good contrast and Kikuchi lines are observed showing a flat surface and of high-crystalline quality. Second-order reconstructions (marked by white arrows) on the azimuth [100] typical of the TiO_2-terminated surface is revealed. (b) AFM topography of the STO substrate after the chemical and heat treatment. (c) Z profile corresponding to the line on (b).

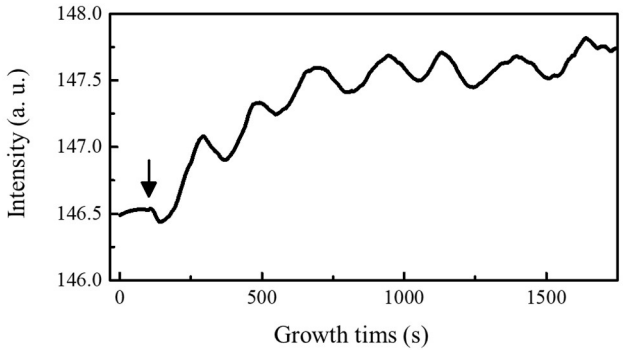

Figure 3. 9 RHEED intensity oscillations from the growth of stoichiometric LCO on prepared TiO_2-terminated STO(001). The vertical arrow indicates the beginning of the growth.

RHEED was used to *in-situ* monitor growth and surface quality. The epitaxial films were grown by layer-by-layer mode as shown in Figure 3. 9 (taking on stoichiometric LCO film as an example).

3.2.2. Structural properties

3.2.2.1. RHEED characterizations

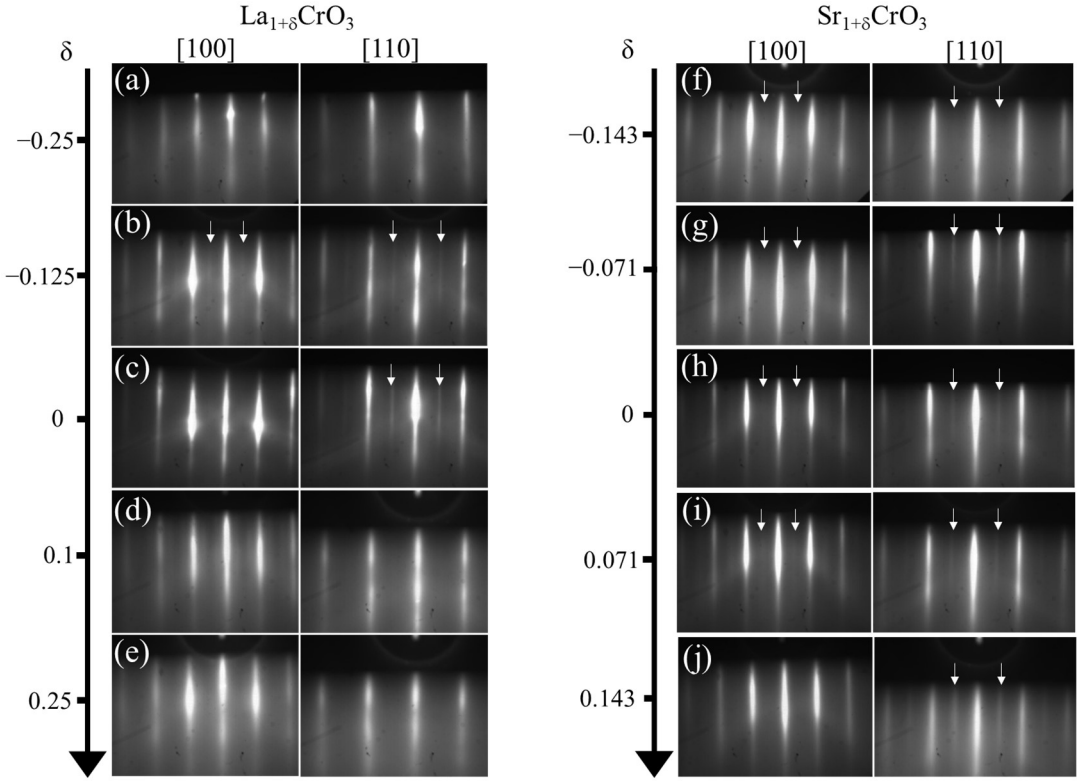

Figure 3. 10 RHEED patterns recorded along the [100] and [110] azimuths (around 200 °C, $P(O_2) = 1\times10^{-9}$ Torr) after growth of the LCO and SCO films. The different corresponding δ values are marked alongside the patterns on the vertical scale. The vertical white arrows inside the patterns indicate second-order reflections demonstrating surface reconstruction in the considered azimuth.

RHEED patterns along both high-symmetry [100] and [110] in-plane crystallographic directions after the growth of the calibration thin films of both $La_{1+\delta}CrO_3$ and $Sr_{1+\delta}CrO_3$ are shown in Figure 3. 10. All the RHEED patterns present well-contrasted streak lines meaning that all the LCO and SCO films are epitaxial with flat surfaces within the δ range (deviation from the cationic stoichiometry; $-0.25 \leq \delta \leq 0.25$ for LCO, and $-0.143 \leq \delta \leq 0.143$ for SCO, estimated after complete characterization).

In more detail, for LCO calibration, when $|\delta| = 0.25$, the streaks are slightly blurred and the background is brighter than that observed for samples with lower $|\delta|$, revealing larger crystalline disorder. For $\delta = -0.125$ (slightly Cr-rich LCO film) and $\delta = 0$ (stoichiometric LCO film), the streaks are sharp along both azimuths, indicating that the surface is well ordered. Additionally, for both these samples, a 2nd order streaky reflection along the [110] direction (indicated by white arrows) is observed. A weak 2nd order streaky reflection also appears along the [100] azimuth for $\delta = -0.125$ whereas only 1st order reflection is observed along this azimuth at $\delta = 0$, which indicates a 2×2 and a 2×1 surface reconstruction for the slightly Cr-rich LCO film ($\delta = -0.125$) and the stoichiometric film ($\delta = 0$), respectively. In contrast, when $\delta = 0.1$ (slightly La-rich LCO film) only 1st order streaks are visible indicating the absence of surface reconstruction.

Similarly, the RHEED patterns of SCO films show the same variation of the streaks as a function of δ. When $|\delta| \leq 0.07$, the streaks are sharp along both azimuths, revealing the well-ordered crystalline surfaces. For $|\delta| = 0.143$, the streaks of [110] azimuth are blurred and the background is brighter than that observed for others. For all SCO films, a 2nd order streaky reflection along the [110] direction is observed. However, a weak 2nd order streaky reflection also appears along the [100] azimuth for $|\delta| \leq 0.07$, which indicates 2×2 surface reconstructions for the stoichiometric film and the slightly nonstoichiometric SCO films.

3.2.2.2. AFM characterizations

AFM working in tapping mode was used to measure the surface morphology of the LCO films, as well as their mean roughness and chemical contrast by phase-shift imaging [34, 36, 37, 38]. AFM images of the film surface are shown in Figure 3. 11. The left panel and the right panel present the topographic images and the phase-lag images, respectively. In agreement with RHEED patterns (Figure 3. 10) and XRR analysis (Figure 3. 14), all the topographic images reveal smooth surfaces with rms roughness less than 0.3 nm. Atomic steps and terraces can be

observed for the Cr-rich LCO films ($\delta < 0$), and are still distinguishable for the stoichiometric film ($\delta = 0$). For the La-rich LCO films ($\delta > 0$), the 'steps and terraces' morphology becomes unclear, and completely disappears at $\delta = 0.25$, even if the surfaces remain globally flat (rms roughness is about 0.25 nm at $\delta = 0.25$). The La-rich surface could present two-dimensional islands of La_2O_3 randomly distributed on the surface, even if the XPS spectra do not show any evidence of the secondary phase in the near-surface region (Figure 3. 22) [3].

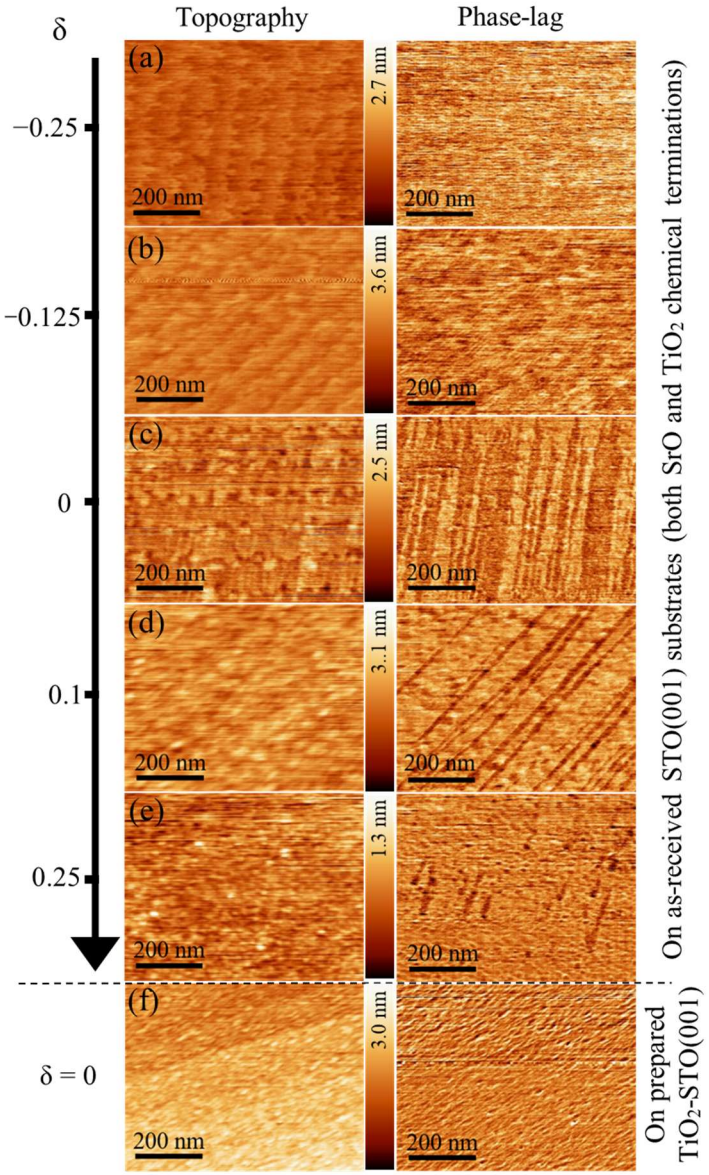

Figure 3. 11 Tapping mode AFM: topographic (left panel) and phase-lag (right panel) images of the LCO epitaxial thin films grown on as-received STO(001) substrate with (a) δ = -0.25, (b) δ = -0.125, (c) δ = 0, (d) δ = 0.1, and (e) δ = 0.25. (f) LCO thin film grown on prepared TiO_2-terminated STO substrate with δ = 0. Taken from Ref. 1.

The phase-lag images reveal chemical contrasts on the flat surfaces, although phase-lag contrast may also appear at step edges due to sharp height differences [34, 36, 37, 38] In Figure 3.

11, strong persistent phase-lag contrast appears at the surface of the stoichiometric film (δ = 0) in which the contrast is roughly half-tone. This contrast indicates a double termination (CrO_2 and LaO) at the surface of the stoichiometric film, due to the replication during the stoichiometric 2D growth of the double termination initially present at the surface of unprepared STO substrate [38]. The half unit-cell steps measured on the topographic image at the phase-lag contrast location is consistent with this interpretation, as detailed in the following. In Figure 3. 12, topographic and phase-lag images of stoichiometric LCO films grown on as-received and treated substrate (Figure 3. 11c and f) are shown with their corresponding profiles for a detailed comparison.

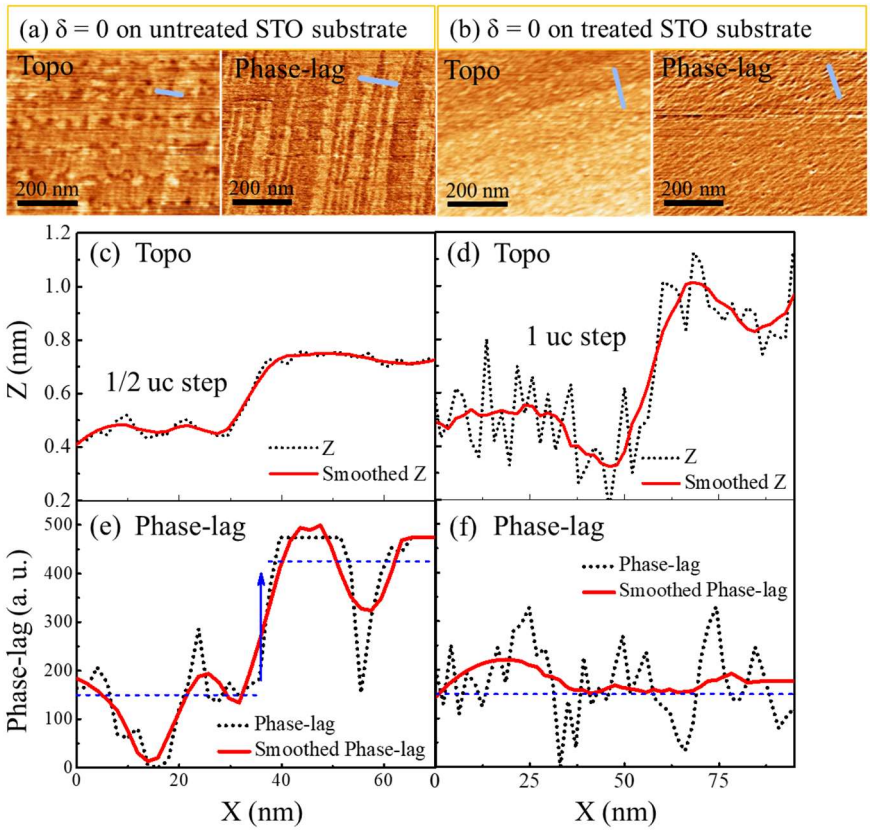

Figure 3. 12 (a-b) AFM topographic and phase-lag images of stoichiometric LCO thin films (δ = 0) on (a) as-received STO substrate and (b) prepared TiO_2-terminated STO substrate. (c-d) Corresponding topographic profiles of LCO on (c) as-received STO substrate and (d) prepared TiO_2-terminated STO substrate. (e-f) Corresponding phase-lag profiles of LCO on (e) as-received STO substrate and (f) prepared TiO_2-terminated STO substrate. The horizontal blue dotted lines in (e-f) are a guide to the eyes and the blue vertical arrow in (e) indicates the phase-lag contrast at half unit-cell step.

Whereas a chemical contrast is revealed on the stoichiometric LCO film grown the as-received substrate (Figure 3. 12a), any contrast is detected in the phase-lag image shown in Figure 3. 12b (right image) indicating a single-termination (most-probably CrO_2) of the LCO film grown on the prepared TiO_2-terminated STO substrate. Topographic height profiles are

shown in Figure 3. 12c and d, indicating that the step height between adjoining terraces is ~2 Å (half unit-cell on as-received STO substrate) and ~4 Å (unit-cell on prepared STO substrate), respectively. The corresponding phase-lag profile (Figure 3. 12e) reveals that a phase-lag shift is measured at half unit-cell high steps on LCO on as-received STO(001), suggesting a lateral chemical separation of each termination (LaO and CrO_2). However, there is no appreciable phase-lag shift measured on LCO on TiO_2-terminated STO(001) (Figure 3. 12f), revealing that each terrace is formed by a single chemical-termination. In this case, this single-termination is most probably CrO_2 if no switching of chemical termination occurs during growth, which seems to be the case since no delay is observed in the RHEED intensity oscillations at the first stage of layer-by-layer growth (Figure 3. 9).

Coherently, this chemical contrast at the film surface decreases and disappears when $|\delta|$ increases, revealing the dominance of one chemical termination at the surface of non-stoichiometric films (LaO when $\delta > 0$ and CrO_2 when $\delta < 0$).

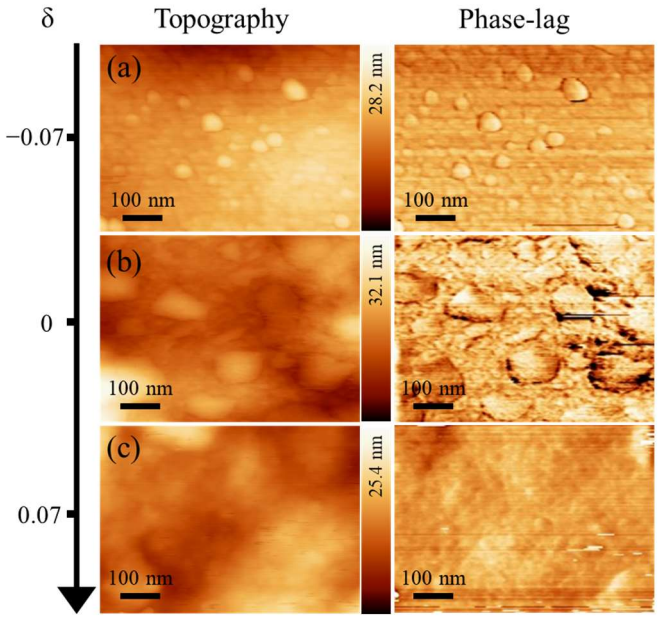

Figure 3. 13 AFM topographic (left panel) and phase-lag (right panel) images of the SCO epitaxial thin films grown on as-received STO(001) substrate with (a) $\delta = -0.07$, (b) $\delta = 0$, and (c) $\delta = 0.07$. Observations done around three weeks after growth.

AFM images of the SCO film surface observed 2-3 weeks after growth are shown in Figure 3. 13. Due to the instability of epitaxial SCO films, XRR/XRD characterizations have been performed preferentially quickly after growth. Only the AFM measurement of $|\delta| < 0.07$ SCO calibration have been performed, showing relatively high rms roughness ($rms_{\delta=-0.07}$ = 6.2 nm, $rms_{\delta=0}$ = 7.1 nm, and $rms_{\delta=+0.07}$ = 6.7 nm). The high surface roughness of SCO films is certainly

due to the high reactivity of SrO-rich surfaces with H_2O and CO_2 of ambient atmosphere forming stable $SrCO_3$ and Sr-hydroxide complex $Sr(OH)_2$.

3.2.2.3. XRR characterizations

XRR was used to measure the thickness, surface and interface roughness, and density of all the films. The XRR curves plotted in Figure 3. 14 include both the experimental raw data (black curves) and the fit (red curves) from a simple single-layer model. The measured experimental data are relatively well described by the fitted curves (especially for LCO films), including the interference periodic Pendellosung fringes, the overall slope, and the decay at the critical angle (below which is the total reflection), yielding values for the thickness (~15 nm for LCO films and ~50 nm for SCO films), and the root-mean-square (rms) surface/interface roughnesses, as well as densities. The extracted values from the fits are summarized in Table 3. 2. The fit may be improved for SCO films by including a more complex multi-layer model taking into account some heterogeneous composition distribution across the film thickness.

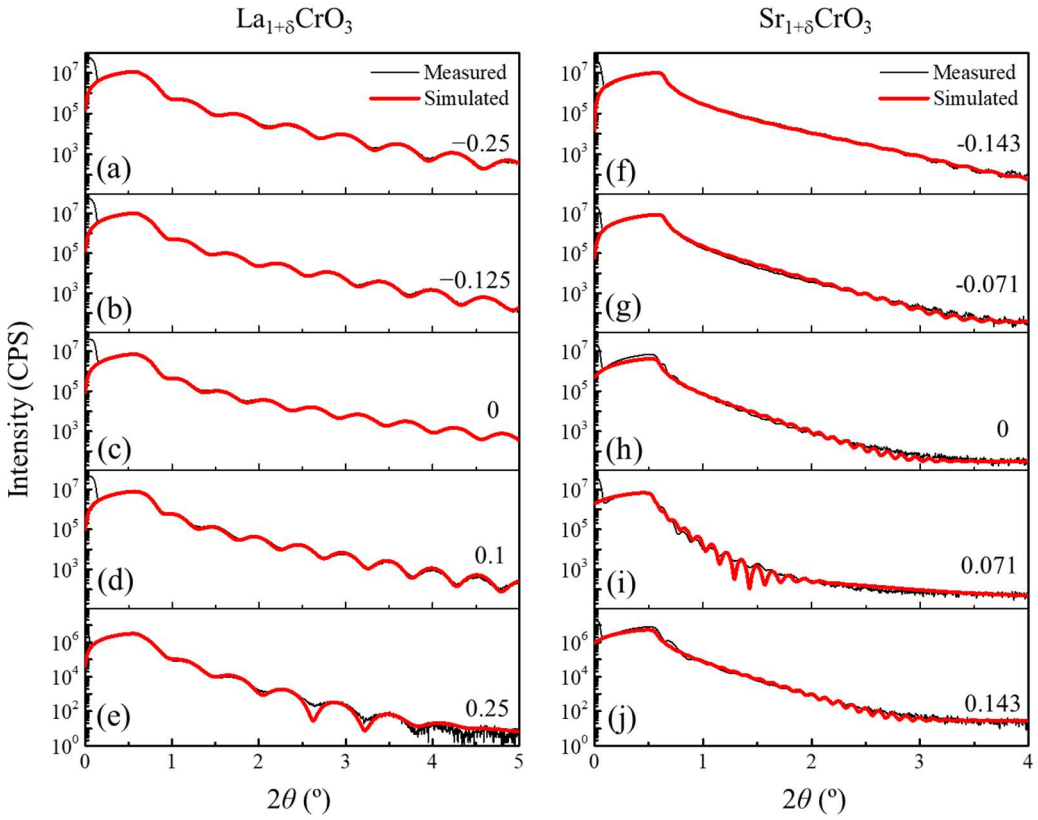

Figure 3. 14 XRR curves for all LCO and SCO calibration films, including the raw data (black lines) and the fitting curves (red lines).

Table 3. 2 Thickness, rms-roughness, and density for all LCO and SCO calibration films extracted from XRR fits.

Film	$La_{1+\delta}CrO_3$					$Sr_{1+\delta}CrO_3$				
δ	-0.25	-0.125	0	0.1	0.25	-0.143	-0.071	0	0.071	0.143
t (nm)	13.8	14.6	15.8	16.9	14.2	38.0	53.0	67.6	54.9	69.1
rms surface (nm)	0.46	0.46	0.30	0.48	0.99	0.73	0.97	1.2	2.05	1.17
rms interface (nm)	0.15	0.15	0.15	0.15	0.15	0.15	0.15	0.15	0.15	0.15
Density ($g \cdot cm^{-3}$)	8.16	8.39	8.46	8.68	8.27	5.53	5.56	5.60	6.23	6.18

3.2.2.4. XRD characterizations

(a) LCO films

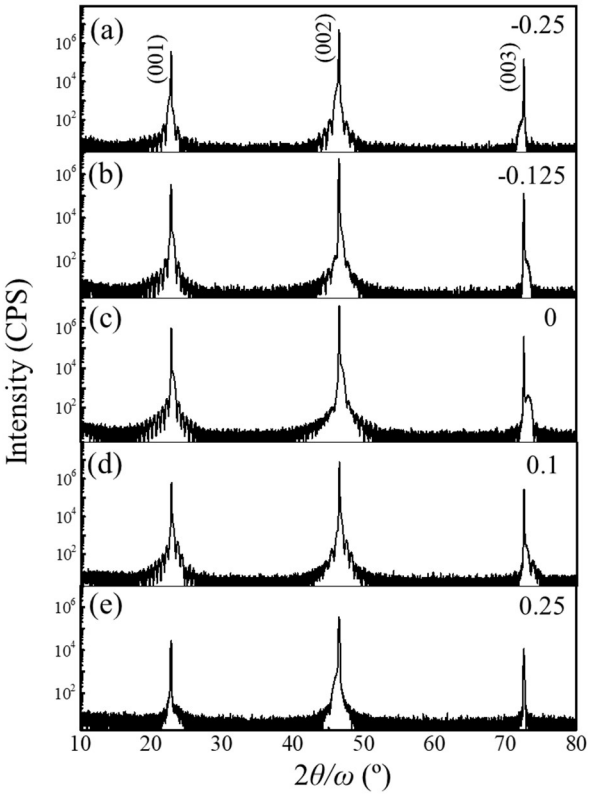

Figure 3. 15 XRD characterizations. Wide $2\theta/\omega$ scans for all LCO films from 10° to 80°.

The structural properties of all LCO films are further investigated by XRD. Wide $2\theta/\omega$ scans (10-80°) reveal only diffraction peaks corresponding to the {00*l*} reflections of the LCO films and STO(001) substrates (shown in Figure 3. 15), indicating that no other orientation or phase than LCO (00*l*) are present in the epitaxial films. Cationic intermixing at the interface with STO and secondary phase formation, which are dependent on the growth conditions and

STO substrate quality, are not observed here by XRD (and XPS, see section 3.2.2.6 below) although a few La-rich precipitates could be present at the nanometer scale close to the interface [3]. The presence of Pendellosung fringes around the diffraction peaks of the films attests to their high-crystalline quality and abrupt interfaces.

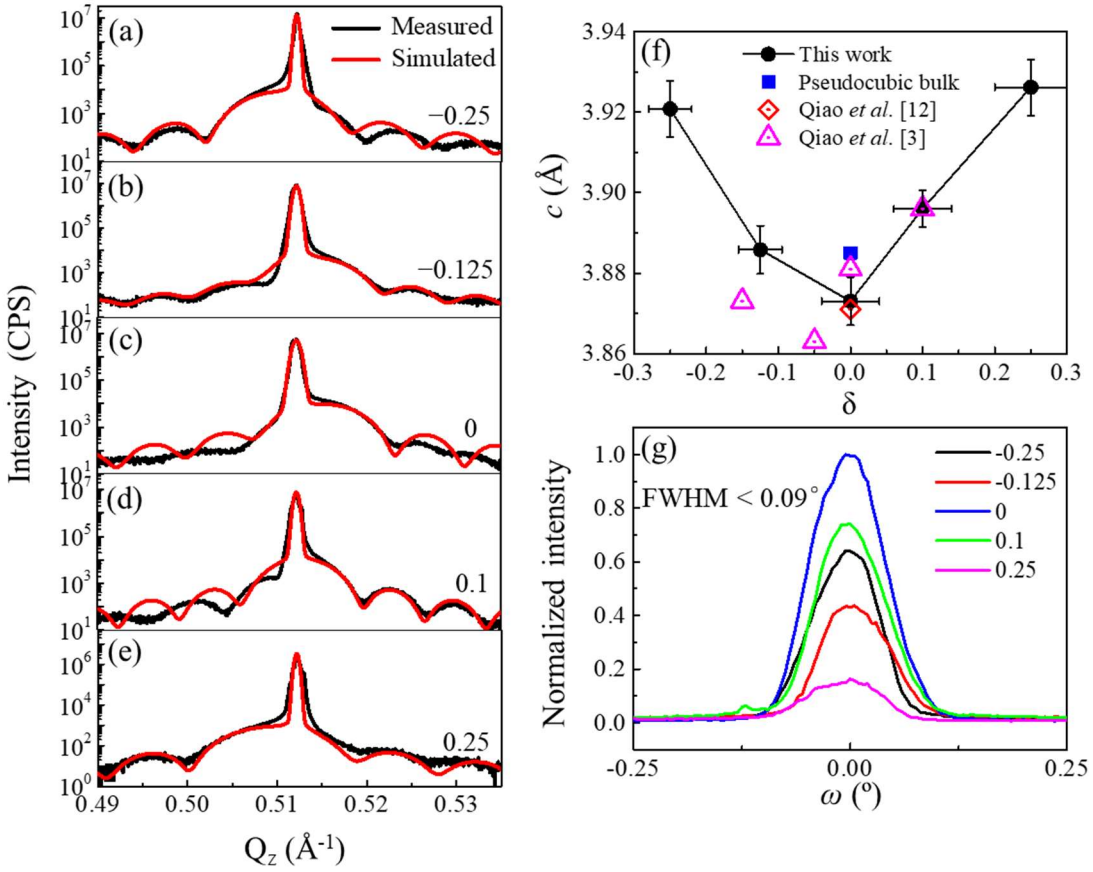

Figure 3. 16 XRD characterizations. (a-e) $2\theta/\omega$ scans near the (002) reflections of LCO thin films and STO substrates for (a) δ = -0.25, (b) δ = -0.125, (c) δ = 0, (d) δ = 0.1, and (e) δ = 0.25. (f) Out-of-plane lattice cell parameter as a function of the δ. (g) ω-scans around the LCO (002) reflection for all the films, normalized to the stoichiometric film (δ = 0). Taken from Ref. 1.

Figure 3. 16a-e shows the XRD $2\theta/\omega$ scans around the (002) reflections of the LCO films and STO substrates plotted in reciprocal space units. The LCO (002) reflection is very close to that of the STO substrate and appears as a shoulder of the substrate peak. Qualitatively, the position of the film reflection decreases in Q_z while deviating from the stoichiometry, which means that the out-of-plane cell parameter of the LCO film (c_{LCO}) increases with cationic-stoichiometry deviation. Both Cr-rich and La-rich films exhibit larger c_{LCO} than that of the stoichiometric LCO film, in agreement with other perovskite oxide films such as $SrTiO_3$ [39, 40, 41]. This standard trend is also observed by Qiao *et al.* (Chambers group) [3], but with a c_{LCO}

minimum shifted at slightly Cr-rich films (δ = -0.05) and not at the stoichiometry (δ = 0). This small composition shift (5%) with this work could be due to (*i*) the uncertainty in the determination of composition and film lattice parameter, and (*ii*) to the ratio and distribution of point cationic defects (vacancy, anti-site) in the films.

Quantitatively, c_{LCO} has been extracted here from fits of the XRD spectra (Figure 3. 16a-e) and is shown as a function of δ in Figure 3. 16f, together with the bulk value and the results of those found in the literature on fully-strained epitaxial LCO films for comparison [2, 3, 12]. The values of this work range from 3.873 to 3.926 Å. The minimal value, recorded for the stoichiometric film, is c_{LCO} = 3.873 Å which is in good agreement with the most recent results of the reference [2], although different values (from 3.871 to 3.881 Å) are reported in different articles from the same group (Chambers group) on fully-strained stoichiometric LCO epitaxial film on STO substrate. Around the stoichiometry, lattice parameters are lower than the LCO pseudocubic bulk value (3.885 Å, blue square), indicating reduced c_{LCO} (-0.31%) owing to the in-plane tensile stress exerted by STO substrate (relative in-plane tensile strain ε_{xx} = 0.51%) [42]. The out-of-plane lattice cell parameter increases up to almost 3.93 Å for clearly non-stoichiometric films: 3.92 Å for δ = -0.25 and 3.926 Å for δ = 0.25. In such cases, these high c_{LCO} values, superior to the substrate lattice parameter, are partly due to the in-plane compressive strain of the epitaxial films, in addition to the effect of cationic-stoichiometry deviation it-self. For δ = 0.1 (slightly La-rich film), c_{LCO} = 3.896 Å, in very good agreement with Qiao's results [3]. For δ = -0.125 (slightly Cr-rich), c_{LCO} = 3.886 Å, which is slightly larger than the Qiao's reported value (~3.873 Å for δ = -0.15).

The ω-scans measured for all the films around the LCO (002) reflection are shown in Figure 3. 16g. The mosaicity of the films (full width at half maximum, FWHM, of these curves) is below 0.09°, comparable to that of the single-crystalline STO substrates, confirming the high-quality of the films with a low level of defects.

The in-plane lattice parameters of the LCO films (a_{LCO}) and the associated anisotropic strain are measured by XRD reciprocal space mapping around the asymmetrical reflection. Figure 3. 17 shows the RSM acquired around the asymmetric (103) reflection of LCO films and the STO substrate. The shoulder of the nodes corresponding to the LCO thin films is shifted along Q_{zz} depending on chemical composition consistently with the $2\theta/\omega$ scans, confirming the variation of c_{LCO} shown in Figure 3. 16. By contrast, the LCO(103) nodes are all aligned vertically with the substrate nodes, indicating that the a_{LCO} is equal to the STO lattice constant (3.905 Å). All LCO films are thus fully coherently strained to the substrates, confirming that

the critical thickness (t_c) from which an epitaxial strain relaxation occurs is well above the thickness of our thin films. This is consistent both with the relatively low lattice mismatch of LCO/STO(001) heteroepitaxy (0.51%) [42] and with previous experimental results (t_c > 50 nm) [12].

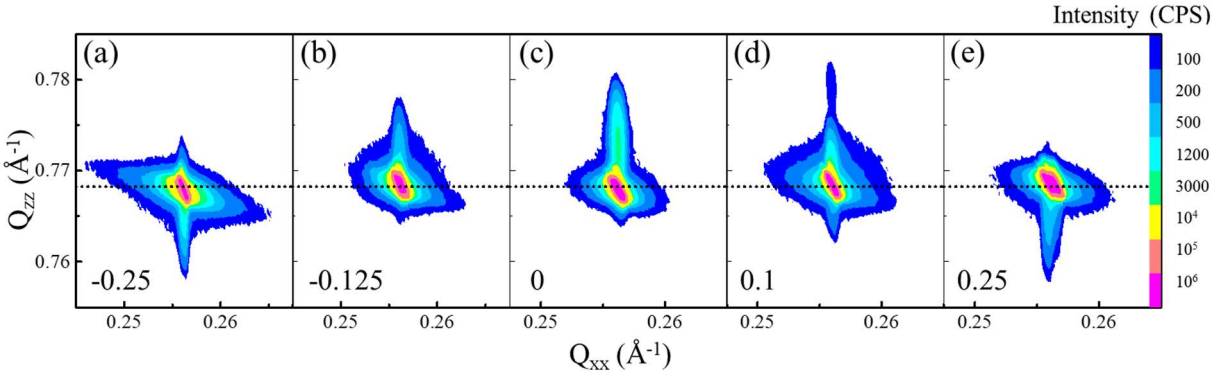

Figure 3. 17 RSM around the asymmetric (103) reflection of the LCO films and STO substrates for (a) δ = -0.25, (b) δ = -0.125, (c) δ = 0, (d) δ = 0.1, and (e) δ = 0.25. The dotted line indicates the Q_{zz} position of the STO substrate related to its out-of-plane lattice parameter. Taken from Ref. 1.

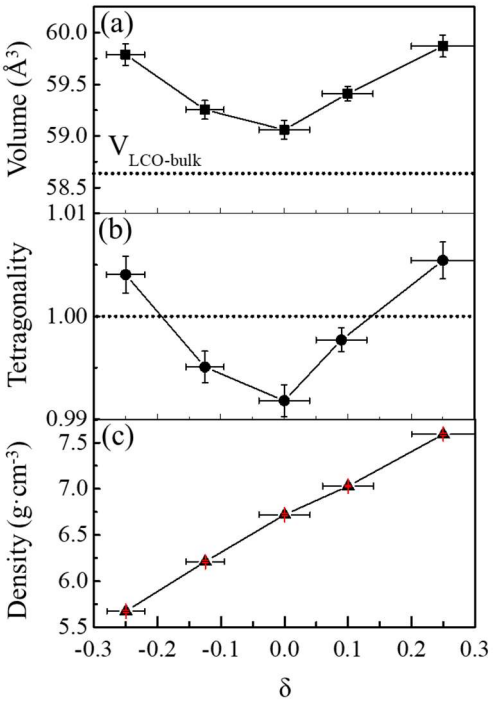

Figure 3. 18 Dependence on δ of (a) the lattice unit-cell volume, (b) the tetragonality *c*/*a*, and (c) the density of LCO thin films. Taken from Ref. 1.

From the measured c_{LCO} and a_{LCO}, the unit-cell volume can be extracted and plotted as a function of δ, as shown in Figure 3. 18a. The unit-cell volume is found to be in-between 59 and 60 Å^3 within the composition range. A trend similar to the evolution of c_{LCO} with δ is observed

since a_{LCO} remains constant with a minimum at stoichiometry. Cationic-stoichiometry deviation might generate point defects such as cationic vacancies that induce expansion of the unit-cell volume from electrostatic repulsions near these charged ionic defects. Around the stoichiometry, for δ = -0.125, 0, and 0.1, the LCO films exhibit values of *a* that exceed *c*, induced by the heteroepitaxial in-plane tensile stress. However, for larger stoichiometric deviation, when δ = ±0.25, it turns to in-plane compressive stress since *c* is larger than *a*, which means that the corresponding bulk pseudocubic lattice parameter in such cases is larger than that of the STO substrate (3.905 Å). The tetragonality (*c*/*a*) is found to vary between 0.99 and 1.01 and is plotted as a function of δ in Figure 3. 18b. For comparison, the tetragonality of the bulk ferroelectric tetragonal $BaTiO_3$ is 1.011. The density of all LCO films was extracted from unit-cell volume and chemical composition (by taking into account the cationic vacancy) and is plotted as a function of δ in Figure 3. 18c. Film density has an approximate linear increasing trend with δ due to the progressive introduction of La with the larger atomic mass in the crystal lattice.

(b) SCO films

After analyzing the structural properties and calibration of LCO films, the SCO calibration needs to be investigated as well to perform composition controlled LSCO solid solutions. It should be noted that contrasting with LCO, the structure of epitaxial SCO thin films is not stable under air. However, according to the RHEED patterns (Figure 3. 10) and the following XRD and RBS results which were measured just after growth to limit the effect of SCO reaction with air, the stoichiometry can also be well confirmed.

Wide $2\theta/\omega$ scans (10-80°) are presented in Figure 3. 19. They reveal that the main diffraction pics correspond to the {00*l*} reflections of the SCO films and STO(001) substrates, meaning that the SCO film is (001) oriented. However, minority lower intensity pics appear in other positions than those of the perovskite meaning that a small secondary phase exists in the films. These pics could correspond to demixed phases composed of SrO and Cr_2O_3. Figure 3. 20a-d show the XRD $2\theta/\omega$ scans around the (002) reflections of the SCO films and STO substrates plotted in reciprocal space units. The position of the film reflection decreases in Q_z while deviating from the stoichiometry, which means that the out-of-plane cell parameter of the SCO film (c_{SCO}) increases also with δ as expected. Both Cr-rich and Sr-rich films exhibit larger c_{SCO} than that of the stoichiometric SCO film. The SCO(002) reflection of the stoichiometric film (δ = 0) is very close to that of the STO substrate and appears as a left shoulder of the

substrate peak. Similar to the LCO films, the presence of Pendellosung fringes around the diffraction peak of the films attests to their high-crystalline quality and abrupt interfaces.

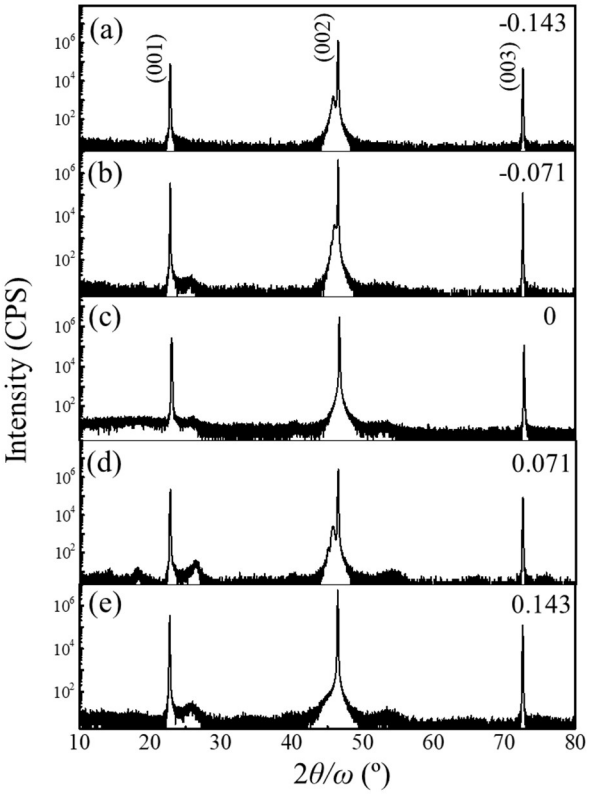

Figure 3. 19 XRD characterizations. Wide $2\theta/\omega$ scans for all SCO films from 10º to 80º.

The out-of-plane lattice parameter c_{SCO} is extracted from fits of the XRD spectra (Figure 3. 20a-e) and is plotted as a function of δ in Figure 3. 20f, together with the values found in the literature for comparison [18]. The c_{SCO} values of this work range from 3.917 to 4.01 Å. The stoichiometric value is c_{SCO} = 3.917 Å which is in good agreement with the literature (3.92 Å) although in this case, the SCO epitaxial films were grown on other oxide substrates (LAO and LSAT) of lower lattice parameters than STO [18]. However, the lattice constant of bulk cubic perovskite SCO is 3.819 Å (blue square in Figure 3. 20f) which is much lower than the stoichiometric film value and the lattice parameter of LSAT substrate for instance. This large c_{SCO} value in the stoichiometric films cannot be explained by the strain effect and is explained by the formation of the rhombohedral phase from oxygen deficiency in the crystal lattice [18]. From Zhang *et al*., perovskite pseudocubic phase should be obtained after annealing in air at 250 °C for 2 hours, and they observe after annealing a decrease of the c_{SCO} around the bulk cubic value, from 3.92 to 3.805 Å on LSAT, and from 3.92 to 3.84 Å on LAO substrate. These residual differences concerning bulk value can now be explained by the epitaxial strain effect with a positive Poisson ratio. However, trying to follow the Zhang's recipe of annealing to

obtain oxidized SCO films with the perovskite pseudocubic phase, our films have become amorphous according to the XRD result (no pic has been found except that of STO substrate).

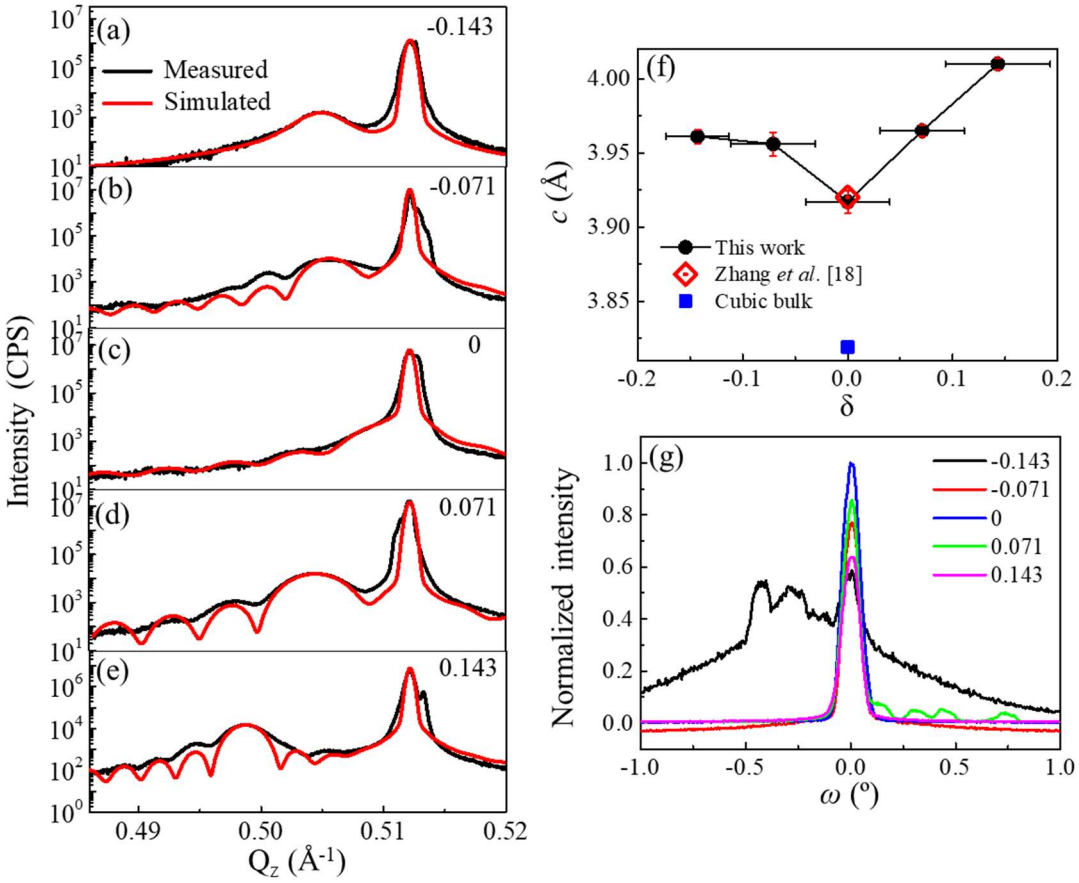

Figure 3. 20 XRD characterizations. (a-d) $2\theta/\omega$ scans near the (002) Bragg reflections of SCO thin films and STO substrates for (a) δ = -0.143, (b) δ = -0.071, (c) δ = 0, (d) δ = 0.071, and (e) δ = 0.143. (f) Out-of-plane lattice cell parameter of SCO films as a function of the δ. (g) ω-scans around the SCO (002) reflection for all the films, normalized to the stoichiometric film (δ = 0).

The ω-scans measured for the SCO films around the (002) reflection are shown in Figure 3. 20g. The FWHM of these curves is below 0.1° (except the one deposed on low-quality-substrate), confirming the high-crystalline quality of the films with a low level of defects.

3.2.2.5. RBS characterizations

The film composition is further confirmed by RBS measurements (Figure 3. 21). RBS using a 2 MeV He^+ beam incident at 6° with a 172° scattering angle was used to check the cationic stoichiometry of both LCO and SCO calibration films. The two stoichiometric films' composition (δ = 0) are examined, in which both of the La/Cr and Sr/Cr atom ratio is 1 within

the instrumental uncertainty, showing a perfect agreement with the XRD results (Figure 3. 16 and Figure 3. 20).

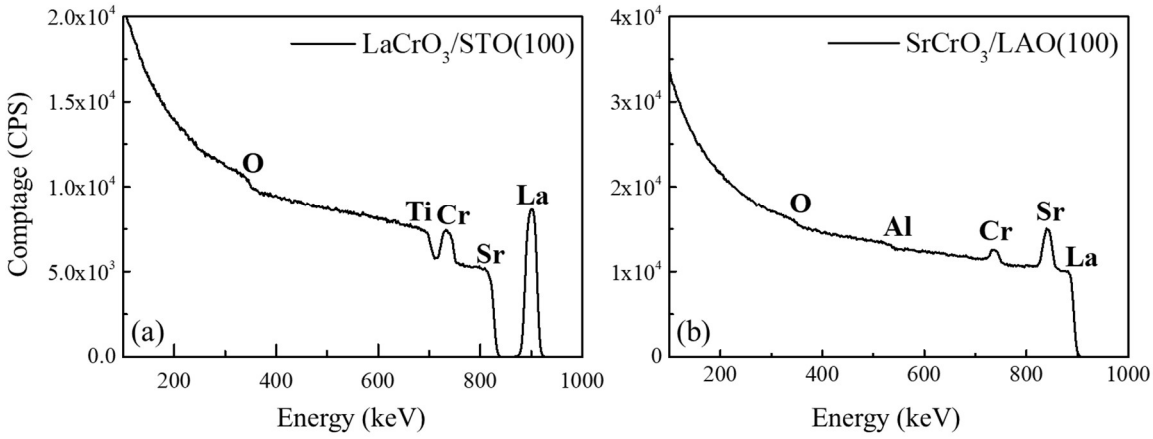

Figure 3. 21 RBS spectra of the stoichiometric (a) LCO and (b) SCO films.

3.2.2.6. XPS characterizations

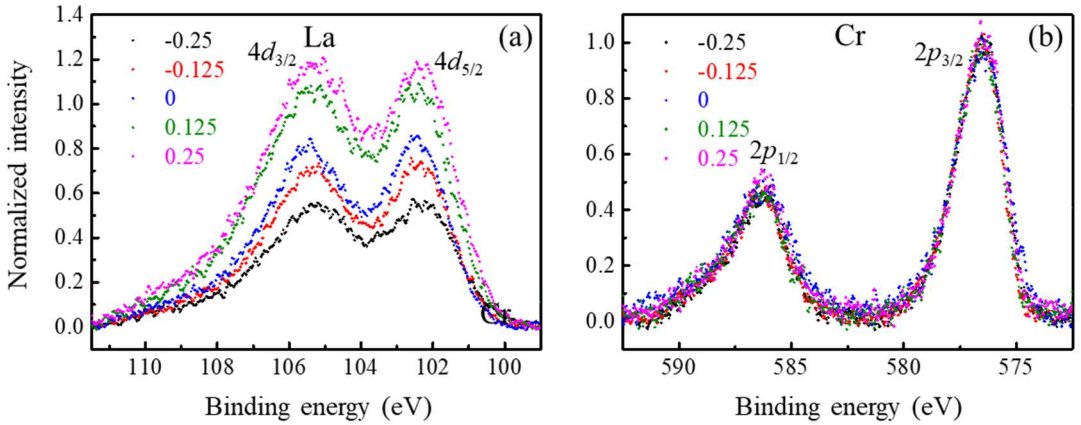

Figure 3. 22 XPS spectra of (a) La 4*d* and (b) Cr 2*p* core levels for all LCO films with δ ranging from -0.25 to 0.25.

XPS core-level spectra were acquired using monochromatic Al Kα radiation ($h\nu$ = 1486.6 eV) at normal emission to probe the near-surface region (≤ 5 nm) only for LCO films. To directly compare binding energies, the Cr $2p_{3/2}$ core-level peaks shown in Figure 3. 22b are all shifted to 576 eV and normalized to 1. For each specimen, the same shift is applied to La 4*d* spectra (Figure 3. 22a). Then, the intensity of the La 4*d* core-level spectra is normalized to the stoichiometric LCO film (δ = 0). The La 4*d* and Cr 2*p* core-level spectra and binding energies are characteristics of La^{3+} and Cr^{3+} for all cationic ratios indicating that the structure of all films remains perovskite-type without extra phase such as the oxidized $LaCrO_4$ phase [12, 27].

3.2.2.7. Conclusion

All these characterization techniques, and especially XRD and RBS, have allowed to attest to the stoichiometric samples and to determine the corresponding growth conditions. The MBE flux can then be tuned via effusion cell temperature, within the measurement uncertainty, to grow stoichiometric epitaxial films of $La_{1-x}Sr_xCrO_3$ solid solutions and study the impact of the substitution ratio x.

3.3. $La_{1-x}Sr_xCrO_3$ solid solutions: impact of substitution ratio x

According to the previous calibration series, the high-crystalline quality *p*-type epitaxial LSCO thin films are prepared via the same method as the calibration films.

3.3.1. Growth conditions

About 30 nm thick epitaxial $La_{1-x}Sr_xCrO_3$ films (x = 0.1, 0.2, 0.25, 0.3, and 0.4) were grown on prepared TiO_2-terminated STO(001) substrates by MBE with a growth rate of ~0.15 nm per minute. The preparation process for such a substrate surface is already described in section 3.2.1. The $P(O_2)$ was kept constant at 1×10^{-7} Torr during the growth, and the growth temperature was set to 700 °C. The STO substrates were annealed for 15 minutes before starting the growth. After deposition, the substrate temperature was lowered to 200 °C at a rate of 50 °C per minute while the background O_2 was pumping out. All LSCO films were subjected to an additional anneal in the air at 300 °C for 2 hours to ensure complete oxidation.

3.3.2. Structural properties

3.3.2.1. RHEED characterizations

RHEED patterns along both high-symmetry [100] and [110] in-plane crystallographic directions after the growth of the LSCO films series are shown in Figure 3. 23. The epitaxial quality of all films is seen. The streaks are sharp along both azimuths with clear contrast. No rings characteristic of polycrystalline quality nor secondary phases are present. Additionally, a 2^{nd} order streaky reflection is observed along the [110] direction for all the samples although

weak for some (indicated by white arrows), which indicates a 2×1 surface reconstruction, in agreement with the observations made on the LCO and SCO stoichiometric films (see Figure 3. 10).

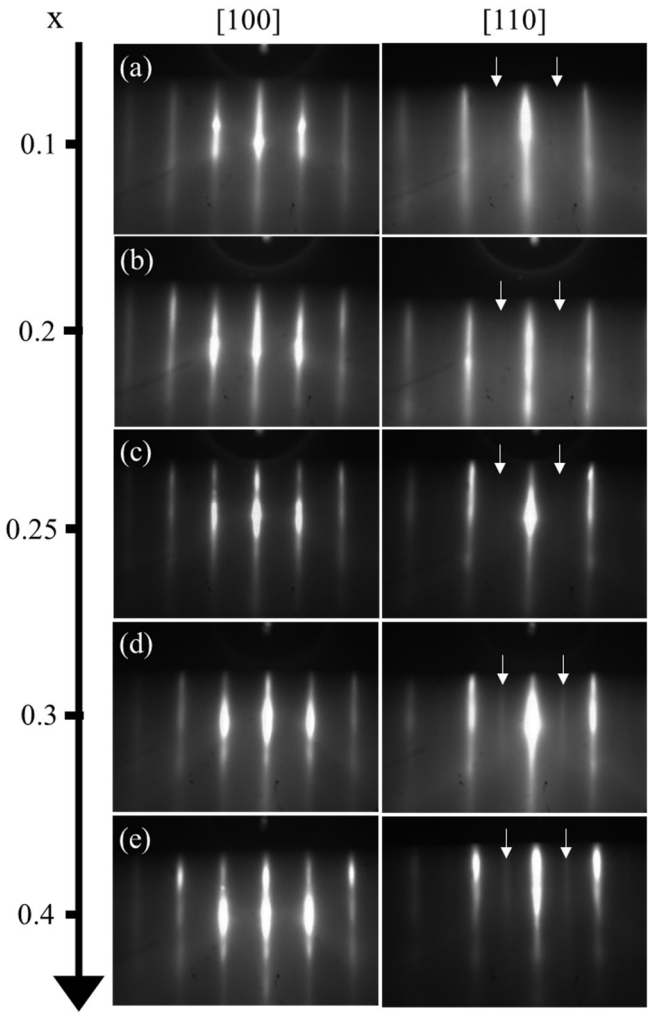

Figure 3. 23 RHEED patterns recorded along the [100] and [110] azimuths (around 200 °C, $P(O_2) = 1\times10^{-9}$ Torr) after growth of the LSCO films with (a) x = 0.1, (b) x = 0.2, (c) x = 0.3, (d) x = 0.4, and (e) x = 0.5. The vertical white arrows indicate second order reflections demonstrating surface reconstruction in the considered azimuth.

3.3.2.2. AFM characterizations

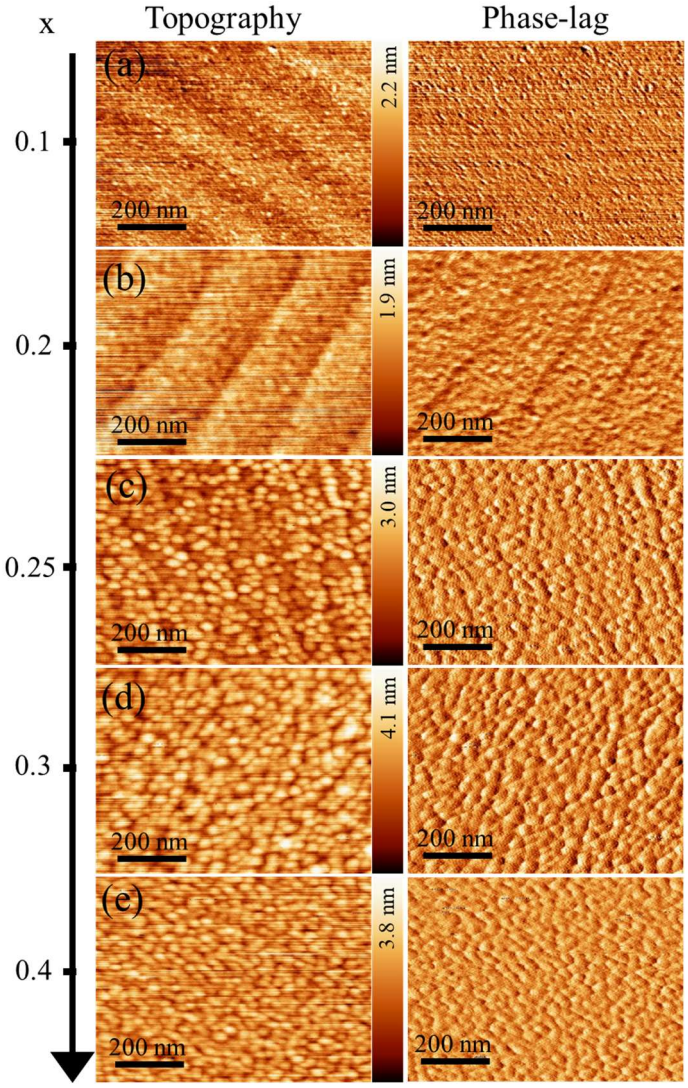

Figure 3. 24 tapping mode AFM: topographic (left panel) and phase-lag (right panel) images of the LSCO films grown on as-received STO(001) substrate with (a) x = 0.1, (b) x = 0.2, (c) x = 0.3, (d) x = 0.4, and (e) x = 0.5. All films were grown on prepared TiO_2-terminated STO(001) substrate.

AFM images of the LSCO films' surface are shown in Figure 3. 24. The left panel and the right panel present the topographic images and the phase-lag images respectively. The film surface roughness seems to increase with x with the presence of 2D islands on the terraces. However, all the rms roughnesses are below 0.6 nm. Moreover, because of the prepared TiO_2-terminated STO substrates, atomic steps and terraces can be observed for the films for $x \leq 0.25$ and still distinguishable for $x > 0.25$ (left images). The phase-lag contrast at adjacent terraces (right panel in Figure 3. 24b, c, and d) is probably due to the step height between adjacent terraces or 2D islands at the surface of the LSCO films. Any other contrast is detected in the right phase-lag images indicating a most probable single-termination (CrO_2) of these LSCO

films grown on TiO_2-terminated STO substrate. As an example, the topographic profile of LSCO with x = 0.25 is shown in Figure 3. 25. The height of the 2D islands is less than two-unit cells, confirming a relatively low surface roughness and a layer-by-layer growth.

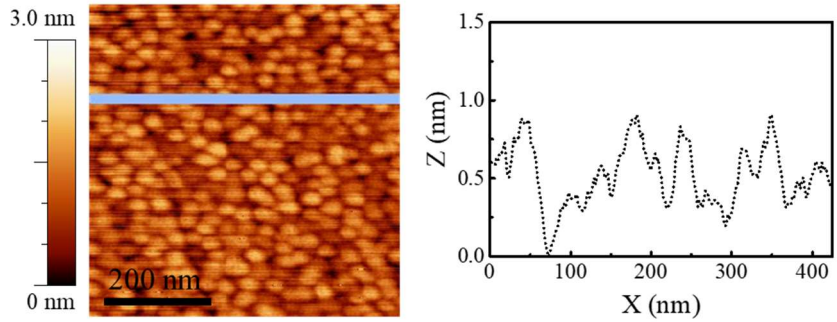

Figure 3. 25 AFM topographic images of LSCO film on the STO substrate, and the corresponding topographic profile. The local rms roughness is 0.4 nm.

3.3.2.3. XRR characterizations

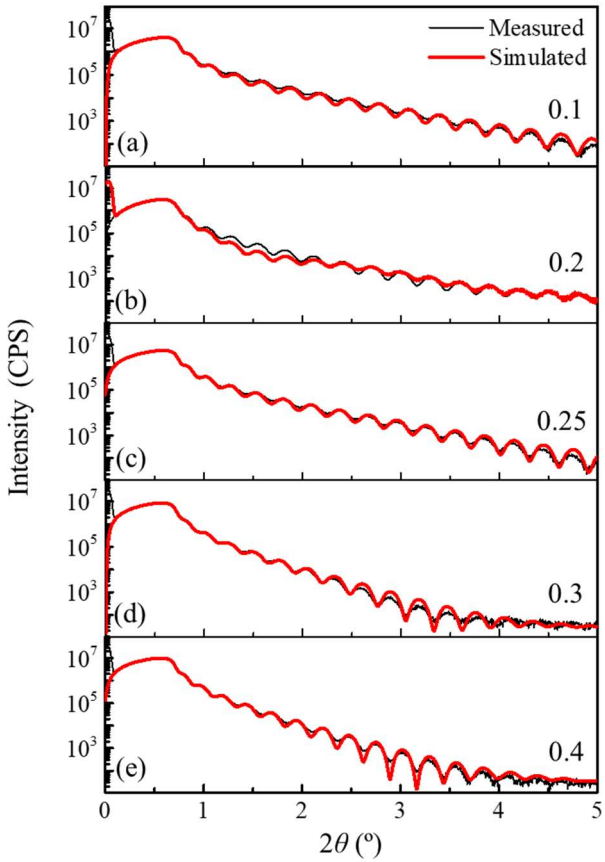

Figure 3. 26 XRR curves for LSCO films, including the raw data (black curve) and the fit (red curve).

XRR was used to measure the thickness of LSCO films. The curves are plotted in Figure

3. 14. The measured experimental data are well described by the fits, including the interference periodic fringes, decay at the critical angle, and the overall slope, yielding values for the thickness (~30 nm), the film density, and the rms surface/interface roughnesses (shown in Table 3. 3). It can be seen that the rms surface roughness increases with x, in agreement with the previous AFM observations above (see Figure 3. 27). This is also consistent with the XRR measurements made on stoichiometric LCO and SCO films of the calibration series for which SCO films presented higher roughness than LCO films (see Table 3. 2).

Table 3. 3 Thickness, rms-roughness, and density of LSCO films extracted from XRR fits.

x	0.1	0.2	0.25	0.3	0.4
t (nm)	28.1	29.0	28.1	30.1	31.6
rms surface (nm)	0.39	0.46	0.54	0.88	0.92
rms interface (nm)	0.15	0.15	0.15	0.15	0.15
Density ($g \cdot cm^{-3}$)	7.45	6.42	6.35	6.30	6.28

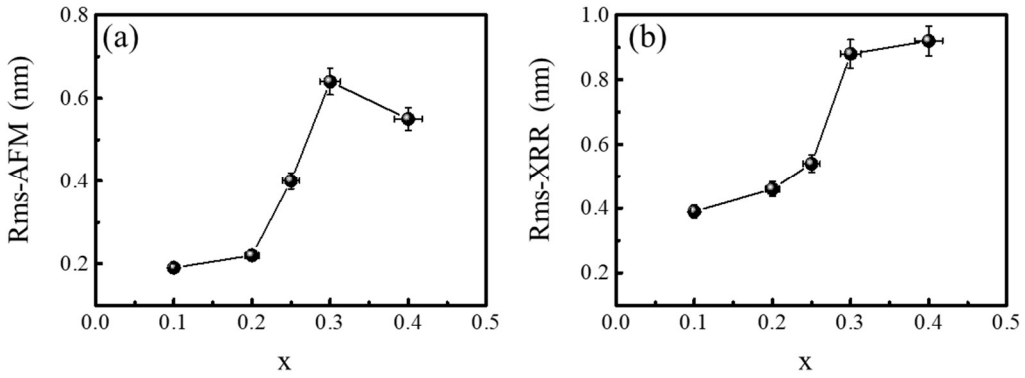

Figure 3. 27 rms-roughness for all LSCO films from (a) AFM measurement and (b) XRR fit.

3.3.2.4. XRD characterizations

The structural properties of LSCO films are investigated by XRD. Wide $2\theta/\omega$ scans (10-80°), shown in Figure 3. 28a-e, reveal only diffraction peaks corresponding to the {00*l*} reflections of the LSCO films and STO substrate, indicating that no other orientation neither phase than LSCO (00*l*) are present in the epitaxial films.

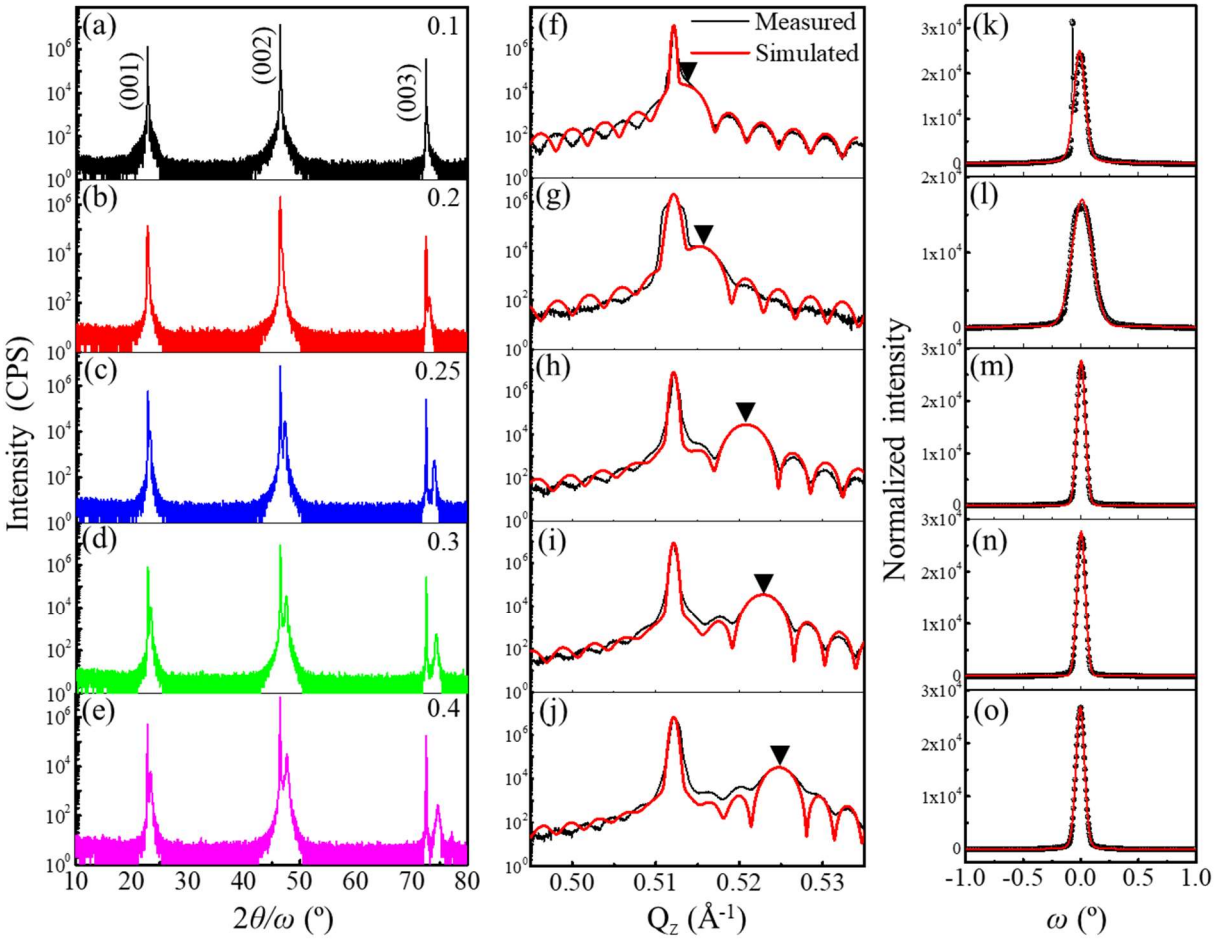

Figure 3. 28 XRD characterizations. (a-e) Wide $2\theta/\omega$ scans for all LSCO films from 10° to 80° for (a) x = 0.1, (b) x = 0.2, (c) x = 0.25, (d) x = 0.3, and (e) x = 0.4. (f-j) Corresponding $2\theta/\omega$ scans near the (002) reflections of LSCO films and STO substrates with fits. (k-o) ω-scans around the LSCO (002) reflection for all the films.

Figure 3. 28f-j shows the XRD $2\theta/\omega$ scans around the (002) reflections of LSCO films and their STO substrate with the fit (red curves). The presence of Pendellosung fringes around the diffraction peak of the films attests to their high-crystalline quality and abrupt interfaces. The out-of-plane lattice parameter of the LSCO films (c_{LSCO}, marked by black inverted triangles in reciprocal space unit) globally decreases with increasing x. The variations of c_{LSCO} and unit-cell volume as a function of x are shown in Figure 3. 29. This tendency is expected from the bulk pseudo-cubic lattice parameters of oxidized LCO (x = 0, c_{LCO} = 3.885 Å) and SCO (x = 1, c_{SCO} = 3.819 Å). This tendency is roughly in agreement with the literature, even if some discrepancy can be observed. The differences between our results and the literature can be explained by epitaxial strain (substrate used), partial elastic relaxation (film thickness). Due to the in-plane tensile strain of these LSCO epitaxial films grown on STO substrates (a_{STO} = 3.905 Å), the c_{LSCO} is lowered than the corresponding bulk values. The films grown on STO substrate

from the other group (blue circles) are not all fully strained, and sometimes even are fully relaxed, which is the case of the point at x = 0.25 where c_{LSCO} is higher by elastic relaxation.

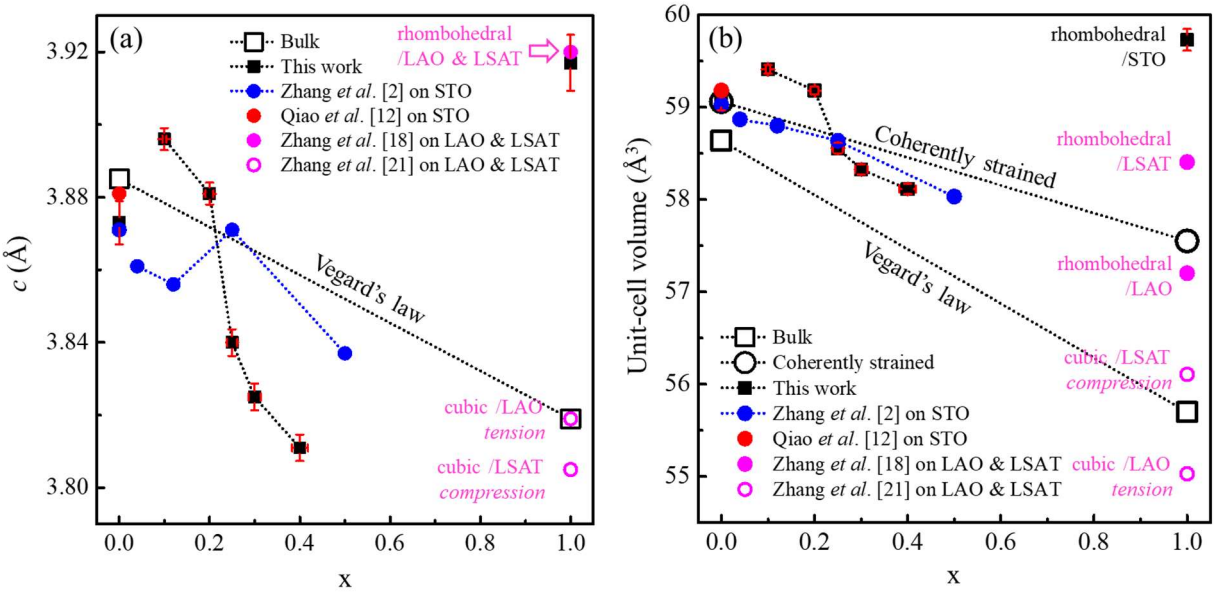

Figure 3. 29 (a) Out-of-plane lattice cell parameter and (b) unit-cell volume as a function of Sr concentration x.

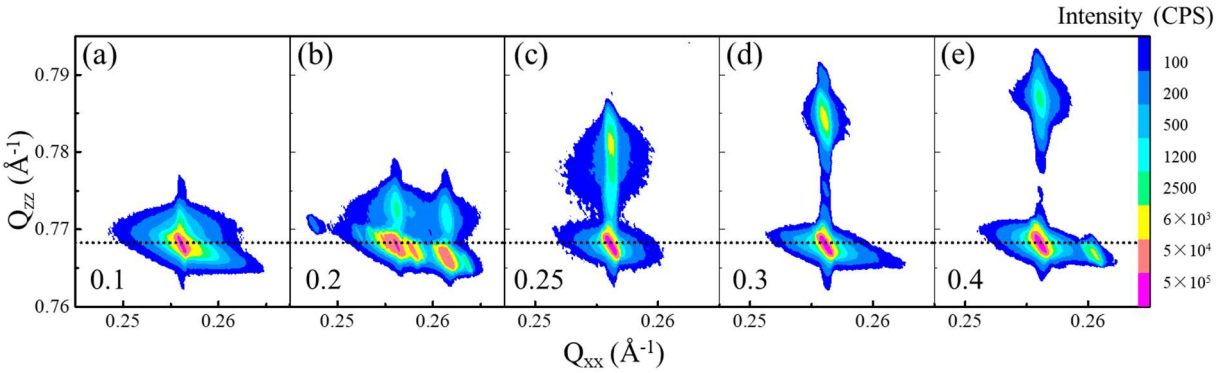

Figure 3. 30 RSM around the asymmetric (103) reflection of the LSCO thin films and STO substrate, for (a) x = 0.1, (b) x = 0.2, (c) x = 0.25, (d) x = 0.3, and (e) x = 0.4. The dotted line indicates the Q_{zz} position of the STO substrate related to its out-of-plane lattice parameter.

The a_{LSCO} and the associated anisotropic strain is measured by RSM around the asymmetrical reflection. Figure 3. 30 shows the RSM acquired around the asymmetric (103) reflection of LSCO films and their STO substrate. The node corresponding to the LSCO thin film is shifted along Q_{zz} depending on chemical composition consistently with the $2\theta/\omega$ scans, confirming the variation of c_{LSCO} shown in Figure 3. 28. By contrast, the LSCO(103) node is aligned vertically with the substrate node, indicating that the a_{LSCO} is equal to the STO lattice constant (3.905 Å). All LSCO films are thus fully coherently strained to the substrates. In Figure 3. 30b, three visible nodes can be distinguished because of the relatively low-crystalline quality

of the STO substrate with different mosaic domains ($\Delta\omega$ = 0.3°). The a_{LSCO}, c_{LSCO}, and unit-cell volume values of LSCO are summarized in Table 3. 4.

Table 3. 4 In-plane and out-of-plane lattice parameters and unit-cell volume extracted from RSM results, as well as the mosaicity of LSCO(002).

x	*a* (Å)	*c* (Å)	Volume (Å^3)	Mosaicity (°)
0	3.905	3.873	59.059	0.09
0.1	3.905	3.896	59.410	0.12
0.2	3.905	3.881	59.181	0.20
0.25	3.905	3.840	58.556	0.08
0.3	3.905	3.825	58.328	0.08
0.4	3.905	3.811	58.114	0.09

3.3.2.5. XPS characterizations

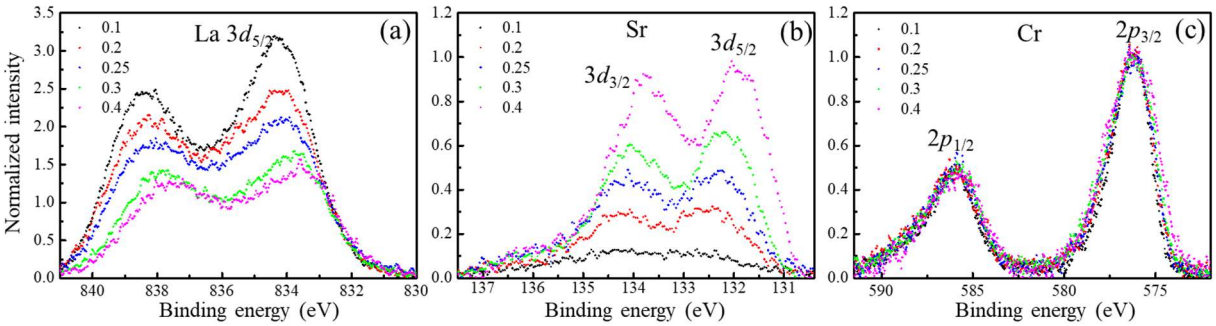

Figure 3. 31 XPS spectra of (a) La $3d_{5/2}$, (b) Sr $3d$, and (c) Cr $2p$ core level for all LSCO films.

Figure 3. 31 shows the XPS core-level spectra of LSCO films. To directly compare binding energies, the Cr $2p_{3/2}$ core-level peaks are all shifted to 576 eV and normalized to 1. For each specimen, the same shift and corresponding normalization are then applied to La $3d_{5/2}$ and Sr $3d$ core-level spectra. The gradient of La $3d_{5/2}$ and Sr $3d$ core-level spectra is observed in Figure 3. 31a and b, which respects the x variation as expected. Therefore, the targeted chemical composition of LSCO as a function of x is confirmed. The physical properties of this series have then been explored. Especially, the impact of x on the electronic and thermoelectric properties has been studied and is presented in the next section.

Table 3. 5 Summary of the chemical properties of the LSCO thin films.

x	[A/(A+B)] (at.%)	[Sr] (at.%)
0.1	0.56	0.11
0.2	0.55	0.18
0.25	0.54	0.27
0.3	0.52	0.39
0.4	0.53	0.49

3.3.3. Physical properties

After the structural properties, both the electronic and thermoelectric properties of the stoichiometric epitaxial films of $La_{1-x}Sr_xCrO_3$ (LSCO) solid-solution series have been investigated at room temperature in-plane. The results of these transport measurements will be presented in the following as a function of x ($0.1 \leq x \leq 0.4$).

3.3.3.1. Electronic properties

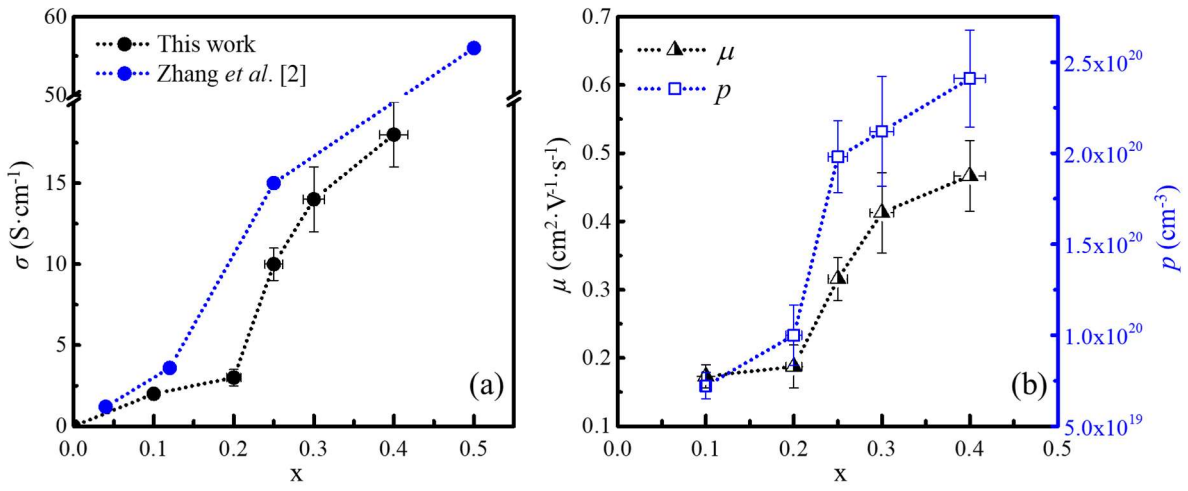

Figure 3. 32 (a) Electrical conductivity σ, (b) hole concentration p, and hole mobility μ of LSCO films obtained from Hall Effect measurement at 300 K.

Room-temperature electronic properties of LSCO films have been measured by the Hall

effect. From these measurements, all the samples exhibit *p*-type conductivity. Figure 3. 32 presents the measured electrical conductivity (σ), hole concentration (p), and hole mobility (μ) of epitaxial LSCO films as a function of x ($0.1 \leq x \leq 0.4$).

LCO (x = 0) is an insulator, its resistivity could be measured neither from the Hall effect nor from the four probes method. From x = 0.1, the LSCO films are then slightly conductive in the range of a few $S \cdot cm^{-1}$, with increasing σ with x: from 2 $S \cdot cm^{-1}$ (x = 0.1) to 18 $S \cdot cm^{-1}$ (x = 0.4), in agreement with literature [2, 27, 28]. However, there are some slight differences and the tendency is not as linear as that of Zhang *et al.* [2]. In particular, around x = 0.2, we could expect a slightly larger electrical conductivity. This slightly low electrical conductivity value at x = 0.2 could be explained by the mosaic multi-domains from the substrate in these films (see multiple high-intensity nodes shown in RSM Figure 3. 30b) affecting the transport properties.

Correspondingly, p is also raised from 7.22×10^{19} to 2.41×10^{20} cm^{-3}. However, these values are about one order of magnitude lower than those reported by Zhang *et al*. However, as presented previously (see section 3.1.3.2 and Chapter I section 1.4.3.2), the hole concentrations reported by Zhang *et al*. are estimated from a small polaron hopping model and not directly measured. This could explain such an important discrepancy with our results.

According to the equation $\mu = \sigma/pe$, the hole mobility of LSCO films can be extracted, which rises with x as well from 0.17 up to 0.47 $cm^2 \cdot V^{-1} \cdot s^{-1}$. In that case, our mobility values are about one order of magnitude higher than those estimated by Zhang *et al*., according to the equation. The difference in the extraction method for transport properties (measurement in our case and model in the Zhang *et al*. case) could explain again such discrepancy. For comparison, these LSCO mobilities are roughly about one order of magnitude lower than *n*-type thermoelectric $Sr_{1-x}La_xTiO_3$ [43, 44, 45], which appears quite reasonable since *p*-type mobility is often lower, up to two orders of magnitude than their *n*-type counterparts, as in other semiconductors like ZnO [46, 47] or GaAs [48].

3.3.3.2. Thermoelectric properties

Thermoelectric properties have been investigated at room temperature. For this purpose, Seebeck coefficients have been measured for all films as a function of x, and the thermoelectric power factor ($PF = S^2\sigma$) has then been estimated. The results are presented in Figure 3. 33.

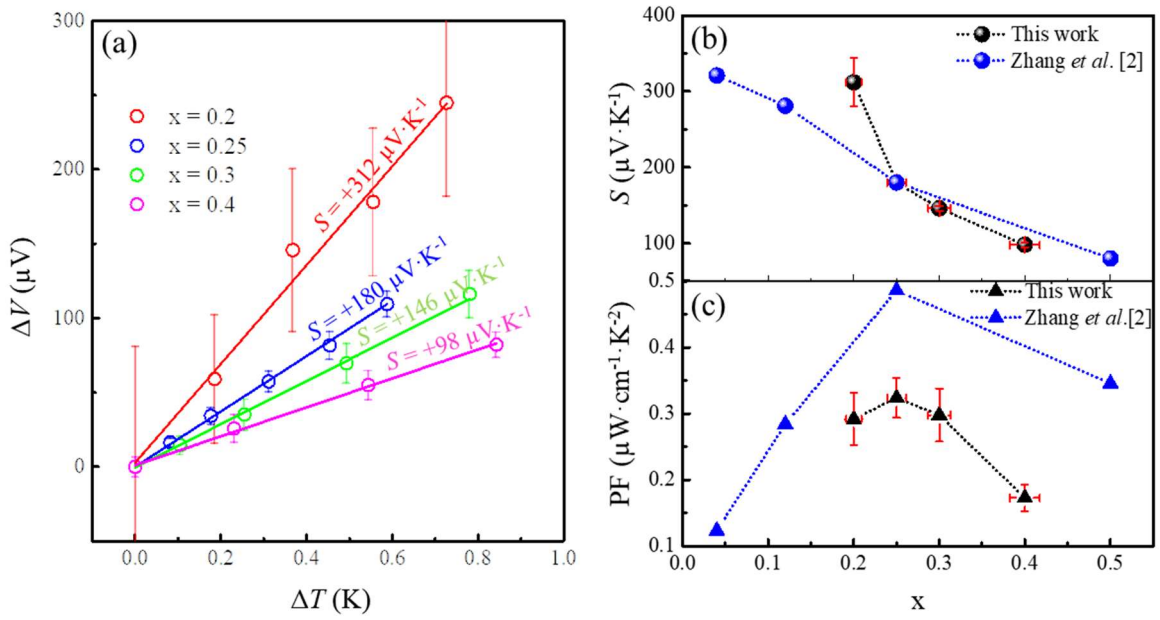

Figure 3. 33 (a) Seebeck measurement at room temperature: ΔV as a function of ΔT in LSCO films. (b) Seebeck coefficient extracted from (a) together with literature values as a comparison, and (c) power factor estimated from the measured S and σ, together with literature values for comparison, both plotted as a function of x.

Figure 3. 33a represents the raw data of ΔV as a function of ΔT measured by differential method at room temperature (see Chapter II). Then, the Seebeck coefficient ($S = \Delta V/\Delta T$) is extracted from the slope of this linear curve from a linear regression fit. It can be seen that S decreases with x increasing. The error bar of each measured point is introduced as well, which can be relatively large, especially for the most resistive films (from difficult electrical contacts). For these reasons, the S of $La_{0.9}Sr_{0.1}CrO_3$ film could not be measured, because electrical contact was not possible in this film. These S values depending on x are in good agreement with previous studies [2]. Figure 3. 33b summarizes the S values measures in our films, which decreases from 312 to 98 $\mu V \cdot K^{-1}$ from x = 0.2 to 0.4, together with the literature values for comparison.

Then the thermoelectric power factor ($PF = S^2\sigma$) can be extracted from both electrical and thermoelectric measurements for all films. PF is plotted as a function of x in Figure 3. 33c, together with literature values for comparison. The PF plot shows a maximum value (~0.34 $\mu W \cdot cm^{-1} \cdot K^{-2}$) around at x = 0.25, in good agreement with literature [2]. LSCO with x = 0.25 ($La_{0.75}Sr_{0.25}CrO_3$) is thus the appropriate chemical composition to achieve the best thermoelectric performance within the stoichiometric LSCO solid solution.

3.4. Conclusion

In this chapter, (00*l*)-oriented $La_{1+\delta}CrO_3$ and $Sr_{1+\delta}CrO_3$ epitaxial thin films with $-0.25 \leq \delta \leq 0.25$ and $-0.143 \leq \delta \leq 0.143$, respectively, were firstly grown on STO(001) substrates by MBE for composition calibration purpose. Despite the large stoichiometry deviation range, all films conserve single-crystallinity, are atomically flat, with mosaicity below 0.1°. Any secondary phase is observed with the different structural characterization techniques used here (RHEED, AFM, XRD, XPS, and RBS). The out-of-plane lattice parameter reaches a minimum at the cationic stoichiometry and increases when deviating from it. The diffracted intensity slightly decreases with δ, most probably due to the introduction of cationic vacancies in the lattice, which must permit to keep the high-crystalline quality structure in all cases even with such large cationic ratio (A/B) variations in the perovskite structure ABO_3.

Then, once both single calibration series (LCO and SCO) have been achieved, the high-crystalline quality films of $La_{1-x}Sr_xCrO_3$ (LSCO) solid solution ($0.1 \leq x \leq 0.4$) were grown on STO (001) oriented substrates prepared with a single TiO_2-termination. All films are epitaxially-strained and show excellent structural properties. Transport measurements at room temperature show that the LSCO films have *p*-type thermoelectric properties. As expected, the transport properties can be tuned by the cationic substitution ratio (x). By increasing x in LSCO, the electrical conductivity increases from 2 $S \cdot cm^{-1}$ (x = 0.1) to 18 $S \cdot cm^{-1}$ (x = 0.4), and the Seebeck coefficient decreases from 312 $\mu V \cdot K^{-1}$ (x = 0.2) to 98 $\mu V \cdot K^{-1}$ (x = 0.4). These values are in good agreement with the literature [28, 2, 27]. The thermoelectric power factor obtained from these measurements is maximum at 25% of the Sr substitution ratio (0.324 $\mu W \cdot cm^{-1} \cdot K^{-2}$, for $La_{0.75}Sr_{0.25}CrO_3$), again in agreement with the literature [2].

Finally, this chapter lays the foundation for the original studies presented in the two following chapters, on the epitaxial strain effect (Chapter IV) and the impact of the deviation of the cationic stoichiometry (Chapter V) in epitaxially strained $La_{0.75}Sr_{0.25}CrO_3$ thin films.

3.5. References

[1] D. Han, M. Bouras, C. Botella, A. Benamrouche, B. Canut, G. Grenet, G. Saint-Girons, and R. Bachelet. Structural properties of strained epitaxial $La_{1+\delta}CrO_3$ thin films. Journal of Vacuum Science & Technology A: Vacuum, Surfaces, and Films, 2019, 37(2): 021512.

[2] K. H. L. Zhang, Y. Du, A. Papadogianni, O. Bierwagen, S. Sallis, L. F. Piper, M. E. Bowden, V. Shutthanandan, P. V. Sushko, and S. A. Chambers. Perovskite Sr-doped $LaCrO_3$ as a new p-type transparent conducting oxide. Advanced Materials, 2015, 27(35): 5191-5195.

[3] L. Qiao, K. H. L. Zhang, M. E. Bowden, T. Varga, V. Shutthanandan, R. Colby, Y. Du, B. Kabius, P. V. Sushko, M. D. Biegalski, and S. A. Chambers. The impacts of cation stoichiometry and substrate surface quality on nucleation, structure, defect formation, and intermixing in complex oxide heteroepitaxy-$LaCrO_3$ on $SrTiO_3$(001). Advanced Functional Materials, 2013, 23(23): 2953-2963.

[4] L. Qiao, H. Y. Xiao, S. M. Heald, M. E. Bowden, T. Varga, G. J. Exarhos, M. D. Biegalski, I. N. Ivanov, W. J. Weber, T. C. Droubay, and S. A. Chambers. The impact of crystal symmetry on the electronic structure and functional properties of complex lanthanum chromium oxides. Journal of Materials Chemistry C, 2013, 1(30): 4527-4535.

[5] M. Tseggai, P. Nordblad, R. Tellgren, H. Rundlöf, G. Andrè and F. Bourèe. Synthesis, nuclear structure, and magnetic properties of $LaCr_{1-y}Mn_yO_3$ (y = 0, 0.1, 0.2, and 0.3). Journal of Alloys and Compounds, 2008, 457(1-2): 532-540.

[6] T. Hashimoto, N. Tsuzuki, A. Kishi, K. Takagi, K. Tsuda, M. Tanaka, K. Oikawa, T. Kamiyama, K. Yoshida, H. Tagawa, and M. Dokiya. Analysis of crystal structure and phase transition of $LaCrO_3$ by various diffraction measurements. Solid State Ionics, 2000, 132(3-4): 181-188.

[7] T. Hashimoto, K. Takagi, K. Tsuda, M. Tanaka, K. Yoshida, H. Tagawa, and M. Dokiya. Determination of the space group of $LaCrO_3$ by convergent-beam electron diffraction. Journal of the Electrochemical Society, 2000, 147(12): 4408.

[8] S. Gražulis, A. Daškevic, A. Merkys, D. Chateigner, L. Lutterotti, M. Quiró, N. R. Serebryanaya, P. Moeck, R. T. Downs, and A. Le Bail. Crystallography open database (COD): An open-access collection of crystal structures and platform for world-wide collaboration. Nucleic Acids Research, 2012, 40(D1): D420-D427.

[9] S. Gražulis, D. Chateigner, R. T. Downs, A. F. T. Yokochi, M. Quirós, L. Lutterotti, E. Manakova, J. Butkus, P. Moeck, and A. Le Bail. Crystallography open database–an open-access collection of crystal structures. Journal of Applied Crystallography, 2009, 42(4): 726-729.

[10] R. T. Downs and M. Hall-Wallace. The american mineralogist crystal structure database. American Mineralogist, 2003, 88(1): 247-250.

[11] J. Yang. Structural analysis of perovskite $LaCr_{1-x}Ni_xO_3$ by Rietveld refinement of X-ray powder diffraction data. Acta Crystallographica Section B: Structural Science, 2008, 64(3): 281-286.

[12] L. Qiao, T. C. Droubay, M. E. Bowden, V. Shutthanandan, T. C. Kaspar, and S. A. Chambers. $LaCrO_3$ heteroepitaxy on $SrTiO_3$(001) by molecular beam epitaxy. Applied Physics Letters, 2011, 99(6): 061904.

[13] G. Brunin. Perovskite Sr-doped $LaCrO_3$: An *ab initio* study (Thesis). Ecole Polytechnique de Louvain, Louvain-la-Neuve, Belgique, 2016.

[14] I. Weinberg and P. Larssen. Electron paramagnetic resonance and antiferromagnetism in $LaCrO_3$. Nature, 1961, 192(4801): 445-446.

[15] T. Arima, Y. Tokura, and J. B. Torrance. Variation of optical gaps in perovskite-type 3d transition-metal oxides. Physical Review B, 1993, 48(23): 17006.

[16] K. Maiti and D. Sarma. Electronic structure of $La_{1-x}Sr_xCrO_3$. Physical Review B, 1996, 54(11): 7816.

[17] P. V. Sushko, L. Qiao, M. Bowden, T. Varga, G. J. Exarhos, F. K. Urban, D. Barton, and S. A. Chambers. Multiband optical absorption controlled by lattice strain in thin-film $LaCrO_3$. Physical Review Letters, 2013, 110(7): 077401.

[18] K. H. L. Zhang, P. V. Sushko, R. Colby, Y. Du, M. E. Bowden, and S. A. Chambers. Reversible nano-structuring of $SrCrO_{3-\delta}$ through oxidation and reduction at low temperature. Nature Communications, 2014, 5(1): 1-7.

[19] J. S. Zhou, C. Q. Jin, Y. W. Long, L. X. Yang, and J. B. Goodenough. Anomalous electronic state in $CaCrO_3$ and $SrCrO_3$. Physical Review Letters, 2006, 96(4): 046408.

[20] L. Ortega-San-Martin, A. J. Williams, J. Rodgers, J. P. Attfield, G. Heymann, and H. Huppertz. Microstrain sensitivity of orbital and electronic phase separation in $SrCrO_3$. Physical Review Letters, 2007, 99(25): 255701.

[21] K. H. L. Zhang, Y. Du, P. Sushko, M. E. Bowden, V. Shutthanandan, L. Qiao, G. Cao, Z. Gai, S. Sallis, L. Piper, and S. A. Chambers. Electronic and magnetic properties of epitaxial perovskite $SrCrO_3$(001). Journal of Physics: Condensed Matter, 2015, 27(24): 245605.

[22] G. Herranz, F. Sánchez, J. Fontcuberta, V. Laukhin, J. Galibert, M. V. García-Cuenca, C. Ferrater, and M. Varel. Magnetic field effect on quantum corrections to the low-temperature conductivity in metallic perovskite oxides. Physical Review B, 2005, 72(1): 014457.

[23] Y. Xu, J. Zhang, G. Cao, C. Jing, and S. Cao. Low-temperature resistivity minimum and weak spin disorder of polycrystalline $La_{2/3}Ca_{1/3}MnO_3$ in a magnetic field. Physical Review B, 2006, 73(22): 224410.

[24] M. Huijben, A. Brinkman, G. Koster, G. Rijnders, H. Hilgenkamp, and D. H. A. Blank. Structure-property relation of $SrTiO_3/LaAlO_3$ interfaces. Advanced Materials, 2009, 21(17): 1665-1677.

[25] A. Annadi, X. Renshaw Wang, K. Gopinadhan, W. M. Lü, A. Roy Barman, Z. Q. Liu, A. Srivastava, S. Saha, Y. L. Zhao, S. W. Zeng, S. Dhar, N. Tuzla, E. Olsson, Q. Zhang, B. Gu, S. Yunoki, S. Maekawa, H. Hilgenkamp, T. Venkatesan, and A. Ariando. Anisotropic two-dimensional electron gas at the $LaAlO_3/SrTiO_3$(110) interface. Nature Communications, 2013, 4(1): 1-7.

[26] N. A. Noor, M. B. Saddique, B. U. Haq, A. Laref, and M. Rashid. Investigations of half-metallic ferromagnetism and thermoelectric properties of cubic $XCrO_3$ (X = Ca, Sr, Ba) compounds via first-principles approaches. Physics Letters A, 2018, 382(42-43): 3095-3102.

[27] K. H. L. Zhang, Y. Du, P. Sushko, M. E. Bowden, V. Shutthanandan, S. Sallis, L. F. Piper, and S. A. Chambers. Hole-induced insulator-to-metal transition in $La_{1-x}Sr_xCrO_3$ epitaxial films. Physical Review B, 2015, 91(15): 155129.

[28] D. P. Karim and A. T. Aldred. Localized level hopping transport in La(Sr)CrO_3. Physical Review B, 1979, 20(6): 2255.

[29] W. J. Weber, C. W. Griffin, and J. L. Bates. Effects of cation substitution on electrical and thermal transport properties of $YCrO_3$ and $LaCrO_3$. Journal of the American Ceramic Society, 1987, 70(4): 265-270.

[30] D. B. Marsh and P. E. Parris. Theory of the Seebeck coefficient in $LaCrO_3$ and related perovskite systems. Physical Review B, 1996, 54(11): 7720.

[31] L. Farrell, K. Fleischer, D. Caffrey, D. Mullarkey, E. Norton, and I. V. Shvets. Conducting mechanism in the epitaxial p-type transparent conducting oxide Cr_2O_3: Mg. Physical Review B, 2015, 91(12): 125202.

[32] R. Bachelet. Oxide single-crystal surfaces: A playground for self-assembled oxide nanostructures. Frontiers in Physics, 2016, 4: 36.

[33] G. Koster, B. L. Kropman, G. J. H. M. Rijnders, D. H. A. Blank, and H. Rogalla. Quasi-ideal strontium titanate crystal surfaces through formation of strontium hydroxide. Applied Physics Letters, 1998, 73(20): 2920-2922.

[34] R. Bachelet, F. Sánchez, J. Santiso, C. Munuera, C. Ocal, and J. Fontcuberta. Self-assembly of $SrTiO_3$(001) chemical-terminations: A route for oxide-nanostructure fabrication by selective growth. Chemistry of Materials, 2009, 21(12): 2494-2498.

[35] M. Kawasaki, K. Takahashi, T. Maeda, R. Tsuchiya, M. Shinohara, O. Ishiyama, T. Yonezawa, M. Yoshimoto, and H. Koinuma. Atomic control of the $SrTiO_3$ crystal surface. Science, 1994, 266(5190): 1540-1542.

[36] R. García, R. Magerle, and R. Perez. Nanoscale compositional mapping with gentle forces. Nature Materials, 2007, 6(6): 405-411.

[37] R. Bachelet, C. Ocal, L. Garzón, J. Fontcuberta, and F. Sánchez. Conducted growth of $SrRuO_3$ nanodot arrays on self-ordered $La_{0.18}Sr_{0.82}Al_{0.59}Ta_{0.41}O_3$(001) surfaces. Applied Physics Letters, 2011, 99(5): 051914.

[38] C. Ocal, R. Bachelet, L. Garzón, M. Stengel, F. Sánchez, and J. Fontcuberta. Nanoscale laterally modulated properties of oxide ultrathin films by substrate termination replica through layer-by-layer growth. Chemistry of Materials, 2012, 24(21): 4177-4184.

[39] C. M. Brooks, L. F. Kourkoutis, T. Heeg, J. Schubert, D. A. Muller and D. G. Schlom. Growth of homoepitaxial $SrTiO_3$ thin films by molecular-beam epitaxy. Applied Physics Letters, 2009, 94(16): 162905.

[40] B. Jalan, R. Engel-Herbert, N. J. Wright and S. Stemmer. Growth of high-quality $SrTiO_3$ films using a hybrid molecular beam epitaxy approach. Journal of Vacuum Science & Technology A: Vacuum, Surfaces, and Films, 2009, 27(3): 461-464.

[41] B. Jalan, P. Moetakef and S. Stemmer. Molecular beam epitaxy of $SrTiO_3$ with a growth window. Applied Physics Letters, 2009, 95(3): 032906.

[42] The relative in-plane epitaxial strain (ε_{xx}) due to the lattice mismatch (f) are defined here as: $\varepsilon_{xx} = (a_{film} - a_{bulk})/a_{bulk}$, and $f = (a_{sub} - a_{bulk})/a_{bulk}$, where a_{film} is the measured in-plane lattice parameter of the film, a_{bulk} the bulk lattice parameter of pseudocubic film, and a_{sub} the lattice parameter of the substrate. Please note that $\varepsilon_{xx} = f$ for fully strained epitaxial films ($a_{film} = a_{sub}$).

[43] M. Apreutesei, R. Debord, M. Bouras, P. Regreny, C. Botella, A. Benamrouche, A. Carretero-Genevrier, J. Gazquez, G. Grenet, S. Pailhès, G. Saint-Girons, and R. Bachelet. Thermoelectric La-doped $SrTiO_3$ epitaxial

layers with single-crystal quality: From nano to micrometers. Science and Technology of Advanced Materials, 2017, 18(1): 430-435.

[44] M. Choi, A. B. Posadas, C. A. Rodriguez, A. O'Hara, H. Seinige, A. J. Kellock, M. M. Frank, M. Tsoi, S. Zollner, V. Narayanan, and A. A. Demkov. Structural, optical, and electrical properties of strained La-doped $SrTiO_3$ films. Journal of Applied Physics, 2014, 116(4): 043705.

[45] J. Son, P. Moetakef, B. Jalan, O. Bierwagen, N. J. Wright, R. Engel-Herbert, and S. Stemmer. Epitaxial $SrTiO_3$ films with electron mobilities exceeding 30,000 $cm^2V^{-1}s^{-1}$. Nature Materials, 2010, 9(6): 482-484.

[46] A. Tsukazaki, A. Ohtomo, and M. Kawasak. High-mobility electronic transport in ZnO thin films. Applied Physics Letters, 2006, 88(15): 152106.

[47] R. T. Longo. Mathematical modeling technique. AIP Advances, 2019, 9(12): 125211.

[48] Electrical properties of GaAs. Retrieved from: http://www.ioffe.ru/SVA/NSM/Semicond/GaAs/electric.html #Hall.

Chapter IV Effect of epitaxial strain

4.1. Introduction

The purpose of this chapter is to present the impact of epitaxial strain on structural and physical properties of $La_{0.75}Sr_{0.25}CrO_3$ (LSCO) thin films (and $LaCrO_3$ as a reference) grown on different pseudo-cubic perovskite oxide substrates with different lattice parameters. After some definitions and a brief literature review on epitaxial strain effects in perovskite oxide films (section 4.1), structural and elastic properties of epitaxially strained LCO and LSCO thin film are investigated (section 4.2). In particular, the Poisson ratio and bulk lattice parameter of LSCO (x = 0.25, giving the maximum thermoelectric power factor in this solid solution) are derived for the first time. These results are published in the Ref. 1. Then, the electronic and thermoelectric properties of this series have also been investigated (section 4.2.3). These corresponding results are submitted for publication [2].

4.1.1. Epitaxial strain in perovskite oxide thin films

In heteroepitaxy, the epitaxial strain can occur when the in-plane lattice parameter of a film (a_{film}) is slightly dissimilar to the lattice constant of a substrate (a_{sub}), or dissimilar but with coincidence site lattices (CSL). If the strain is elastic, reduction (in-plane compressive strain) or elongation (in-plane tensile strain) of the in-plane lattice parameter of the film can occur [3]. When $a_{film} \neq a_{sub}$, the structure of the film tries to take the structure of the substrate, causing elastic structural changes (mainly in BO_6 octahedron rotation, tilting, distortion, and/or the change in B-O bond length) from the bulk atomic position [4]. If the difference between the lattice parameters is too important, plastic strain/relaxation can occur in the films via the introduction of defects like dislocations, vacancies, etc. as in domain matching epitaxy (DME) [5]. Epitaxial strain, or so-called strain engineering, in thin films refers to elastic strain. Epitaxial strain engineering is an effective way to tune functionalities in epitaxial oxide thin films where strong coupling between lattice and spin/charge/orbital may exist [3, 6, 7, 8, 9, 10]. It can even create new functionalities that don't exist in their bulk counterpart [11, 12].

The relative epitaxial in-plane strain (ε_{xx}) induced in a film is defined here as:

$$\varepsilon_{xx} = \frac{a_{film} - a_{bulk}}{a_{bulk}} \quad (4.1)$$

where a_{bulk} is the bulk lattice parameter of (pseudo)cubic film. The lattice mismatch (or

so-called misfit, f_0) between the substrate and the film is defined here as:

$$f_0 = \frac{a_{sub} - a_{bulk}}{a_{bulk}} \tag{4.2}$$

In fully strained films, $a_{film} = a_{sub}$, and thus, $\varepsilon_{xx} = f_0$. A positive sign indicates an in-plane tensile strain, whereas a negative sign indicates an in-plane compressive strain. If the Poisson ratio is positive (most of the materials, and see definition below), for the in-plane compressively-strained films ($a_{film} > a_{sub}$), the lattice is reduced along with the in-plane directions and expanded along the out-of-plane direction (Figure 4. 1a). Whereas, for the in-plane tensely-strained films ($a_{film} < a_{sub}$), the lattice expands along with the in-plane directions and reduces along the out-of-plane direction (Figure 4. 1b).

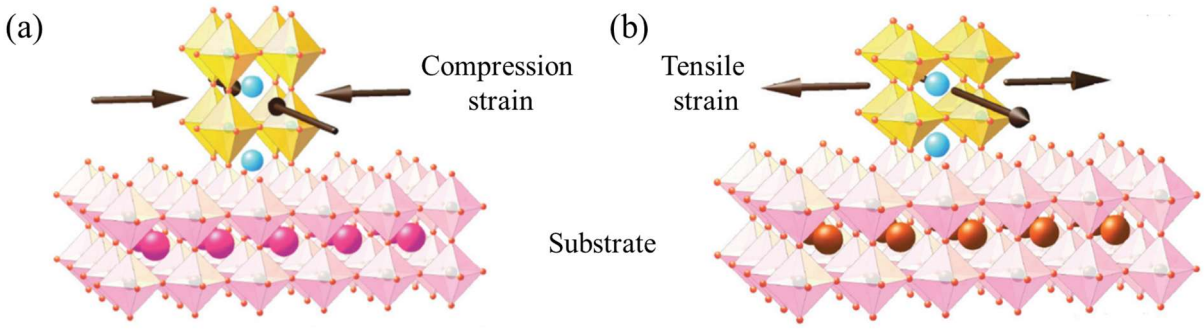

Figure 4. 1 Sketch of the epitaxial strain in perovskite heterostructures. (a) Compressive and (b) tensile strain is induced in a film through the use of lattice-mismatched substrates. For compressive strain, $a_{film} > a_{sub}$, whereas for tensile strain, $a_{film} < a_{sub}$. Taken from Ref. 3.

4.1.2. Substrate selection for heteroepitaxy of perovskite oxide thin films

In most cases, for the best quality or property tuning purpose, the lattice constant and structure of heteroepitaxial thin films should be compatible with those of the substrate used [4]. For most of the perovskite oxides, their lattice constants range from 3.8 to 4 Å [3, 13]. Fortunately, there are many perovskite single-crystal oxide substrates available commercially with lattice constants ranging from 3.7 to 4.2 Å [3, 6, 7, 14, 15], as shown in Figure 4. 2. With a judicial choice of the substrate, high-crystalline quality thin films can be grown with various strain states. Among various available perovskite oxide substrates, insulating $SrTiO_3$ (STO) is still the most popular one, which has a cubic structure with a lattice constant of 3.905 Å, in the middle range of the most functional oxides.

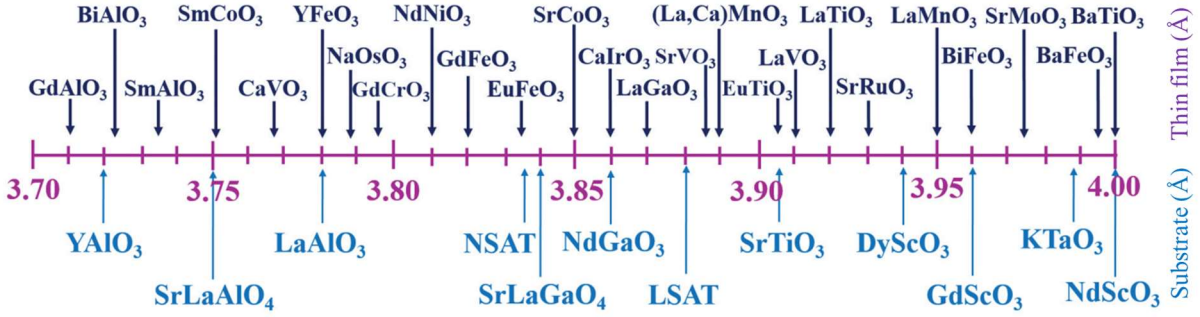

Figure 4. 2 List of cubic and/or pseudocubic substrates and thin films with their lattice parameter ranging from 3.7 to 4 Å. Taken from Ref. 3.

4.1.3. Some reports of epitaxial strain effects in perovskite oxide films

From the structural/elastic point of view, although various studies have dealt with strain-dependent structural properties from films subjected to different epitaxial strains, the extraction of Poisson ratio (v) and bulk lattice parameter (a_{bulk}) is mostly absent. Only a few previous studies report the extraction of v from strained epitaxial perovskite-oxide thin films. Chen *et al.* [16] grew multiferroic $BiFeO_3$ thin films on different substrates chosen to provide the widest possible range of lattice mismatch (from -2.8% to +6%) and measured a v value of 0.49 for the rhombohedral-like phase of this oxide. Adamo *et al.* [17] derived a v = 0.37 for epitaxial $La_{0.7}Sr_{0.3}MnO_3$ thin film. Choi *et al.* [18] grew $La_xSr_{1-x}TiO_3$ films with different doping/substitution ratios (from 5% to 25%) on different substrates resulting in lattice mismatch strain ranging from -2.9% to +1.1%, and although the measured v is not given, the study indicates that Sr substitution by La tends to decrease the v concerning $SrTiO_3$. Niu *et al.* [19] evidenced the formation of two $SrTiO_3$ phases having different v values during the epitaxial growth of this oxide on silicon. Concerning the *p*-type Sr-doped $LaCrO_3$, bulk lattice parameter as well as Poisson ratio were unknown despite its technological importance and our published results [1].

From the physical properties point of view, strain engineering has been extensively studied to tune ferroic properties [20, 21, 22]. As well as ferroic oxides, studies have been also reported about the effects of epitaxial strain on the transport properties of conducting oxides. Vailionis *et al.* [23] have studied the tensile effect on resistivity of $SrRuO_3$ and $CaRuO_3$ films grown on different substrates. They observed that the thin layers under large in-plane tensile strain have larger resistivities than their less strained or compressively-strained counterparts. Similarly, Grutter *et al.* [24] found that the compressively-strained $SrRuO_3$ film has a lower

resistivity, while the in-plane compressive strain increases from -0.64% ($SrRuO_3/SrTiO_3$) to -1.58% ($SrRuO_3$/LSAT). Smaller in-plane lattice parameters and larger out-of-plane lattice parameters correspond to lower resistivity values. Recently, Kan *et al*. [25] reported the influence of the epitaxial strain in compressively and tensely-strained $SrRuO_3$ films on their thermoelectric properties. They demonstrated that the tensely-strained film has a higher Seebeck coefficient than the compressively-strained film. Besides, Adamo *et al*. [17] have investigated the effect of biaxial strain on $La_{0.7}Sr_{0.3}MnO_3$ thin films deposited on different single crystalline substrates, varying the substrate-induced biaxial strain from -2.3% to +3.2%. They indicated that the $La_{0.7}Sr_{0.3}MnO_3$ films with a small amount of in-plane strain (≤ 0.6%) have the lowest resistivity value (~1 mΩ·cm) at room temperature. Their resistivity increases significantly with tensile strain, and the films become insulating with high compressive strain. Likewise, Choi *et al*. [18] studied the structural, optical, and room-temperature electrical properties of La-doped $SrTiO_3$ transparent epitaxial thin films with La substitution ratio varying from 5% to 25% grown on different substrates with lattice mismatch strain ranging from -2.9% to +1.1%. They found that the Hall mobility of fully-strained films decreases with increasing strain regardless of the sign of strain. Concerning *p*-type Sr-doped $LaCrO_3$, no result has been reported yet despite its technological importance, and our results on this point are submitted for publication [2].

4.2. Strain effects in epitaxial Sr-doped $LaCrO_3$ thin films

In this section, high-crystalline quality strained epitaxial LCO and $La_{0.75}Sr_{0.25}CrO_3$ (LSCO) thin films were grown on four different (001)-oriented cubic and/or pseudocubic perovskite-oxide substrates: $LaAlO_3$ (LAO), $(LaAlO_3)_{0.3}(Sr_2AlTaO_6)_{0.7}$ (LSAT), STO and $DyScO_3$ (DSO), with different lattice constants, as sketched in Figure 4. 3. Firstly, the epitaxial strain effect on structural properties (both in-plane and out-of-plane lattice parameters) of the thin films is investigated, and the v, as well as the a_{bulk} of LSCO, are extracted. The parameters significantly differ from those measured for LCO film. These results are published in Ref. 1. Secondly, the room-temperature in-plane transport and thermoelectric properties of LSCO are also investigated. We will show that epitaxial strain is an efficient parameter to control the electric transport and thermoelectric properties of *p*-type LSCO thin films, which is of importance for integrated LSCO-based devices. These corresponding results are submitted for publication [2].

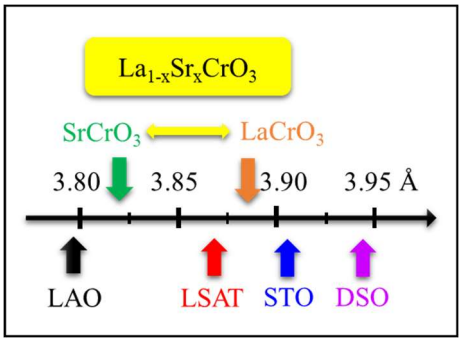

Figure 4. 3 Bulk lattice constants of the LSCO films and substrates involved in the study. Taken from Ref. 1.

4.2.1. Growth conditions

Four different (001)-oriented cubic/pseudocubic perovskite-oxide substrates, namely LAO, LSAT, STO, and DSO with lattice constants of 3.796 Å, 3.868 Å, 3.905 Å, and 3.944 Å, respectively [14], were used to grow in the same campaign (but different runs) the strained epitaxial LCO (~15 nm) and LSCO (~30 nm) thin films by solid-source MBE in an ultra-high vacuum chamber having a base pressure less than 1×10^{-9} Torr. La, Sr, and Cr were evaporated from effusion cells in co-deposition. The fluxes were measured before the growth using a Bayard-Alpert (BA) gauge (after subtraction of the background pressure) and checked using a quartz crystal microbalance (QCM) (shown in detail in Chapter III). The stoichiometry was calibrated using flux measurements by BA gauge and QCM, XRD, RBS, and XPS (see Chapter III) [26]. The growth rate was ~0.1 nm/min for LCO films and ~0.15 nm/min for LSCO films. The substrates were annealed under the growth conditions for 15 minutes to remove surface impurities before starting the growth at T = 700 °C and $P(O_2) = 1\times10^{-7}$ Torr. After deposition, the substrate temperature was lowered to 200 °C at a rate of 50 °C/min while the background O_2 was pumping out. All the films were grown on as-received substrates, except the LSCO grown on STO, for which the substrate was treated to be terminated by a TiO_2 plane (see Chapter III). All films were subjected to an additional anneal in the air at 300 °C for 2 hours to ensure complete oxidation.

4.2.2. Control of the microstructural quality

The microstructural quality of both LCO & LSCO epitaxially strained thin films have been checked by different techniques (RHEED, AFM, XRR, XPS) before those structural properties (lattice parameters in particular) were investigated by XRD.

4.2.2.1. RHEED characterizations

(a) LCO

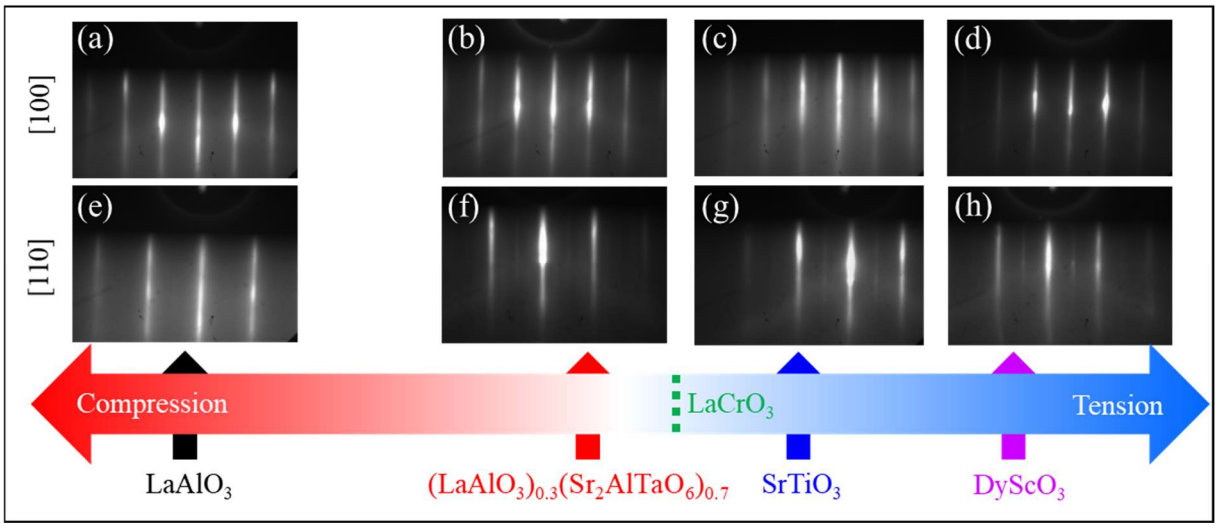

Figure 4. 4 RHEED patterns recorded along the [100] and [110] azimuths (around 200 °C, $P(O_2)$ = 1×10^{-9} Torr) after the growth of LCO films on (a, e) LAO, (b, f) LSAT, (c, g) STO, and (d, h) DSO substrates.

RHEED was used to qualitatively check *in-situ* the structural quality of the films. The RHEED patterns recorded at the end of the growth of the LCO thin films on the four different substrates along the high-symmetry [100] and [110] in-plane crystallographic directions are shown in Figure 4. 4. All the patterns present well-contrasted streak lines showing that the films are heteroepitaxial with very flat surfaces.

(b) LSCO

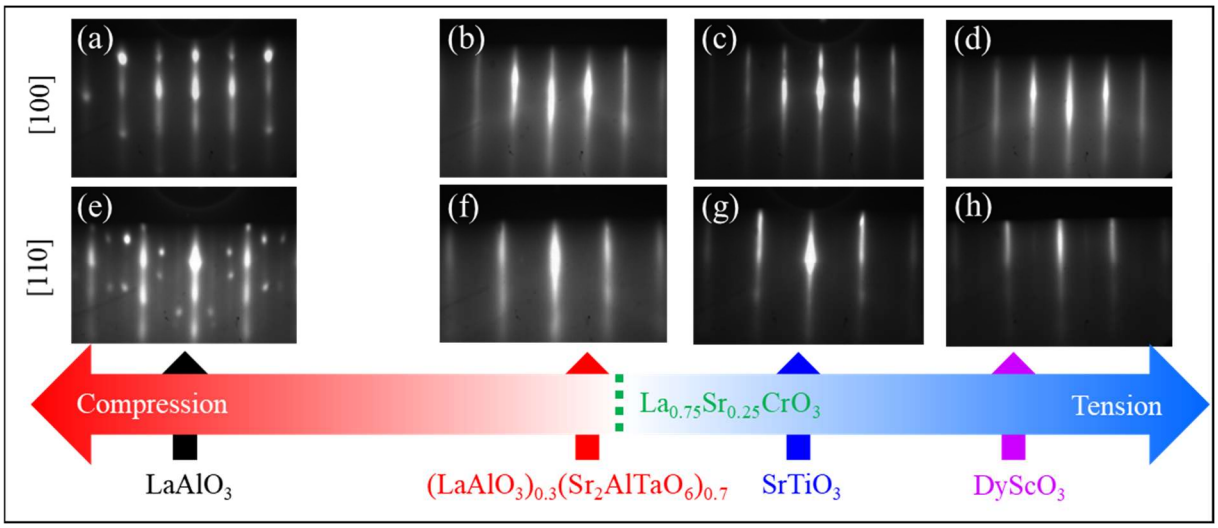

Figure 4. 5 RHEED patterns recorded along the [100] and [110] azimuths (around 200 °C, $P(O_2)$ = 1×10^{-9} Torr) after the growth of LSCO films on (a, e) LAO, (b, f) LSAT, (c, g) STO, and (d, h) DSO substrates.

The RHEED patterns recorded at the end of the growth of the LSCO thin films on the four different substrates along the high-symmetry [100] and [110] in-plane crystallographic directions are shown in Figure 4. 5. All the patterns, except that corresponding to the film grown on the LAO substrate (Figure 4. 5a and e), present well-contrasted streak lines indicating that the films' surfaces are very flat. For the film grown on LAO, the rather spotty pattern indicates that the film is slightly rougher than the others, which has been confirmed by AFM and XRR measurements (see below in sections 4.2.2.2 and 4.2.2.3).

4.2.2.2. AFM characterizations of LSCO films

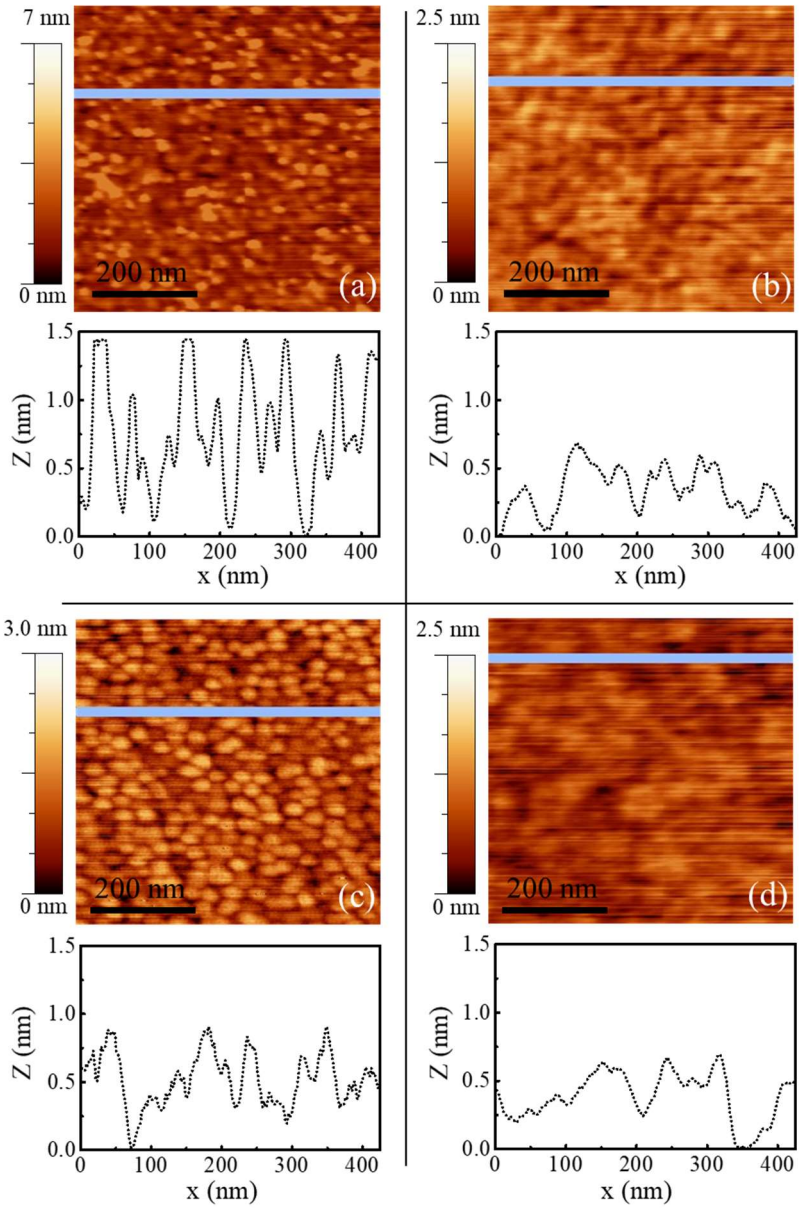

Figure 4. 6 (a-d) AFM topographic images of LSCO films on (a) LAO, (b) LSAT, (c) STO, and (d) DSO substrates, and their corresponding topographic profiles below.

AFM working in tapping mode was used to measure the surface morphology and local rms surface roughness of the LSCO films. The rms surface roughnesses measured locally by AFM topographic images of LSCO films epitaxially grown on LAO, LSAT, STO, and DSO substrates (shown in Figure 4. 6) are very low: 0.58, 0.32, 0.38, and 0.23 nm, respectively, in good agreement with RHEED (Figure 4. 5) and XRR results (Table 4. 1). It is worth noting that the film with the highest roughness corresponds to that with the most in-plane compressive strain and the one with the lowest roughness to that with the most in-plane tensile strain. This may indicate a tendency with the strain, concordant with RHEED and XRR results.

4.2.2.3. XRR characterizations

XRR was used to measure the thickness of all LCO and LSCO films. The curves are plotted in Figure 4. 7. The measured experimental data are well described by the red fitted curves, including the interference fringe periodicity and the overall slope, yielding values for the films' thicknesses, and the root-mean-square (rms) surface/interface roughnesses (summarized in Table 4. 1).

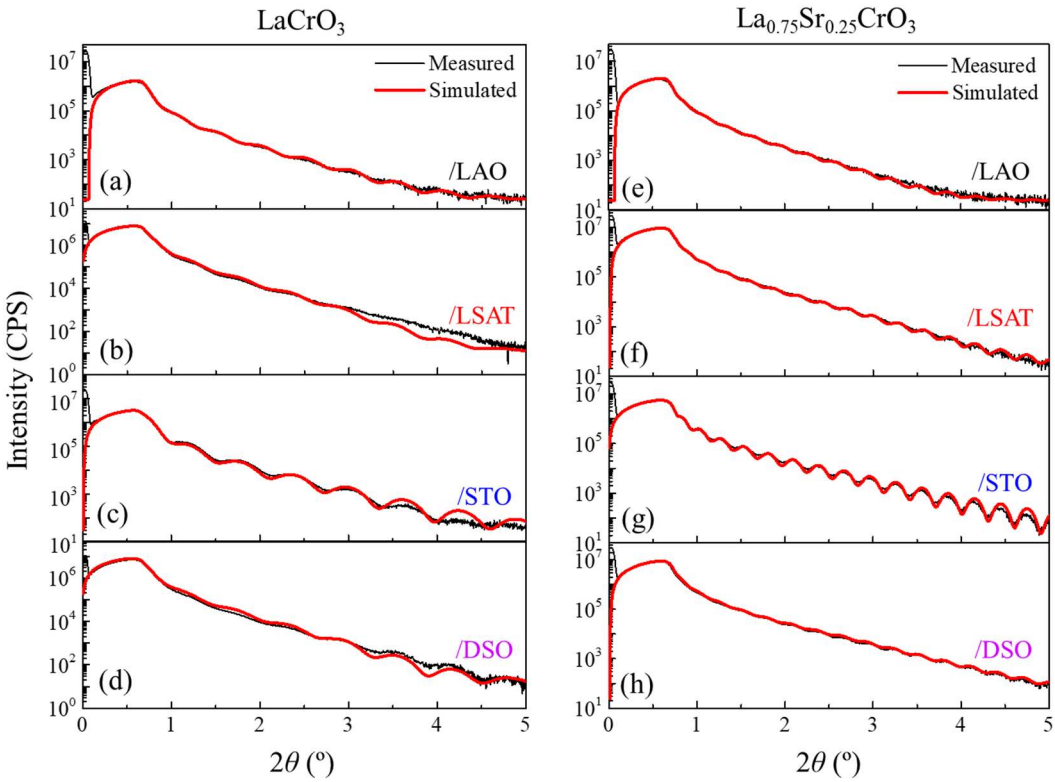

Figure 4. 7 XRR curves for all (a-d) LCO and (e-h) LSCO films, including the raw data (black lines) and the fitting curves (red lines).

Table 4. 1 Thickness and rms-roughness for all LCO and LSCO films from XRR fits.

Fit parameter	$LaCrO_3$				$La_{0.75}Sr_{0.25}CrO_3$			
	/LAO	/LSAT	/STO	/DSO	/LAO	/LSAT	/STO	/DSO
t (nm)	16.6	14.5	13.7	13.8	27.2	29.9	28.2	29.0
rms surface (nm)	0.63	0.61	0.54	0.62	0.72	0.58	0.54	0.49
rms interface (nm)	0.15	0.15	0.15	0.15	0.15	0.15	0.15	0.15

All the films present low surface roughness below ~0.7 nm. The LSCO/LAO film surface has an rms roughness of 0.72 nm that is slightly larger than that of LCO films and the three other LSCO films on LSAT, STO, and DSO substrates, which are all below 0.6 nm (Table 4. 1). The rms surface roughness of LSCO films tends to decrease from compressive strain to tensile strain (Table 4. 1 and Figure 4. 8), in relatively good agreement with RHEED and AFM observations.

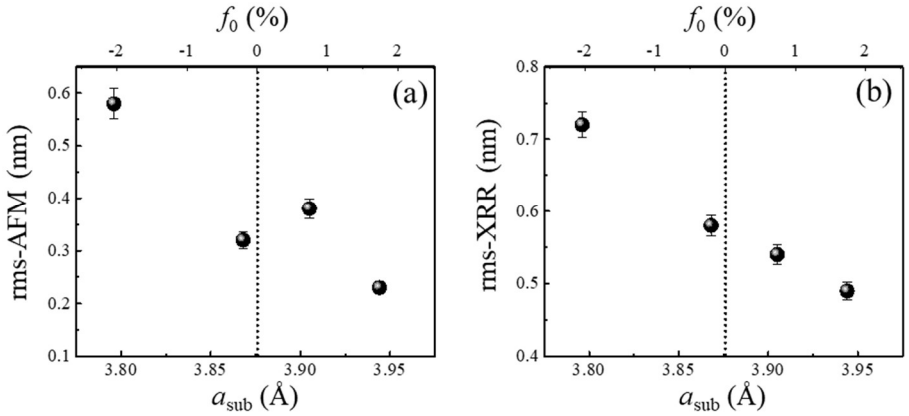

Figure 4. 8 rms-roughness for all LSCO films from (a) AFM measurement and (b) XRR fit.

4.2.2.4. XPS characterizations

XPS was used to check the composition of LCO and LSCO thin films, as well as the good oxidation state of the films by fitting the Cr $2p_{3/2}$ core-level spectra components. The fit of the Cr $2p_{3/2}$ core-level spectra reveals 25% of Cr^{4+} component in LSCO films and only Cr^{3+} component in LCO films (Figure 4. 10), in agreement with the targeted composition and oxygen stoichiometry [27].

To directly compare binding energies, the Cr $2p_{3/2}$ peaks (Figure 4. 9b and e) are all shifted to 576 eV and normalized to 1. For each specimen, the same shift and normalization are then applied to La 4*d* and Sr 3*d* spectra. The measured compositions are summarized in

Table 4. 2. Even if slight differences can be observed between samples [≤ 1 at.% on x, and ≤ 6 at.% on the A/(A+B) cationic ratio], the targeted composition of all the films is reached within the instrumental uncertainties.

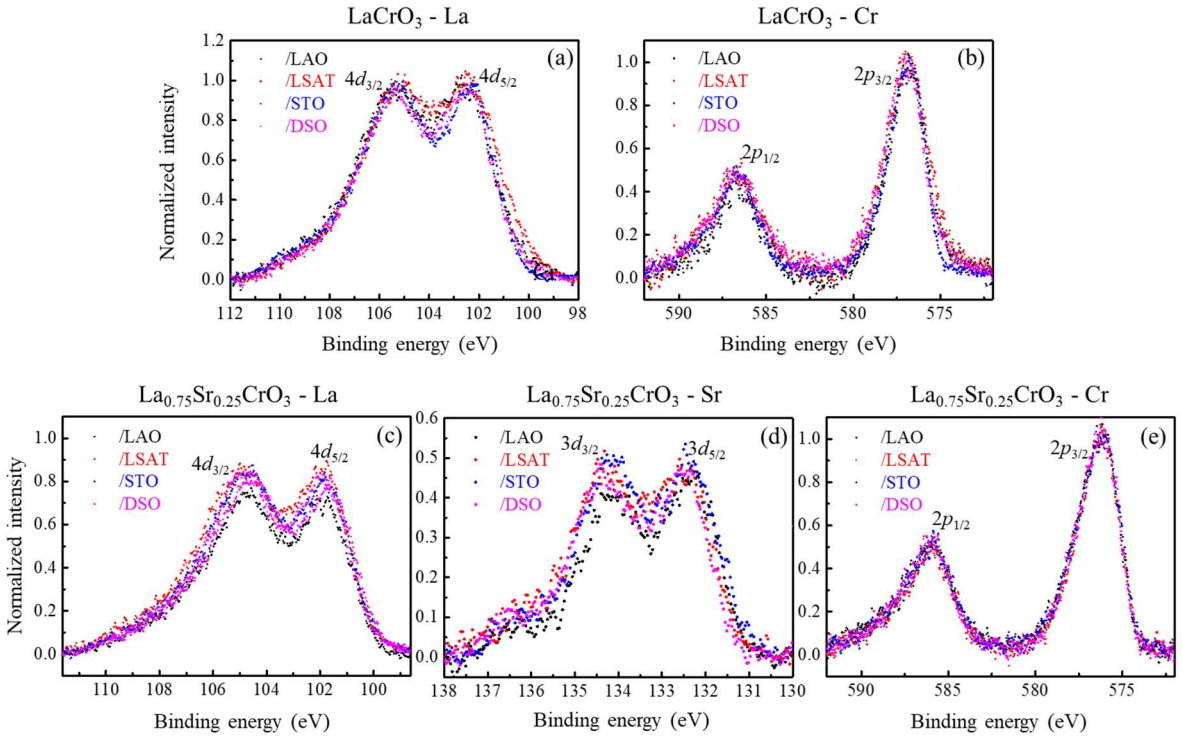

Figure 4. 9 XPS measurements of (a) La 4*d* and (b) Cr 2*p* core level for all LCO films, as well as (c) La 4*d*, (d) Sr 3*d*, and (e) Cr 2*p* core level for all LSCO films.

Table 4. 2 Chemical compositions measured by XPS in the surface region of LCO and LSCO films.

Chemical composition	$LaCrO_3$				$La_{0.75}Sr_{0.25}CrO_3$			
	/LAO	/LSAT	/STO	/DSO	/LAO	/LSAT	/STO	/DSO
[A/(A+B)] (at%)	54.1	54.0	50.0	50.8	49.8	56.2	54.5	52.9
[Sr/(Sr+La)] (at%)	0.0	0.0	0.0	0.0	23.8	24.8	24.5	26.0

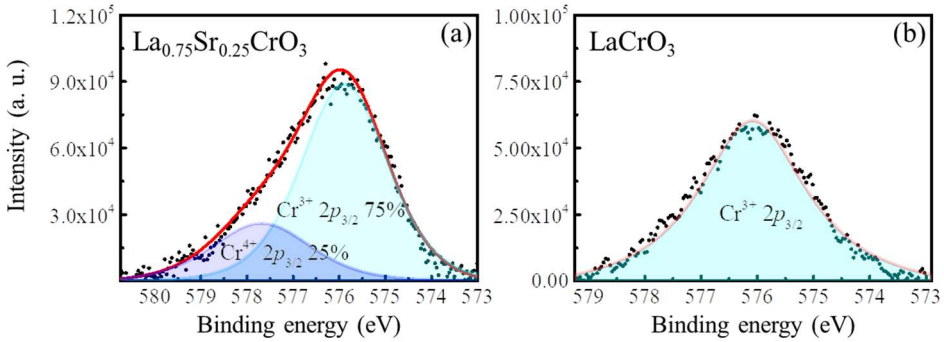

Figure 4. 10 Fit results of the Cr $2p_{3/2}$ line for (a) LSCO and (b) LCO films.

4.2.3. Tuning lattice strain: determination of Poisson ratio and bulk lattice parameter

4.2.3.1. In LCO

The structural and elastic properties of LCO films are investigated by XRD. Wide $2\theta/\omega$ scans from 10° to 80°, shown in Figure 4. 11, reveal only diffraction peaks corresponding to the {00*l*} reflections of the LCO films and substrates, indicating that no other orientation nor other phases than LCO(00*l*) are present in the epitaxial films.

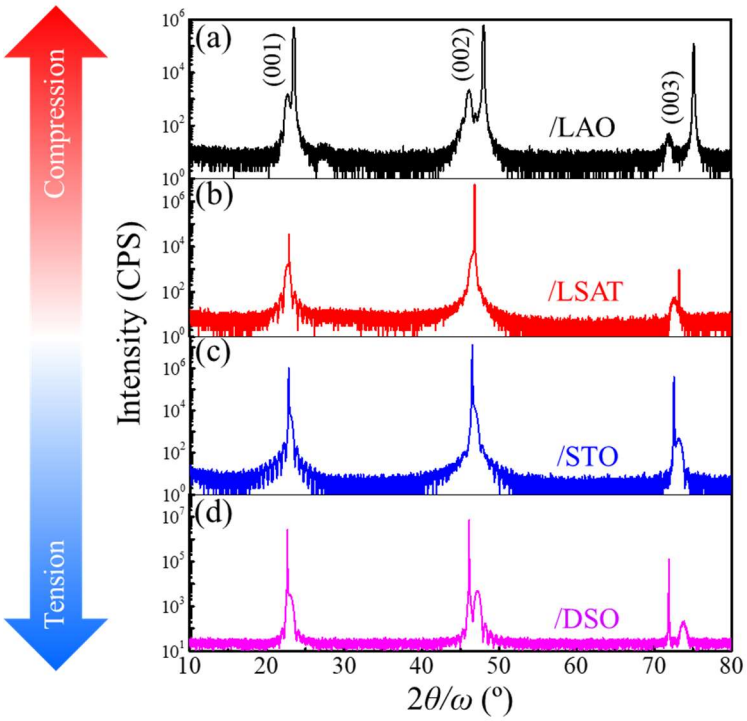

Figure 4. 11 XRD characterizations. $2\theta/\omega$ scans from 10º to 80º on LCO films grown on different substrates.

Figure 4. 12a-d show the XRD $2\theta/\omega$ scans around the (002) reflections of LCO films and their corresponding substrates in reciprocal space units. The presence of Pendellosung fringes around the diffraction peaks of films attests to their high-crystalline quality and abrupt interfaces. The out-of-plane lattice parameter of the LCO films (c_{LCO}) decreases with increasing substrate lattice constant, as expected due to increasing in-plane strain, which is ruled by elasticity Hooke's law with positive Poisson ratio [28]. The c_{LCO} values are 3.951 Å, 3.891 Å, 3.883 Å, and 3.853 Å for LCO films on LAO, LSAT, STO, and DSO substrates, respectively.

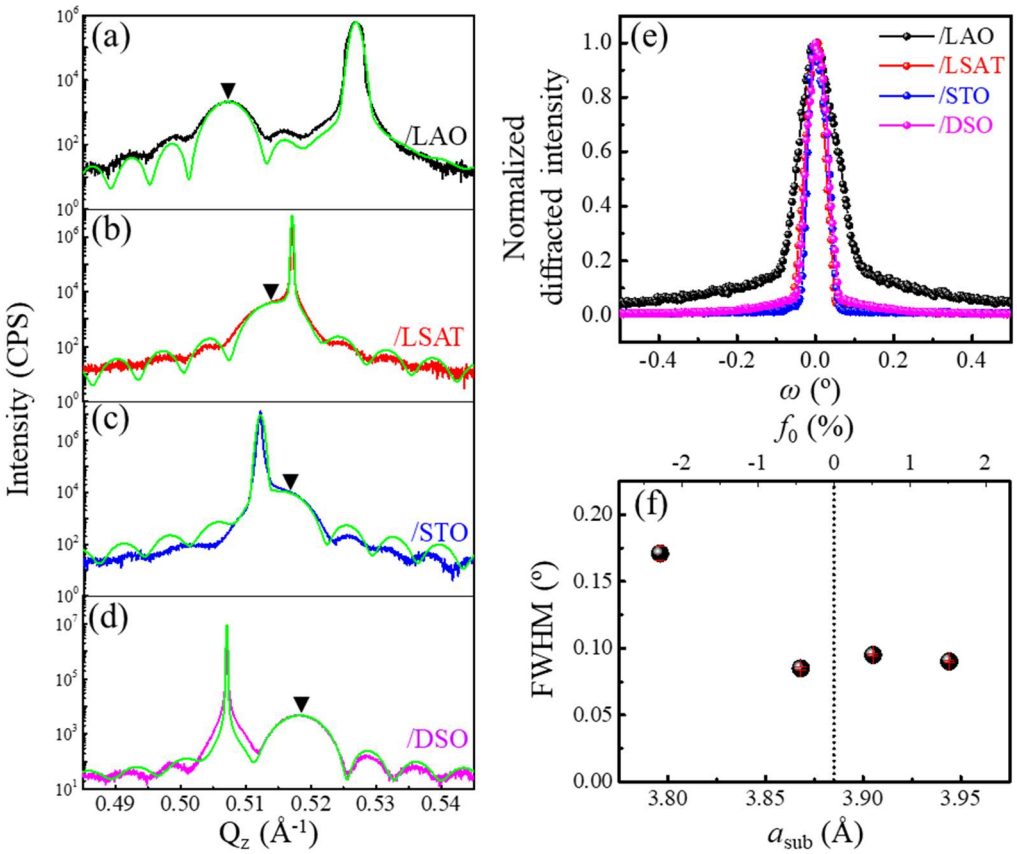

Figure 4. 12 XRD $2\theta/\omega$ scans near the (002) reflections on LCO films grown on (a) LAO, (b) LSAT, (c) STO, and (d) DSO with corresponding fitting curves. The position of LCO(002) is marked by a black inverted triangle. (e) Normalized XRD ω-scans around the LCO(002) reflection for all films. (f) Mosaicity values as a function of the lattice constant of the substrate used.

The ω-scans measured for all the films around the LCO(002) reflection are shown in Figure 4. 12e. Figure 4. 12f shows the mosaicity (full width at half maximum, FWHM, of the curves in Figure 4. 12e) which is below 0.1° for all films, except for LCO on LAO for which the mosaicity is slighter larger about 0.17°, indicating high structural quality. For the LCO film grown on the LAO substrate, the slightly larger mosaicity is probably partially because of the relatively poor crystalline quality of the substrate, the largest compressive in-plane stress, and partial plastic relaxation (see following Figure 4. 13a).

The in-plane parameters of the LCO thin films (a_{LCO}) are measured by RSM around the asymmetrical (103) reflections (shown in Figure 4. 13). This RSM besides confirm the tendency extracted from Figure 4. 12a-d for the out-of-plane lattice parameter. The main intensity of the LCO(103) nodes are completely aligned vertically with that of the substrates, indicating that the a_{LCO} is equal to that of the substrate, and thus that the films are fully strained by the substrates. However, for the LCO films on LAO substrate, the node

asymmetry attests for the beginning of partial strain relaxation, but still far to reach its bulk value. This beginning of partial relaxation of LCO on LAO is most probably due to a large lattice mismatch (-2.29%, the largest lattice mismatch of the series, see Table 4. 3) [29].

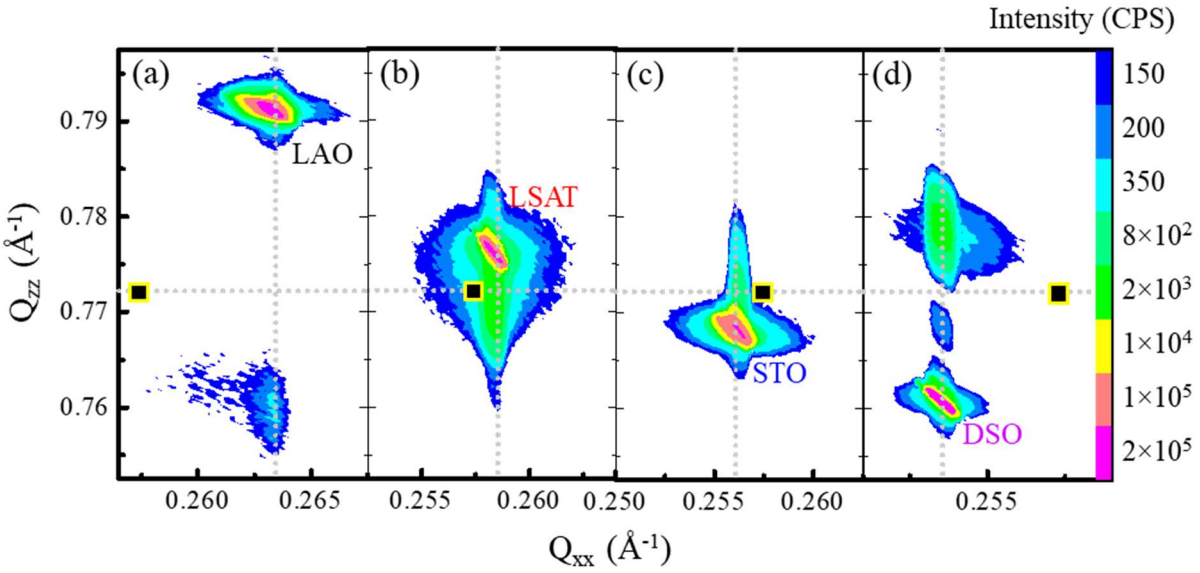

Figure 4. 13 RSM recorded around the asymmetric (103) reflection of LCO thin films on (a) LAO, (b) LSAT, (c) STO, and (d) DSO substrates. The vertical dotted lines indicate the Q_{xx} position of the (103) reflection of the substrates. The squares on the horizontal dotted line indicate the position of bulk LCO (relaxed films), considering however the low thermal expansion mismatch between the substrates and the films (inducing a slight thermal strain from the substrate during the cooling down from growth temperature to room temperature) [30, 31].

Table 4. 3 Summary of the structural and chemical properties of the LCO thin films.

Substrate	Lattice mismatch (%)	Thickness (nm)	[A/(A+B)] (at%)	*a* (Å)	*c* (Å)	Mosaicity (°)	Substrate roughness (nm)	Film roughness (nm)
LAO	-2.29	16.6	54.1	3.796	3.951	0.17	0.15	0.63
LSAT	-0.44	14.5	54.0	3.868	3.891	0.08	0.15	0.61
STO	0.51	13.7	50.0	3.905	3.883	0.10	0.15	0.54
DSO	1.52	13.8	50.8	3.944	3.853	0.09	0.15	0.62

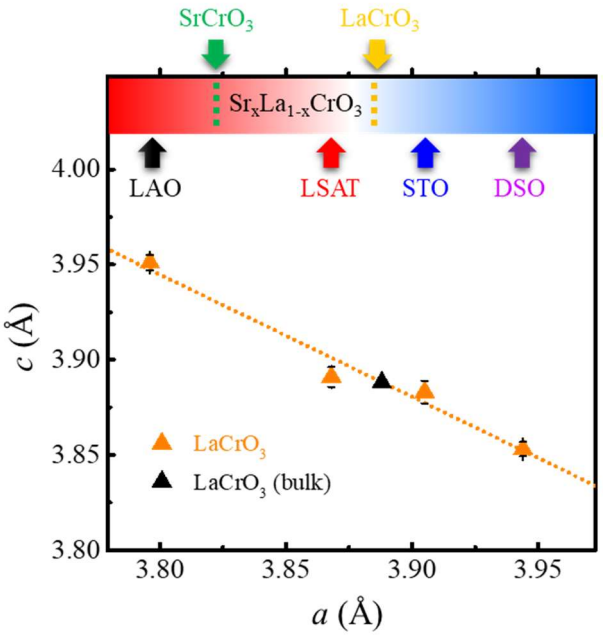

Figure 4. 14 Out-of-plane lattice parameter *c* as a function of in-plane lattice parameter *a* for LCO epitaxial films (orange triangles) on the four different substrates. The dotted line represents the fit from a linear regression. The black triangle represents the lattice constant of bulk LCO derived from our fit, in very good agreement with the literature [32, 34].

The dependence of the out-of-plane lattice parameters (c) to the in-plane lattice parameter (a) is shown for LCO films in Figure 4. 14. The $c(a)$ function is linear as expected from the elastic strain of pseudocubic LCO, and it can be fitted using the equation:

$$c = -\frac{2\nu}{1-\nu}a + \frac{1+\nu}{1-\nu}a_{\text{bulk}} \tag{4.3}$$

The measured Poisson ratio (ν = 0.24) and bulk lattice constant of LCO (a_{bulk} = 3.888 Å) are extracted from such fit, which leads to elastic and structural parameters very similar to those found in the literature (ν = 0.23 and a_{bulk} = 3.885 Å) [33, 34], further confirming the validity of this method.

Figure 4. 15 shows a summary of the structural properties (lattice parameters and associated strains) of the epitaxial LCO films as a function of the substrate lattice constants and the structural mismatch (f_0). The out-of-plane strain (ε_{zz}) is inversely equal to the in-plane strain (ε_{xx}), consistently with the measured ν value (Figure 4. 15a and b). The LCO thin films can endure a relatively large strain up to 2% and can present relatively large (pseudo)tetragonality (c/a) up to 1.04 (Figure 4. 15c). The unit-cell volume is found to be in-between 57 and 60 Å^3 ($V_{\text{b-LCO}}$ = 58.637 Å^3) and the relative volume change vary also in the

2.5% range (Figure 4. 15d). Film density is found around 6.78 g·cm^{-3} (in a standard range from 6.44 to 6.76 g·cm^{-3} due to the transition of the perovskite phase in the literature). Hence, the same method is applied to epitaxial LSCO film that would have a great impact on the physical properties which is barely unexplored to date.

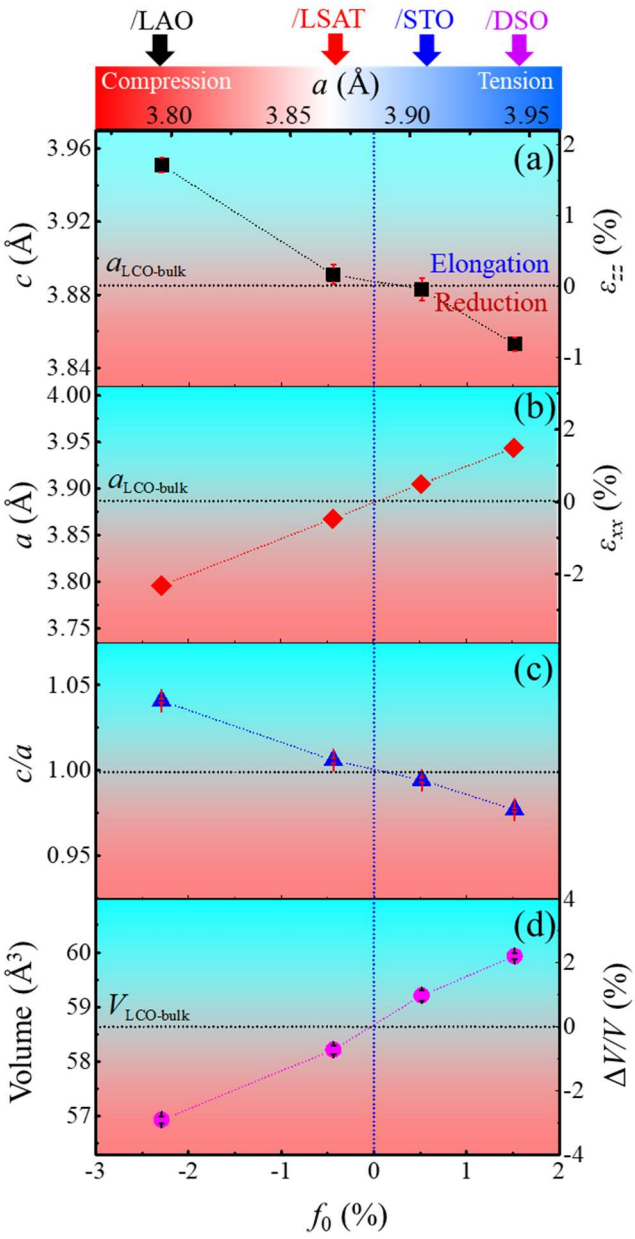

Figure 4. 15 Summary of the structural properties of LCO films as a function of the substrate lattice constant and the structural mismatch f_0. (a) Out-of-plane lattice parameter c and out-of-plane strain ε_{zz}. (b) In-plane lattice parameter a and in-plane strain ε_{xx}. (c) The tetragonality c/a. (d) The unit-cell volume and the relative volume change $\Delta V/V$.

4.2.3.2. In LSCO

Structural and elastic properties of LSCO films epitaxially strained on the different perovskite oxide substrates are now presented. The structural and elastic properties of LCO films are investigated by XRD.

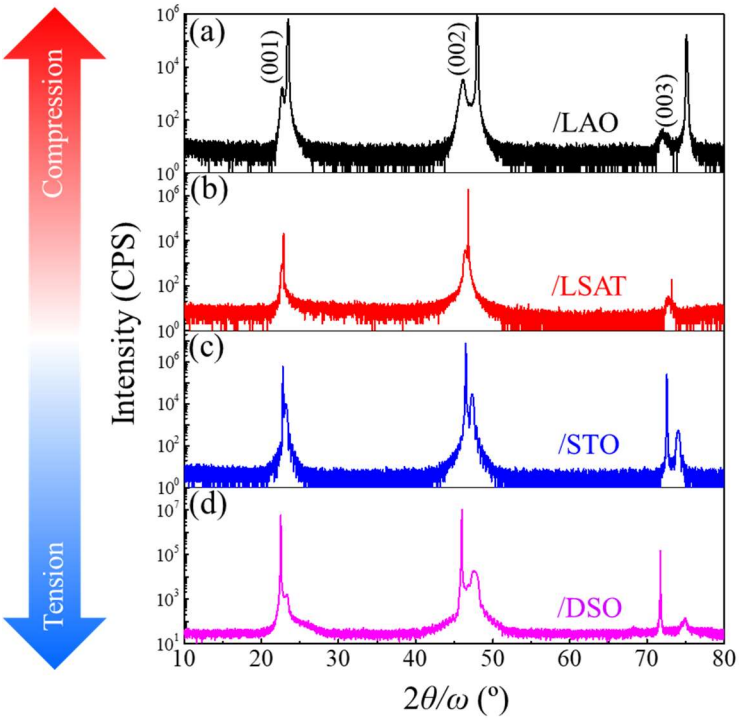

Figure 4. 16 XRD characterizations. $2\theta/\omega$ scans from 10° to 80° on LSCO films grown on different substrates.

Wide $2\theta/\omega$ scans (10°-80°, shown in Figure 4. 16a-d) reveal only diffraction peaks corresponding to the {00*l*} reflections of the LSCO films and substrates, indicating that no other orientation nor other phases than LSCO(00*l*) are present in the epitaxial films. Besides, the half XRD pole figure (Figure 4. 17) performed on the LSCO film on LAO (the largest lattice mismatch -2.06%) does not reveal any secondary crystalline phase neither other orientation.

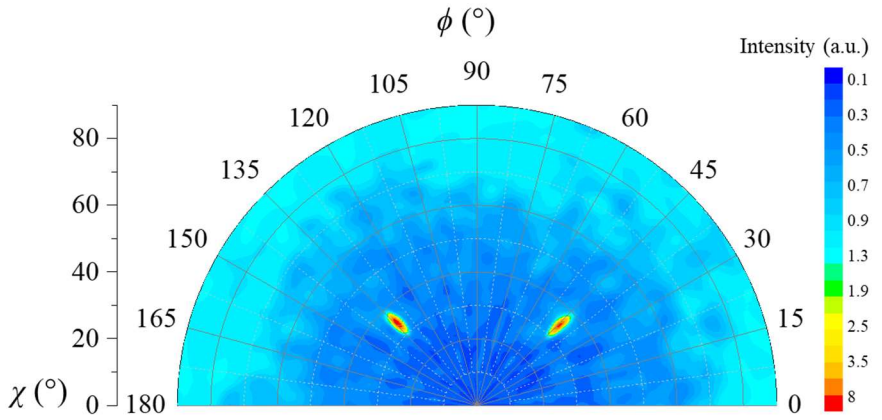

Figure 4. 17 Half XRD pole figure of the (111) reflection of LSCO film on LAO substrate ($2\theta = 40.628°$).

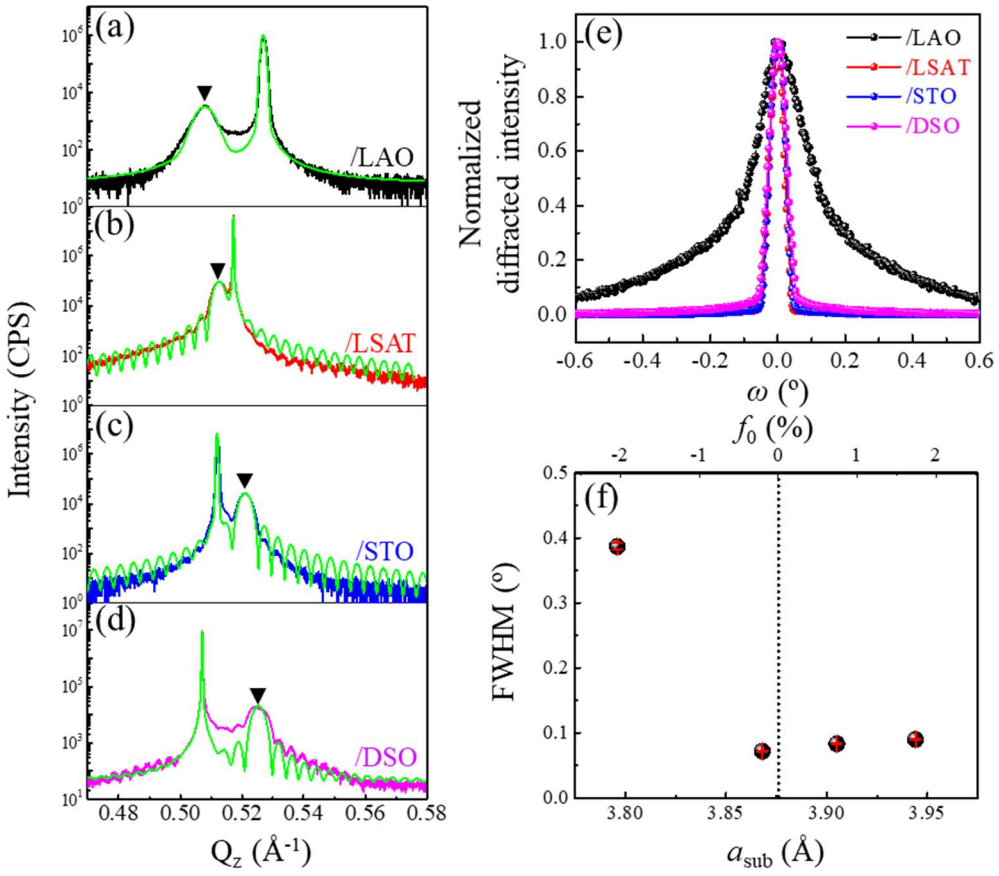

Figure 4. 18 XRD $2\theta/\omega$ scans near the (002) reflections on LSCO films grown on (a) LAO, (b) LSAT, (c) STO, and (d) DSO substrates with corresponding fitting curves. The position of LSCO(002) is marked by a black inverted triangle. (e) Normalized XRD ω-scans around the LSCO (002) reflection for all films. (f) Mosaicity values as a function of the lattice constant of the substrate used. Taken from Ref. 1.

Figure 4. 18a-d show the XRD results around the LSCO(002) reflections and their corresponding substrates. The out-of-plane lattice parameter of the LSCO films (c_{LSCO}) decreases with increasing substrate lattice constant, as expected due to the increasing in-plane

strain. As observed for LCO films, this is ruled by elasticity Hooke's law with a positive Poisson ratio [28]. The c_{LSCO} values are 3.943 Å, 3.904 Å, 3.844 Å, and 3.804 Å for LSCO films on LAO, LSAT, STO, and DSO substrates, respectively. Although the films are of similar thickness (~30 nm), the (002) peaks of LSCO films on LAO and DSO are wider than those of LSCO films on LSAT and STO with lower lattice mismatch, indicating a wider distribution of out-of-plane lattice parameter. Most probably, a beginning of strain relaxation occurs at this thickness with such a large lattice mismatch. For the LSCO film on DSO, two close secondary maxima seem to be visible, indicating the presence of two main out-of-plane parameters (3.795 Å and 3.815 Å), but both being much lower than the expected/measured bulk value (3.876 Å, see Figure 4. 21a below). A single fit with the main component leads to a mean out-of-plane parameter of 3.804 Å (Figure 4. 18d) in perfect agreement within the instrumental resolution with the maximum of the (103) node in the following RSM (Figure 4. 20d) corresponding to fully strained component.

The ω-scans measured for all the films around the LSCO(002) reflection are shown in Figure 4. 18e. The mosaicity (FWHM of these curves) is below 0.1° for all films except for LSCO on LAO, indicating high structural quality (Figure 4. 18f). For the LSCO film grown on the LAO substrate, the mosaicity is larger although relatively low of about 0.38°. Like that of the LCO/LAO film, the larger mosaicity is certainly because of the poor substrate crystalline quality, as observed in $2\theta/\omega$ scans (larger substrate peak) and ω-scans on (002) substrate reflection (substrate mosaicity being large and similar to that of the film, see Figure 4. 19). On this substrate, the in-plane (compressive) stress being the largest, from largest lattice mismatch, and partial plastic relaxation with 3D morphology (Figure 4. 20a) can also contribute to increasing the film mosaicity.

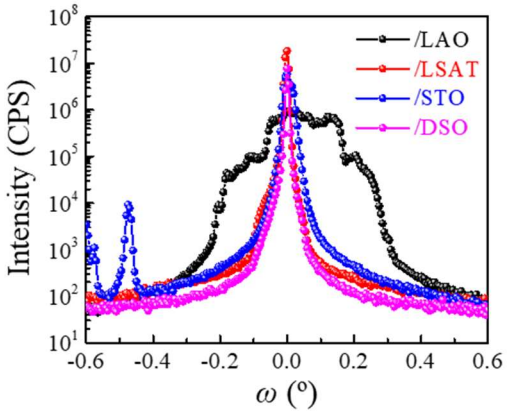

Figure 4. 19 XRD ω-scans around the (002) reflection of the substrates.

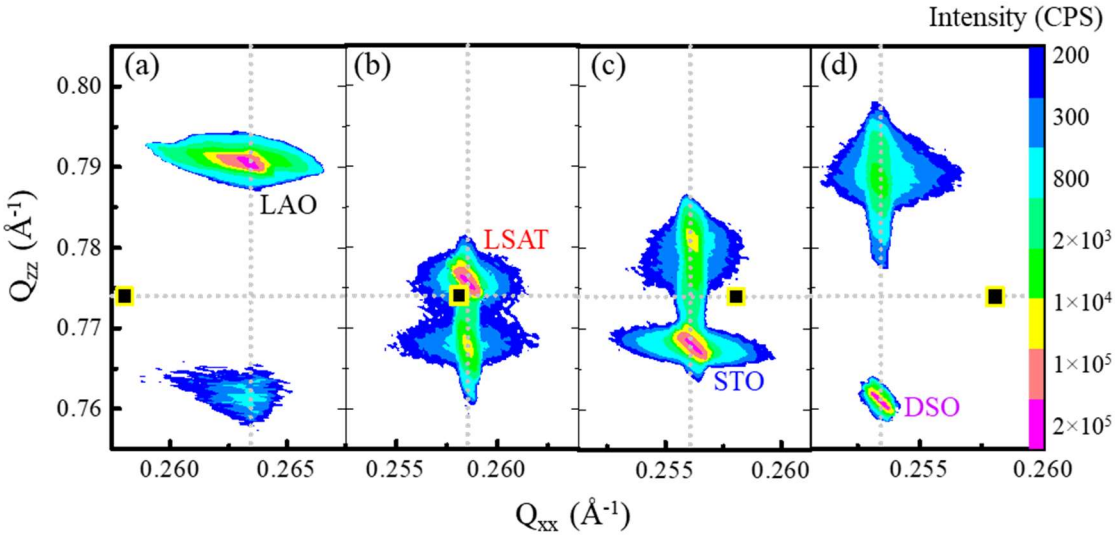

Figure 4. 20 RSM recorded around the asymmetric (103) reflections of LSCO thin films on (a) LAO, (b) LSAT, (c) STO, and (d) DSO substrates. The vertical dotted lines indicate the Q_{xx} position of the (103) reflection of the substrates. The squares on the horizontal dotted line indicate the position of bulk LSCO (relaxed films) extracted in this work.

The RSM around the asymmetrical (103) reflections of the LSCO films are shown in Figure 4. 20, which confirms the out-of-plane lattice parameter variation extracted from Figure 4. 16a-d. For all the films the main intensity of the LSCO(103) node is aligned vertically with that of the substrates, indicating that the main in-plane lattice parameter of the LSCO thin films (a_{LSCO}) is identical to that of the corresponding substrates. However, as observed with the epitaxial LCO thin film on LAO (Figure 4. 13a), for the LSCO film on the LAO substrate, the (103) node asymmetry also attests for the beginning of a partial strain relaxation, which is most probably due to a larger lattice mismatch (-2.06%) on this substrate [29]. Looking into more details, the (103) nodes of the LSCO films on DSO are also slightly asymmetric, indicating also a beginning of a partial strain relaxation because of large tensile strain (+1.75 %). The asymmetry broadening for these two films with the largest mismatches (on LAO and DSO) is elongated towards a slightly different position than the bulk position. Although low, thermal expansion mismatch between the film and substrates can mitigate this discrepancy, as in the case of LCO films [30, 31]. The remaining difference could be caused by slight cationic segregations, as observed with other Cr-based oxides but with spinel structure [35]. In the following, the Poisson ratio and bulk lattice constant of LSCO is derived from the fully strained part of the films.

The dependence of the out-of-plane to the in-plane lattice parameter is shown in Figure 4. 21a for LSCO films, together with LCO films as reference. The $c(a)$ function is linear as expected from the elastic strain of pseudocubic LSCO, and it is fitted with linear regression

using equation (4.7). The Poisson ratio (v = 0.32 ± 0.02), as well as the bulk lattice constant (a_{bulk} = 3.876 Å) and C_{12}/C_{11} ≈ 0.5 of LSCO, are extracted from such fit. We showed previously that such method and $c(a)$ fit applied to LCO films (Figure 4. 14) have confirmed the LCO bulk values found in literature: the measured v = 0.24 versus 0.23, and a_{bulk} = 3.888 Å versus 3.885 Å [33, 34]. These results on LSCO films show that 25% of the Sr substitution ratio significantly increases the v by more than 30% concerning LCO. This change might also be related to the change in Cr valence state in addition to the Sr/La substitution. To well discriminate the cause, other LSCO films with a lower oxidation state would have to be elaborated to get the same Cr valence as in LCO films. Figure 4. 21b indicates that the bulk lattice constant of LSCO ($a_{b\text{-}LSCO}$ = 3.876 Å) is linearly in-between that of LCO ($a_{b\text{-}LCO}$ = 3.885 Å) [34] and $SrCrO_3$ (SCO) ($a_{b\text{-}SCO}$ = 3.819 Å) [36, 37], which is expected from a Vegard's law and is in agreement with the literature [38]. The $a_{b\text{-}LSCO}$ is thus in-between of that of LSAT and STO substrates (closer to LSAT whose lattice constant is 3.868 Å) and reveals that the LSCO film with the lowest epitaxial strain is the one grown on LSAT substrate.

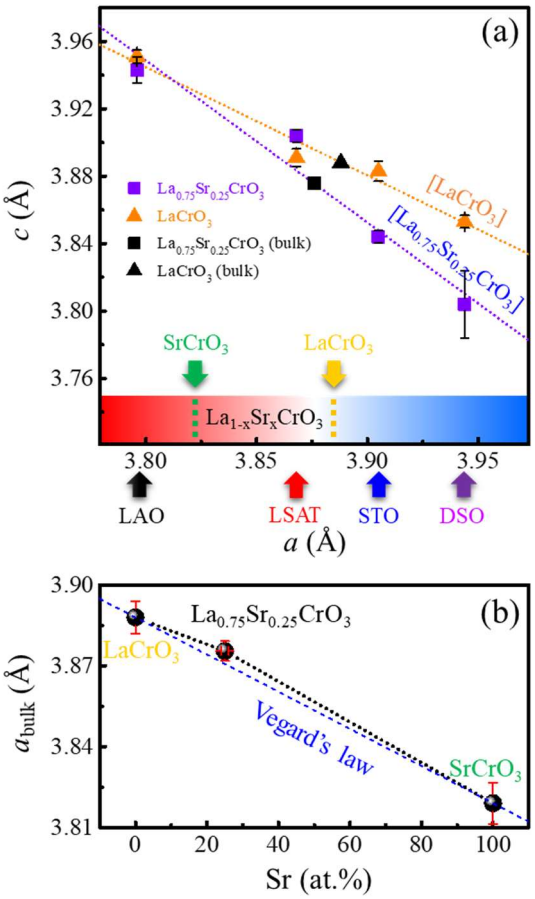

Figure 4. 21 (a) c as a function of a for both LSCO (violet squares) and LCO (orange triangles) epitaxial films on the four different substrates. The dotted lines represent the fits from linear regression in both cases. The black square and triangle represent the bulk lattice constants of both LSCO and LCO derived from these fits. (b) Bulk $La_{1-x}Sr_xCrO_3$ lattice constant as a function of the A-site Sr/(La+Sr) substitution ratio (x).

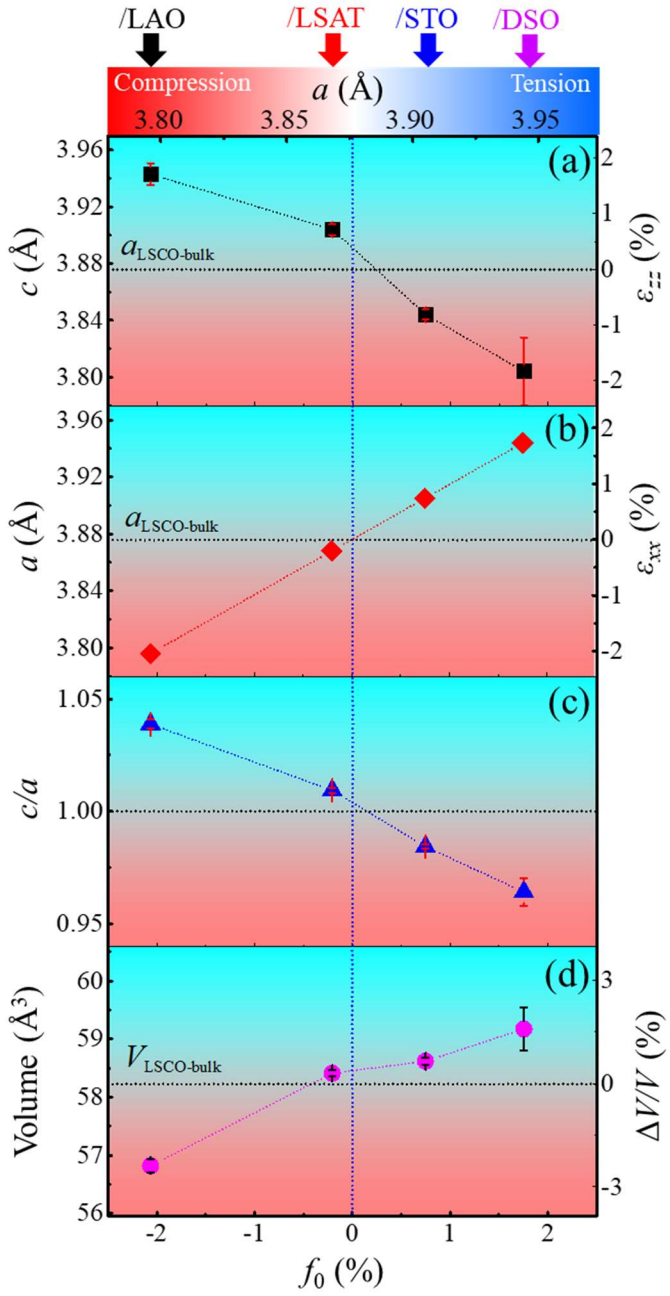

Figure 4. 22 Summary of the structural properties of LSCO films as a function of the lattice constant of the used substrates and the structural mismatch f_0. (a) Out-of-plane lattice parameter c and out-of-plane strain ε_{zz}. (b) In-plane lattice parameter a and in-plane strain ε_{xx}. (c) The (pseudo)tetragonality c/a. (d) The unit-cell volume and the relative volume change $\Delta V/V$. Taken from Ref. 1.

Figure 4. 22 shows a summary of the structural properties of the epitaxial LSCO films as a function of the a_{sub} and the f_0. The ε_{zz} is inversely equal to the ε_{xx}, consistently with the measured ν value (Figure 4. 22a and b). For $\nu = 1/3$, $\varepsilon_{zz} = -\varepsilon_{xx}$. The LSCO epitaxial thin films can endure a relatively large strain up to 2% and can present relatively large (pseudo)tetragonality (c/a) almost up to 1.05, shown in Figure 4. 22c, much more important

than bulk tetragonal ferroelectric $BaTiO_3$ film (c/a = 1.01) for instance. The unit-cell volume is found to be in-between 57 and 59 Å^3 ($V_{b\text{-}LSCO}$ = 58.231 Å^3) and the relative volume change vary also in the 2% range (Figure 4. 22d). Film density is found around 6.45 g·cm^{-3} for all films consistently with the bulk density. All the (micro)structural properties of the LSCO films are finally summarized in Table 4. 4. With these elastic properties, the epitaxial strain could thus have a great impact on the physical properties of LSCO films which have not been studied so far (see next section 4.2.4).

Table 4. 4 Summary of the structural and chemical properties of the LSCO thin films.

Substrate	Lattice mismatch (%)	Thickness (nm)	[A/(A+B)] (at.%)	[Sr] (at.%)	a (Å)	c (Å)	Mosaicity (°)	Substrate roughness (nm)	Film roughness (nm)
LAO	-2.06	27.2	49.8	23.8	3.796	3.943	0.38	0.15	0.72
LSAT	-0.21	29.9	56.2	24.8	3.868	3.904	0.07	0.15	0.58
STO	0.75	28.2	54.5	24.5	3.905	3.844	0.08	0.15	0.54
DSO	1.75	29.0	52.9	26.0	3.944	3.804	0.09	0.15	0.49

4.2.4. Tuning the electronic and thermoelectric properties of $La_{0.75}Sr_{0.25}CrO_3$

The electronic transport and thermoelectric properties of these strained LSCO films were measured in-plane by Hall effect and Seebeck coefficient measurements (see Chapter II). The corresponding results of these electronic transport and thermoelectric properties at room temperature are shown as a function of f_0 in Figure 4. 23. Based on these measurements, all the samples exhibit *p*-type conductivity, as expected.

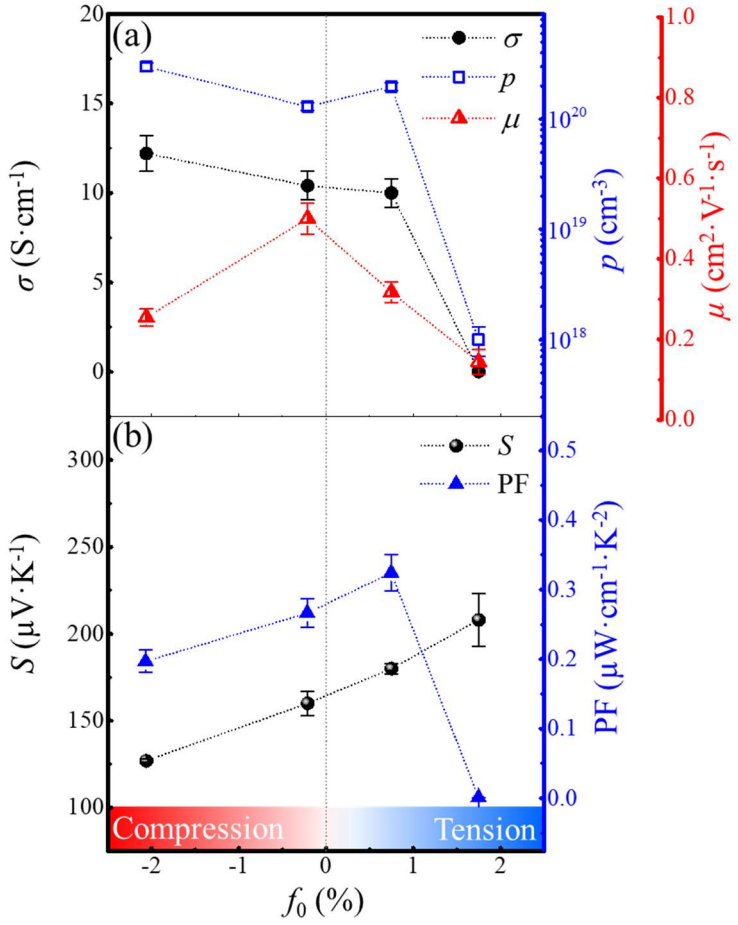

Figure 4. 23 Room-temperature (a) electrical conductivity σ, hole carrier concentration p, and mobility μ of LSCO films on different substrates obtained from Hall Effect measurements, as well as (b) measured Seebeck coefficient S, and thermoelectric power factor PF as a function of lattice mismatch f_0 (*i.e.* in-plane strain). Taken from Ref. 2.

Figure 4. 23a presents the variation of measured σ, hole carrier concentration (p), and hole mobility (μ) of LSCO films with different epitaxial strain values. σ varies with strain by three orders of magnitude, with values ranging from 0.02 to 12.2 S·cm^{-1}, and in particular decreases noticeably for large in-plane tensile strain. On the STO substrate, σ is around 10 S·cm^{-1}, which is in perfect agreement with previous results reported by the Chambers' group [39]. The measured p of the LSCO film grown on the STO substrate is about 2×10^{20} cm^{-3}, whereas it has been estimated by a small polaron hopping model by the Chambers' group to be one order of magnitude higher (around 4×10^{21} cm^{-3}) [39]. The measured p of LSCO films is consistent with the variation of σ, showing that the reduction of the conductivity is related to a reduction of the charge carrier concentration. Similarly, Vailionis *et al.* [23] studied the effect of strain on the resistivity (ρ) of $SrRuO_3$ and $CaRuO_3$ perovskite films grown on different substrates. They observed that the thin films under large in-plane tensile strain have larger ρ

than their less strained or compressively-strained counterparts. Confirming the tendency, the same trend has also been observed in $LaNiO_3$ thin films [40, 41]. May *et al*. [42] found that strain systematically modifies both the Ni-O-Ni bond angles and Ni-O lengths in this functional perovskite oxide, which has a strong effect on its transport properties. The strain can strongly bend/shift the bands [43], yielding anisotropic band structures in anisotropically strained films. Such a strain must affect the density of activated charge carriers and thus the global electrical conductivity. Indeed, consistently with our observations, high-pressure studies on other thermoelectric materials in the few GPa range show that compressive strain tends to enhance the free-charge carrier concentration by reducing the bandgap [44]. Furthermore, as *n*-type La-doped STO films [18], the other possible reasons for the difference of activated hole concentration of LSCO at a relative high substitution ratio (25%) includes charge self-compensation [45], surface depletion layers [46], and the presence of a small number of residual oxygen vacancies leading to *n*-type charge carriers [47]. Indeed, the tetragonality is strongly linked with oxygen vacancies created along the elongation direction, as in $SrTiO_3$ in which the Ti-O-Ti bonds are longer when oxygen vacancies are present [48, 49, 50]. In-plane organization of oxygen vacancies created along the tensile strain could lead to a reduction of the *p*-type conductivity by compensation of *n*-type carriers preferentially activated in that in-plane direction from anisotropic band structure. The μ was deduced from the equation: $\mu = \sigma/pe$, where e is the hole electric charge (1.6×10^{-19} eV). The μ decreases with absolute strain, as already reported for *n*-type La-doped STO epitaxial films [18]. The μ value of LSCO films is found to be between 0.1 and 0.5 $cm^2\cdot V^{-1}\cdot s^{-1}$ at room temperature depending on the absolute strain, which is one order of magnitude higher than those estimated by the Chambers' group from the small polaron hopping model [39]. For other comparisons, it is roughly about one order of magnitude lower than *n*-type La-doped STO epitaxial films [18, 51, 52], and three orders of magnitude lower than high-mobility *n*-type La-doped $BaSnO_3$ epitaxial films [53, 54, 55], or *p*-type doped GaAs-based III-V semiconductors [56]. It is worth noting that the μ is often lower, up to two orders of magnitude than the electron mobility for the same core semiconductor materials, as in ZnO [57, 58] or GaAs [59] for instance.

Figure 4. 23b displays the Seebeck coefficient (S) and thermoelectric power factor ($PF = S^2\sigma$) as a function of strain at room temperature. The positive S for all samples (marked by black circles) confirms that holes are the dominant free charge carriers in these films. It is worth noting again that for the LSCO/STO film, S is found to be 180 $\mu V\cdot K^{-1}$, which is in perfect agreement with the most recent results of the Chambers' group (See also Chapter III)

[39]. The *S* increases monotonously with in-plane strain from 127 (compressive) to 208 $\mu V \cdot K^{-1}$ (tensile), consistently with other observations made on various thermoelectric materials under high-pressures (decreasing *S* with pressure) [44], and as recently reported by Kan *et al*. on $SrRuO_3$ epitaxial films in which both in-plane resistivity (ρ) and *S* of the compressively-strained $SrRuO_3$ film are lower than those of the tensely-strained film [25].

The corresponding thermoelectric power factor (PF, calculated for each film according to the equation $PF = S^2\sigma$) slightly increases from clear in-plane compressive strain to moderate in-plane tensile strain, and abruptly drops at a larger tensile strain, driven by the electrical conductivity. Interestingly, the PF of LSCO/STO (+0.75% of in-plane tensile strain) is slightly higher (0.32 $\mu W \cdot cm^{-1} \cdot K^{-2}$) than that of the film on LSAT (-0.21% of in-plane compressive strain, 0.27 $\mu W \cdot cm^{-1} \cdot K^{-2}$), meaning that a slight in-plane tensile strain can enhance the PF value, though a larger absolute strain decreases it. However, although large tensile strain on LSCO/DSO decreases the PF value (associated with the conductivity drop), it yields the highest thermopower *S*.

4.3. Conclusion

In this chapter, high-crystalline quality thin films of $LaCrO_3$ (LCO) and $La_{0.75}Sr_{0.25}CrO_3$ (LSCO) were epitaxially grown by MBE on four different (001)-oriented (pseudo)cubic perovskite-oxide substrates: LAO, LSAT, STO, and DSO, resulting in different compressive and tensile strain from -2.29% to +1.52% (for LCO films) and from -2.06% to +1.75% (for LSCO films). All the films crystallize in the perovskite structure, are fully (001)-oriented, flat, and epitaxially strained. The out-of-plane of LCO and LSCO films widely vary from 3.951 to 3.853 Å, and from 3.943 to 3.804 Å, respectively. The Poisson ratio and the bulk lattice constant of LCO are firstly extracted from these measurements (ν = 0.24 and a_b = 3.888 Å), which are very similar to the values found in the literature [33, 34]. Then, the elastic properties of LSCO are investigated via the same method (ν = 0.32 and a_b = 3.876 Å), which significantly differs from that of LCO. The LSCO solid solutions appear to obey structural Vegard's law and the relatively large Poisson ratio enables flexible tuning of its physical properties by elastic epitaxial strain.

Indeed, electronic transport and thermoelectric properties of the strained LSCO films have been investigated and have shown substantial strain-depend trends/values. Room-temperature electrical conductivity ranging from 0.02 to 12.2 $S \cdot cm^{-1}$ and hole mobility

ranging from 0.08 to 0.5 $cm^2 \cdot V^{-1} \cdot s^{-1}$ is measured depending on the in-plane strain. Thanks to the evolution from compressively-strained film to tensely-strained film, the measured Seebeck coefficient increases from 127 to 208 $\mu V \cdot K^{-1}$. Both the thermoelectric power factor and mobility of less strained LSCO films are found to be higher than that of more strained films regardless of the sign of strain. These observations indicate that the epitaxial in-plane strain can effectively modify the room-temperature transport properties and the Seebeck coefficient of LCO-based *p*-type conductive layers, affecting their thermoelectric properties. These results are of importance as they provide indispensable basic information on the structural and physical properties of material presenting strong applicative potential. Besides, the method used here to extract the structural and elastic properties from epitaxial layers can be straightforwardly applied to other complex oxides, and the strain-depend transport and thermoelectric properties can inspire further studies on other thermoelectric oxides/materials.

4.4. References

[1] D. Han, M. Bouras, C. Botella, A. Benamrouche, B. Canut, G. Grenet, G. Saint-Girons, and R. Bachelet. Poisson ratio and bulk lattice constant of $(Sr_{0.25}La_{0.75})CrO_3$ from strained epitaxial thin films. Journal of Applied Physics, 2019, 126(8): 085304.

[2] D. Han, M. Bouras, C. Botella, A. Benamrouche, B. Canut, G. Grenet, G. Saint-Girons, and R. Bachelet. Tuning of thermoelectric power factor in *p*-type Sr-doped $LaCrO_3$ thin films by epitaxial strain. Submitted to ACS Applied Electronic Materials, 2020.

[3] D. G. Schlom, L. Q. Chen, C. B. Eom, K. M. Rabe, S. K. Streiffer, and J. M. Triscone. Strain tuning of ferroelectric thin films. Annual Review of Materials Research, 2007, 37: 589-626.

[4] A. Biswas and Y. H. Jeong. *Strain effect in epitaxial oxide heterostructures*. In Epitaxy. IntechOpen, 2017.

[5] J. Narayan and B. C. Larson. Domain epitaxy: A unified paradigm for thin film growth. Journal of Applied Physics, 2003, 93(1): 278-285.

[6] D. G. Schlom, L. Q. Chen, C. J. Fennie, V. Gopalan, D. A. Muller, X. Pan, R. Ramesh, and R. Uecker. Elastic strain engineering of ferroic oxides. MRS Bulletin, 2014, 39(2): 118-130.

[7] A. R. Damodaran, J. C. Agar, S. Pandya, Z. Chen, L. Dedon, R. Xu, B. Apgar, S. Saremi, and L. W. Martin. New modalities of strain-control of ferroelectric thin films. Journal of Physics: Condensed Matter, 2016, 28(26): 263001.

[8] Y. Yang, I. C. Infante, B. Dkhil, and L. Bellaiche. Strain effect on multiferroic $BiFeO_3$ films. Comptes Rendus Physique, 2015, 16(2): 193-203.

[9] R. Ramesh. Complex functional oxide heterostructures. Current Science, 2013, 105(8): 1107.

[10] J. Ravichandran. Thermoelectric and thermal transport properties of complex oxide thin films, hetero-structures and superlattices. Journal of Materials Research, 2017, 32(1): 183-203.

[11] J. H. Haeni, P. Irvin, W. Chang, R. Uecker, P. Reiche, Y. L. Li, S. Choudhury, W. Tian, M. E. Hawley, B. Craigo, A. K. Tagantsev, X. Q. Pan, S. K. Streiffer, L. Q. Chen, S. W. Kirchoefer, J. Levy, and D. G. Schlom. Room-temperature ferroelectricity in strained $SrTiO_3$. Nature, 2004, 430(7001): 758-761.

[12] J. H. Lee, L. Fang, L. F. E. Vlahos, X. Ke, Y. W. Jung, L. F. Kourkoutis, J. W. Kim, P. J. Ryan, T. Heeg, M. Roeckerath, M. Goian Bernhagen, R. Uecker, P. C. Hammel, K. M. Rabe, S. Kamba, J. Schubert, J. W. Freeland, D. A. Muller, C. J. Fennie, P. Schiffer, V. Gopalan, E. J. Halperin, and D. G. Schlom. A strong ferroelectric ferromagnet created by means of spin-lattice coupling. Nature, 2010, 466(7309): 954-958.

[13] L. Q. Jiang, J. K. Guo, H. B. Liu, M. Zhu, X. Zhou, P. Wu, and C. H. Li. Prediction of lattice constant in cubic perovskites. Journal of Physics and Chemistry of Solids, 2006, 67(7): 1531-1536.

[14] D. G. Schlom, L. Q. Chen, X. Pan, A. Schmehl, and M. A. Zurbuchen. A thin film approach to engineering functionality into oxides. Journal of the American Ceramic Society, 2008, 91(8): 2429-2454.

[15] M. Opel. Spintronic oxide grown by laser-MBE. Journal of Physics D: Applied Physics, 2011, 45(3): 033001.

[16] Z. Chen, Z. Luo, C. Huang, Y. Qi, P. Yang, L. You, C. Hu, T. Wu, J. Wang, C. Gao, T. Sritharan, and L. Chen. Low-symmetry monoclinic phases and polarization rotation path mediated by epitaxial strain in multiferroic $BiFeO_3$ thin films. Advanced Functional Materials, 2011, 21(1): 133-138.

[17] C. Adamo, X. Ke, H. Q. Wang, H. L. Xin, T. Heeg, M. E. Hawley, W. Zander, J. Schubert, P. Schiffer, D. A. Muller, L. Maritato, and D. G. Schlom. Effect of biaxial strain on the electrical and magnetic properties of (001) $La_{0.7}Sr_{0.3}MnO_3$ thin films. Applied Physics Letters, 2009, 95(11): 112504.

[18] M. Choi, A. B. Posadas, C. A. Rodriguez, A. O'Hara, H. Seinige, A. J. Kellock, M. M. Frank, M. Tsoi, S. Zollner, V. Narayanan, and A. A. Demkov. Structural, optical, and electrical properties of strained La-doped $SrTiO_3$ films. Journal of Applied Physics, 2014, 116(4): 043705.

[19] G. Niu, J. Penuelas, L. Largeau, B. Vilquin, J. L. Maurice, C. Botella, G. Hollinger, and G. Saint-Girons. Evidence for the formation of two phases during the growth of $SrTiO_3$ on silicon. Physical Review B, 2011, 83(5): 054105.

[20] K. J. Choi, M. Biegalski, Y. L. Li, A. Sharan, J. Schubert, R. Uecker, P. Reiche, Y. B. Chen, X. Q. Pan, V. Gopalan, L. Q. Chen, D. G. Schlom, and C. B. Eom. Enhancement of ferroelectricity in strained $BaTiO_3$ thin films. Science, 2004, 306(5698): 1005-1009.

[21] R. J. Zeches, M. D. Rossell, J. X. Zhang, A. J. Hatt, Q. He, C. H. Yang, A. Kumar, C. H. Wang, A. Melville, C. Adamo, G. Sheng, Y. H. Chu, J. F. Ihlefeld, R. Erni, C. Ederer, V. Gopalan, L. Q. Chen, D. G. Schlom, N. A. Spaldin, L. W. Martin, and R. Ramesh. A strain-driven morphotropic phase boundary in $BiFeO_3$. Science, 2009, 326(5955): 977-980.

[22] X. Z. Lu and J. M. Rondinelli. Epitaxial-strain-induced polar-to-nonpolar transitions in layered oxides. Nature Materials, 2016, 15(9): 951-955.

[23] A. Vailionis, W. Siemons, and G. Koster. Room temperature epitaxial stabilization of a tetragonal phase in $ARuO_3$ (A = Ca and Sr) thin films. Applied Physics Letters, 2008, 93(5): 051909.

[24] A. Grutter, F. Wong, E. Arenholz, M. Liberati, and Y. Suzuki. Enhanced magnetization in epitaxial $SrRuO_3$ thin films via substrate-induced strain. Journal of Applied Physics, 2010, 107(9): 09E138.

[25] D. Kan and Y. Shimakawa, Strain effect on thermoelectric properties of $SrRuO_3$ epitaxial thin films. Applied Physics Letters, 2019, 115(2): 022403.

[26] D. Han, M. Bouras, C. Botella, A. Benamrouche, B. Canut, G. Grenet, G. Saint-Girons, and R. Bachelet. Structural properties of strained epitaxial $La_{1+\delta}CrO_3$ thin films. Journal of Vacuum Science & Technology A: Vacuum, Surfaces, and Films, 2019, 37(2): 021512.

[27] S. A. Chambers. *Probing Perovskite Interfaces and Superlattices with X-ray Photoemission Spectroscopy*. In Hard X-ray Photoelectron Spectroscopy (HAXPES), edited by J. C. Woicik, Springer, London, 2016.

[28] J. Y. Tsao. *Materials fundamentals of molecular beam epitaxy*. Academic Press, London, 1993.

[29] The out-of-plane and in-plane epitaxial strain (ε_{zz} and ε_{xx}, respectively) due to the lattice mismatch $f = (a_{sub} - a_{film}) / a_{film}$ are defined here as: $\varepsilon_{zz} = (c_{film} - a_{bulk}) / a_{bulk}$ and $\varepsilon_{xx} = (a_{film} - a_{bulk}) / a_{bulk}$, where c_{film} and/or a_{film} is the measured out-of-plane/in-plane lattice parameter of the film, a_{bulk} the bulk lattice constant. The relaxation ratio R is defined here as $(a_{film} - a_{sub}) / (a_{bulk} - a_{sub})$, where a_{sub} is the in-plane parameter of corresponding substrate.

[30] R. Moalla, B. Vilquin, G. Saint-Girons, G. Sebald, N. Baboux, and R. Bachelet. Dramatic effect of thermal expansion mismatch on the structural, dielectric, ferroelectric and pyroelectric properties of low-cost epitaxial PZT films on $SrTiO_3$ and Si. CrystEngComm, 2016, 18(11): 1887-1891.

[31] The thermal expansion coefficients at room temperature of LCO, LAO, LSAT, STO and DSO are 8.5×10^{-6} K^{-1}, 10×10^{-6} K^{-1}, 8.2×10^{-6} K^{-1}, 9×10^{-6} K^{-1}, and 8.4×10^{-6} K^{-1}, respectively.

[32] T. Hashimoto, K. Takagi, K. Tsuda, M. Tanaka, K. Yoshida, H. Tagawa, and M. Dokiya. Determination of the space group of $LaCrO_3$ by convergent‐beam electron diffraction. Journal of the Electrochemical Society, 2000, 147(12): 4408.

[33] S. A. Suvorov and A. P. Shevchik. A heating module equipped with lanthanum chromite-based heaters. Refractories and Industrial ceramics, 2004, 45(3): 196-200.

[34] L. Qiao, T. C. Droubay, M. E. Bowden, V. Shutthanandan, T. C. Kaspar, and S. A. Chambers. $LaCrO_3$ heteroepitaxy on $SrTiO_3$(001) by molecular beam epitaxy. Applied Physics Letters, 2011, 99(6): 061904.

[35] M. D. Scafetta, Z. Yang, S. R. Spurgeon, M. E. Bowden, T. C. Kaspar, S. M. Heald, and S. A. Chambers. Epitaxial growth and atomic arrangement in Fe_2CrO_4 on crystal symmetry matched (001) $MgAl_2O_4$. Journal of Vacuum Science & Technology A: Vacuum, Surfaces, and Films, 2019, 37(3): 031511.

[36] K. H. L. Zhang, K. Xi, M. G. Blamire, and R. G. Egdell. P-type transparent conducting oxides. Journal of Physics: Condensed Matter, 2016, 28(38): 383002.

[37] K. H. L. Zhang, P. V. Sushko, R. Colby, Y. Du, M. E. Bowden, and S. A. Chambers. Reversible nano-structuring of $SrCrO_{3-\delta}$ through oxidation and reduction at low temperature. Nature Communications, 2014, 5(1): 1-7.

[38] K. H. L. Zhang, Y. Du, P. V. Sushko, M. E. Bowden, V. Shutthanandan, S. Sallis, L. F. J. Piper, and S. A. Chambers. Hole-induced insulator-to-metal transition in $La_{1-x}Sr_xCrO_3$ epitaxial films. Physical Review B, 2015, 91(15): 155129.

[39] K. H. L. Zhang, Y. Du, A. Papadogianni, O. Bierwagen, S. Sallis, L. F. Piper, M. E. Bowden, V. Shutthanandan, P. V. Sushko, and S. A. Chambers. Perovskite Sr-doped $LaCrO_3$ as a new p-type transparent conducting oxide. Advanced Materials, 2015, 27(35): 5191-5195.

[40] J. Son, P. Moetakef, J. M. LeBeau, D. Ouellette, L. Balents, S. J. Allen, and S. Stemmer. Low-dimensional Mott material: Transport in ultrathin epitaxial $LaNiO_3$ films. Applied Physics Letters, 2010, 96(6): 062114.

[41] E. J. Moon, B. A. Gray, M. Kareev, J. Liu, S. G. Altendorf, F. Strigari, L. H. Tjeng, J. W. Freeland, and J. Chakhalian. Strain-dependent transport properties of the ultra-thin correlated metal, $LaNiO_3$. New Journal of Physics, 2011, 13(7): 073037.

[42] S. J. May, J.-W. Kim, J. M. Rondinelli, E. Karapetrova, N. A. Spaldin, A. Bhattacharya, and P. J. Ryan. Quantifying octahedral rotations in strained perovskite oxide films. Physical Review B, 2010, 82(1): 014110.

[43] V. Laukhin, O. Copie, M. J. Rozenberg, R. Weht, K. Bouzehouane, N. Reyren, E. Jacquet, M. Bibes, A. Barthélémy, and G. Herranz. Electronic subband reconfiguration in a d^0-perovskite induced by strain-driven structural transformations. Physical review letters, 2012, 109(22): 226601.

[44] N. V. Morozova, I. V. Korobeinikov, and S. V. Ovsyannikov. Strategies and challenges of high-pressure methods applied to thermoelectric materials. Journal of Applied Physics, 2019, 125(22): 220901.

[45] N. G. Eror and U. Balachandran. Self-compensation in lanthanum-doped strontium titanate. Journal of Solid State Chemistry, 1981, 40(1): 85-91.

[46] A. Ohtomo and H. Y. Hwang. Surface depletion in doped $SrTiO_3$ thin films. Applied Physics Letters, 2004, 84(10): 1716-1718.

[47] G. Herranz, M. Basletić, M. Bibes, C. Carrétéro, E. Tafra, E. Jacquet, K. Bouzehouane, C. Deranlot, A. Hamzić, J. M. Broto, A. Barthélémy, and A. Fert. High mobility in $LaAlO_3/SrTiO_3$ heterostructures: Origin, dimensionality, and perspectives. Physical Review Letters, 2007, 98(21): 216803.

[48] J. Carrasco, F. Illas, N. Lopez, E. A. Kotomin, Yu. F. Zhukovskii, R. A. Evarestov, Yu. A. Mastrikov, S. Piskunov, and J. Maier. First-principles calculations of the atomic and electronic structure of F centers in the bulk and on the (001) surface of $SrTiO_3$. Physical Review B, 2006, 73(6): 064106.

[49] H. Lee, T. Mizoguchi, T.Yamamoto, S. L.Kang, and Y. Ikuhara. First-principles calculation of defect energetics in cubic-$BaTiO_3$ and a comparison with $SrTiO_3$. Acta Materialia, 2007, 55(19): 6535-6540.

[50] T. Tanaka, K. Matsunaga, Y. Ikuhara, and T. Yamamoto. First-principles study on structures and energetics of intrinsic vacancies in $SrTiO_3$. Physical Review B, 2003, 68(20): 205213.

[51] J. Son, P. Moetakef, B. Jalan, O. Bierwagen, N. J. Wright, R. Engel-Herbert, and S. Stemmer. Epitaxial $SrTiO_3$ films with electron mobilities exceeding 30,000 $cm^2V^{-1}s^{-1}$. Nature Materials, 2010, 9(6): 482-484.

[52] M. Apreutesei, R. Debord, M. Bouras, P. Regreny, C. Botella, A. Benamrouche, A. Carretero-Genevrier, J. Gazquez, G. Grenet, S. Pailhès, G. Saint-Girons, and R. Bachelet. Thermoelectric La-doped $SrTiO_3$ epitaxial layers with single-crystal quality: From nano to micrometers. Science and Technology of Advanced Materials, 2017, 18(1): 430-435.

[53] H. J. Kim, U. Kim, H. M. Kim, T. H. Kim, H. S. Mun, B. Jeon, K. T. Hong, W. Lee, C. Ju, K. H. Kim, and K. Char. High mobility in a stable transparent perovskite oxide. Applied Physics Express, 2012, 5(6): 061102.

[54] S. Raghavan, T. Schumann, H. Kim, J. Y. Zhang, T. A. Cain, and S. Stemmer. High-mobility $BaSnO_3$ grown by oxide molecular beam epitaxy. APL Materials, 2016, 4(1): 016106.

[55] H. Paik, Z. Chen, E. Lochocki, S. H. Ariel, A. Verma, N. Tanen, J. Park, M. Uchida, S. Shang, B. Zhou, M. Brützam, R. Uecker, Z. Liu, D. Jena, K. M. Shen, D. A. Muller, and D. G. Schlom. Adsorption-controlled growth of La-doped $BaSnO_3$ by molecular-beam epitaxy. APL Materials, 2017, 5(11): 116107.

[56] Parameters of GaAs-based III-V semiconductors and heterostructures. Retrieved from: http://www.ioffe.ru/SVA/NSM/Semicond/index.html.

[57] A. Tsukazaki, A. Ohtomo, and M. Kawasaki. High-mobility electronic transport in ZnO thin films. Applied Physics Letters, 2006, 88(15): 152106.

[58] F. X. Xiu, Z. Yang, L. J. Mandalapu, D. T. Zhao, and J. L. Liu. Photoluminescence study of Sb-doped p-type ZnO films by molecular-beam epitaxy. Applied Physics Letters, 2005, 87(25): 252102.

[59] Electrical properties and basic parameters of GaAs semiconductors. Retrieved from: http://www.ioffe.ru/SVA/NSM/Semicond/GaAs/electric.html#Hall.

Chapter V Effect of deviation from cationic stoichiometry

5.1. Introduction

The purpose of this chapter is to present the effect of deviations from cationic stoichiometry ([A/B] different from 1) on the structural and thermoelectric properties of *p*-type epitaxial $La_{0.75}Sr_{0.25}CrO_3$ films which have not been reported yet in the literature. After a brief literature review on the impact of such deviation from cationic stoichiometry in perovskite oxides on the structural, electronic and thermoelectric properties (section 5.1), our results on *p*-type (001)-oriented epitaxial $(La_{0.75}Sr_{0.25})_{1+\delta}CrO_3$ thin films (with $|\delta| \leq 0.3$) grown by MBE on single-crystalline $SrTiO_3$ substrates will be presented (section 5.2). After a brief presentation of the growth conditions of this series (5.2.1) and on how the microstructural properties of the layers can be controlled (5.2.2), the impact of δ on the crystal structural properties (5.2.3) as well as the thermoelectric properties (5.2.4) is presented.

5.1.1. Impact of the deviation from cationic stoichiometry on the structural properties in perovskite oxides

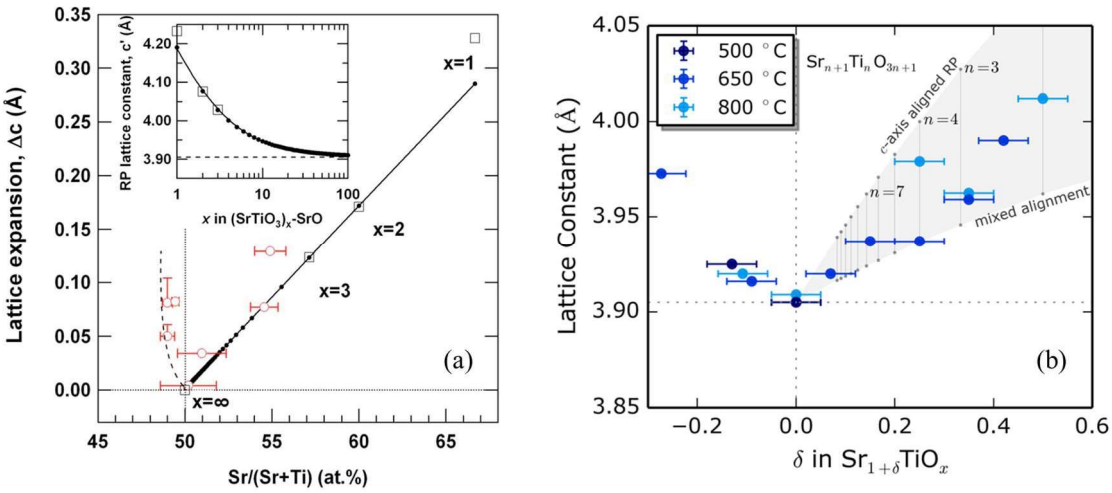

Figure 5. 1 (a) Lattice expansion as a function of Sr/(Sr+Ti) cationic ratio. The closed circles are the calculated data and open squares are the reported bulk values. Taken from Ref. 4. (b) The apparent out-of-plane lattice constant measured by XRD for $Sr_{1+\delta}TiO_x$ films versus Sr:Ti stoichiometry ratio determined by RBS. Taken from Ref. 5.

In Chapter III, it was already presented that the deviation from stoichiometry can expand the mean lattice parameter and then increase the mean unit-cell volume of oxide perovskites because of the introduction of point defects and/or planar defects. Generally, stoichiometric composition in bulk perovskite oxides induces the minimum lattice parameter [1, 2, 3]. The

thin-film perovskite oxides also show the same properties, such as well-known $SrTiO_3$ (STO) shown in Figure 5. 1 [4, 5, 6]. The out-of-plane lattice parameter always increases whatever the sign of deviation.

5.1.2. Impact of the deviation from cationic stoichiometry on the thermoelectric properties in perovskite oxides

As introduced in Chapter I (see section 1.2.4), strategies to improve the performance of thermoelectric materials, thus to increase the figure of merit $ZT = S^2\sigma/(\kappa_e + \kappa_L)$, involve band structure engineering as well as phonon engineering via chemical/structural composition control through the insertion of point defects like cationic vacancies or planar defects like stacking faults for instance [7, 8, 9, 10, 11, 12, 13]. Since the insertion of such defects in the crystalline lattice can substantially lower the lattice thermal conductivity, studies of the impact of the deviation from cationic stoichiometry in thermoelectric perovskite oxides (ABO_3) are thus of high interest in this field. However, only a few studies report such on the thermoelectric properties of *p*-type perovskite oxides films. In this section, reports mentioning such studies in perovskite oxides are presented, not limited to epitaxial thin films, but also in polycrystalline ceramics and both in *n*-type and *p*-type thermoelectrics.

5.1.2.1. In polycrystalline ceramics

In addition to grain boundaries or other planar defects, point defects such as cationic vacancies can act as well as phononic scattering centers in polycrystalline ceramics, lowering the global thermal conductivity. The electronic and thermoelectric properties are also affected by these cationic vacancies due to changes in the band structure.

Among the various complex perovskite oxides, Anzai *et al.* [14] studied the thermoelectric properties of *p*-type $La_{1-x}Sr_xCoO_3$ powders as a single phase of a rhombohedral perovskite-type structure containing A-site vacancies. As shown in Figure 5. 2a, they found that around 5 at.% A-site vacancy induces an increase in the electrical conductivity (σ). The Seebeck coefficient (S) is only slightly reduced with the presence of 5 at.% A-site vacancies (Figure 5. 2b). However, the A-site vacancies induce an increase of the thermoelectric power factor (PF = $S^2\sigma$) with 10 Sr at.% doping only with sintering in air and produce almost no

change with sintering in O_2 (Figure 5. 2c and d).

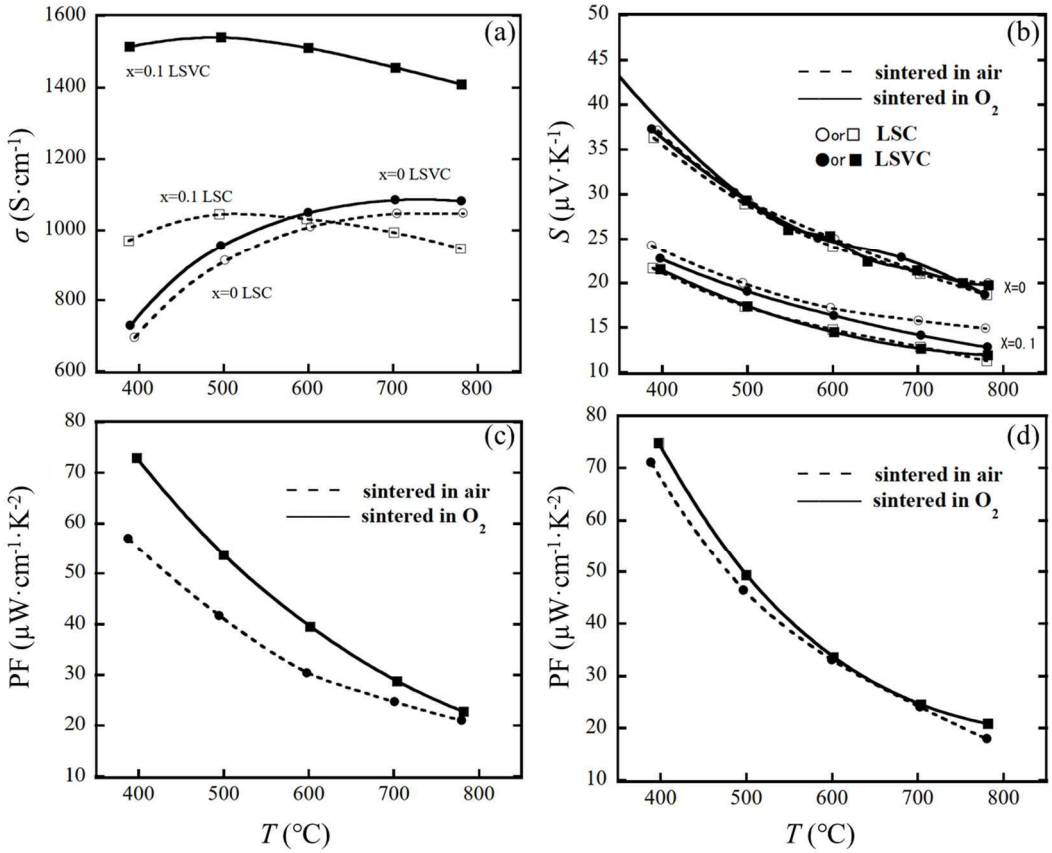

Figure 5. 2 Temperature dependence of (a) electrical conductivity σ and (b) Seebeck coefficient S of $La_{1-x}Sr_xCoO_3$ and $La_{0.95-x}Sr_x\square_{0.05}CoO_3$, (c) and (d) thermoelectric power factor of $La_{0.9}Sr_{0.1}CoO_3$ and $La_{0.85}Sr_{0.1}\square_{0.05}CoO_3$, respectively. Taken from Ref. 14.

Lu *et al.* [11] demonstrated a relatively high *ZT* of thermoelectric A-site-deficient $La_xSr_{1-3x/2}TiO_{3-\delta}$ ceramics (Figure 5. 3). When $x \leq 0.3$, both the *S* and κ are significantly reduced (Figure 5. 3a and c respectively), σ is increased (Figure 5. 3b) via tuning the x value. Thus, the *ZT* value is improved to nearly 0.1 at 473 K (Figure 5. 3d). However, when $x \geq 0.4$, *S* displays a slight increase (Figure 5. 3e), σ is decreased at 473 K (Figure 5. 3f), showing an opposite trend compared with $x \leq 0.3$. Although *ZT* is enhanced by A-site vacancy (x = 0.1 at 473 K), as x increases, both the vacancy and the [La/Sr] ratio are increased. Therefore, improving *ZT* cannot be completely attributed to the induced A-site vacancy. Because for the stoichiometric $La_xSr_{1-x}TiO_3$, the *S* decreases, and the σ increases as a function of x (shown in Chapter I).

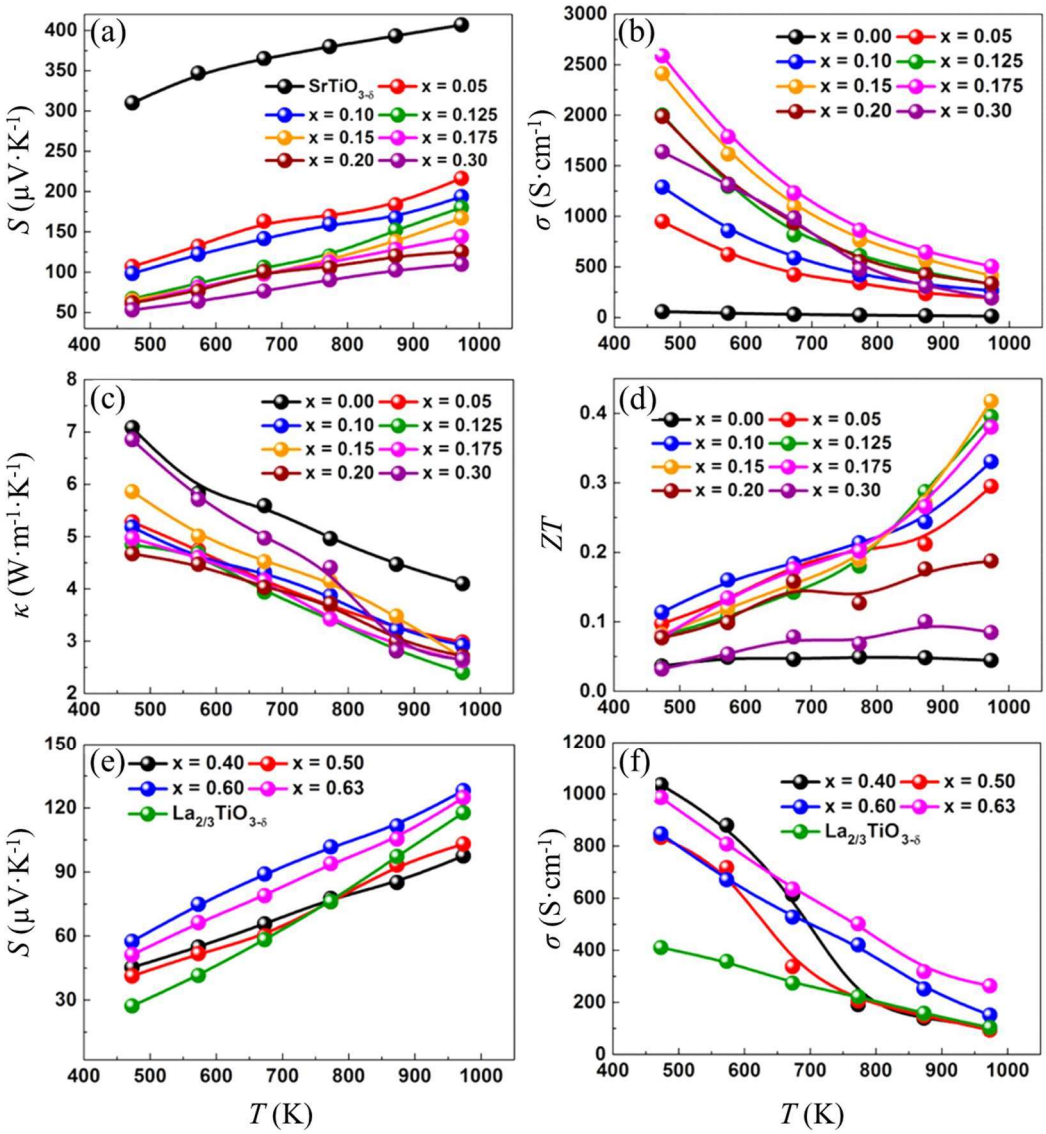

Figure 5. 3 Temperature dependence of (a) Seebeck coefficient S, (b) electrical conductivity σ, (c) thermal conductivity κ, and (d) figure of merit ZT for $x \leq 0.3$, (e) Seebeck coefficient S and (f) electrical conductivity σ for $x \geq 0.4$ $La_xSr_{1-3x/2}TiO_{3-\delta}$ ceramics sintered in N_2/5% H_2 at 1773 K for 6 hours. Taken from Ref. 11.

Moreover, Popuri *et al.* [15] showed that introducing A-site vacancies in STO results in a glass-like thermal conductivity. Figure 5. 4a reveals that $\kappa(T)$ is rapidly decreased with increasing vacancy concentration, and becomes almost temperature independent for x = 0.8. Figure 5. 4b shows that, for the conducting $Sr_{0.8}La_{0.13}\square_{0.07}Ti_{0.95}Nb_{0.05}O_{3-\delta}$ sample, the κ = 2.5 $W \cdot m^{-1} \cdot K^{-1}$ approaches Cahill *et al.*'s minimum value for $SrTiO_3$ (1.4 $W \cdot m^{-1} \cdot K^{-1}$ at 300 K and 1.8 $W \cdot m^{-1} \cdot K^{-1}$ at 1000 K) [16].

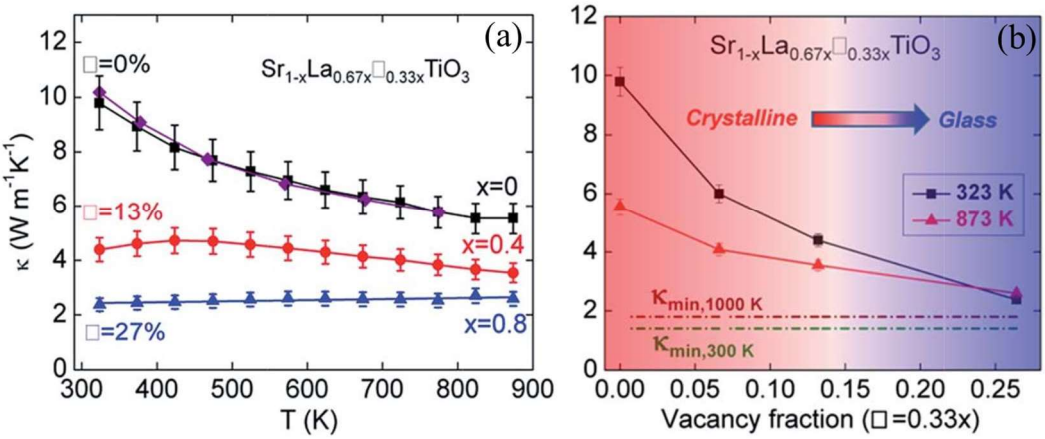

Figure 5. 4 (a) Temperature dependence of κ for the $Sr_{1-x}La_{0.67x}\square_{0.33x}TiO_3$. (b) Vacancy concentration dependence of the κ at 323 and 873 K for the $Sr_{0.8}La_{0.13}\square_{0.07}Ti_{0.95}Nb_{0.05}O_{3-\delta}$. The color gradation indicates the gradual transition from crystalline to glass-like behavior. Taken from Ref. 15.

5.1.2.2. In epitaxial thin films

Similarly to polycrystalline samples, if the deviation from stoichiometry is introduced into thin films, controllable epitaxial films may also offer the opportunity to increase *ZT* value by band structure engineering (increasing thermoelectric power factor) and by phononic engineering (decreasing thermal conductivity). The studies reported on epitaxial films mainly deal with the impact on thermal conductivity (κ) and not on global thermoelectric properties. A few studies have shown however an impact on electronic properties (conductivity and mobility) in *n*-type Nb-doped STO films [4, 17].

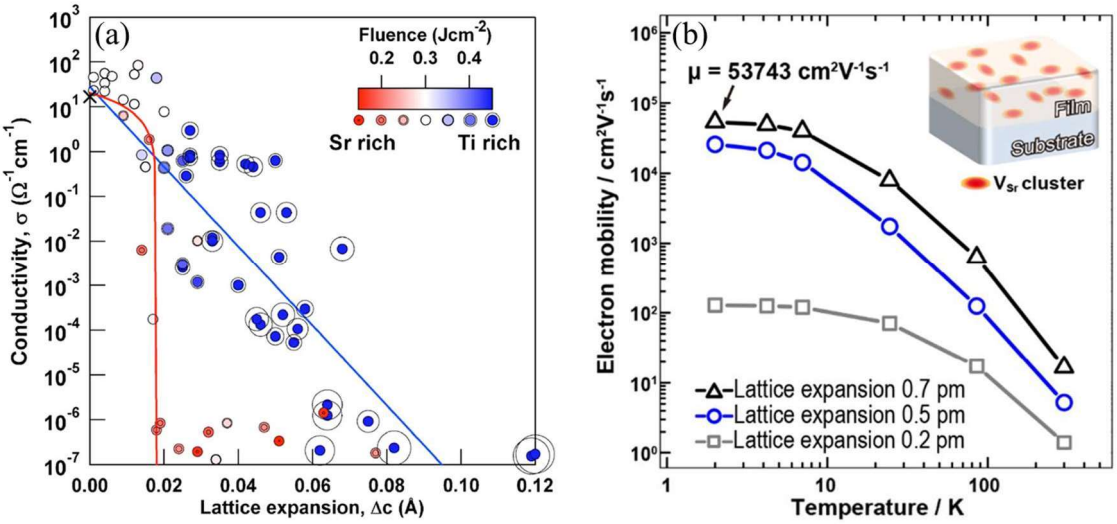

Figure 5. 5 (a) The relationship between conductivity and lattice expansion of postannealed STO films. A cross symbol at zero lattice expansion indicates the conductivity of a 0.1 at.% Nb-doped bulk single crystal. Taken from Ref. 4. (b) Temperature dependence of electron mobilities of STO films with a variety of lattice expansions. Taken from Ref. 17.

Ohnishi *et al.* [4] studied the Nb-doped STO films lose σ as their lattice parameter expands. Figure 5. 5a suggests that the mobile carrier density (equivalent to the σ) gradually decreases in Ti-rich films and shows an abrupt drop with expanding lattice on the Sr-rich side. Kobayashi *et al.* [17] presented the electron mobility of Ti-excess STO films as a function of temperature for a range of lattice expansion values. In the film with the largest lattice expansion of 0.7 pm, the electron mobility is greater than 53000 $cm^2 \cdot V^{-1} \cdot s^{-1}$ at 2 K.

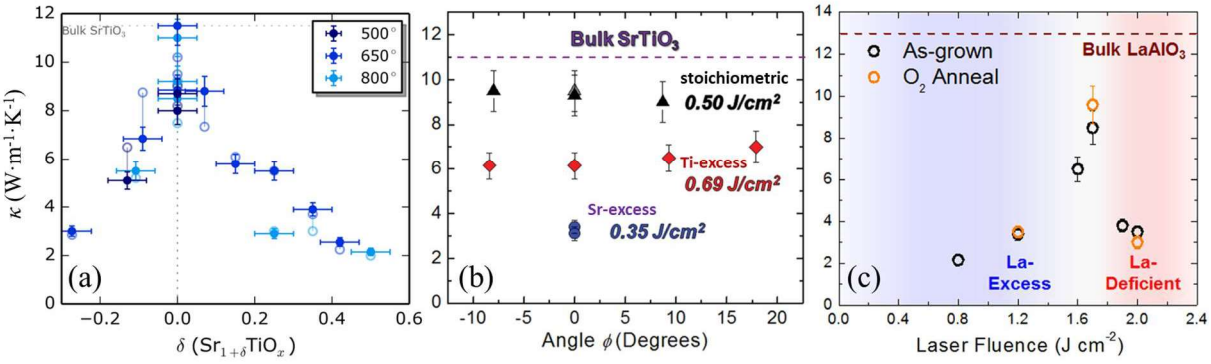

Figure 5. 6 (a) The dependence of longitudinal thermal conductivity concerning film composition with Sr-excess STO films showing the largest decrease. Taken from Ref. 6. (b) Time-domain thermoreflectance (TDTR) results for STO films grown on $NdGaO_3$(110) substrates as a function of deposition geometry and laser fluence. The dashed line indicates the κ of bulk STO. In general, films with excess Sr (blue circles) exhibit a drastic reduction of κ, those with excess Ti (red diamonds) show a somewhat diminished κ, and nearly stoichiometric (black triangles) show the highest κ. Taken from Ref. 18. (c) The κ of $LaAlO_3$ films as a function of laser fluence for as-grown (black, open circles) and post-annealed (orange, open circle) samples. After annealing, negligible changes in κ are observed in La-excess and La-deficient samples (some data points overlap). Taken from Ref. 19.

Brooks *et al.* [6] tuned the κ in homoepitaxial STO films via off-stoichiometry. As displayed in Figure 5. 6a, the longitudinal κ (along the direction perpendicular to the substrate surface) can be modified by as much as 80%, from 11.5 $W \cdot m^{-1} \cdot K^{-1}$ for stoichiometric homoepitaxial STO to 2 $W \cdot m^{-1} \cdot K^{-1}$ for 50 at.% Sr-excess homoepitaxial $Sr_{1+\delta}TiO_x$ films by incorporating additional periodic SrO planar defects in the structure. It is worth noting that a slight stoichiometry variation of "only" 10 at.% can thus decrease a lot the global thermal conductivity by ~50% down to ~6 $W \cdot m^{-1} \cdot K^{-1}$. Furthermore, Breckenfeld *et al.* [18] reported the variations of the structural, dielectric, and thermal properties of nonstoichiometric STO thin films. In particular, they found that, with Sr-excess and Sr-deficiency, κ can be reduced by 65% and 35% respectively. Meanwhile, the same group [19] also studied the effect of growth-induced non-stoichiometry on the thermal and dielectric properties of $LaAlO_3$ thin films. With only 3-5% La-excess and La-deficiency, κ is much reduced by 60-80%.

5.2. Impact of the deviation from cationic stoichiometry in $La_{0.75}Sr_{0.25}CrO_3$ epitaxial films

In this section, high-crystalline quality epitaxially-strained $(La_{0.75}Sr_{0.25})_{1+\delta}CrO_3$ (LSCO) thin films were grown by MBE on (001)-oriented STO. The targeted stoichiometry deviation δ ranges from -0.3 to 0.3 is induced in LSCO films by adjusting the [Sr/Cr] and [La/Cr] flux ratios after the composition calibrations. The effect of this deviation on the structural and room-temperature in-plane electronic and thermoelectric properties of the films has been investigated and are presented in this section.

5.2.1. Growth conditions

This series of LSCO epitaxial thin films were prepared on single-crystalline STO(001) substrates (MaTecK GmbH) by solid-source MBE (same growth conditions as that described in Chapter III). The Sr, La, and Cr fluxes were calibrated using a Bayard-Alpert ionization gauge and a quartz microbalance (see Chapter III) [20]. All the films were grown at 700 °C and $P(O_2) = 1\times10^{-7}$ Torr on as-received substrates, except the stoichiometric LSCO grown on prepared STO, for which the substrate was treated to be terminated by a TiO_2 plane (Chapter III). After growth, they were subjected to additional annealing in air at 300 °C for 2 hours for complete oxidation. The insulating behavior of the substrate was checked in the backside afterward. Hall effect measurement was used for characterizing the electrical properties of the films at room temperature. For such measurement, Cr/Au bonding pads were also deposited on the four corners of the squared samples in this case. Hall effect as well as the Seebeck coefficient measurements are already introduced in detail in Chapter II and section 5.1.2.

5.2.2. Control of the microstructure

5.2.2.1. RHEED characterizations

RHEED patterns along both high-symmetry [100] and [110] in-plane crystallographic directions are shown in Figure 5. 7, which presents as-grown LSCO films on STO substrates as a function of δ. All the patterns present streak lines, meaning that all the films are heteroepitaxial with flat surfaces.

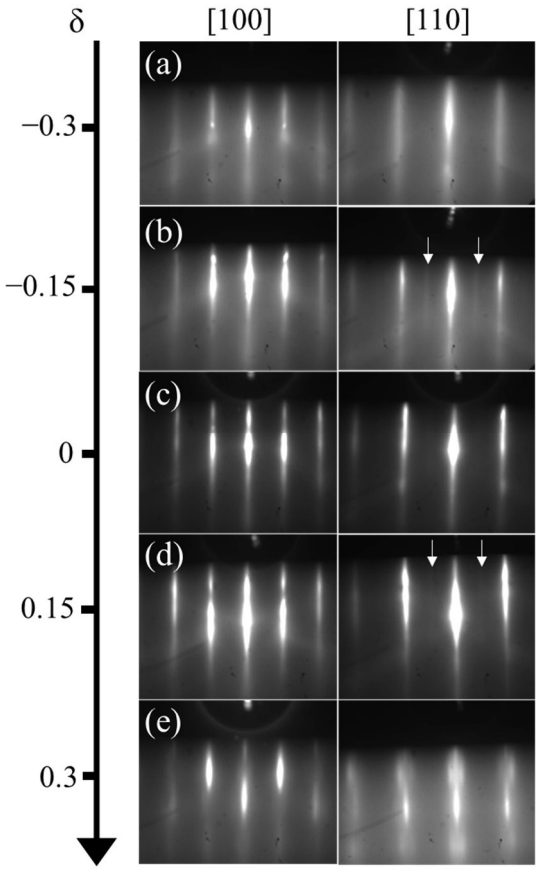

Figure 5. 7 RHEED patterns recorded along the [100] and [110] azimuths (around 200 °C, $P(O_2) = 1\times10^{-9}$ Torr) after growth of the LSCO films with (a) δ = -0.3, (b) δ = -0.15, (c) δ = 0, (d) δ = 0.15, and (e) δ = 0.3.

For $|\delta| \leq 0.15$ (Figure 5. 7b, c, and d), the streaks are sharp and well contrasted along both azimuths, indicating that the surfaces are well ordered. However, for $|\delta| = 0.3$ (Figure 5. 7a and e), the streaks are blurred, and that along the [110] direction becomes thick and the background is brighter than that observed for samples with lower |δ|, revealing greater crystalline disorder. For $|\delta| > 0.3$, there is a high probability that the perovskite structure would not be formed and the film appears amorphous. Additionally, for both $|\delta| = 0.15$ films, a weak 2nd order streaky reflection along the [110] direction (indicated by white arrows) is observed whereas only 1st order reflection is observed along this azimuth at stoichiometry, which indicates a 2×1 surface reconstruction for the slightly Cr-excess and slightly Cr-deficient LSCO films ($|\delta| = 0.15$). In contrast, for stoichiometric films (δ = 0) as well as Cr-excess and Cr-deficient LSCO films (when $|\delta| = 0.3$), only 1st order streaks are visible indicating the absence of surface reconstruction.

5.2.2.2. AFM characterizations

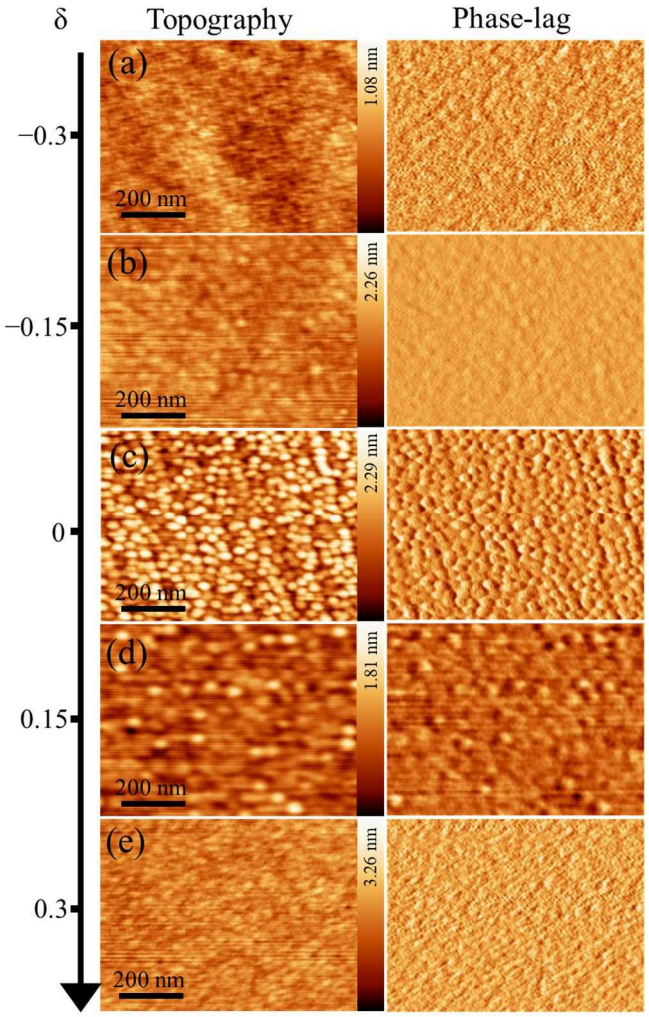

Figure 5. 8 AFM topographic (left panel) and phase-lag (right panel) images of the LSCO films grown on as-received STO(001) substrate with (a) δ = -0.3, (b) δ = -0.15, (c) δ = 0, (d) δ = 0.15, and (e) δ = 0.3. Only the stoichiometric film (δ = 0) is grown on a prepared TiO_2-terminated STO(001) substrate.

AFM images of the LSCO film surfaces are shown in Figure 5. 8. The left panel and the right panel present the topographic images and the phase-lag images, respectively. Atomic steps and terraces can be observed for the stoichiometric LSCO film which is grown on prepared TiO_2-terminated STO substrate (Figure 5. 8c), as already shown in Chapter III and IV (section 3.2.1 and 4.2.2.2). The persistent contrast at adjacent terraces in the right phase-lag image is due to the step height between adjoining terraces at the surface, resulting in a higher local rms roughness ~0.4 nm. All other topographic images reveal relatively smooth surfaces with local rms roughnesses less than 0.25 nm. Any contrast is detected in the corresponding right phase-lag images of off-stoichiometric films.

5.2.2.3. XRR characterizations

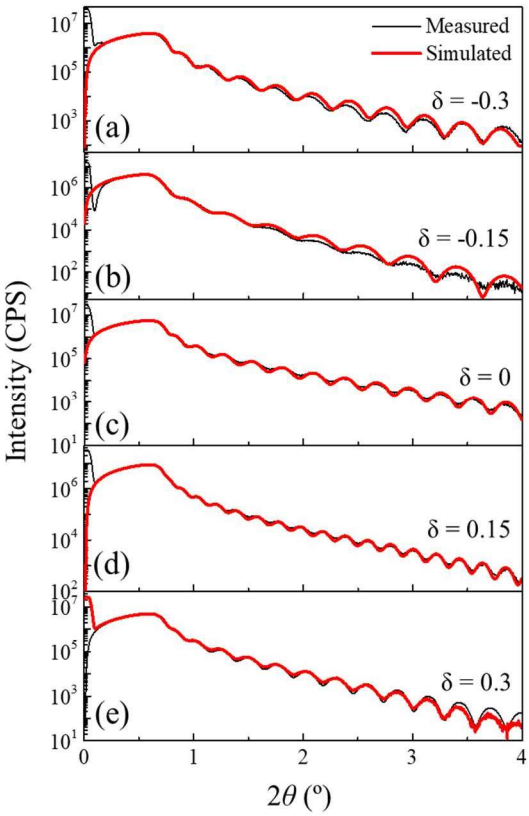

Figure 5. 9 XRR curves for all LSCO films, including the raw data (black lines) and the fitting curves (red lines).

XRR was used to measure the thickness, density, and surface roughness of LSCO films. The curves are plotted in Figure 5. 9. The measured experimental data are well described by the fitting curves (red), including the interference fringe periodicity and the overall slope, yielding values for the thickness, the rms surface/interface roughnesses, and density, which are summarized in Table 5. 1.

5.2.2.4. XPS characterizations

Figure 5. 10 shows the XPS spectra of LSCO films. The Cr $2p_{3/2}$ peaks are all shifted to 576 eV and normalized to 1. For each specimen, the same shift and corresponding normalization are then applied to La 4*d* and Sr 3*d* spectra. The gradual deviation of the cationic stoichiometry (A/B) in the series is revealed by the gradual increase/decrease of the normalized intensity in the La 4*d* and Sr 3*d* core-level spectra in Figure 5. 10a and b, respectively, depending on δ. However, it doesn't respect the variation of the deviation from

stoichiometry as expected, especially for the films with |δ| = 0.3.

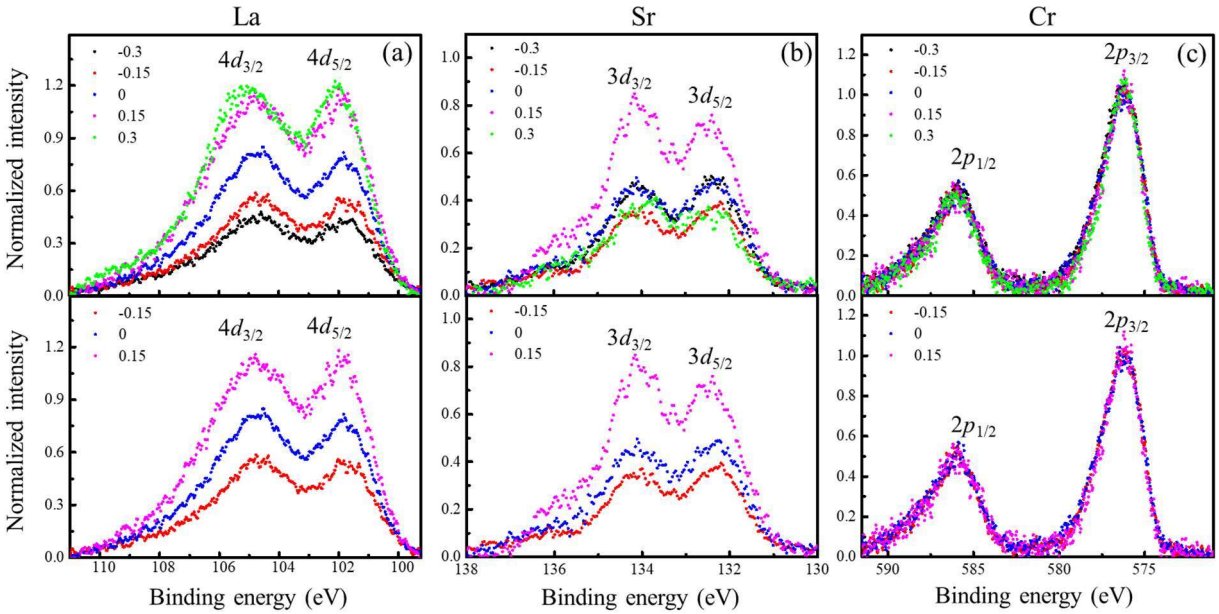

Figure 5. 10 XPS spectra of (a) La 4*d*, (b) Sr 3*d*, and (c) Cr 2*p* core levels of LSCO films for each δ.

The chemical compositions are also summarized in Table 5. 1. It can be seen that there is a difference between the targeted δ (according to the fluxes' ratio) and δ_{XPS} (calculated by XPS spectra). The [Sr]/[Sr+La] value which supposes to be 0.25 (A-site: $La_{0.75}Sr_{0.25}$) varies from 0.32 (δ = -0.3) to 0.21 (δ = 0.3). Therefore, the chemical compositions of these LSCO films with |δ| = 0.3 are probably not those targeted (because of flux measurement uncertainties), even if such XPS measurements involve important uncertainties that may be even larger, especially on such complex oxides containing presumably point and planar defects. If only considering |δ| ≤ 0.15, the XPS spectra are displayed in the second line of Figure 5. 10. The gradual change in normalized intensity of Sr 3*d* and La 4*d* core-level spectra then well respects the variation of δ. The [Sr]/[Sr+La] ratio of LSCO films with δ = -0.15, 0, and 0.15 remains around 0.25 (from 0.26 to 0.25, shown in Table 5. 1) although the $|\delta_{XPS}|$ value is still higher than the targeted |δ|. However, the lattice parameters analyzed by XRD (see next section 5.2.3) show a coherent tendency within the all |δ| range, giving more confidence in the composition extracted from the flux measurement (targeted δ) rather than from the XPS measurements (δ_{XPS}). To confirm this analysis, the composition of the films would have been analyzed by other spectroscopy techniques, like SIMS our RBS, although containing rather large uncertainties as well.

Table 5. 1 Summary of the thickness, rms-roughness from XRR fits, and chemical compositions of the LSCO films at room temperature.

δ	*t* (nm)	[A/(A+B)] (at.%)	δ_{XPS}	[Sr/La+Sr] (at.%)	rms interface roughness (nm)	rms surface roughness (nm)	Density ($g \cdot cm^{-3}$)
-0.3	25.0	35.8	-0.44	0.32	0.15	0.68	6.18
-0.15	20.0	43.5	-0.23	0.26	0.15	0.85	6.27
0	28.2	49.9	0	0.25	0.15	0.54	6.35
0.15	40.8	55.8	0.26	0.26	0.15	0.56	6.36
0.3	30.5	60.3	0.52	0.21	0.15	0.72	6.61

5.2.3. Impact on the structural properties

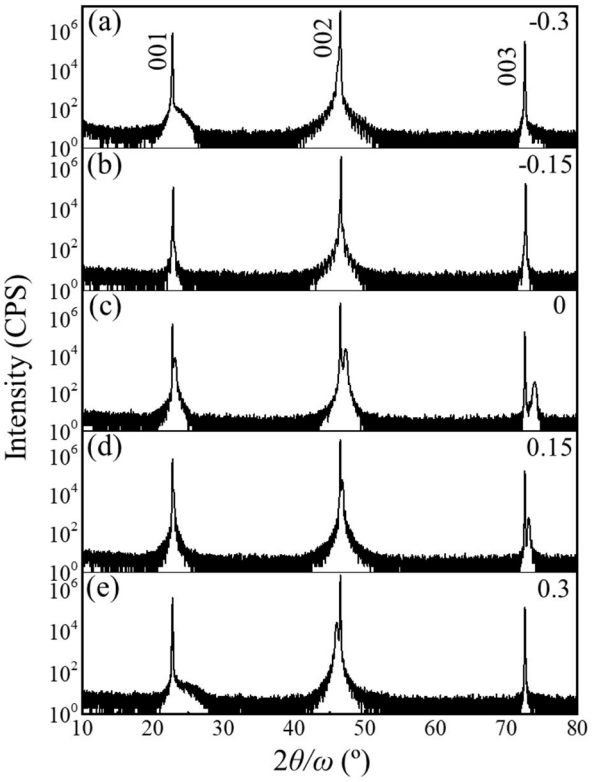

Figure 5. 11 XRD characterizations. $2\theta/\omega$ scans from 10° to 80° on all LSCO films.

The structural properties of all LSCO films are investigated by XRD. Wide $2\theta/\omega$ scans (10-80°, shown in Figure 5. 11) reveal only diffraction peaks corresponding to the {00*l*} reflections of the films, indicating that no other phases neither other orientations than LSCO(00*l*) are present in the epitaxial films.

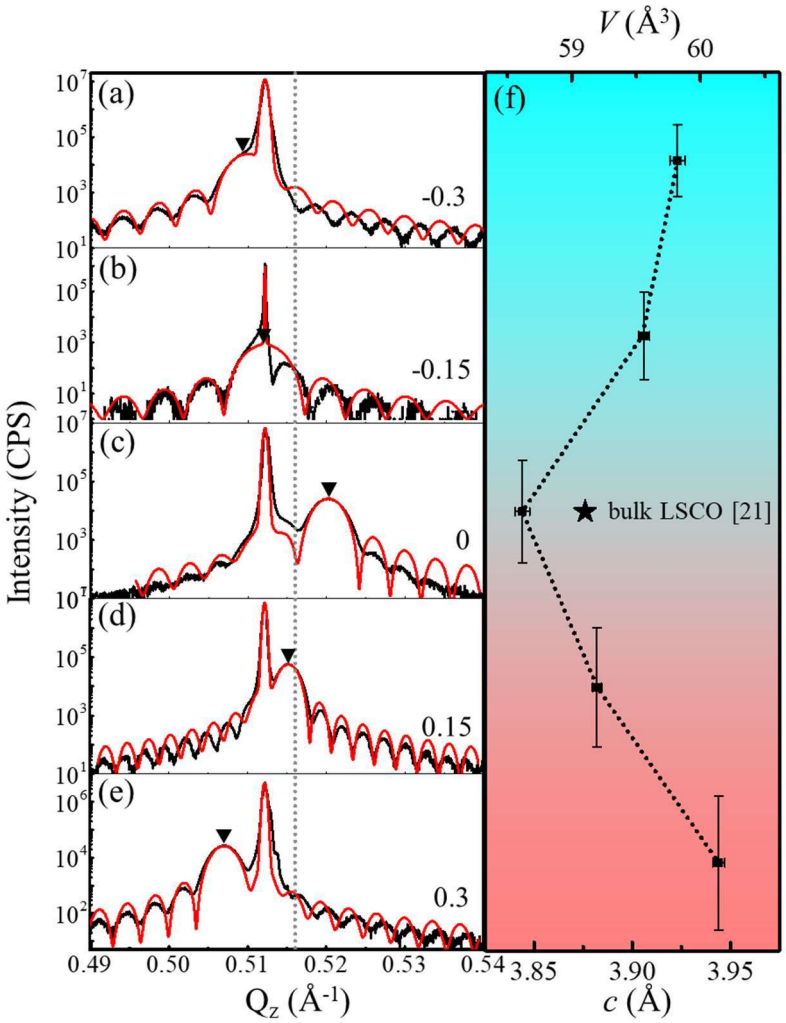

Figure 5. 12 XRD 2θ/ω scans near the (002) reflections on LSCO films grown on STO(001) substrates with corresponding fitting curves, (a) δ = -0.3, (b) δ = -0.15, (c) δ = 0, (d) δ = 0.15, and (e) δ = 0.3. The position of LSCO(002) is marked by a black inverted triangle. The position of bulk stoichiometric $La_{0.75}Sr_{0.25}CrO_3$ is marked with a vertical black dotted line. (f) Measured out-of-plane lattice parameters *c* and calculated unit-cell volume *V* of LSCO films as a function of δ. The horizontal error bars are linked to *c*.

Figure 5. 12a-e show the XRD 2θ/ω scans around the (002) reflections of all LSCO films and their STO substrates plotted in reciprocal space units. The position of bulk stoichiometric $La_{0.75}Sr_{0.25}CrO_3$ has been extracted by our previous study (a_{LSCO} = 3.876 Å) [21] and is marked with a vertical black dotted line through Figure 5. 12a-e. From Cr-excess to (Sr, La)-excess, the position of the LSCO peak can be seen (marked by black inverted triangles), which increases from δ = -0.3 up to a maximum at the stoichiometry (δ = 0), and then decreases with increasing δ up to δ = 0.3. This tendency is as expected from the all targeted δ range. For δ < 0 (Cr-excess LSCO), the LSCO(002) reflections are however close to that of the STO substrate and appear as a left shoulder of the substrate peak (Figure 5. 12a and b). As already shown in Chapter IV, the peak of the stoichiometric film appears at larger Q_z values than bulk

stoichiometric LSCO, indicating that the out-of-plane lattice parameter of epitaxially-strained LSCO film (c_{LSCO}) on STO substrate is smaller than that of bulk LSCO (tensile strain on STO). For $|\delta| > 0$, the (002) LSCO reflections show a decreasing trend with Q_z, revealing a lattice expansion with $|\delta|$, as expected. For all the samples with $|\delta| > 0$, the (002) LSCO reflection appears at lower Q_z values than bulk stoichiometric LSCO, indicating that these epitaxial films have all a corresponding bulk lattice parameter larger than the bulk stoichiometric LSCO. These films are either still in tensile strain when c_{LSCO} is lower than the STO substrate lattice parameter (the case of $\delta = 0.15$) or in compressive strain if larger ($|\delta| > 0.3$). The film with $\delta = -0.15$ appears to be almost relaxed on the STO substrate ($c_{LSCO} \sim c_{STO}$). To properly determine the corresponding bulk lattice parameters (and the strain values) for each $|\delta| > 0$, we would have to grow strained epitaxial films series for each $|\delta| > 0$ on different substrates with different strain states as presented for stoichiometric LSCO films ($\delta = 0$) in Chapter IV. In Figure 5. 12f, the corresponding c_{LSCO} extracted from the fits of the $2\theta/\omega$ diffraction profiles, reaches a minimum at the stoichiometry and then increases with $|\delta|$, as expected. The c_{LSCO} values are summarized in Table 5. 2.

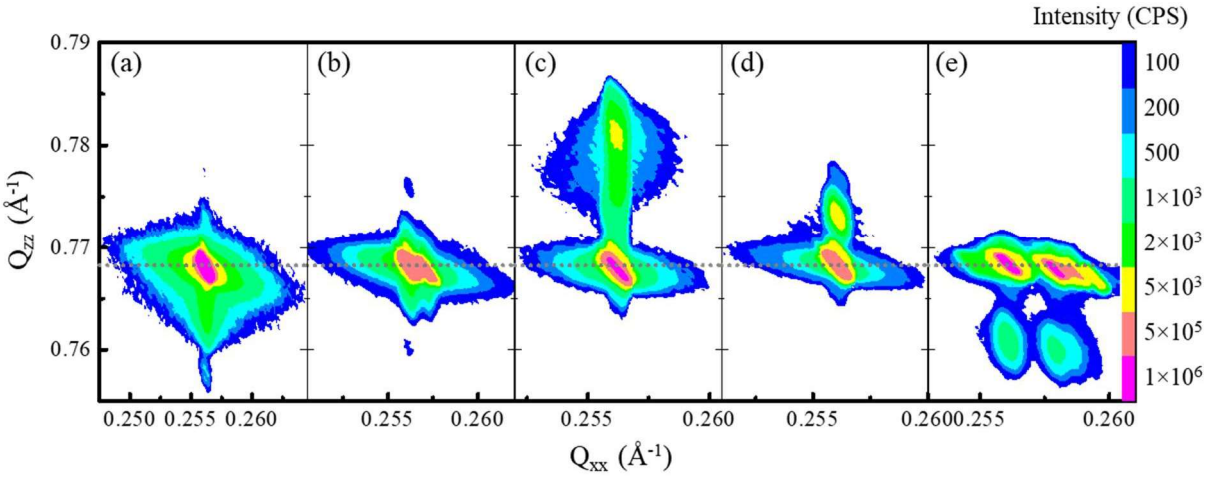

Figure 5. 13 RSM recorded around the asymmetric (103) reflection of LSCO thin films for (a) $\delta = -0.3$, (b) $\delta = -0.15$, (c) $\delta = 0$, (d) $\delta = 0.15$, and (e) $\delta = 0.3$. The horizontal dotted line indicates the Q_{zz} position of the STO substrate related to its out-of-plane lattice parameter.

To check that all the LSCO films are fully strained to their substrates, reciprocal space maps of the (103) asymmetric reflection are measured, as shown in Figure 5. 13. For all films the LSCO (103) node is aligned vertically with the substrate's node, indicating that the $a_{LSCO} = a_{STO} = 3.905$ Å. This coherently strained epitaxial growth of these LSCO films is similar to that of $La_{1+\delta}CrO_3$ films (shown in Figure 3. 17, Chapter III). These maps reveal as well as the associated anisotropic strain of the films (different Q_{zz} positions of the film node depending

on δ), in agreement with the $2\theta/\omega$ scans. The related parameters are then summarized in Table 5. 2. The shoulder of the nodes corresponding to the LSCO films bounces along Q_{zz} depending on chemical composition consistently with the $2\theta/\omega$ scans, confirming the variation of c_{LSCO} shown in Figure 5. 12f. In Figure 5. 13b and e, two visible nodes can be distinguished, especially for δ = 0.3, again because of the relatively low-crystalline quality of the commercial STO substrate having mosaic domains.

From the measured c_{LSCO} and a_{LSCO}, the variation in the deduced pseudo-cubic unit-cell volume of LSCO films as a function of δ is shown in Figure 5. 12f. The unit-cell volume shows the same trend as c_{LSCO}, because a_{LSCO} keeps constant. As already discussed, this trend is expected from stoichiometry deviation, which tends to enlarge the mean unit-cell volume. This can be caused by (*i*) the formation of point defects like charged ionic vacancies in the lattice and/or (*ii*) planar defects like stacking faults (intercalation of AO or BO_2 plane in the perovskite structure with slightly larger interatomic distance). In epitaxially-strained ABO_3 films, the mean out-of-plane lattice parameter is consequently enlarged, like in the references of other perovskite oxides: as STO for instance [5, 22, 23] and $LaCrO_3$ from our previous work [20]. The unit-cell volume of the stoichiometric LSCO film (58.617 $Å^3$) is the one closest to the standard bulk LSCO volume value (58.231 $Å^3$).

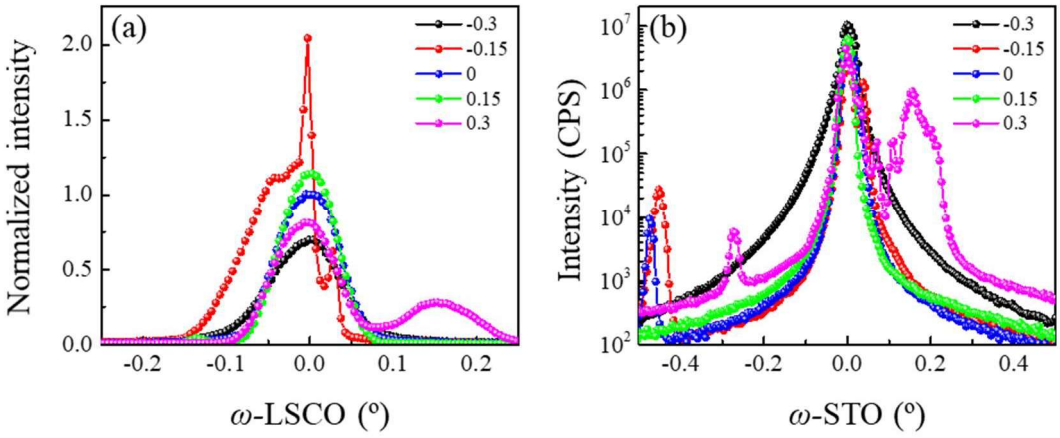

Figure 5. 14 XRD ω-scans around the (002) reflection for all (a) LSCO and (b) STO substrates.

The mosaicity (full width at half maximum, FWHM, all normalized to 1) of the rocking curves around the (002) film peak is below 0.1° for all LSCO films (shown in Figure 5. 14), confirming the good crystalline quality of samples even with large cationic stoichiometry deviation. The mosaicity of the non-stoichiometric films is slightly larger than that of the stoichiometric one (0.07°), in agreement with the RHEED observations (Figure 5. 7).

Table 5. 2 Summary of the structural properties and chemical compositions of the LSCO films at room temperature.

δ	[Sr]/[La+Sr]	*a* (Å)	*c* (Å)	Strain	Mosaicity (°)	Volume (Å^3)
-0.3	2.12	3.905	3.923	compressive	0.1	59.823
-0.15	2.83	3.905	3.906	relaxed	0.09	59.547
0	3.01	3.905	3.844	tensile	0.07	58.617
0.15	2.82	3.905	3.882	tensile	0.07	59.200
0.3	3.78	3.905	3.944	compressive	0.09	60.142

5.2.4. Impact on electronic and thermoelectric properties

In this section, the effects of the deviation from cationic stoichiometry in $(La_{0.75}Sr_{0.25})_{1+\delta}CrO_3$ films on their electronic and thermoelectric properties are presented. These transport properties are measured along the in-plane direction and at room temperature.

5.2.4.1. Electronic properties

Results from Hall effect and Seebeck coefficient measurements done at room-temperature on the $(La_{0.75}Sr_{0.25})_{1+\delta}CrO_3$ (LSCO) films are shown in Figure 5. 15 as a function of cationic stoichiometry deviation (δ). The LSCO films with large cationic stoichiometry deviation ($|\delta| = 0.3$) are too much insulating to be measured. Based on these measurements, all the other films with $|\delta| \leq 0.15$ exhibit *p*-type conductivity and a high hole concentration. Figure 5. 15a presents the variation of measured electrical conductivity (σ), hole concentration (p), and mobility (μ) of these LSCO films. The Sr substitution ratio on La site (Sr doping ratio) remains constant at 25 at.% for all films, as targeted (see Table 5. 1).

The stoichiometric LSCO film ($\delta = 0$) exhibits the highest σ (10 S·cm^{-1}), which is slightly higher than that of the A-deficient film ($\delta = -0.15$, ~9 S·cm^{-1}), and clearly higher than B-deficient film ($\delta = 0.15$, 6.7 S·cm^{-1}). The σ of this latest B-deficient film ($\delta = 0.15$) is reduced by almost a factor of two concerning that of the stoichiometric film. A higher δ value presumably brings a larger amount of crystalline (point and planar) defects in the perovskite structure, which reduces the σ of LSCO film. If the cationic stoichiometry deviation is fully

converted into cationic vacancies only, LSCO films with δ = -0.15, 0, and 0.15 can be seen as $La_{0.64}Sr_{0.21}\square_{0.15}CrO_3$ ($La_{0.57}Sr_{0.2}\square_{0.23}CrO_3$ considering δ_{XPS}), $La_{0.75}Sr_{0.25}CrO_3$, and $La_{0.75}Sr_{0.25}Cr_{0.87}\square_{0.13}O_3$ ($La_{0.74}Sr_{0.26}Cr_{0.8}\square_{0.2}O_3$ considering δ_{XPS}), respectively (see Table 5. 1). However, similar deviations in $SrTiO_3$ for instance induce planar defects such as stacking faults [5].

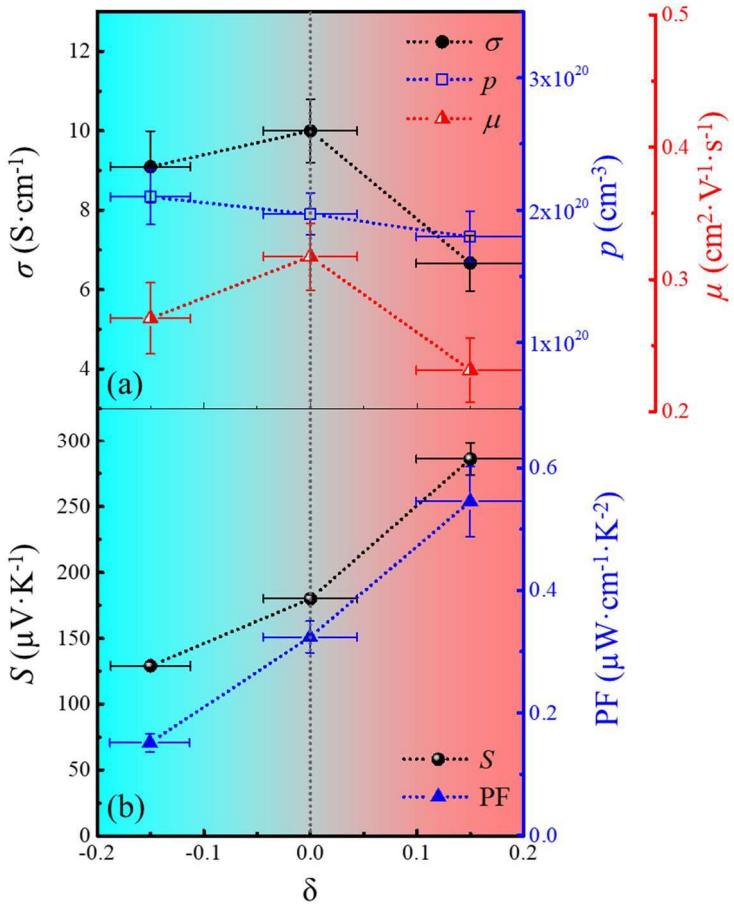

Figure 5. 15 Room-temperature (a) electrical conductivity σ, hole concentration p, and mobility μ of LSCO films obtained from Hall effect measurements, as well as (b) measured Seebeck coefficient S, and thermoelectric power factor (PF = $S^2\sigma$) as a function of δ.

It is worth noting that, from XPS measurements, the fit of the Cr $2p_{3/2}$ core-level spectra has revealed ~25% of Cr^{4+} component (and ~75% of Cr^{3+} component) for all these samples whatever the δ value (section 5.2.2.4, and fits for stoichiometric LSCO in Chapter IV section 4.2.2.4). In other words, it seems that the elemental oxidation states are independent of the cation stoichiometry deviation, within the instrumental uncertainties. The charge carrier concentration very slightly decreases with the increase of δ but keeps constant around 2×10^{20} cm^{-3}. A-deficient LSCO shows a very slightly higher carrier concentration than B-deficient films (Figure 5. 15a). According to the equation $\mu = \sigma/pe$, the hole mobility of LSCO films

can be easily extracted, which reduces with |δ| value. The μ measured on the stoichiometric LSCO film is 0.32 $cm^2 \cdot V^{-1} \cdot s^{-1}$, whereas those of A-deficient and B-deficient films are 0.27 $cm^2 \cdot V^{-1} \cdot s^{-1}$ and 0.23 $cm^2 \cdot V^{-1} \cdot s^{-1}$, respectively. For these non-stoichiometric films, the presumable point and/or planar defects may hinder the migration of charge carriers in the lattice, resulting in a decrease of the mobility with δ.

The observed trends depending on δ can be due to two combined effects: (*i*) from differences in chemical composition (and induced crystalline defects), and (*ii*) from differences in epitaxial strain anisotropy (because of different corresponding bulk lattice parameters) as shown in Chapter IV. From the results of Chapter IV, the electrical conductivity and the hole concentration have globally the tendency to decrease with epitaxial strain, from compressive to tensile strain, with a large decay at the large strain on the DSO substrate. In this chapter on this series, from the XRD results (see section 5.2.3), the films are relaxed (δ = -0.15), tensile (δ = 0), and slightly tensile (δ = 0.15). The observed trend here does not follow the trend to the tensile strain only, indicating that the chemical composition effect (crystalline defects) dominates, or is strong enough to significantly impact, the transport behavior here in addition to epitaxial strain effects.

5.2.4.2. Thermoelectric properties

Figure 5. 15b presents the results from the Seebeck coefficient (*S*) measurements performed in-plane at room temperature. The positive sign of *S* value for all samples confirms that the holes are dominant charge carriers in these films, as already mentioned. Also, for the stoichiometric LSCO film, *S* is 180 $\mu V \cdot K^{-1}$, which is in very good agreement with the most recent result of Chambers' group, as already mentioned in Chapter III [24]. *S* increases continuously as a function of δ (from A-deficient to B- deficient LSCO films). This tendency is rather consistent with the Hall effect transport measurements revealing that both the electronic conductivity and hole concentration tend to decrease with δ within the instrumental uncertainties (the lowest for δ = 0.15, for which the largest *S* is measured consistently).

From the results presented in Chapter IV on the strain effects, *S* increases with the epitaxial strain (from compressive to tensile strain). Considering the strain state of the LSCO films depending on δ (relaxed at δ = -0.15, tensile at δ = 0, and slightly tensile at δ = 0.15; see section 5.2.3), the observed *S* trend cannot be only explained from strain effect only. As well as for the electronic properties, the chemical composition (crystalline defects) dominates or is

strong enough to significantly impact, the thermopower (S) here in addition to epitaxial strain effects.

Referring to the S equation (1.2) introduced in Chapter I, and assuming that the effective mass (m^*) is constant for the same type of material, S is explained to be enhanced with δ due to the slight decrease of p. Furthermore, the corresponding thermoelectric power factor is calculated for each film according to the equation PF = $S^2\sigma$, which also shows the same rising trend as S. The stoichiometric film displays a PF value of about 0.33 $\mu W \cdot cm^{-1} \cdot K^{-2}$, in relatively good agreement with the literature (0.49 $\mu W \cdot cm^{-1} \cdot K^{-2}$ from Ref. 24). The PF of Cr-deficient film is more than three times than that of A-deficient film. Although the Cr-deficient film has a relatively low σ, the high S value (second-order in $S^2\sigma$) dominates and provides a higher PF of about 0.55 $\mu W \cdot cm^{-1} \cdot K^{-2}$. We show here for the first time that the PF of LSCO films can be improved by Cr-deficiency. This provides a new effective means for the enhancement of thermoelectric performance (ZT) of p-type LSCO films, especially as such cationic off-stoichiometry should show, besides, a reduced thermal conductivity concerning its stoichiometric LSCO counterpart (see next chapter conclusion and perspectives).

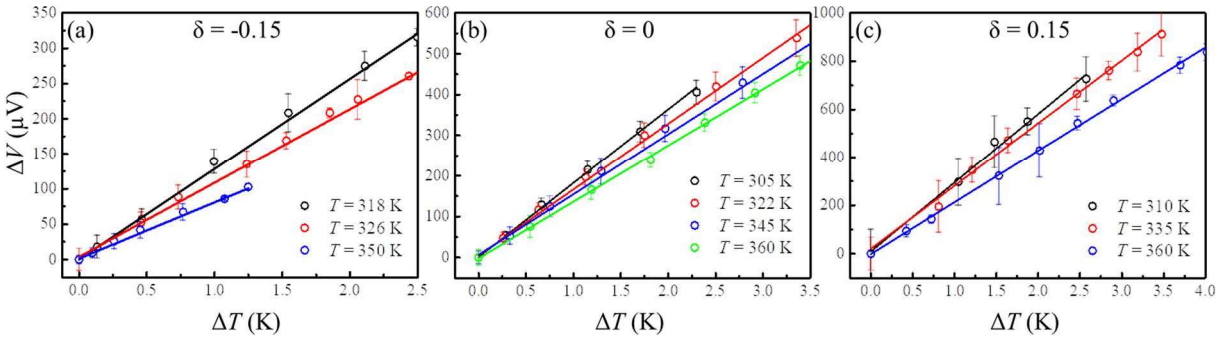

Figure 5. 16 Measured ΔV in the function of ΔT at different temperatures for each δ. The different slopes $\Delta V/\Delta T$ give the Seebeck coefficients S that are reported in Figure 5. 17.

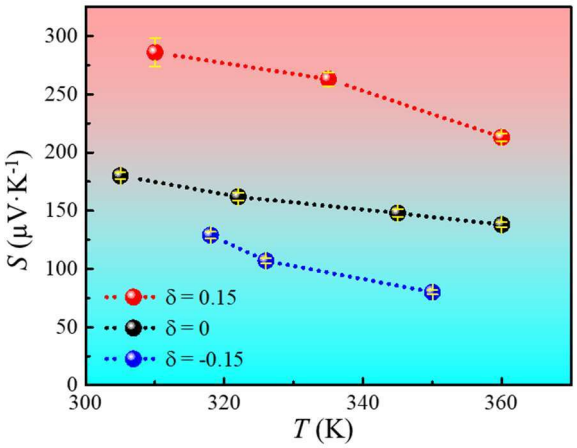

Figure 5. 17 Temperature-dependent Seebeck coefficient S of LSCO films for each δ.

Figure 5. 17 represents the temperature-dependent in-plane *S* for LSCO films with different δ values, extracted from the raw *S* measurements ($S = \Delta V/\Delta T$ at different *T*) presented below in Figure 5. 16a, b, and c, for δ = -0.15, 0 and 0.15, respectively. The error bar of each measured point in Figure 5. 16a, b, and c is shown as well, and it has a relatively large uncertainty for δ = 0.15 because of larger resistivity, as also shown in Chapter III (Figure 3. 31a). On the contrary, the stoichiometric LSCO film shows greater accuracy because of the relatively higher σ (Figure 5. 15a). Fortunately, the observed trend of *S* with temperature is still robust. *S* slightly decreases with increasing temperature (Figure 5. 17), consistently with the temperature-dependent resistivity curve (decreasing resistivity with *T*) reported for stoichiometric LSCO films (see Chapter III section 3.1.3.2) [25]. The slight decrease of *S* indicates that the LSCO films can still have a relatively good thermoelectric performance from room temperature up to 360 K which is the temperature range of most applications.

5.3. Conclusion

In this chapter, high-crystalline quality epitaxial $(La_{0.75}Sr_{0.25})_{1+\delta}CrO_3$ thin films were grown by MBE on (001)-oriented STO substrates with δ varying from -0.3 to 0.3. All the films crystallize in the perovskite structure, are single-phase, fully (001)-oriented, flat, and epitaxially-strained. The mean out-of-plane lattice parameter of LSCO films decreases with reducing |δ| from 3.944 to 3.844 Å, while it reaches the minimum at the stoichiometry as expected. Different δ values presumably induce different ratios of point defects (cationic vacancies either on A-site or B-site), in addition to possible planar defects (stacking faults). Since the LSCO films with |δ| = 0.3 are insulating (with our measurement instruments), the characterization of the physical properties (electronic and thermoelectric) has been only achieved for $|\delta| \leq 0.15$ films.

Room-temperature electrical conductivity and Hall mobility are maximum at the cationic stoichiometry (σ = 10 $S \cdot cm^{-1}$, μ = 0.32 $cm^2 \cdot V^{-1} \cdot s^{-1}$, respectively). However, within instrumental uncertainties, the electrical conductivity and charge carrier (hole) concentration tend to decrease when δ increases. This behavior is consistent with the Seebeck coefficient measurements where *S* increases with δ. We have shown here for the first time that the PF of LSCO films can be improved by Cr-deficiency. This provides a new effective means for the enhancement of thermoelectric performance (*ZT*) of *p*-type LSCO films, especially as such

cationic off-stoichiometry should show a reduced thermal conductivity concerning its stoichiometric LSCO counterpart.

5.4. References

[1] J. Carrasco, F. Illas, N. Lopez, E. A. Kotomin, Yu. F. Zhukovskii, R. A. Evarestov, Yu. A. Mastrikov, S. Piskunov, and J. Maier. First-principles calculations of the atomic and electronic structure of F centers in the bulk and on the (001) surface of $SrTiO_3$. Physical Review B, 2006, 73(6): 064106.

[2] H. Lee, T. Mizoguchi, T.Yamamoto, S. L.Kang, and Y. Ikuhara. First-principles calculation of defect energetics in cubic-$BaTiO_3$ and a comparison with $SrTiO_3$. Acta Materialia, 2007, 55(19): 6535-6540.

[3] T. Tanaka, K. Matsunaga, Y. Ikuhara, and T. Yamamoto. First-principles study on structures and energetics of intrinsic vacancies in $SrTiO_3$. Physical Review B, 2003, 68(20): 205213.

[4] T. Ohnishi, K. Shibuya, T. Yamamoto, and M. Lippmaa. Defects and transport in complex oxide thin films. Journal of Applied Physics, 2008, 103(10): 103703.

[5] C. M. Brooks, L. Fitting Kourkoutis, T. Heeg, J. Schubert, D. A. Muller, and D. G. Schlom. Growth of homoepitaxial $SrTiO_3$ thin films by molecular beam epitaxy. Applied Physics Letters, 2009, 94(16): 162905.

[6] C. M. Brooks, R. B. Wilson, A. Schäfer, J. A. Mundy, M. E. Holtz, D. A. Muller, J. Schubert, D. G. Cahill, and D. G. Schlom. Tuning thermal conductivity in homoepitaxial $SrTiO_3$ films via defects. Applied Physics Letters, 2015, 107(5): 051902.

[7] L. Yang, Z. G. Chen, M. S. Dargusch, and J. Zou. High performance thermoelectric materials: Progress and their applications. Advanced Energy Materials, 2018, 8(6): 1701797.

[8] K. Biswas, J. He, I. D. Blum, C. Wu, T. P. Hogan, D. N. Seidman, V. P. Dravid, and M. G. Kanatzidis. High-performance bulk thermoelectrics with all-scale hierarchical architectures. Nature, 2012, 489(7416): 414-418.

[9] J. He, M. G. Kanatzidis, and V. P. Dravid. High performance bulk thermoelectrics via a panoscopic approach. Materials Today, 2013, 16(5): 166-176.

[10] C. J. Vineis, A. Shakouri, A. Majumdar, and M. G. Kanatzidis. Nanostructured thermoelectrics: Big efficiency gains from small features. Advanced Materials, 2010, 22(36): 3970-3980.

[11] Z. Lu, H. Zhang, W. Lei, D. C. Sinclair, and I. M. Reaney. High-figure-of-merit thermoelectric La-doped A-site-deficient $SrTiO_3$ ceramics. Chemistry of Materials, 2016, 28(3): 925-935.

[12] F. Azough, S. S. Jackson, D. Ekren, R. Freer, M. Molinari, S. Yeandel, P. Goddard, S. C. Parker, D. Hernandez Maldonado, D. M. Kepaptsoglou, and Q. M. Ramasse. Concurrent La and A-site vacancy doping modulates the thermoelectric response of $SrTiO_3$: Experimental and computational evidence. ACS Applied Materials & Interfaces, 2017, 9(48): 41988-42000.

[13] G. Ren, J. Lan, K. J. Ventura, X. Tan, Y. Lin, and C. Nan. Contribution of point defects and nano-grains to thermal transport behaviours of oxide-based thermoelectrics. NPJ Computational Materials, 2016, 2(1): 1-9.

[14] M. Anzai, H. Kawakami, M. Saito, and H. Yamamura. Thermoelectric properties of p-type perovskite compounds $LaCoO_3$ systems containing the A-site vacancy. IOP Conference Series: Materials Science and Engineering, IOP Publishing, 2011, 18(14): 142005.

[15] S. R. Popuri, A. J. M. Scott, R. A. Downie, M. A. Hall, E. Suard, R. Decourt, M. Polletc, and J. W. G. Bos. Glass-like thermal conductivity in $SrTiO_3$ thermoelectrics induced by A-site vacancies. RSC Advances, 2014, 4(64): 33720-33723.

[16] D. G. Cahill, S. K. Watson, and R. O. Pohl. Lower limit to the thermal conductivity of disordered crystals. Physical Review B, 1992, 46(10): 6131.

[17] S. Kobayashi, Y. Mizumukai, T. Ohnishi, N. Shibata, Y. Ikuhara, and T. Yamamoto. High electron mobility of Nb-doped $SrTiO_3$ films stemming from rod-type Sr vacancy clusters. ACS Nano, 2015, 9(11): 10769-10777.

[18] E. Breckenfeld, R. Wilson, J. Karthik, A. R. Damodaran, D. G. Cahill, and L. W. Martin. Effect of growth induced (non)stoichiometry on the structure, dielectric response, and thermal conductivity of $SrTiO_3$ thin films. Chemistry of Materials, 2012, 24(2): 331-337.

[19] E. Breckenfeld, R. B. Wilson, and L. W. Martin. Effect of growth induced (non)stoichiometry on the thermal conductivity, permittivity, and dielectric loss of $LaAlO_3$ films. Applied Physics Letters, 2013, 103(8): 082901.

[20] D. Han, M. Bouras, C. Botella, A. Benamrouche, B. Canut, G. Grenet, G. Saint-Girons and R. Bachelet. Structural properties of strained epitaxial $La_{1+\delta}CrO_3$ thin films. Journal of Vacuum Science & Technology A: Vacuum, Surfaces, and Films, 2019, 37(2): 021512.

[21] D. Han, M. Bouras, C. Botella, A. Benamrouche, B. Canut, G. Grenet, G. Saint-Girons, and R. Bachelet. Poisson ratio and bulk lattice constant of $(Sr_{0.25}La_{0.75})CrO_3$ from strained epitaxial thin films. Journal of Applied Physics, 2019, 126(8): 085304.

[22] B. Jalan, R. Engel-Herbert, N. J. Wright, and S. Stemmer. Growth of high-quality $SrTiO_3$ films using a hybrid molecular beam epitaxy approach. Journal of Vacuum Science & Technology A: Vacuum, Surfaces, and Films, 2009, 27(3): 461-464.

[23] B. Jalan, P. Moetakef, and S. Stemmer. Molecular beam epitaxy of $SrTiO_3$ with a growth window. Applied Physics Letters, 2009, 95(3): 032906.

[24] K. H. Zhang, Y. Du, A. Papadogianni, O. Bierwagen, S. Sallis, L. F. Piper, M. E. Bowden, V. Shutthanandan, P. V. Sushko, and S. A. Chambers. Perovskite Sr-doped $LaCrO_3$ as a new p-type transparent conducting oxide. Advanced Materials, 2015, 27(35): 5191-5195.

[25] K. H. L. Zhang, Y. Du, P. Sushko, M. E. Bowden, V. Shutthanandan, S. Sallis, L. F. Piper, and S. A. Chambers. Hole-induced insulator-to-metal transition in $La_{1-x}Sr_xCrO_3$ epitaxial films. Physical Review B, 2015, 91(15): 155129.

Conclusion and perspectives:

Towards oxide-based thermoelectric micromodules

6.1. Conclusion

Perovskite oxides have received much attention as an alternative thermoelectric material due to tunable electronic properties and large Seebeck coefficients, in addition to chemical/thermal stability in air, as well as abundance and low toxicity of the constituting elements. However, contrary to *n*-type, there is a lack of *p*-type thermoelectric perovskite oxides, though required for the fabrication of a complete thermoelectric module. Up to now, the only *p*-type perovskite oxide showing rather good thermoelectric properties is Sr-doped $LaCrO_3$ (*i.e.* $La_{1-x}Sr_xCrO_3$ solid solution). However, its thermoelectric properties have almost not been investigated so far. This Ph.D. work aimed at studying the correlation between structural, electronic, and thermoelectric properties of *p*-type Sr-doped $LaCrO_3$ in the form of high-crystalline quality thin films epitaxially grown by molecular beam epitaxy (MBE) on (pseudo)cubic perovskite-oxide (001)-oriented substrates. This elaboration technique, offering control of the structure and chemical composition at the atomic scale, has allowed studying the effect of the following key parameters in strained epitaxial films: (*i*) Sr doping/substitution level (Chapter III), (*ii*) epitaxial strain (Chapter IV), and (*iii*) cationic stoichiometry deviation (Chapter V).

Firstly, after proper composition calibrations [1], high-quality $La_{1-x}Sr_xCrO_3$ thin films were epitaxially grown on $SrTiO_3$ (STO) substrate. The impacts of the Sr doping/substation level (x) on the structural, electronic, and thermoelectric properties were investigated, especially in the $0 \leq x \leq 0.4$ range. The structural properties of $La_{1-x}Sr_xCrO_3$ solid solution roughly obey Vegard's law between $LaCrO_3$ (a_{bulk} = 3.885 Å) to $SrCrO_3$ (a_{bulk} = 3.819 Å). The electronic and thermoelectric properties can be well controlled by the Sr doping/substitution level (x). Room-temperature electronic conductivity (σ), hole concentration (p), and mobility (μ) increase with x ($0.1 \leq x \leq 0.4$) in the ranges of 1-20 $S \cdot cm^{-1}$, 6×10^{19}-2.5×10^{20} cm^{-3}, and 0.1-0.5 $cm^2 \cdot V^{-1} \cdot s^{-1}$, respectively. Accordingly, the Seebeck coefficient (S) decreases when x increases from ~300 $\mu V \cdot K^{-1}$ (x = 0.2) to ~100 $\mu V \cdot K^{-1}$ (x = 0.4). The thermoelectric power factor ($PF = S^2\sigma$) reaches a maximum about ~0.35 $\mu W \cdot cm^{-1} \cdot K^{-2}$ around x = 0.25. These results are in good agreement with the literature [2, 3].

Secondly, setting the composition to that leading to the largest thermoelectric PF at x = 0.25, high-crystalline quality $La_{0.75}Sr_{0.25}CrO_3$ (LSCO) thin films were epitaxially strained on different (pseudo)cubic perovskite oxide substrates [$LaAlO_3$, $(LaAlO_3)_{0.3}(Sr_2TaAlO_6)_{0.7}$ so-called LSAT, $SrTiO_3$, and $DyScO_3$] having different lattice parameters (a_{LAO} = 3.796 Å,

a_{LSAT} = 3.868 Å, a_{STO} = 3.905 Å, a_{DSO} = 3.944 Å, respectively) allowing to access to a wide range of in-plane strain from -2.06% (compressive) to +1.75% (tensile). The effects of epitaxial strain on the structural, elastic, electronic, and thermoelectric properties have then been investigated at room temperature. The Poisson ratio and bulk lattice constant of $La_{0.75}Sr_{0.25}CrO_3$ were determined for the first time with this series (ν_{LSCO} = 0.32, and $a_{bulk\text{-}LSCO}$ = 3.876 Å). They significantly differ from that of bulk $LaCrO_3$ (ν = 0.23, $a_{bulk\text{-}LCO}$ = 3.885 Å). These results have been published [4]. The relatively large Poisson ratio in LSCO (0.32) compared to that of $LaCrO_3$ (0.23) has enabled flexible tuning of its physical properties by elastic epitaxial strain. In particular, we have shown that both in-plane electrical conductivity and hole concentration globally tend to slightly decrease with the epitaxial strain (in the range of 10 $S \cdot cm^{-1}$ and 2×10^{20} cm^{-3}, respectively, from compressive to moderate tensile strain). A large decrease of about two or three orders of magnitude has been observed at high tensile strain (down to 0.02 $S \cdot cm^{-1}$ and 10^{18} cm^{-3}, respectively). Hole mobility is maximum for the most relaxed film (on LSAT) and decreases with strain (whatever the sign), consistently with other observations reported in the literature [5]. Accordingly, the Seebeck coefficient (S) continuously increases with epitaxial strain, from 127 $\mu V \cdot K^{-1}$ (compressive) to 208 $\mu V \cdot K^{-1}$ (tensile). The corresponding thermoelectric power factor (PF = $S^2\sigma$) reaches a maximum of around 0.35 μW cm^{-1} K^{-2} for the film in the tensile strain on STO larger than the more relaxed film (in slight compressive strain on LSAT). These interesting results showing how strain can be used to enhance the LSCO thermoelectric factor are submitted for publication [6].

Finally, the effects of the deviation from cationic stoichiometry on the structural and in-plane electronic and thermoelectric properties were investigated in $(La_{0.75}Sr_{0.25})_{1+\delta}CrO_3$ epitaxially strained thin films grown on STO substrate with $-0.3 \leq \delta \leq 0.3$. High-quality single-phase flat epitaxially strained thins films have been grown despite quite large stoichiometry deviation. As expected, large lattice expansion is observed when deviating from the stoichiometry, from c_{LSCO} = 3.844 Å (at δ = 0) to c_{LSCO} = 3.944 Å (at δ = 0.3), confirming the introduction of punctual and/or planar defects with δ. Since the LSCO films with $|\delta| = 0.3$ are insulating (within the limitations of our measurements), the characterization of the physical properties (electronic and thermoelectric) has been only performed for $|\delta| \leq 0.15$ films. Room-temperature electrical conductivity and hole mobility are maximum at the cationic stoichiometry (σ = 10 $S \cdot cm^{-1}$, μ = 0.32 $cm^2 \cdot V^{-1} \cdot s^{-1}$, respectively). However, within the instrumental uncertainties, the electrical conductivity and charge carrier (hole) concentration tend to slightly decrease when δ increases. This behavior is coherent with the Seebeck

coefficient measurements where *S* clearly increases with δ, from ~125 $\mu V \cdot K^{-1}$ (at δ = -0.15, A-deficient) to ~280 $\mu V \cdot K^{-1}$ (at δ = 0.15, B-deficient). We have shown here for the first time that the corresponding thermoelectric PF of LSCO films can be improved by ~50% up to 0.55 $\mu W \cdot cm^{-1} \cdot K^{-2}$ by Cr-deficiency (at δ = 0.15), in comparison to ~0.35 $\mu W \cdot cm^{-1} \cdot K^{-2}$ (at δ = 0) and ~0.16 $\mu W \cdot cm^{-1} \cdot K^{-2}$ (at δ = -0.15). This provides a new effective mean for the enhancement of thermoelectric performance (*ZT*) of *p*-type LSCO films, especially as such cationic off-stoichiometry should show, besides, a reduced thermal conductivity as compared to their stoichiometric LSCO counterpart.

6.2. Work in progress and perspectives

The following studies are under progress as perspectives of this project:

(a) Measurement of the thermal conductivity (by 3ω method) of LSCO with $-0.3 \leq \delta \leq 0.3$ (from Chapter V)

(b) Achieving low contact resistance with metallic electrodes on both *p*-type LSCO and *n*-type SLTO

(c) Achieving epitaxial integration on silicon (especially intrinsic silicon) and assessing its impact on the thermoelectric properties

(d) Microfabrication of a thermoelectric oxide module (ANR MITO)

6.2.1. Thermal conductivity and full *ZT* measurement of LSCO epitaxial films

It would be very interesting to measure the thermal conductivity of $La_{1-x}Sr_xCrO_3$ epitaxial thin films, which remains unknown and is expected to be lower than that of $LaCrO_3$ and $SrCrO_3$, as observed for other solid solutions (down to the so-called alloy limit) such as $Si_{1-x}Ge_x$ [7] or $Sr_xBa_{1-x}TiO_3$ [8] for instance. Especially, the thermal conductivity of LSCO should be rather low, lower than 4.5 $W \cdot m^{-1} \cdot K^{-1}$ as reported for bulk $LaCrO_3$ [9], of about 2 $W \cdot m^{-1} \cdot K^{-1}$ as reported for bulk $LaCrO_3$ as well [10] or less as reported for $La_{0.85}Sr_{0.15}CrO_3$ [11]. This low thermal conductivity value is important for thermoelectric devices to help maintaining a thermal difference and to enhance the overall thermoelectric performance (*ZT* value). A thermal conductivity study would be especially interesting for the cationic

off-stoichiometry series, $(La_{0.75}Sr_{0.25})_{1+\delta}CrO_3$, for which a slight cationic stoichiometry deviation (Cr-deficient) induces an enhancement of the thermoelectric power factor (PF = $S^2\sigma$), in addition to an expected reduction of the thermal conductivity (κ) by the introduction of point defects (Cr vacancy) and/or planar defects (stacking faults such as supplementary AO planes), that would enhance even more the overall figure of merit (ZT = PF/κ) (see Chapter V). Indeed, these thermal conductivity measurements have started with a collaboration with CETHIL using the 3ω method [12]. This task will be continued with the Ph.D. thesis of M. d'Esperonnat (INL, 2019-2022).

The thermal conductivity measurement of thin films is much more difficult than that of bulk materials because it is difficult to discriminate the response of the thin layer from that of the substrate. The electrical 3ω method [12, 13, 14, 15, 16, 17, 18], reported in the early '90s by D. Cahill to measure κ in dielectric films [13] is also suitable to characterize insulating bulk single-crystal materials such as oxide substrates [19]. This method, involving heating by Joule effect through a metallic wire deposited on the sample (Figure 6. 1), can be applied to characterize thermoelectric thin films using an insulating layer between the conducting film surface and the heater. The detailed principle of this technique can be found elsewhere [12, 20, 21].

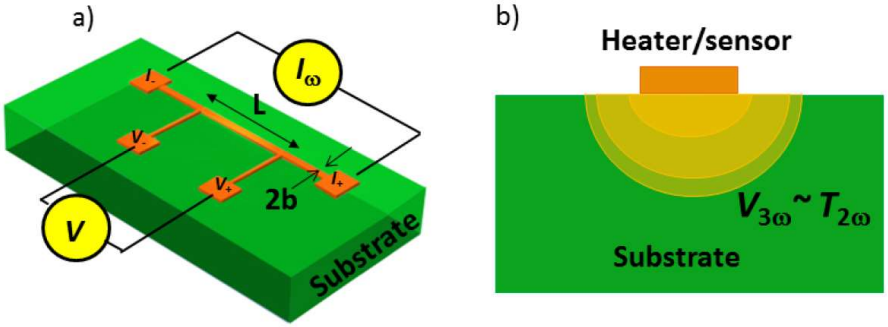

Figure 6. 1 Deposited metallic wire on top of the substrate. (a) Heater/sensor in the 3ω method. (b) Cross-sectional view. Taken from Ref. 20 and 21.

6.2.2. Measurement of the contact resistance with metallic electrodes

Contact resistance between the thermoelectric materials and the conductive interconnects is crucial in a thermoelectric module since there are many *p*-*n* leg pairs with metallic interconnects in-between each. For instance, contact resistance larger than 10^{-10} $\Omega \cdot m^2$ would be detrimental for the module functionality (limited/no current flow in generator mode, and heating by Joule effect in targeted cooling mode) [22]. In the framework of the ANR MITO

project, various conductive materials have been investigated to build an oxide thermoelectric module with the lowest possible contact resistance: metallic Pt, Ti/Au, Cr/Au, and $SrRuO_3$ conductive oxide. The contact resistance is measured using top electrodes patterned by transmission line model (TLM) or circular TLM (CTLM) masks [23, 24, 25] using the photolithography process shown above. This task has also been handled by R. Moalla on both *n*-type La-doped $SrTiO_3$ and *p*-type Sr-doped $LaCrO_3$ thermoelectric epitaxial films. An article is in preparation for these measurements and corresponding results.

6.2.3. Epitaxial integration on silicon

Various *p*-type Sr-doped $LaCrO_3$ epitaxial films have shown high quality and tunable functionalities. Since silicon is still the most used microelectronic platform, heteroepitaxy on Si(001) is particularly for compact integration microelectronic devices. However, this task is challenging because of strong dissimilarities (structural, chemical, and thermal) existing between perovskite oxides and silicon. As other functional perovskite oxides, one possibility to monolithically integrate LSCO epitaxial films on silicon is to use heteroepitaxial $SrTiO_3$/Si(001) buffer layer [26, 27, 28, 29, 30, 31, 32]. This well-known single-crystalline $SrTiO_3$/silicon platform opens the way to the design of more compact, multifunctional, and high-performance technological components based on functional perovskite oxides. For instance, an attempt to fabricate an integrated micro thermoelectric module based on perovskite oxides, partly constituted of LSCO *p*-type legs, is of interest for integrated cooler or thermal energy harvesters for IoT. Such a challenging achievement is the goal of the project ANR MITO (2018-2021) [33]. In this section, the $SrTiO_3$/Si(001) structural matching, the Si surface preparation, the growth conditions of epitaxial $SrTiO_3$ (STO) layer on Si(001) substrate by MBE as well as the first LSCO films epitaxially grown on $SrTiO_3$/Si(001) are presented.

6.2.3.1. $SrTiO_3$/Si(001) structural matching

The STO has a cubic perovskite structure with a lattice constant of 3.905 Å at room temperature, while silicon has a diamond structure with a lattice constant of 5.431 Å. An epitaxial relationship between STO(001) and Si(001) can be found by in-plane rotation of the cell lattices by 45° ($[100]_{STO}$ // $[110]_{Si}$) allowing heteroepitaxy (as shown in Figure 6. 2). The

epitaxial relationship can be written as follows: [100] STO(001) // [110] Si(001). The lattice mismatch at room temperature is around -1.66% between STO (a_{STO} = 3.905 Å) and Si ($a_{Si}/\sqrt{2}$ = 3.84 Å) [34].

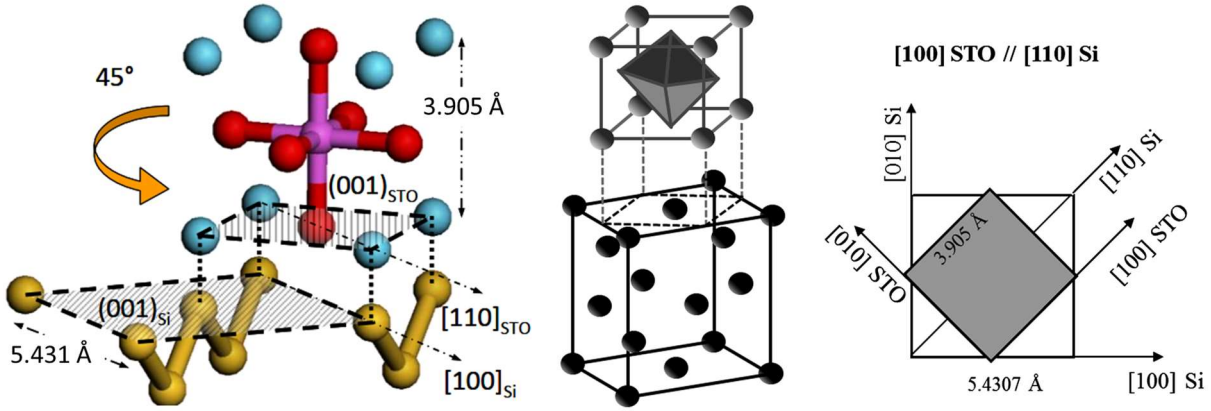

Figure 6. 2 Schematic illustrations of the epitaxial relationship between perovskite oxides and Si unit cells. The atomic model of the epitaxial relationship between the STO(001) layer and the Si(001) substrate. Taken from Ref. 35 and 28.

6.2.3.2. Preparation of the silicon substrate for $SrTiO_3$/Si(001) heteroepitaxy

First, the Si(001) substrate surface has to be prepared to be ready for the early stage of the epitaxial growth of $SrTiO_3$/Si(001). In the following, the Si preparation procedure done at INL is presented. After embedded adsorbed carboxyl-group species by SiO_2 formed in an ozone UV box, an HF-based acid chemical etching is realized to selectively remove the global SiO_2 layer. Then, a ~1-2 nm thick clean SiO_2 layer is regrown in the ozone UV box and is further thermally desorbed *in-situ* in the MBE chamber assisted by Sr, as reported by Wei *et al.* [36]. After this thermal desorption, the Si(001) surface is passivated by half monolayer of Sr (from $SrSi_2$ covalent bonds) and is then ready for the first epitaxial $SrTiO_3$ monolayers [26, 27, 29, 30]. Details on such stage are monitored in-situ by RHEED as shown in Figure 6. 3.

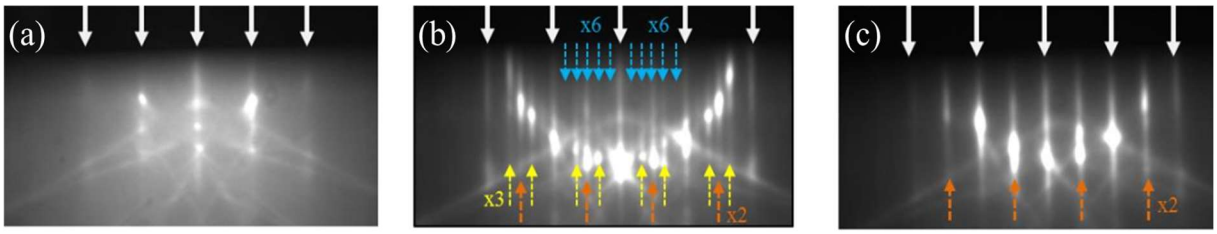

Figure 6. 3 RHEED evaluation of the Si(001) surface along the [110] azimuth during Sr passivation. (a) The surface after chemical treatment; (b) appearance of 3×2 and 6×2 reconstructions of Sr on Si; (c) 1×2 reconstruction after complement of the Sr monolayer under $P(O_2) = 5\times10^{-8}$ Torr at 400 °C. Taken from Ref. 35.

6.2.3.3. Epitaxial growth of $SrTiO_3$ on Si(001)

The epitaxial growth of STO on Si has been well developed at INL for ~15 years [37, 38, 39, 40, 41]. About 10 monolayers of STO are firstly deposited on Si at relatively low temperatures (350-390 °C) under a low oxygen partial pressure (5×10^{-8} Torr) to avoid degradation of the interface. It is important to note that the partial pressure of oxygen $P(O_2)$ should not exceed about 5×10^{-8} Torr at the first growth stage to avoid a Si surface reaction with oxygen and the formation of silica which could prevent the epitaxial growth of $SrTiO_3$. An excess of Sr is then necessary to guarantee the crystallization of STO at this relatively low temperature [30]. This layer is partially amorphous but has an abrupt interface with Si and is then annealed under vacuum at around 440 °C for recrystallization. The first 10 monolayers are used as a template for the second growth.

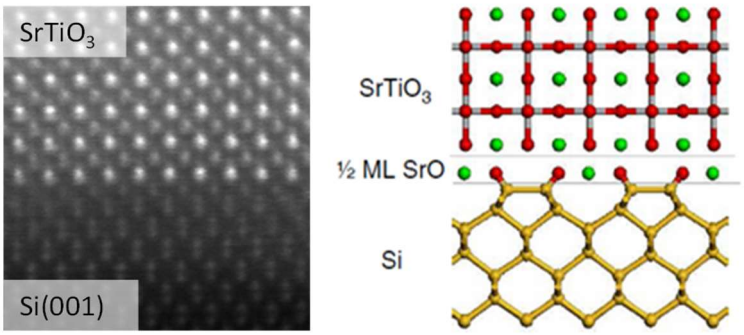

Figure 6. 4 Schematic illustrations of the epitaxial oxide heterostructure on Si and a cross-sectional transmission electron microscopy image of the STO/Si interface. Taken from Ref. 30 and 31.

Figure 6. 4 shows a cross-sectional transmission electron microscopy image of the epitaxial STO/Si interface from these growth conditions [30, 31]. A clear abrupt interface between the single-crystal STO film and Si can be observed without the SiO_2 layer. Then, the optimal conditions for the subsequent stoichiometric STO layer are 420 °C and $P(O_2) = 1\times10^{-7}$ Torr.

Figure 6. 5a and b show the RHEED patterns of an STO layer about 37 nm thick along the [100] and [110] azimuths. Well-contrasted lines reveal a good crystalline quality of a film having a flat surface. The absence of the 2nd order reconstruction on two azimuths proves the good stoichiometry [42]. Figure 6. 5c indicates only diffraction peaks corresponding to the {00*l*} reflections of the STO film and substrate. No other orientation nor other phases than STO(00*l*) are present in the epitaxial film.

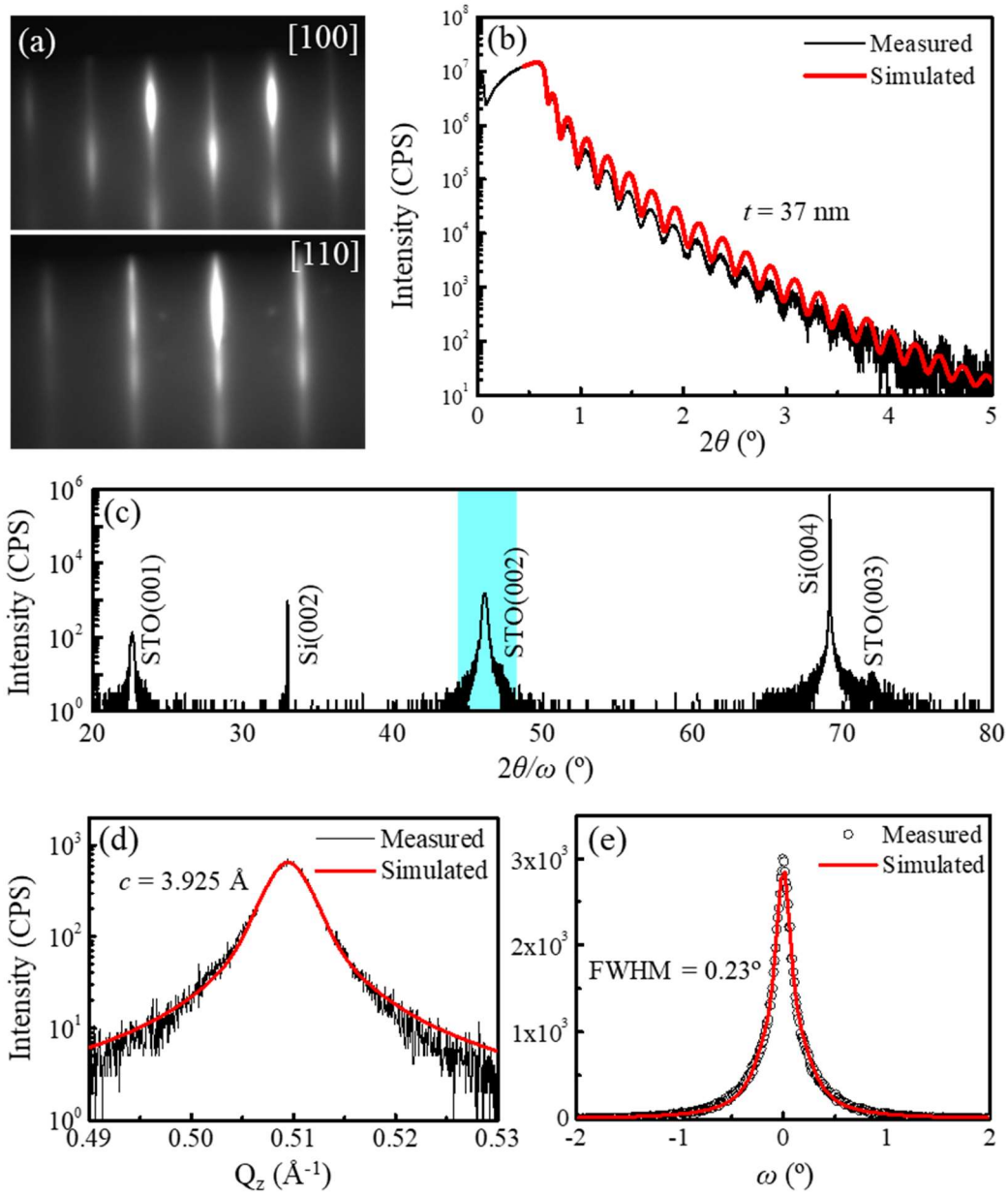

Figure 6. 5 (a) RHEED patterns of STO/Si along the [100] and [110] azimuths. (b) XRR curve of STO/Si including the raw data (black line) and the fitting curve (red line). (c) XRD $2\theta/\omega$ scans from 20º to 80º. (d) XRD analysis near the (002) reflection. (e) XRD ω-scan around the STO(002) reflection.

The out-of-plane lattice parameter is extracted from Figure 6. 5d (c_{STO} = 3.925 Å). This lattice expansion can be due to either the theoretical in-plane compression or most probably to off-stoichiometry from Sr excess in the early stage of the growth and oxygen vacancies from the low oxygen partial pressures. The mosaicity, measured on the STO(002) reflection, of this STO epitaxial layer, is 0.23° (Figure 6. 5e), which is slightly larger than that of STO layers epitaxially grown on perovskite oxide substrates. Noted that the position of STO(002) depends on the growth conditions, such as the temperature (thermal strain), the partial pressure of oxygen (oxygen vacancies, interfacial SiO_2 regrowth, and flux deviation), cationic

stoichiometry (Sr excess in the early stage), thickness (structural relaxation), etc [30, 32, 35, 41].

6.2.3.4. Epitaxial growth of $La_{0.75}Sr_{0.25}CrO_3$ thin film on $SrTiO_3$/Si(001)

The STO/Si(001) can be used as a pseudo-substrate of excellent quality for the subsequent epitaxial growth of functional oxides, as the *p*-type $La_{1-x}Sr_xCrO_3$ and *n*-type $La_xSr_{1-x}TiO_3$ thermoelectric perovskite oxides for instance. In this section, epitaxial $La_{0.75}Sr_{0.25}CrO_3$ (LSCO) thin film was grown by MBE on the STO/Si(001) template presented above. The same growth conditions as the LSCO/STO(001) layer were used: 700 °C, $P(O_2) = 1\times10^{-7}$ Torr, and 0.15 nm/min (~30 nm in total).

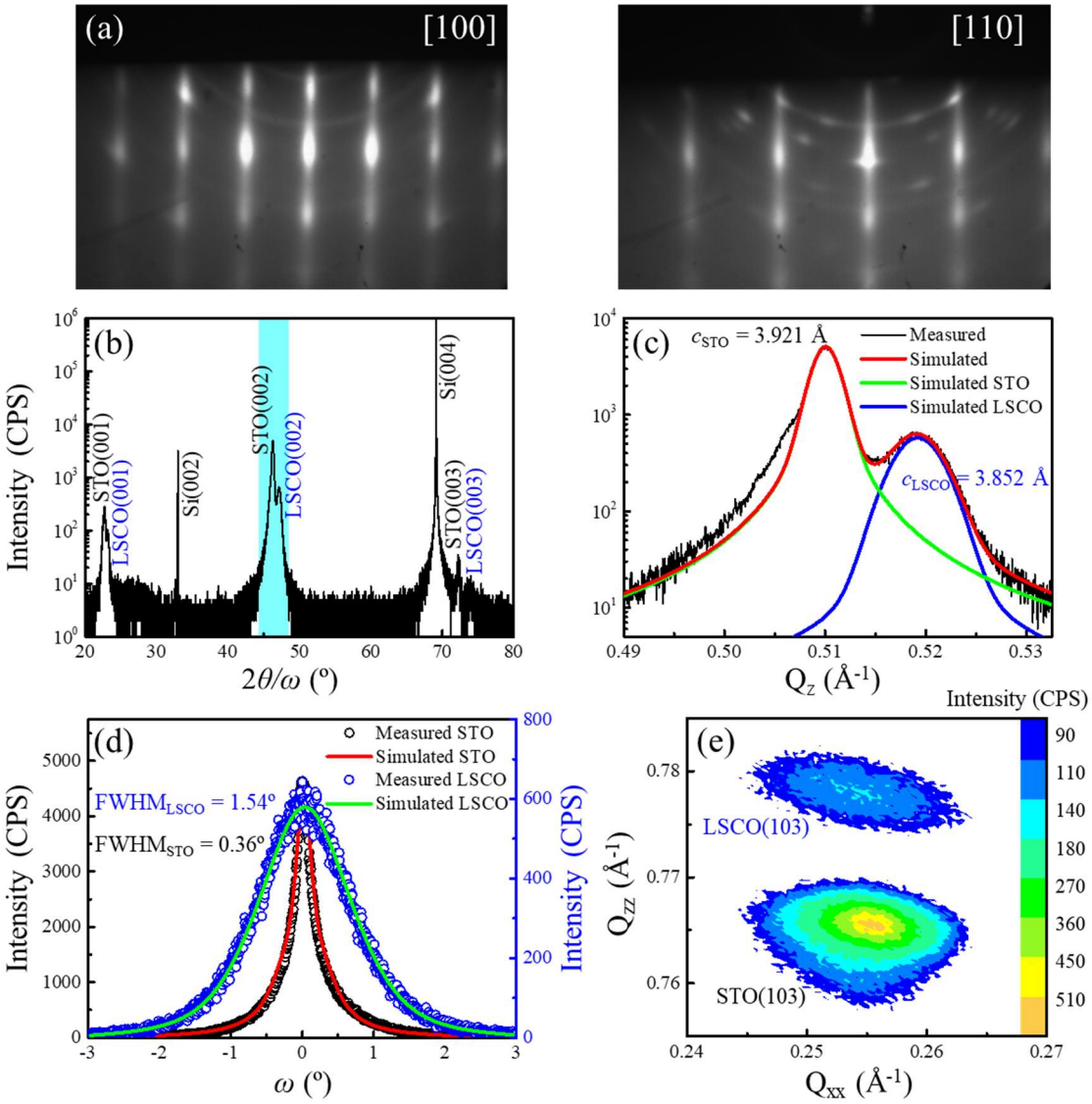

Figure 6. 6 (a) RHEED patterns of LSCO/STO/Si along the [100] and [110] azimuths. (b) XRD 2θ/ω scans from 20° to 80°. (c) XRD analysis near the (002) reflection. (d) XRD ω-scans around the STO(002) and LSCO(002) reflections. (e) RSM recorded around the asymmetric (103) reflection of LSCO thin film on STO/Si.

Figure 6. 6a shows the RHEED patterns recorded at the end of the growth of 28 nm thick LSCO thin films. There is no 2nd order reconstruction on two azimuths, which confirms the stoichiometry. Rather spotty patterns indicate that the film is slightly rougher than LSCO films directly grown on perovskite oxide substrates shown in Chapter IV for instance. A slight sign of polycrystalline (visible Debye-Scherrer rings) can be seen in Figure 6. 6a. This can be explained by the relatively low thermal instability of the $SrTiO_3$/Si layer and possible cationic interdiffusions, probably enhanced by Sr-excess and defects in the STO layer. However, in Figure 6. 6b, it is not quite clear from the wide XRD scan to distinguish other phases and orientations from the perovskite LSCO(00*l*). The out-of-plane lattice parameters of epitaxially-strained LSCO and STO are extracted from Figure 6. 6c (c_{LSCO} = 3.852 Å and c_{STO} = 3.921 Å), and confirmed by the RSM measurement around the asymmetrical (103) reflection (Figure 6. 6e). The in-plane lattice parameter of the LSCO layer (a_{LSCO}) is about 3.922 Å. The ω-scans measured around the LSCO(002) and STO(002) reflections are shown in Figure 6. 6d. The mosaicities are 1.54° and 0.36° respectively. Due to the crystalline quality and instability of the STO/Si template, the quality of LSCO is relatively lower than those grown on perovskite oxide substrates as shown in Chapter IV for instance (*i.e.* LSCO on LAO, LSAT, STO, and DSO commercial perovskite-type substrates). Note that the full width at half maxima (FWHM) of the STO(002) reflection shown in Figure 6. 6d (0.23°) is slightly larger than that shown in Figure 6. 5e (0.36°). Slight degradation occurs in the STO layer during the LSCO growth at high temperature (700 °C) which is much higher than that used for the STO layer growth (420 °C).

XPS was used to estimate the chemical composition (Figure 6. 7). To directly compare binding energies, the Cr $2p_{3/2}$ peaks (Figure 6. 7c) are all shifted to 576 eV and normalized to 1. For each sample, the same shift and normalization are then applied to La 4*d* and Sr 3*d* spectra (Figure 6. 7a and b respectively). The targeted chemical compositions within instrumental uncertainties of LSCO films grown on LAO, LSAT, STO, and DSO substrates are already summarized in Table 4.2 in Chapter IV. It can be seen that the XPS spectra of LSCO grown on STO/Si (green curves) coincide well with all other curves, indicating the good stoichiometry of this LSCO layer grown on STO/Si(001).

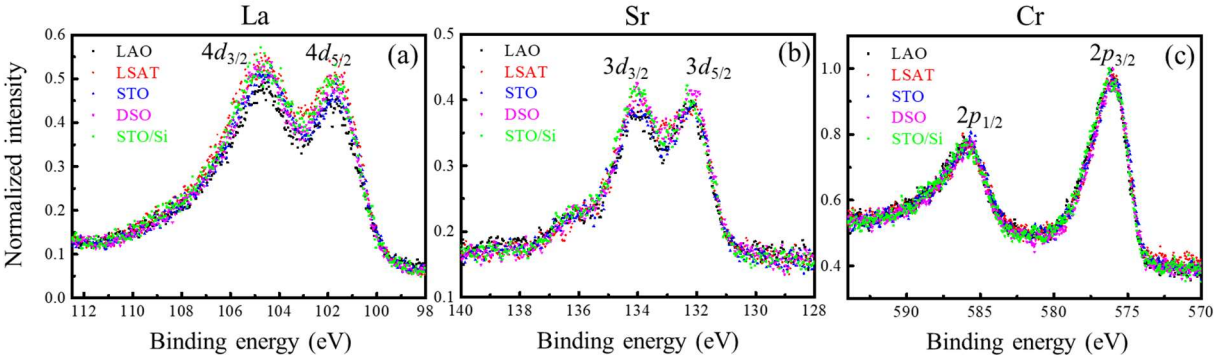

Figure 6. 7 XPS measurements of (a) La 4*d*, (b) Sr 3*d*, and (c) Cr 2*p* core level for LSCO films grown on different substrates.

6.2.4. Micro-fabrication of functional thermoelectric perovskite-oxide module

After the integration on silicon, the thermoelectric micromodule (µ-TE) has to be fabricated with microelectronic technology processes. However, such a fabrication requires various challenging selective etching steps and localized epitaxial oxide growth on STO/Si(001). These challenging technological developments are under progress within the project ANR MITO and are mainly handled by R. Moalla. These tasks are beyond the scope of my Ph.D. thesis.

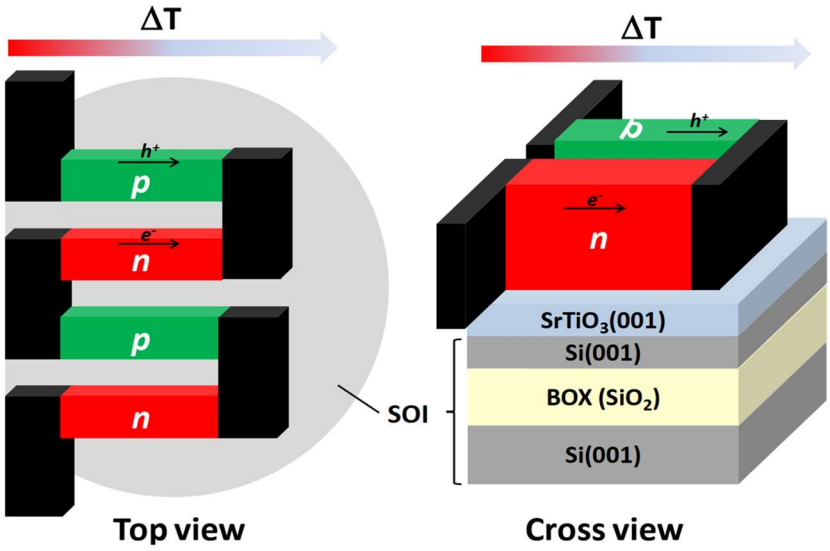

Figure 6. 8 Simplified sketch of a planar thermoelectric micromodule architecture in top- and cross-view on silicon-on-insulator (SOI).

Figure 6. 8 shows the targeted module planar architecture of the µ-TE. Since the generated output voltage of the module is proportional to the number of micro *p*-*n* leg pairs

($N_{p\text{-}n}$) and the temperature difference ($U = N_{p\text{-}n} \times \Delta T \times S$), the number and length of leg pairs can be maximized to obtain the highest output power density. The patterned leg-pairs and interconnects will be sequentially deposited on 2-inch SOI wafers with the previous epitaxial $SrTiO_3$ layer with sequential photolithography and lift-off process.

The final micro-module is planned to be tested in power generation mode (via Seebeck effect). Then, it could be judged whether the μ-TE is efficient and can be integrated close to microelectronic devices. With the emergence of more low-power devices and the gradual improvement of thermoelectric materials (*ZT*, low toxicity, stability, abundance…), μ-TE devices would be applied in more fields and achieve success in the future market.

6.3. References

[1] D. Han, M. Bouras, C. Botella, A. Benamrouche, B. Canut, G. Grenet, G. Saint-Girons, and R. Bachelet. Structural properties of strained epitaxial $La_{1+\delta}CrO_3$ thin films. Journal of Vacuum Science & Technology A: Vacuum, Surfaces, and Films, 2019, 37(2): 021512.

[2] K. H. L. Zhang, Y. Du, A. Papadogianni, O. Bierwagen, S. Sallis, L. F. Piper, M. E. Bowden, V. Shutthanandan, P. V. Sushko, and S. A. Chambers. Perovskite Sr-doped $LaCrO_3$ as a new p-type transparent conducting oxide. Advanced Materials, 2015, 27(35): 5191-5195.

[3] K. H. L. Zhang, Y. Du, P. Sushko, M. E. Bowden, V. Shutthanandan, S. Sallis, L. F. Piper, and S. A. Chambers. Hole-induced insulator-to-metal transition in $La_{1-x}Sr_xCrO_3$ epitaxial films. Physical Review B, 2015, 91(15): 155129.

[4] D. Han, M. Bouras, C. Botella, A. Benamrouche, B. Canut, G. Grenet, G. Saint-Girons, and R. Bachelet. Poisson ratio and bulk lattice constant of $(Sr_{0.25}La_{0.75})CrO_3$ from strained epitaxial thin films. Journal of Applied Physics, 2019, 126(8): 085304.

[5] M. Choi, A. B. Posadas, C. A. Rodriguez, A. O'Hara, H. Seinige, A. J. Kellock, M. M. Frank, M. Tsoi, S. Zollner, V. Narayanan, and A. A. Demkov. Structural, optical, and electrical properties of strained La-doped $SrTiO_3$ films. Journal of Applied Physics, 2014, 116(4): 043705.

[6] D. Han, M. Bouras, C. Botella, A. Benamrouche, B. Canut, G. Grenet, G. Saint-Girons, and R. Bachelet. Tuning of thermoelectric power factor in p-type Sr-doped $LaCrO_3$ thin films by epitaxial strain. Submitted to ACS Applied Electronic Materials, 2020.

[7] Y. Lee, A. J. Pak, and G. S. Hwang. What is the thermal conductivity limit of silicon germanium alloys? Physical Chemistry Chemical Physics, 2016, 18(29): 19544-19548.

[8] J. Ravichandran, A. K. Yadav, R. Cheaito, P. B. Rossen, A. Soukiassian, S. J. Suresha, J. C. Duda, B. M. Foley, C. Lee, Y. Zhu, A. W. Lichtenberger, J. E. Moore, D. A. Muller, D. G. Schlom, P. E. Hopkins, A.

Majumdar, R. Ramesh, and M. A. Zurbuchen. Crossover from incoherent to coherent phonon scattering in epitaxial oxide superlattices. Nature Materials, 2014, 13(2): 168-172.

[9] N. Sakai and S. Stølen. Heat capacity and thermodynamic properties of lanthanum (III) chromate (III): $LaCrO_3$, at temperatures from 298.15 K. Evaluation of the thermal conductivity. The Journal of Chemical Thermodynamics, 1995, 27(5): 493-506.

[10] S. A. Suvorov and A. P. Shevchik. A heating module equipped with lanthanum chromite-based heaters. Refractories and Industrial ceramics, 2004, 45(3): 196-200.

[11] W. J. Weber, C. W. Griffin, and J. L. Bates. Effects of cation substitution on electrical and thermal transport properties of $YCrO_3$ and $LaCrO_3$. Journal of the American Ceramic Society, 1987, 70(4): 265-270.

[12] W. Jaber and P. O. Chapuis. Non-idealities in the 3ω method for thermal characterization in the low-and high-frequency regimes. AIP Advances, 2018, 8(4): 045111.

[13] D. G. Cahill. Thermal conductivity measurement from 30 to 750 K: the 3ω method. Review of Scientific Instruments, 1990, 61(2): 802-808.

[14] T. Borca-Tasciuc, A. Kumar, and G. Chen. Data reduction in 3ω method for thin-film thermal conductivity determination. Review of Scientific Instruments, 2001, 72(4): 2139-2147.

[15] D. De Koninck. Thermal conductivity measurements using the 3-omega technique: Application to power harvesting microsystems (Thesis). McGill University, Montreal, Canada, 2008.

[16] J. Y. Duquesne, D. Fournier, and C. Fretigny. Analytical solutions of the heat diffusion equation for 3ω method geometry. Journal of Applied Physics, 2010, 108(8): 086104.

[17] T. Hänninen. Implementing the 3-omega technique for thermal conductivity measurements (Thesis). University of Jyväskylä, Jyväskylä, Finland, 2013.

[18] W. Jaber, A. Assy, S. Lefevre, S. Gomès, and P. O. Chapuis. Thermal conductivity measurements with the 3ω method and scanning thermal microscopy. 19th International Workshop on Thermal Investigations of ICs and Systems (THERMINIC). IEEE, 2013: 54-57.

[19] E. Langenberg, E. Ferreiro-Vila, V. Leborán, A. O. Fumega, V. Pardo, and F. Rivadulla. Analysis of the temperature dependence of the thermal conductivity of insulating single crystal oxides. APL Materials, 2016, 4(10): 104815.

[20] W. Jaber. Phonon heat conduction probed by means of an electro-thermal method involving deposited micro and nanowires (Thesis). Institut National des Sciences Appliquées de Lyon, Lyon, France, 2016.

[21] A. Pic. Numerical and experimental investigations of self-heating phenomena in 3D Hybrid Bonding imaging technologies (Thesis). Institut National des Sciences Appliquées de Lyon, Lyon, France, 2019.

[22] R. Enright, S. Lei, G. Cunningham, I. Mathews, R. Frizzell, and A. Shen. Integrated thermoelectric cooling for silicon photonics. ECS Journal of Solid State Science and Technology, 2017, 6(3): N3103.

[23] J. H. Bahk, T. Favaloro, and A. Shakouri. *Thin film thermoelectric characterization techniques*, Chapter 3 in Annual Review of Heat Transfer, edited by G. Chen. Begell House Inc. New York, 2013.

[24] G. A. Slack and D. M. Rowe. *Handbook of thermoelectrics*. CRC Press Book, 1995.

[25] D. K. Schroder. Chapter 3 in *Semiconductor material and device characterization*. John Wiley & Sons, 2006.

[26] J. W. Reiner, A. M. Kolpak, Y. Segal, K. F. Garrity, S. Ismail-Beigi, C. H. Ahn, and F. J. Walker. Crystalline oxides on silicon. Advanced Materials, 2010, 22(26-27): 2919-2938.

[27] A. A. Demkov and A. B. Posadas. *Integration of functional oxides with semiconductors*. Springer, New York, 2014.

[28] S. H. Baek and C. B. Eom. Epitaxial integration of perovskite-based multifunctional oxides on silicon. Acta Materialia, 2013, 61(8): 2734-2750.

[29] R. A. McKee, F. J. Walker, and M. F. Chisholm. Crystalline oxides on silicon: The first five monolayers. Physical Review Letters, 1998, 81(14): 3014.

[30] G. Saint-Girons, R. Bachelet, R. Moalla, B. Meunier, L. Louahadj, B. Canut, A. Carretero -Genevrier, J. Gazquez, P. Regreny, C. Botella, J. Penuelas, M. G. Silly, F. Sirotti, and G. Grenet. Epitaxy of $SrTiO_3$ on silicon: The knitting machine strategy. Chemistry of Materials, 2016, 28(15): 5347-5355.

[31] J. M. Vila-Fungueiriño, R. Bachelet, G. Saint-Girons, M. Gendry, M. Gich, J. Gazquez, E. Ferain, F. Rivadulla, J. Rodriguez-Carvajal, N. Mestres, and A. Carretero-Genevrier. Integration of functional complex oxide nanomaterials on silicon. Frontiers in Physics, 2015, 3: 38.

[32] R. Moalla, B. Vilquin, G. Saint-Girons, G. Le Rhun, E. Defay, G. Sebald, N. Baboux, and R. Bachelet. Huge gain in pyroelectric energy conversion through epitaxy for integrated self-powered nanodevices. Nano Energy, 2017, 41: 43-48.

[33] Website of the project ANR MITO. Retrieved from: https://anr.fr/Project-ANR-17-CE05-0018.

[34] J. W. Park, S. H. Baek, C. W. Bark, M. D. Biegalski, and C. B. Eom. Integration of epitaxial colossal magnetoresistive films onto Si (100) using $SrTiO_3$ as a template layer. Applied Physics Letters, 2005, 86(1): 012503.

[35] R. Moalla. Couches minces d'oxydes pyroélectriques épitaxiées sur Si pour la récupération d'énergie thermique (Thesis). Institut des Nanotechnologies de Lyon, Ecole Centrale de Lyon, Lyon, France, 2016.

[36] Y. Wei, X. Hu, Y. Liang, D. C. Jordan, B. Craigo, R. Droopad, Z. Yu, A. Demkov, J. L. Edwards Jr., and W. J. Ooms. Mechanism of cleaning Si (100) surface using Sr or SrO for the growth of crystalline $SrTiO_3$ films. Journal of Vacuum Science & Technology B: Microelectronics and Nanometer Structures Processing, Measurement, and Phenomena, 2002, 20(4): 1402-1405.

[37] G. Delhaye, C. Merckling, M. El-Kazzi, G. Saint-Girons, M. Gendry, Y. Robach, G. Hollinger, L. Largeau, and G. Patriarche. Structural properties of epitaxial $SrTiO_3$ thin films grown by molecular beam epitaxy on Si(001). Journal of Applied Physics, 2006, 100(12): 124109.

[38] G. Delhaye, M. El-Kazzi, M. Gendry, G. Hollinger, and Y. Robach. Hetero-epitaxy of $SrTiO_3$ on Si and control of the interface. Thin Solid Films, 2007, 515(16): 6332-6336.

[39] G. Niu. Epitaxy of crystalline oxides for functional materials integration on silicon (Thesis). Institut des Nanotechnologies de Lyon, Ecole Centrale de Lyon, Lyon, France, 2010.

[40] G. Niu, B. Vilquin, J. Penuelas, C. Botella, G. Hollinger, and G. Saint-Girons. Heteroepitaxy of $SrTiO_3$ thin films on Si(001) using different growth strategies: Toward substratelike quality. Journal of Vacuum Science & Technology B, Nanotechnology and Microelectronics: Materials, Processing, Measurement, and Phenomena, 2011, 29(4): 041207.

[41] L. Louahadj. Développement de l'épitaxie par jets moléculaires pour la croissance d'oxydes fonctionnels sur semiconducteurs (Thesis). Institut des Nanotechnologies de Lyon, Ecole Centrale de Lyon, Lyon, France, 2014.

[42] A. P. Kajdos and S. Stemmer. Surface reconstructions in molecular beam epitaxy of $SrTiO_3$. Applied Physics Letters, 2014, 105(19): 191901.

Résumé de thèse étendu en français

1. Introduction

1.1. Contexte global

D'une manière générale, les énergies renouvelables et la récupération d'énergie, sans émission de gaz à effet de serre, jouent un rôle de plus en plus important dans notre monde toujours plus énergivore qui connaît une crise environnementale/climatique sans précédent. Plus particulièrement, à l'échelle des dispositifs microélectroniques, de nombreux petits capteurs sans fils composant l'internet des objets en pleine expansion peuvent être alimentés de manière autonome par des dispositifs de récupération d'énergie. Ces développements s'intègrent dans la vision « More than Moore » actuelle de l'industrie microélectronique qui consiste en l'intégration de diverses fonctionnalités sur puce autres que des fonctions de mémoire et logique. D'autre part, la chaleur dissipée par les microdispositifs opto-électroniques est perdue ou non contrôlée. Pourtant, il y a un besoin de contrôler efficacement la température des microdispositifs ou de tirer profit de cette source de chaleur (énergie thermique). La recherche dans le domaine de la thermoélectricité et des matériaux thermoélectriques, qui lie l'énergie thermique à l'énergie électrique, a connu un regain d'intérêt ces dernières décennies du fait de ce contexte global.

1.2. Thermoélectricité et matériaux thermoélectriques

1.2.1. Introduction

Comme son nom l'indique, la thermoélectricité lie l'énergie thermique (flux de chaleur) à l'énergie électrique (courant électrique) dans un matériau. Un matériau thermoélectrique est un matériau fonctionnel qui permet de convertir directement l'énergie thermique en énergie électrique de manière réciproque. Lorsqu'une différence de température existe entre les deux extrémités d'un matériau, une différence de potentiel électrique se forme dans le matériau par effet *Seebeck*. A l'inverse, lorsqu'une différence de potentiel est maintenue aux bornes du matériau thermoélectrique, une différence de température est induite par effet *Peltier*. Par conséquent, les matériaux thermoélectriques sont particulièrement adaptés pour les applications de récupération d'énergie thermique (génération d'électricité) et de refroidissement (gestion de l'énergie thermique). Les domaines d'application peuvent être très variés, allant de l'aérospatial à la microélectronique, en passant par les objets du quotidien avec l'internet des objets et

l'alimentation de leurs capteurs communiants sans fil qui sont souhaités autonomes.

En plus des qualités de stabilité chimique et thermique, de l'abondance, de la non toxicité et des faibles coûts des éléments qui composent le matériau thermoélectrique, leur performance thermoélectrique est définie par un facteur de mérite adimensionnel (*ZT)* comme suit [1] :

$$Z = \frac{S^2\sigma}{\kappa} \qquad (1)$$

où S, σ, κ et T sont respectivement le coefficient Seebeck ($S = \Delta V/\Delta T$), la conductivité électrique ($\sigma = \rho^{-1}$), la conductivité thermique et la température absolue.

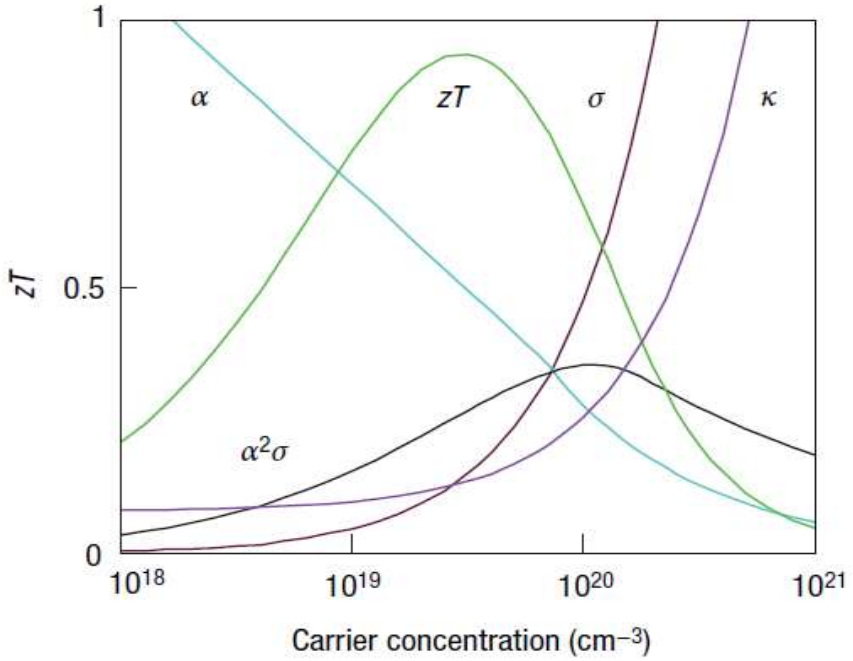

Figure 1 La valeur *ZT* implique un compromis entre la conductivité électrique σ, le coefficient de Seebeck α et la conductivité thermique κ en fonction de la concentration de porteurs. Le facteur de puissance thermoélectrique $\alpha^2\sigma$ est maximisé à une concentration de porteurs plus élevée que *ZT*. De la ref. 1.

Le facteur de mérite *ZT* peut être vu comme un rapport de deux composantes : la performance de conversion thermoélectrique (facteur de puissance thermoélectrique PF = $S^2\sigma$) et la conductivité thermique comprenant une partie électronique et une autre phononique de réseau ($\kappa = \kappa_e + \kappa_L$). Les matériaux thermoélectriques les plus performants (maximum de *ZT*) sont des semiconducteurs fortement dopés, ou dit dégénérés dans la gamme des 10^{19}-10^{20} cm^{-3} (Figure 1 [1]). L'optimisation des matériaux thermoélectriques (augmentation du *ZT*) repose sur l'ingénierie de structure de bande (optimisation du dopage, maximisation du coefficient de

Seebeck) afin d'augmenter le PF, et l'ingénierie phononique (nanostructuration, défauts, inclusions…) afin de diminuer la conductivité thermique globale.

1.2.2. Principaux matériaux thermoélectriques traditionnels

À l'heure actuelle, la plupart des matériaux thermoélectriques appliqués et ayant de bonnes performances sont des alliages métalliques, notamment à base de tellurures, d'antimoine et selenium : $(Bi,Sb)_2Te_3$, PbTe, $CoSb_3$, SiGe, SnSe, etc., et leurs valeurs *ZT* peuvent atteindre 1 à 3 en fonction de leur température de fonctionnement et leur structuration (Figure 2) [1, 2, 3, 4, 5].

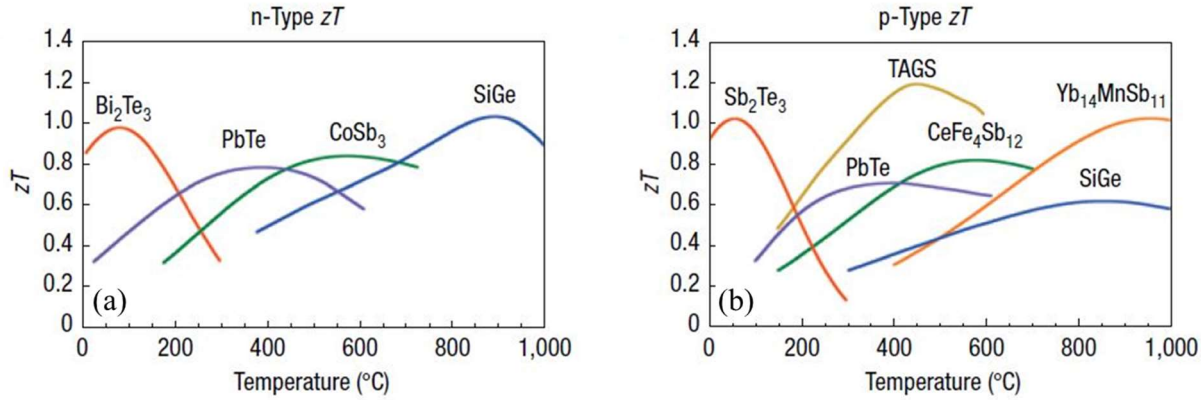

Figure 2 *ZT* de matériaux commerciaux pour la production d'énergie thermoélectrique résumé en 2008, (a) type *n* et (b) type *p*. De la ref. 1.

Au cours des dernières décennies, l'émergence de certains nouveaux types de matériaux thermoélectriques, tels que les alliages semi-Heusler, les phases clathrates, skutterudites, zintl, les oxydes, en plus des différentes nanostructurations et dopages possibles, a permis d'augmenter les facteurs de mérites rendant possible un développement de plus grande ampleur et des études plus approfondies des mécanismes intrinsèques thermoélectriques.

1.2.3. Oxydes pérovskites comme matériaux thermoélectriques alternatifs

Les oxydes ont commencé à être considérés dans le domaine de la thermoélectricité depuis les publications des résultats sur les cobaltites de sodium Na_xCoO_2 ayant une structure en feuillets [6, 7, 8]. Quelques années plus tard, de grands facteurs de puissance, comparables à ceux

de Bi_2Te_3 de référence, ont été publiés avec le titanate de strontium ($SrTiO_3$) dopé au La [9]. Ces publications ont montré que les oxydes en général, et de structure pérovskite (ABO_3) en particulier, peuvent être utilisés comme matériaux thermoélectriques alternatifs [10]. Les oxydes de structure pérovskite ont l'avantage d'être très flexible chimiquement et donc d'avoir des propriétés accordables par substitutions cationiques partielles. Selon la littérature, leur valeur *ZT* la plus élevée obtenue expérimentalement est proche de 0.4 [11] (voir Figure 3). Cependant, les oxydes thermoélectriques de structure pérovskite sont principalement de type *n* (*i.e.* $SrTiO_{3-\delta}$, $SrTiO_3$ dopé La, $SrTiO_3$ dopé Nb) et présentent des meilleures performances thermoélectriques que celles de type *p* (*i.e.* $LaCrO_3$ dopé Sr, $LaMnO_3$ dopé Sr). Les lacunes d'oxygène qui conduisent à un dopage *n*, sont un paramètre important à prendre en compte et contrôler. Par conséquent, il y a un besoin de développer des oxydes de structure pérovskite avec des propriétés thermoélectriques de type *p* améliorées. Cette thèse s'inscrit dans ce contexte particulier.

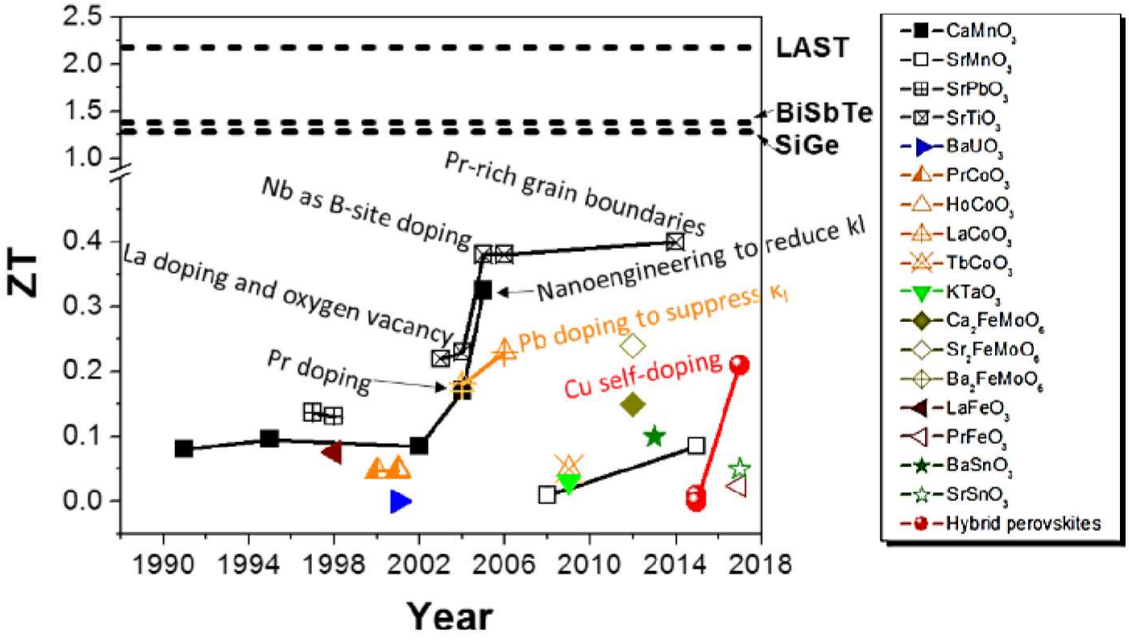

Figure 3 Résumé des valeurs *ZT* des pérovskites oxydes par année. Les valeurs *ZT* de tous les matériaux ont été extraites de la littérature à sa température de fonctionnement optimale. Les trois lignes en pointillés sont les valeurs *ZT* de BiSbTe [12], $AgPb_{18}SbTe_{20}$ (LAST) [13], et SiGe [14], ayant une température différente. De la ref. 11.

1.3. Objectifs de la thèse

Cette thèse doctorale porte sur la croissance et l'étude de films épitaxiés thermoélectriques

de $LaCrO_3$ dopé au Sr (solutions solides $La_{1-x}Sr_xCrO_3$) de type *p*. L'impact de différents paramètres (taux de dopage/substitution cationique, déformation épitaxiale, déviation par rapport à la stœchiométrie cationique) sur leurs propriétés structurales et thermoélectriques est étudié. Cette thèse s'intègre dans le projet ANR MITO (first MIcro-Thermoelectric module based on Oxides) [15] visant à intégrer des matériaux thermoélectriques prometteurs à base d'oxydes pérovskites dans des modules thermoélectriques micrométriques pour la gestion thermique efficace (refroidissement ou récupération) sur les plates-formes micro-optoélectroniques.

2. Méthodes expérimentales

Cette section, résumant le Chapitre II, est dédiée à présenter les principales techniques expérimentales qui ont été utilisées lors de mes études doctorales. Elles sont classées en trois catégories en fonction des étapes expérimentales successives : d'abord la croissance des couches minces, puis les caractérisations structurales et enfin les mesures des propriétés physiques (électroniques et thermoélectriques).

2.1. Méthode d'élaboration : épitaxie par jet moléculaire (MBE)

L'épitaxie par jet moléculaire (MBE), qui a été utilisée pour la première fois dans les années 1970 par A. Y. Cho et J. R. Arthur [16, 17], est une technique de croissance cristalline de couche atomique par couche atomique, basée sur l'émission d'un flux atomique ou moléculaire sur un substrat monocristallin chauffé dans un environnement à ultra-vide (UHV) [18]. L'épitaxie survient lorsqu'il y a un certain accord cristallographique entre la couche et le substrat (orientation préférentielle de la couche hors plan et dans le plan avec le substrat). La technique MBE est capable de produire des hétérostructures épitaxiées de très haute qualité et haute pureté avec un contrôle précis des compositions chimiques et des interfaces à l'échelle de la fraction de monocouche atomique. Cette technique, d'abord utilisé pour les semiconducteurs, est moins mature pour la croissance des oxydes fonctionnels. Dans cette thèse, nous avons utilisé des cellules à effusion de Knudsen pour tous les éléments à évaporer par effet Joule (La, Sr, Cr, Ti) et de l'oxygène moléculaire (O_2) comme source oxydante. Les conditions de croissance (température, pressions partielles d'oxygène, vitesse de croissance…) sont rappelées en début de chaque section pour chaque séries présentées. Cette méthode de mesure produit une

incertitude de composition chimique inférieure à 4,4%.

2.2. Caractérisations des propriétés structurales

Nous avons utilisés différents outils de caractérisation *in-situ* et *ex-situ* pour caractériser les propriétés structurales des couches minces (morphologie de surface, qualité cristalline, épaisseur, paramètres de maille, composition chimique, etc). Les principales utilisées sont décrites brièvement ci-dessous.

2.2.1. Diffraction d'électrons de haute énergie en réflexion (RHEED)

Les propriétés structurales des films minces sont caractérisées dès la croissance *in-situ* grâce à la diffraction d'électrons de haute énergie en réflexion (RHEED) qui est installé sur le bâti de croissance MBE. C'est une technique non destructive qui permet de contrôler la qualité cristalline et la morphologie qualitative des surfaces. Il s'agit du premier outil de caractérisation donnant des informations importantes pendant et après la croissance.

2.2.2. Microscopie à force atomique (AFM)

La microscopie à force atomique (AFM) est une technique de champ proche permettant de caractériser la morphologie et la rugosité de surface avec une résolution sub-nanométrique en hauteur sur une surface de quelques micromètres. Elle permet également de mesurer un contraste chimique de surface si la surface est plane par friction (déflexion latérale de la pointe) en mode contact (Friction Force Microscopy, FFM) ou par analyse des phases en mode oscillatoire (tapping).

2.2.3. Réflectométrie et diffraction des rayons X (XRR et XRD)

La diffraction des rayons X (XRD) permet d'étudier les propriétés structurales des matériaux. Selon la loi de Bragg, la diffraction résulte de diffusions élastiques cohérentes d'ondes électromagnétiques dans un réseau régulier de diffuseurs (arrangement répétitif d'atomes dans un cristal par exemple). L'INL est équipé d'un diffractomètre SmartLab Rigaku

avec une anode tournante en cuivre de haute brillance (9 kW) et monochromateur Ge(220) à deux réflexions ($\lambda_{Cu\ K\ \alpha 1}$ = 1,54056 Å). A ces longueurs d'onde, parce que la longueur d'onde des rayons X émis est du même ordre de grandeur que les distances inter-réticulaires (d_{hkl}, espacement entre les plans cristallins), la diffraction régie par la loi de Bragg permet de sonder la structure atomique (paramètres de maille, l'orientation cristalline, défauts cristallins, mosaïcité…). Dans cette thèse, diverses mesures telles que la réflectivité des rayons X (XRR), les mesures hors plan standards ($2\theta/\omega$ scans), ainsi que des cartographies de l'espace réciproque (RSM) et des mesures de figures de pôle ont été utilisées.

2.2.4. Spectrométrie photoélectronique par rayons X (XPS)

La spectrométrie photoélectronique par rayons X (XPS) permet de caractériser le degré d'oxydation des éléments (leur valence), leur environnement chimique (liaisons), ainsi que la composition élémentaire d'un matériau. L'INL est équipé d'XPS avec une anode en Al et monochromateur ($h\nu_{Al\ K\alpha}$ = 1486,6 eV). Ces énergies permettent de mesurer les électrons excités et photoémis par les rayons X issus des atomes se situant à 5-10 nm de profondeur. Ces photoélectrons sont émis avec une certaine énergie cinétique et mesurés par l'instrument, permettant de remonter aux énergies de liaison. La plage d'erreur de notre XPS est de 5-15%, au-dessus de celle de mesure du flux. Dans mes études, j'utilise des compositions d'éléments plus précises données par les mesures de flux.

2.2.5. Spectrométrie de rétrodiffusion de Rutherford (RBS)

La spectrométrie de rétrodiffusion de Rutherford (RBS) peut également être utilisée pour déterminer la composition chimique des films en analysant la perte d'énergie des ions légers à hautes énergies (de 0,5 à 5 MeV) traversant le matériau. Cette technique a été utilisée en collaboration avec B. Canut (INL) sur quelques échantillons afin de confirmer les points stœchiométriques en accord avec les résultats d'XPS. Les résultats concordent avec ceux de XRD/RHEED avec une incertitude de 10%.

2.3. Caractérisation des propriétés physiques

Dans cette section, les principales techniques de mesures utilisées dans ma thèse pour caractériser les propriétés électroniques et thermoélectriques des couches minces sont brièvement présentées.

2.3.1. Propriétés électroniques par méthode quatre pointes et effet Hall

La résistivité (ρ) est la capacité d'un matériau à entraver le flux de charges électriques sous un champ électrique appliqué. La conductivité électrique (σ) est l'inverse de la résistivité ($\sigma = \rho^{-1}$). En plus de la méthode de mesures par quatre pointes permettant de mesurer la résistivité (ρ) des couches minces par des droites I-V, l'effet Hall permet de mesurer, en plus de la résistivité, la densité (p) et mobilité (μ) des porteurs de charges libres sous un champ magnétique [19]. Les mesures par effet Hall ont été effectuées en géométrie Van der Pauw [20].

2.3.2. Propriétés thermoélectriques par des mesures du coefficient Seebeck

Le coefficient Seebeck (S) est un paramètre thermoélectrique conceptuellement simple à mesurer. Lorsqu'un échantillon est soumis à un gradient de température, le rapport de la différence de potentiel électrique mesurée (ΔV) et de la différence de température (ΔT) entre deux points quelconques donne $S = \Delta V/\Delta T$ du matériau. Les conditions importantes à satisfaire sont les conditions à l'équilibre électrique (aucun flux net), les mesures de température et de tension aux mêmes points avec une très bonne précision (~0.1 °C et ~1 μV) et le contact ohmique entre les fils de tension et l'échantillon [21]. La structure du montage utilisé à l'INL pendant ma thèse est présentée dans la Figure 4. La description détaillée des différentes méthodes de mesure a été expliquée par D. M. Rowe [22, 23].

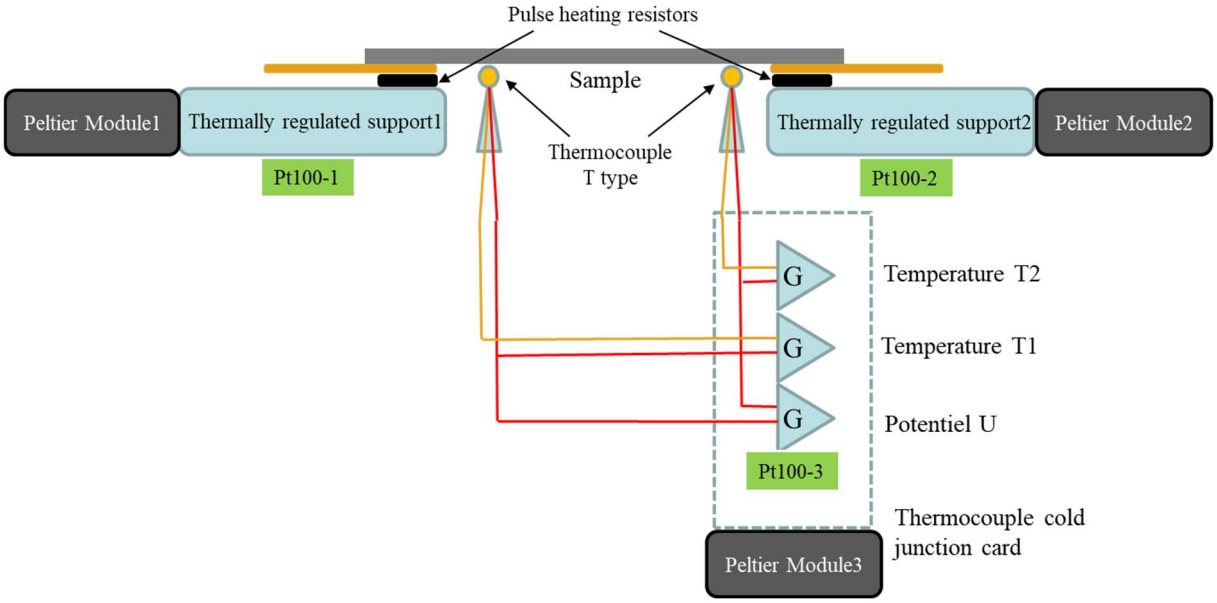

Figure 4 Schéma de principe du banc de mesure du coefficient Seebeck en couche mince développé à l'INL.

3. Effet de la substitution cationique (x)

Cette section résume le Chapitre III de ma thèse qui présente les propriétés structurales, électriques et thermoélectriques des solutions solides $La_{1-x}Sr_xCrO_3$, après avoir pris soin de bien calibrer la stœchiométrie cationique avec $LaCrO_3$ (x = 0) et $SrCrO_3$ (x = 1). Les résultats correspondant à la calibration de $LaCrO_3$ ont été publiés dans la référence [24].

3.1. Séries de calibration $LaCrO_3$ et $SrCrO_3$

3.1.1. Conditions de croissance

Des films minces épitaxiés de $La_{1+\delta}CrO_3$ (LCO) de ~15 nm d'épaisseur ($-0,25 \leq \delta \leq +0,25$) et de $Sr_{1+\delta}CrO_3$ (SCO) de ~60 nm d'épaisseur ($-0,15 \leq \delta \leq +0,15$) ont été crûs par MBE sur des substrats monocristallins de $SrTiO_3$ (STO) orientés (001) à des vitesses de ~0,1 et ~0,67 nm/min, respectivement, par co-évaporation de Sr, La et Cr. Les flux ont été mesurés avant la croissance à l'aide d'une jauge d'ionisation Bayard-Alpert (après soustraction du vide de base) et vérifiés à l'aide d'une microbalance à quartz (QCM).

3.1.2. Propriétés structurales

Comme mentionné dans la section 2.2, différentes techniques ont été utilisées pour caractériser les propriétés (micro)structurales de ces couches de calibrations : RHEED, AFM, XRR, XRD, XPS, RBS. Nous montrerons ci-dessous les principaux résultats issus de ces mesures.

La XRR a été utilisée pour mesurer l'épaisseur et les rugosités (rms) de surface/interface de tous les films LCO et SCO (résumées dans Tableau 1).

Tableau 1 Épaisseur et rugosité-rms pour tous les films de calibration.

Film	$La_{1+\delta}CrO_3$					$Sr_{1+\delta}CrO_3$				
δ	-0,25	-0,125	0	0,1	0,25	-0,143	-0,071	0	0,071	0,143
t (nm)	13,8	14,6	15,8	16,9	14,2	38,0	53,0	67,6	54,9	69,1
rms surface (nm)	0,46	0,46	0,30	0,48	0,99	0,73	0,97	1,2	2,05	1,17
rms interface (nm)	0,15	0,15	0,15	0,15	0,15	0,15	0,15	0,15	0,15	0,15
Densité ($g \cdot cm^{-3}$)	8,16	8,39	8,46	8,68	8,27	5,53	5,56	5,60	6,23	6,18

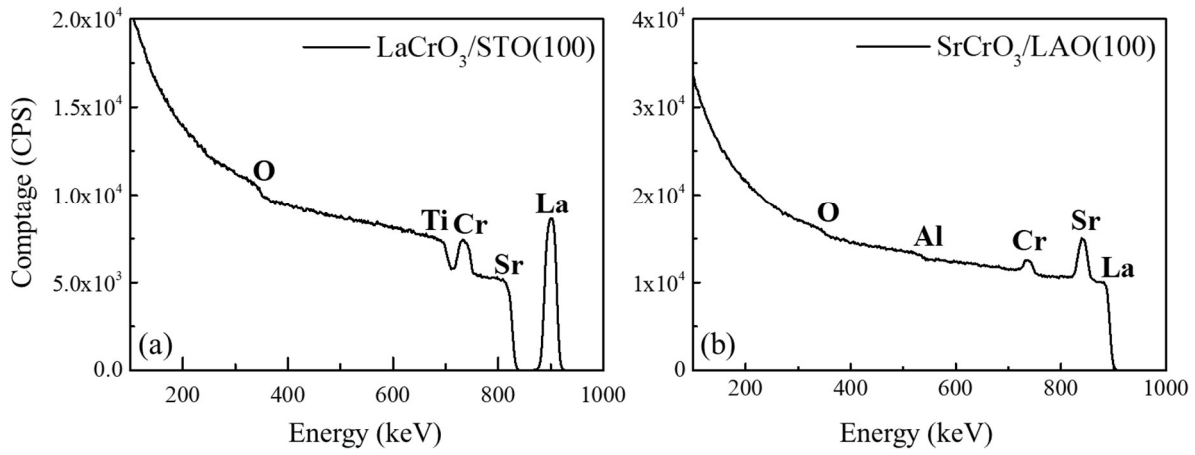

Figure 5 Spectres RBS des films stœchiométriques LCO et SCO.

RBS a été utilisé pour vérifier la stœchiométrie cationique des films de calibration LCO et SCO. La composition des deux films stœchiométriques est examinée, dans laquelle le rapport atomique [La/Cr] et [Sr/Cr] est bien de 1 (voir Figure 5), montrant un très bon accord avec les résultats XRD (voir Figure 7).

Les motifs RHEED le long des directions cristallographiques planes à symétrie élevée [100] et [110] après la croissance des couches minces d'étalonnage de $La_{1+\delta}CrO_3$ sont représentés sur Figure 6. Tous les motifs RHEED se présentent bien des stries contrastées signifiant que tous les films LCO sont épitaxiés avec des surfaces planes dans la gamme (écart par rapport à la stœchiométrie cationique, $-0{,}25 \leq \delta \leq 0{,}25$ pour le LCO, estimé après avoir terminé caractérisation).

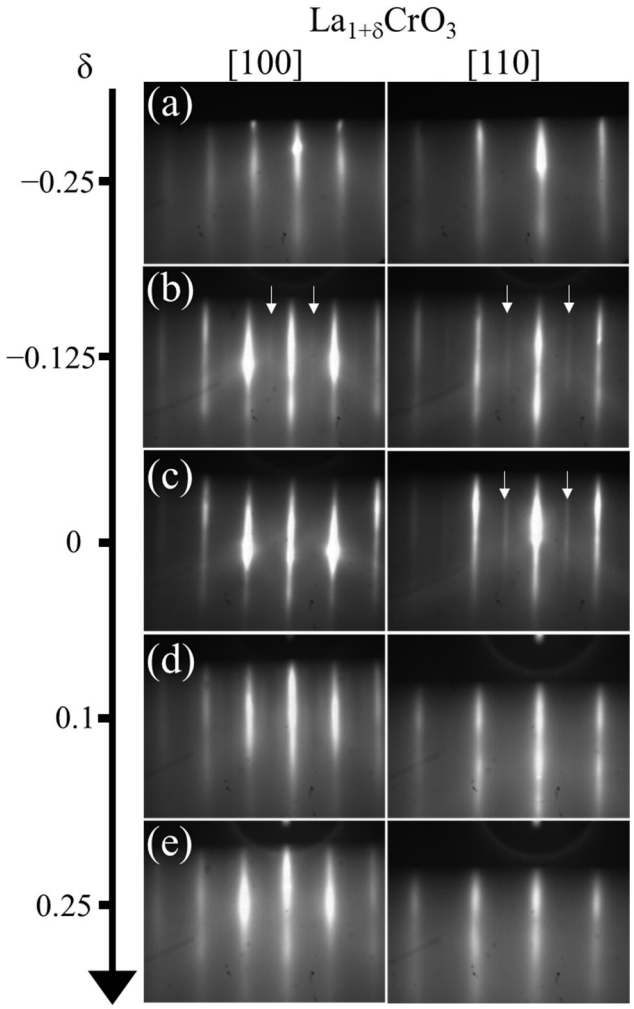

Figure 6 Images RHEED le long des azimuts [100] et [110] (prises à environ 200 °C, et à $P(O_2) = 1\times10^{-9}$ Torr) après la croissance des films de LCO. Les flèches verticales blanches indiquent des réflexions de 2ème ordre démontrant une reconstruction de surface selon l'azimut considéré.

Plus en détail, pour l'étalonnage LCO, lorsque $|\delta| = 0{,}25$, les stries sont légèrement floues

et le fond est plus clair que celui observé pour les échantillons avec un |δ| plus faible, révélant un désordre cristallin plus important. Pour δ = -0,125 (film LCO légèrement riche en Cr) et δ = 0 (film LCO stœchiométrique), les stries sont nettes le long des deux azimuts, indiquant que la surface est bien ordonnée. De plus, pour ces deux échantillons, une réflexion striée de second ordre le long de la direction [110] (indiquée par des flèches blanches) est observée. Une faible réflexion striée de 2ème ordre apparaît également le long de l'azimut [100] pour δ = -0,125 alors que seule une réflexion de 1er ordre est observée le long de cet azimut à δ = 0, ce qui indique une reconstruction de surface 2×2 et 2×1 pour le légèrement Film LCO riche en Cr (δ = -0,125) et film stœchiométrique (δ = 0), respectivement. En revanche, lorsque δ = 0,1 (film LCO légèrement riche en La), seules des stries de 1er ordre sont visibles indiquant l'absence de reconstruction de surface.

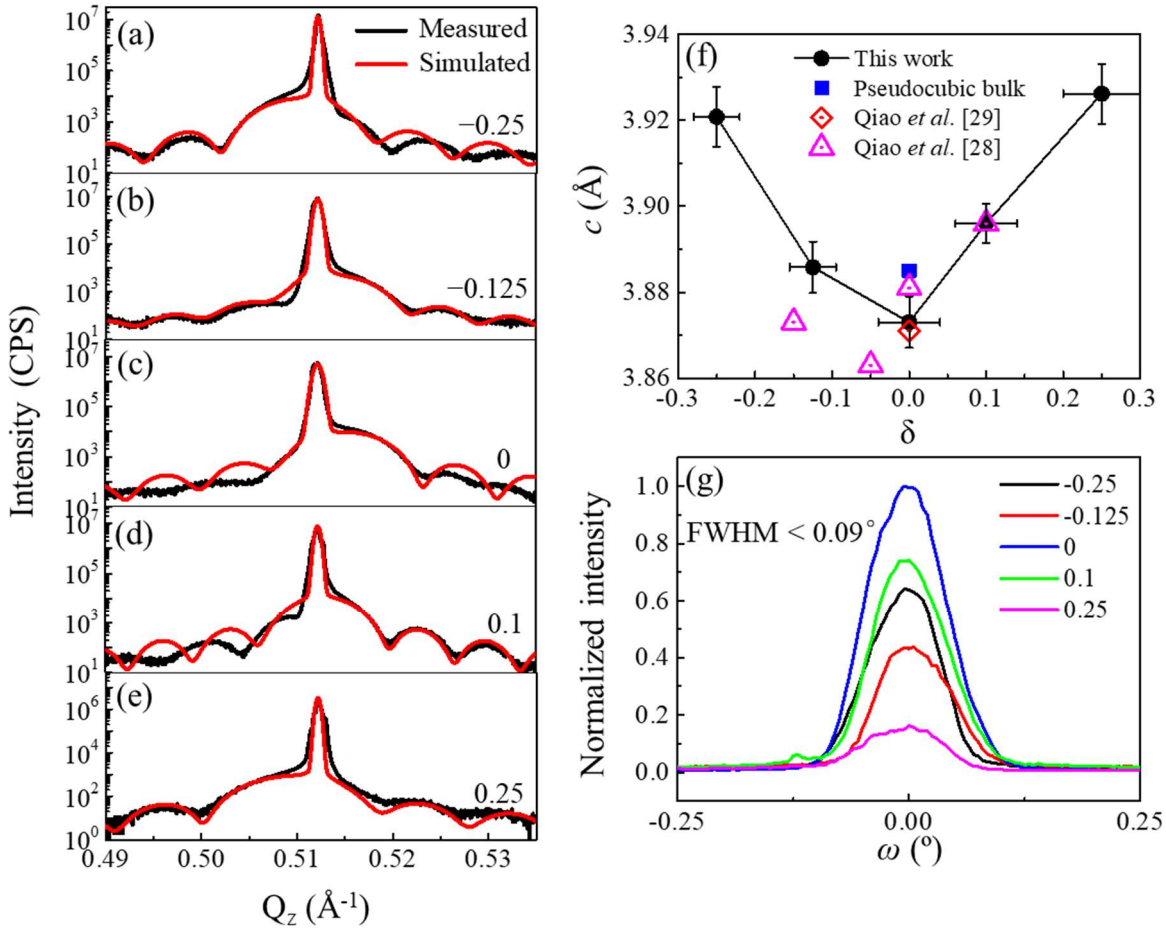

Figure 7 (a-e) Scans XRD 2θ/ω près des réflexions (002) des films LCO et des substrats pour différents δ. (f) Paramètre de maille hors plan en fonction de δ. (g) ω-scans autour de la réflexion (002) pour tous les films, normalisés au film stœchiométrique (δ = 0). (h) Intensité diffractée intégrée normalisée des scans montrés en (g) en fonction de δ.

La Figure 7 montre les scans XRD $2\theta/\omega$ autour des réflexions (002) des films LCO et des substrats STO tracés en unités spatiales réciproques. La réflexion LCO(002) est très proche de celle du substrat STO et apparaît comme un épaulement du pic du substrat. Qualitativement, la position de la réflexion du film diminue en Q_z avec la déviation par rapport à la stœchiométrie, ce qui signifie que le paramètre de maille hors plan du film LCO (c_{LCO}) augmente avec cette déviation. Les films Cr-riches et La-riches présentent les c_{LCO} plus grands que celui du film stœchiométrique, en accord avec d'autres films d'oxyde de pérovskite tels que $SrTiO_3$ [25, 26, 27]. Cette tendance est également observée par Qiao *et al*. [28], mais avec un minimum de c_{LCO} décalé sur les films légèrement riches en Cr (δ = -0,05) au lieu de la stœchiométrie (δ = 0). Ce petit décalage de composition (5%) avec ce travail pourrait être dû à *i*) l'incertitude dans la détermination de la composition et du paramètre de maille de film, et *ii*) le rapport et la distribution des défauts cationiques ponctuels dans le film.

Quantitativement, le c_{LCO} a été extrait des fits des spectres XRD (Figure 7a-e) et est montré en fonction de δ sur Figure 7f, ainsi que les résultats de la littérature sur les films LCO épitaxiés pour comparaison [28, 29, 30]. La valeur minimale est c_{LCO} = 3,873 Å (δ = 0), ce qui est en bon accord avec les résultats les plus récents de la référence [30], bien que des valeurs différentes (de 3,871 à 3,881 Å) soient rapportées dans différents articles du même groupe. Autour de la stœchiométrie, les paramètres de maille sont inférieurs à la valeur apparente pseudocubique LCO (3,885 Å, carré bleu), indiquant une réduction du c_{LCO} (-0,31%) en raison de la contrainte en tension dans le plan exercée par le substrat STO (ε_{xx} = 0,51%) [31]. Les films sont tous contraints par rapport au substrat, comme l'indique les cartographies de l'espace réciproque sur des réflexions asymétriques (montré dans la Figure 8). Le paramètre de maille hors plan augmente jusqu'à près de 3,93 Å pour les films clairement non stœchiométriques : 3,92 Å pour δ = -0,25 et 3,926 Å pour δ = 0,25. Dans de tels cas, ces valeurs élevées de c_{LCO}, supérieures au paramètre de maille du substrat, sont en partie dues à la contrainte en compression dans le plan des films épitaxiés, en plus de l'effet de déviation stœchiométrique cationique lui-même. Pour δ = 0,1 (film légèrement riche en La), c_{LCO} = 3,896 Å, en très bon accord avec les résultats de Qiao. Pour δ = -0,125 (légèrement riche en Cr), c_{LCO} = 3,886 Å, ce qui est légèrement supérieur à la valeur indiquée par Qiao (~3,873 Å pour δ = -0,15).

Les ω-scans mesurés pour tous les films autour de la réflexion LCO(002) sont présentés sur la Figure 7g. La mosaïcité des films (FWHM) est inférieure à 0,09°, confirmant la très bonne qualité des films avec un faible niveau de désorientation polaire.

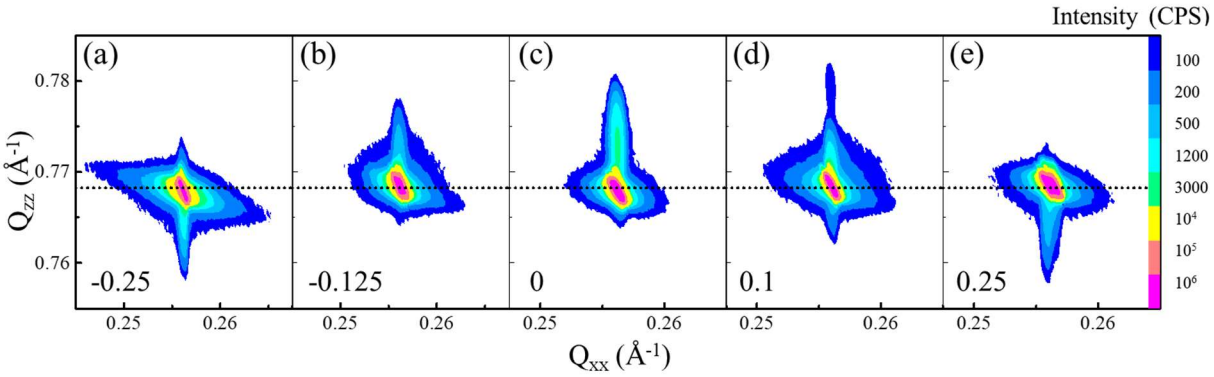

Figure 8 RSM autour de la réflexion asymétrique (103) des couches minces LCO et des substrats STO pour (a) δ = -0,25, (b) δ = -0,125, (c) δ = 0, (d) δ = 0,1 et (e) δ = 0,25. La ligne pointillée indique la position Q_{zz} du substrat STO.

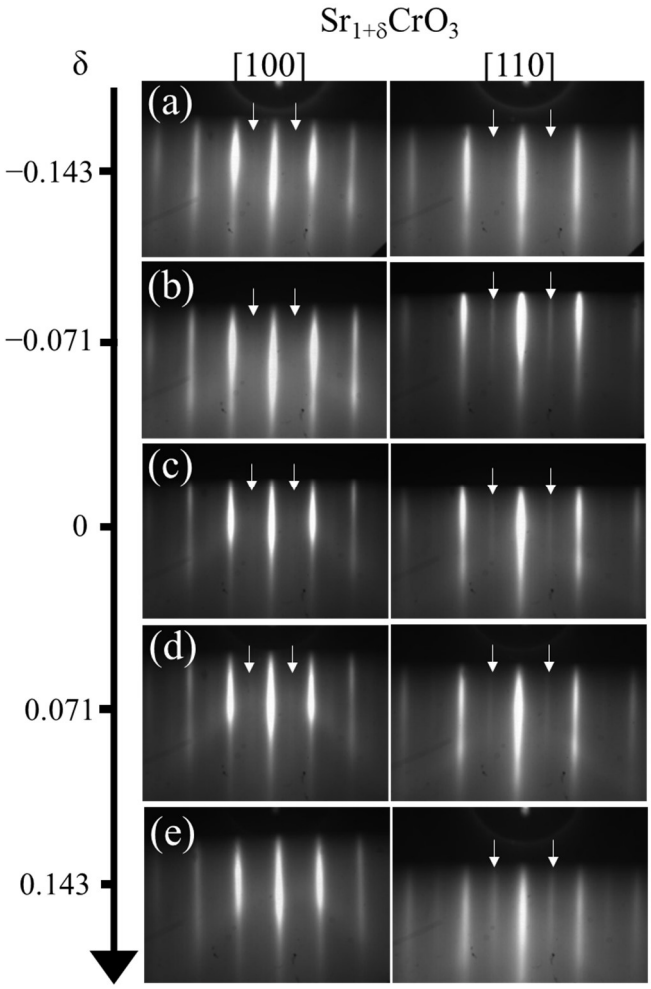

Figure 9 Images RHEED le long des azimuts [100] et [110] (prises à environ 200 °C, et à $P(O_2) = 1\times10^{-9}$ Torr) après la croissance des films de SCO. Les flèches verticales blanches indiquent des réflexions de 2ème ordre démontrant une reconstruction de surface selon l'azimut considéré.

Les images RHEED des films SCO (Figure 9) montrent la même variation des raies en fonction de δ comme LCO. Quand $|\delta| \leq 0{,}07$, les raies sont nettes le long des deux azimuts, révélant que les films sont bien épitaxiés et que leurs surfaces sont planes. Pour $|\delta| = 0{,}143$, les raies le long de l'azimut [110] sont plus larges et le fond est plus clair que celles observées pour les autres, révélant un désordre cristallin plus important sur cette surface. Pour tous les films SCO, une raie de 2ème ordre est observée le long de la direction [110]. Cependant, une faible raie de 2ème ordre apparaît également le long de l'azimut [100] pour $|\delta| \leq 0{,}07$, ce qui indique des reconstructions de surface 2×2 pour le film stœchiométrique et les films légèrement non stœchiométriques.

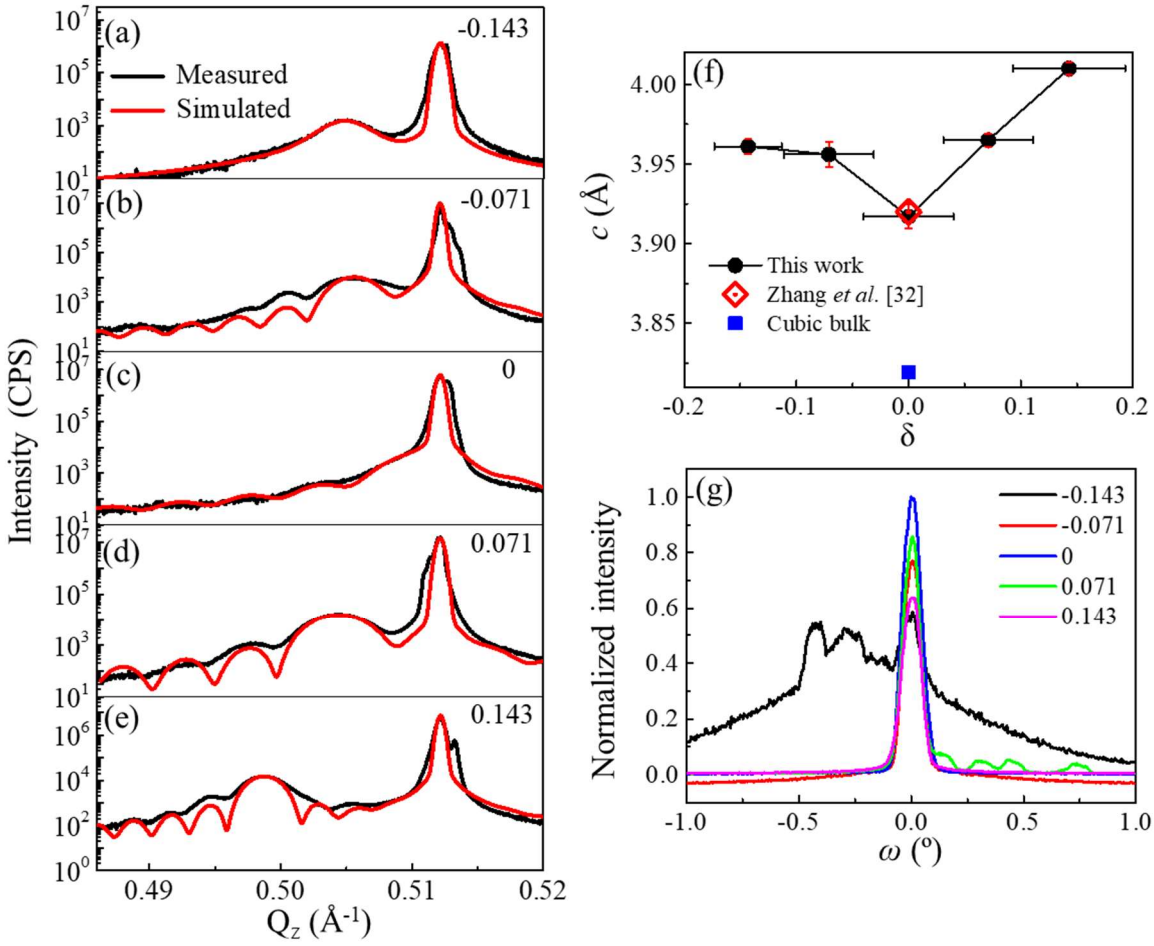

Figure 10 (a-e) Scans XRD $2\theta/\omega$ près des réflexions (002) des films SCO et des substrats pour différents δ. (f) Paramètre de maille hors plan en fonction de δ. (g) ω-scans autour de la réflexion (002) pour tous les films, normalisés au film stœchiométrique (δ = 0). (h) Intensité diffractée intégrée normalisée des scans montrés en (g) en fonction de δ.

La Figure 10a-e montre les scans XRD $2\theta/\omega$ autour des réflexions (002) des films SCO.

Le paramètre de maille hors plan du film SCO (c_{SCO}) augmente également avec δ comme prévu. Le c_{SCO} est extrait des fits des spectres XRD et résumé en fonction de δ sur Figure 10f, avec les valeurs trouvées dans la littérature pour comparaison [32]. Les c_{SCO} de ce travail varient de 3,917 à 4,01 Å et la valeur stœchiométrique est c_{SCO} = 3,917 Å, ce qui est en très bon accord avec le résultat de la référence (3,92 Å) [32]. Les ω-scans mesurés pour les films SCO autour de la réflexion sont présentés sur la figure 6g. Le FWHM de ces courbes est inférieure à 0,1°, confirmant la bonne qualité cristalline des films avec une faible désorientation polaire. L'intensité diffractée diminue progressivement avec δ, représentée sur Figure 10h, en raison de l'introduction de défauts ponctuels et/ou planaires dans le réseau cristallin.

3.2. Solutions solides $La_{1-x}Sr_xCrO_3$: impact du taux de substitution x

3.2.1. Conditions de croissance

Des films épitaxiés $La_{1-x}Sr_xCrO_3$ (LSCO) de ~30 nm d'épaisseur (x = 0,1, 0,2, 0,25, 0,3 et 0,4) ont été crûes par MBE avec une vitesse de ~0,15 nm/min sur des substrats STO(001) traités pour avoir une terminaison TiO_2. Tous les films ont été recuits à l'air à 300 °C pendant 2 heures pour assurer une oxydation complète. Le caractère isolant du substrat STO après ce recuit a été vérifié par des mesures électriques en face arrière.

3.2.2. Propriétés structurales

Les propriétés de ces films ont été caractérisées par RHEED, AFM, XRR, XRD et XPS. Les principaux résultats issus de ces mesures sont montrés ci-dessous.

3.2.2.1. Caractérisations XRR

Les épaisseurs et rugosités (rms) des surfaces et interfaces ont été mesurées par XRR. Les résultats sont reportés dans la Tableau 2. On peut voir que la rugosité de surface augmente avec le taux de substitution (x), en accord avec les observations AFM (non montré ici).

Tableau 2 Épaisseur, rugosité (rms) et densité des films LSCO.

x	0,1	0,2	0,25	0,3	0,4
t (nm)	28,1	29,0	28,2	30,1	31,6
rms surface (nm)	0,39	0,46	0,54	0,88	0,92
rms interface (nm)	0,15	0,15	0,15	0,15	0,15
Densité ($g \cdot cm^{-3}$)	7,45	6,42	6,35	6,30	6,28

3.2.2.2. Caractérisations RHEED & XRD

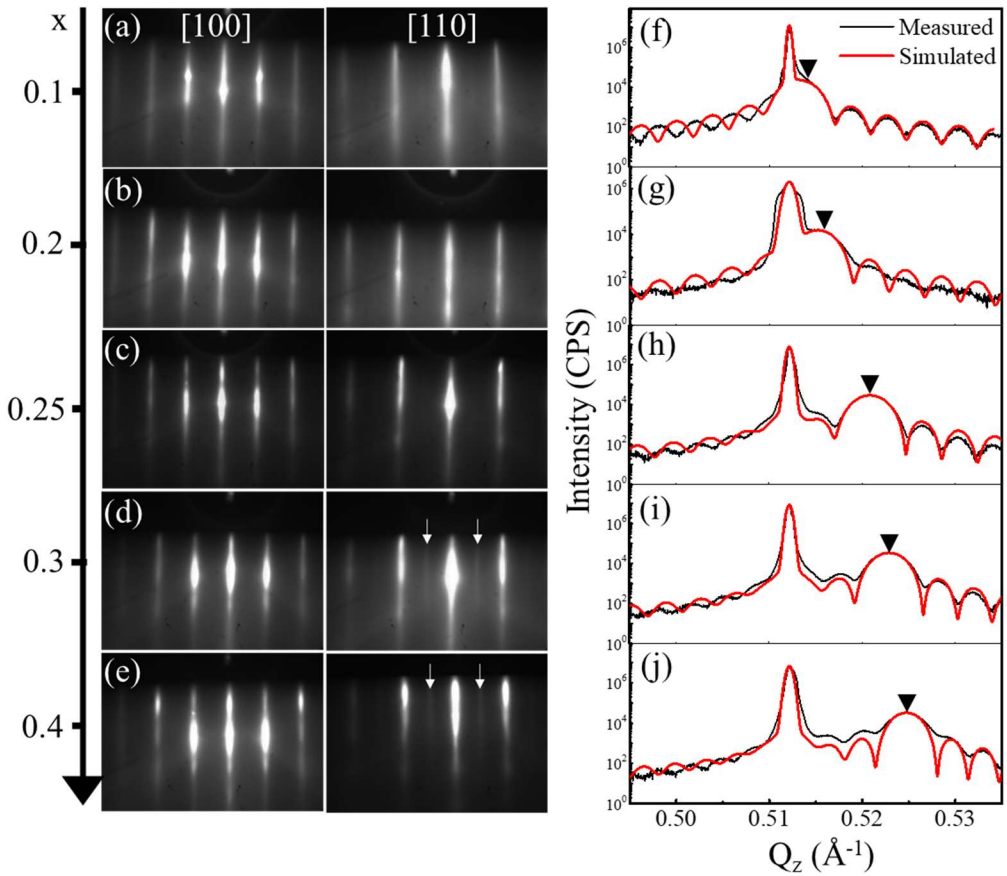

Figure 11 (a-e) Images RHEED le long des azimuts [100] et [110] (prises à environ 200 °C, et à $P(O_2) = 1 \times 10^{-9}$ Torr) après la croissance des films. Les flèches verticales blanches indiquent des réflexions de 2ème ordre démontrant une reconstruction de surface selon l'azimut considéré. (f-j) Scans XRD $2\theta/\omega$ tracés avec les unités du réseau réciproque près des réflexions (002) des films et des substrats pour différents x.

Les images RHEED le long des directions cristallographiques [100] et [110] après la croissance de la série des films LSCO sont montrés sur la Figure 11a-e. Les raies sont nettes le long des deux azimuts, indiquant que les films sont bien épitaxiés avec une surface plane et ordonnée. Des réflexions de 2ème ordre le long de la direction [110] (indiquée par des flèches blanches) est observée pour x = 0,3 et 0,4, ce qui indique une reconstruction de surface 2×1 pour ces compositions. Sinon, pour les trois autres films LSCO avec une concentration de Sr relativement faible, seule une réflexion de 1er ordre apparaît indiquant une absence de reconstruction de surface pour ces compositions (x ≤ 0,25).

La Figure 11f-j montre les scans XRD $2\theta/\omega$ autour des réflexions (002) des films LSCO et de leurs substrats avec des courbes de fit en rouges. La présence de franges de Pendellösung autour des pics de diffraction des films atteste de leur bonne qualité cristalline des films et de leurs interfaces (abruptes). Le paramètre de maille hors plan des films LSCO (c_{LSCO}, marqué par des triangles noirs inversés dans l'unité de l'espace réciproque) diminue avec l'augmentation d'x, en raison de la contrainte dans le plan. Tous les films sont contraints sur le substrat, comme l'atteste les cartographies de l'espace réciproque (RSM) sur une réflexion asymétrique (montré dans la Figure 12).

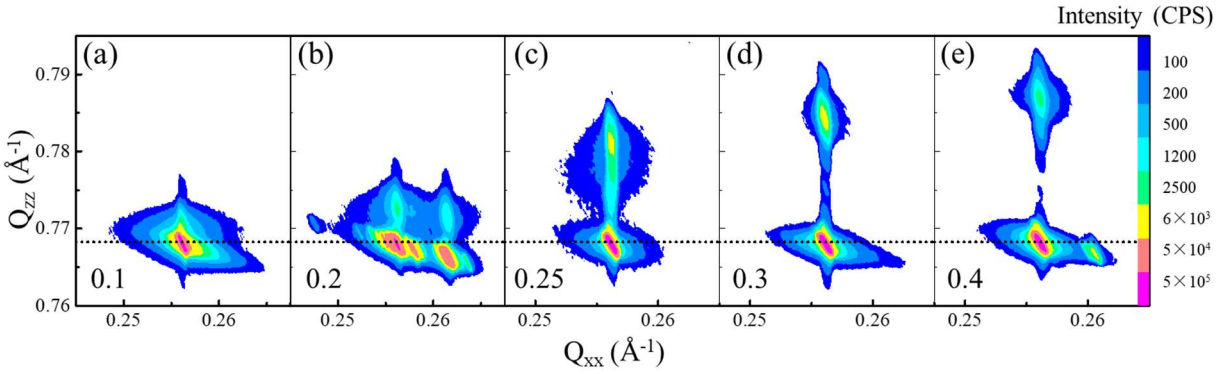

Figure 12 RSM autour de la réflexion asymétrique (103) des couches minces LSCO et du substrat STO, pour (a) x = 0,1, (b) x = 0,2, (c) x = 0,25, (d) x = 0,3 et (e) x = 0,4. La ligne pointillée horizontale indique la position Q_{zz} du substrat STO.

Les variations de c_{LSCO} et de V_{LSCO} en fonction d'x sont directement montrées sur Figure 13. Les carrés pleins noirs sont extraits de ce travail, et les cercles pleins bleus sont les valeurs trouvées dans la littérature [30]. La variation c_{LSCO} suit globalement une loi de Vegard [33]. Pour 0 < x < 1, le c_{LSCO} diminue avec l'augmentation de x, en assez bon accord qualitativement avec la littérature même si des différences significatives existent [30, 33]. Ces différences s'expliquent par les différences d'épaisseur et donc d'état de contrainte. Par exemple, le film à x = 0,25 de

la référence 30 est entièrement relaxé contrairement à notre film pour la même composition. Le paramètre de maille dans le plan de LSCO (a_{LSCO}) relaxé de la littérature [30] est donc proche de 3,892 Å (au lieu de celui du substrat STO 3,905 Å pour le nôtre) ce qui induit une augmentation du paramètre de maille hors plan (c_{LSCO} = 3,871 Å) en comparaison avec notre couche contrainte en tension pour cette composition.

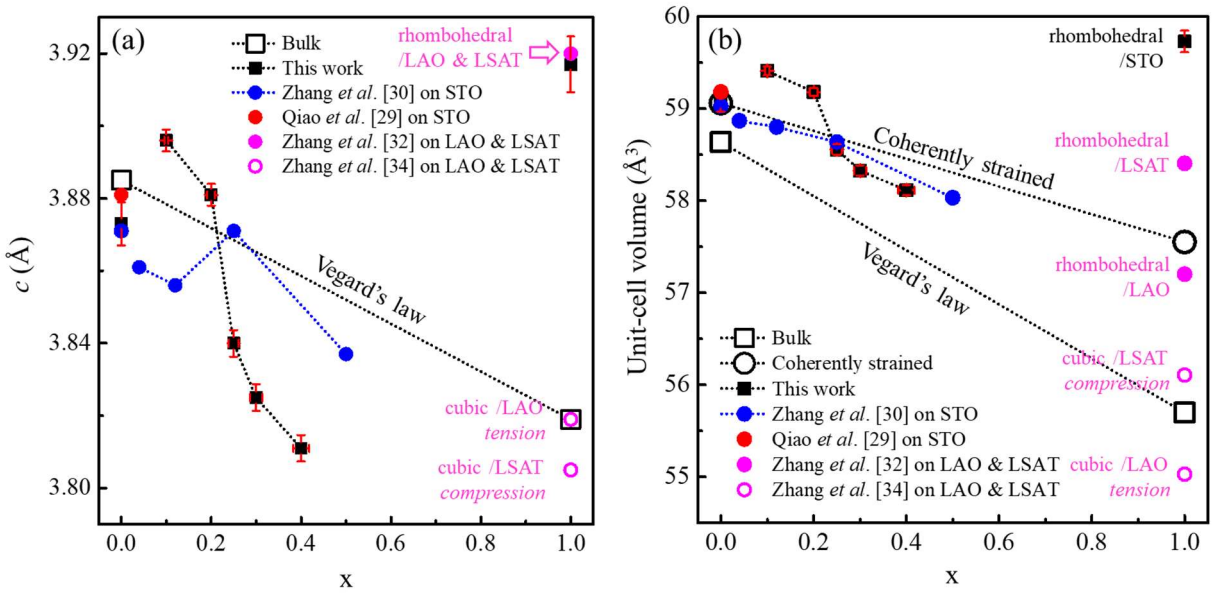

Figure 13 Paramètre de maille hors plan et volume en fonction de la concentration de Sr.

Tableau 3 Paramètres de maille dans le plan *a* et hors plan *c* et volume de la maille extraits par RSM.

x	*a* (Å)	*c* (Å)	Volume (Å^3)
0	3,905	3,873	59,059
0,1	3,905	3,896	59,410
0,2	3,905	3,881	59,181
0,25	3,905	3,840	58,556
0,3	3,905	3,825	58,328
0,4	3,905	3,811	58,114

Le paramètre de maille dans le plan a_{LSCO} est mesuré par RSM autour de la réflexion asymétrique (103) (Figure 12). Les valeurs de a_{LSCO}, c_{LSCO} et volume de LSCO sont résumées dans Tableau 3. Le nœud (103) correspondant au film mince LSCO est déplacé le long de Q_{zz}

en fonction de la composition chimique de manière cohérente avec les $2\theta/\omega$ scans, confirmant la variation de c_{LSCO} indiquée sur Figure 13. Comme indiqué plus haut, tous ces films LSCO sont entièrement contraints par rapport au substrat puisque le nœud LSCO(103) est aligné verticalement avec le nœud de substrat, indiquant que a_{LSCO} est égal au paramètre de maille de STO (3,905 Å).

3.2.2.3. Caractérisations XPS

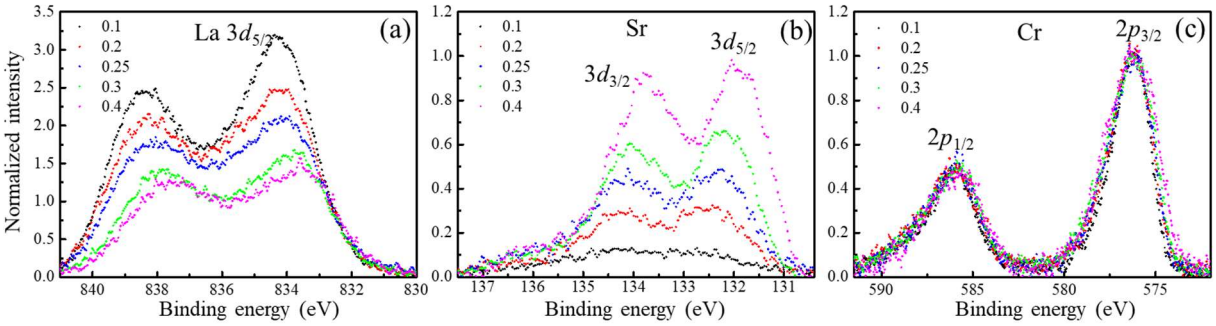

Figure 14 XPS de (a) La $3d_{5/2}$, (b) Sr $3d$ et (c) Cr $2p$ pour tous les films LSCO.

Tableau 4 Résumé des propriétés chimiques des couches minces LSCO.

x	[A/(A+B)] (at.%)	[Sr] (at.%)
0,1	0,56	0,11
0,2	0,55	0,18
0,25	0,54	0,27
0,3	0,52	0,39
0,4	0,53	0,49

La Figure 14 montre les spectres XPS des niveaux de cœur La $3d_{5/2}$, Sr $3d$ et Cr $2p$ des films LSCO. Afin de comparer directement les énergies de liaison, les pics Cr $2p_{3/2}$ sont tous décalés à 576 eV et normalisés à 1. Pour chaque échantillon, le même décalage et la normalisation correspondante sont ensuite appliqués aux spectres La $3d_{5/2}$ et Sr $3d$ Le gradient de substitution sur le site A (x) peut être apprécié sur les spectres de La $3d_{5/2}$ et Sr $3d$ sur la Figure 14a et b, respectant la variation x comme prévu. La composition chimique du LSCO en fonction de x est confirmée par ces analyses dans les limites de la résolution instrumentale (Tableau 4).

3.2.3. Propriétés physiques

3.2.3.1. Propriétés électroniques

Les propriétés électroniques mesurées par effet Hall à température ambiante des films LSCO sont présentées sur la Figure 15 en fonction d'x : conductivité électrique (σ), concentration (p) et mobilité (μ) des porteurs de charge (trous). La densité de porteurs ainsi que la conductivité électrique augmentent avec x comme attendu [34, 33, 30]. σ est augmentée de 2 (x = 0,1) à 18 S·cm^{-1} (x = 0,4). p augmente de 7,22×10^{19} cm^{-3} (x = 0,1) à 2,41×10^{20} cm^{-3} (x = 0,4). Selon l'équation $\mu = \sigma/pe$, la mobilité des films LSCO peut être facilement calculée, qui augmente également avec x.

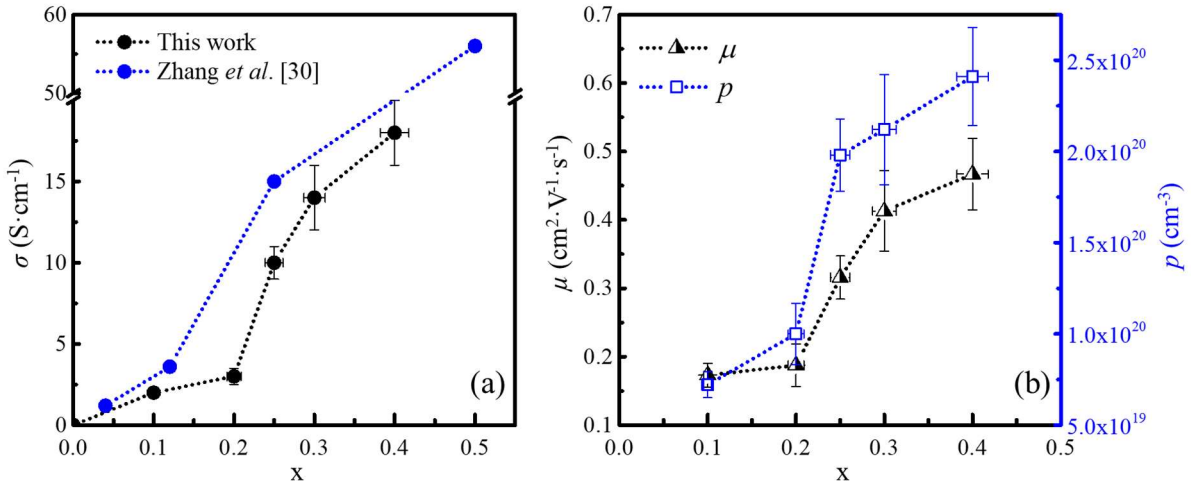

Figure 15 (a) Conductivité électrique σ, (b) concentration p et mobilité μ des porteurs de charge (trous) dans les films LSCO obtenus à partir des mesures par effet Hall.

3.2.3.2. Propriétés thermoélectriques

La Figure 16a représente les données brutes de ΔV en fonction de ΔT mesurées par la méthode différentielle à température ambiante, et donc le coefficient de Seebeck (S) déduit par la relation $S = \Delta V/\Delta T$, pour chaque taux de substitution cationique x. Le film $La_{0.9}Sr_{0.1}CrO_3$ (x = 0,1) n'a pas pu être mesuré convenablement, à cause de mauvais contacts électriques en surface, probablement à cause de la trop faible conductivité électrique à cette composition. Pour x compris entre 0,2 et 0,4, on peut voir que la valeur S (pente) diminue avec l'augmentation de x comme attendu [34, 30]. La barre d'erreur de chaque point mesuré est également introduite, avec

une incertitude relativement grande à x = 0,2. Pour x ≥ 0,25, la précision est plus grande en raison de σ plus élevé. La Figure 16b résume le S qui diminue de 312 à 98 $\mu V \cdot K^{-1}$ de x = 0,2 à 0,4, tandis que σ augmente de 3 à 18 $S \cdot cm^{-1}$. Comme attendu, le facteur de puissance ($PF = S^2\sigma$) atteint un maximum (0,324 $\mu W \cdot cm^{-1} \cdot K^{-2}$) pour un certain dopage (à x = 0,25), en assez bon accord avec la littérature [30].

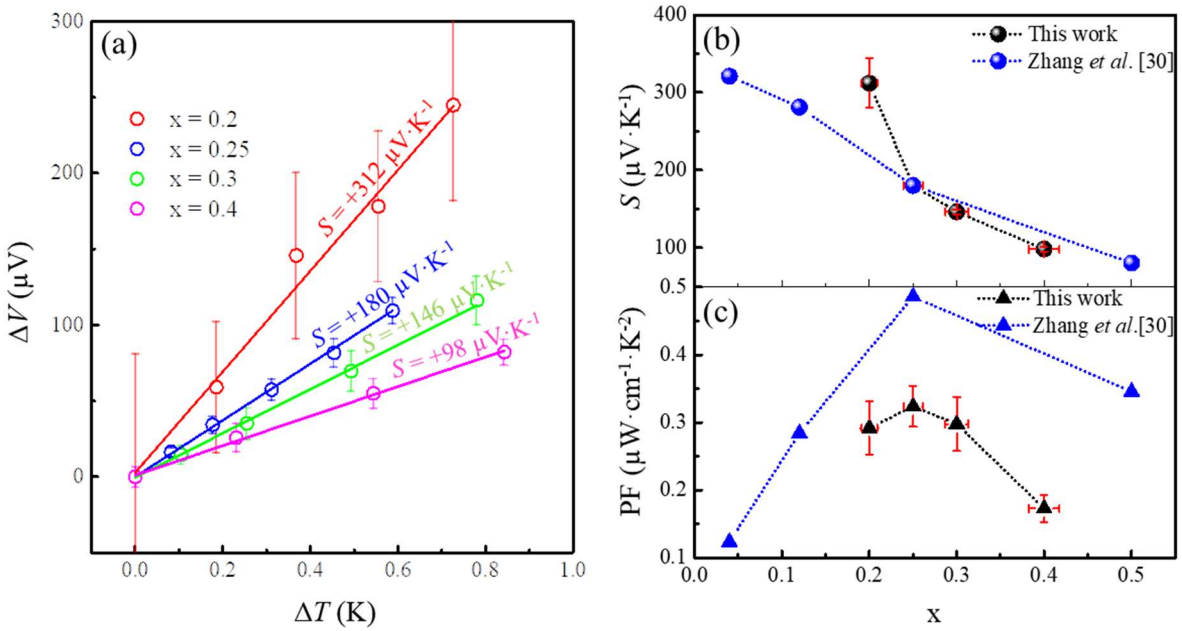

Figure 16 (a) ΔV mesurés en fonction de ΔT donnant le coefficient Seebeck des films LSCO. (b) Coefficient Seebeck et (c) facteur de puissance thermoélectrique en fonction de x.

4. Effet de la déformation épitaxiale

Cette section résume le Chapitre IV de ma thèse dédié à l'étude originale de l'impact des contraintes induites par l'épitaxie sur les propriétés structurales, élastiques, électroniques et thermoélectriques de films minces de $La_{0.75}Sr_{0.25}CrO_3$ (LSCO). Des films de $LaCrO_3$ (LCO) ont été également été élaborés en parallèle et pris comme référence dans l'étude de propriétés élastiques. Les résultats correspondant à ce chapitre sont partiellement publiés dans les références [35, 36].

4.1. Conditions de croissance

Pour cette étude de l'impact des contraintes d'épitaxie, quatre substrats différents d'oxydes

de structure pérovskite cubique ou pseudocubique ont été utilisés pour faire croître les films minces épitaxiés de LCO et LSCO par MBE : $LaAlO_3$ (LAO), $(LaAlO_3)_{0.3}(Sr_2AlTaO_6)_{0.7}$ (LSAT), STO et $DyScO_3$ (DSO), ayant des paramètres de maille de 3,796 Å, 3,868 Å, 3,905 Å et 3,944 Å, respectivement [37] (voir Figure 17). La vitesse de croissance était de ~0,1 nm/min pour les films de LCO et de ~0,15 nm/min pour les films de LSCO. L'épaisseur et la rugosité (rms) issues des mesures XRR, ainsi que la composition chimique issue des mesures XPS sont résumées dans le Tableau 5. Selon les mesures XRR, la rugosité de surface des films LSCO a tendance à diminuer avec l'augmentation de la contrainte en tension.

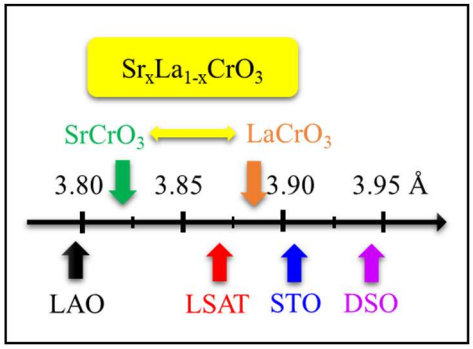

Figure 17 Paramètres de maille des films et substrats impliqués dans ce chapitre.

Tableau 5 Épaisseur et rugosité-rms et composition chimique mesurée pour tous les films LCO et LSCO.

Paramètre	$LaCrO_3$				$La_{0.75}Sr_{0.25}CrO_3$			
	/LAO	/LSAT	/STO	/DSO	/LAO	/LSAT	/STO	/DSO
t (nm)	16,6	14,5	13,7	13,8	27,2	29,9	28,2	29,0
rms surface (nm)	0,63	0,61	0,54	0,62	0,72	0,58	0,54	0,49
rms interface (nm)	0,15	0,15	0,15	0,15	0,15	0,15	0,15	0,15
[A/(A+B)] (at%)	54,1	54,0	50,0	50,8	49,8	56,2	54,5	52,9
[Sr/(Sr+La)] (at%)	0,0	0,0	0,0	0,0	23,8	24,8	24,5	26,0

4.2. Propriétés structurales de $LaCrO_3$

Le RHEED a été utilisé pour vérifier la qualité structurale qualitative des films de LCO. Les diagrammes enregistrés à la fin de la croissance de chaque film sur les quatre substrats

différents sont montrés sur la Figure 18a-d le long de la direction cristallographique [100]. Tous les diagrammes présentent des raies bien contrastées montrant que les films sont hétéroépitaxiés avec des surfaces très planes, en accord avec les mesures XRR (Tableau 5) et les images topographiques AFM (non montrées ici).

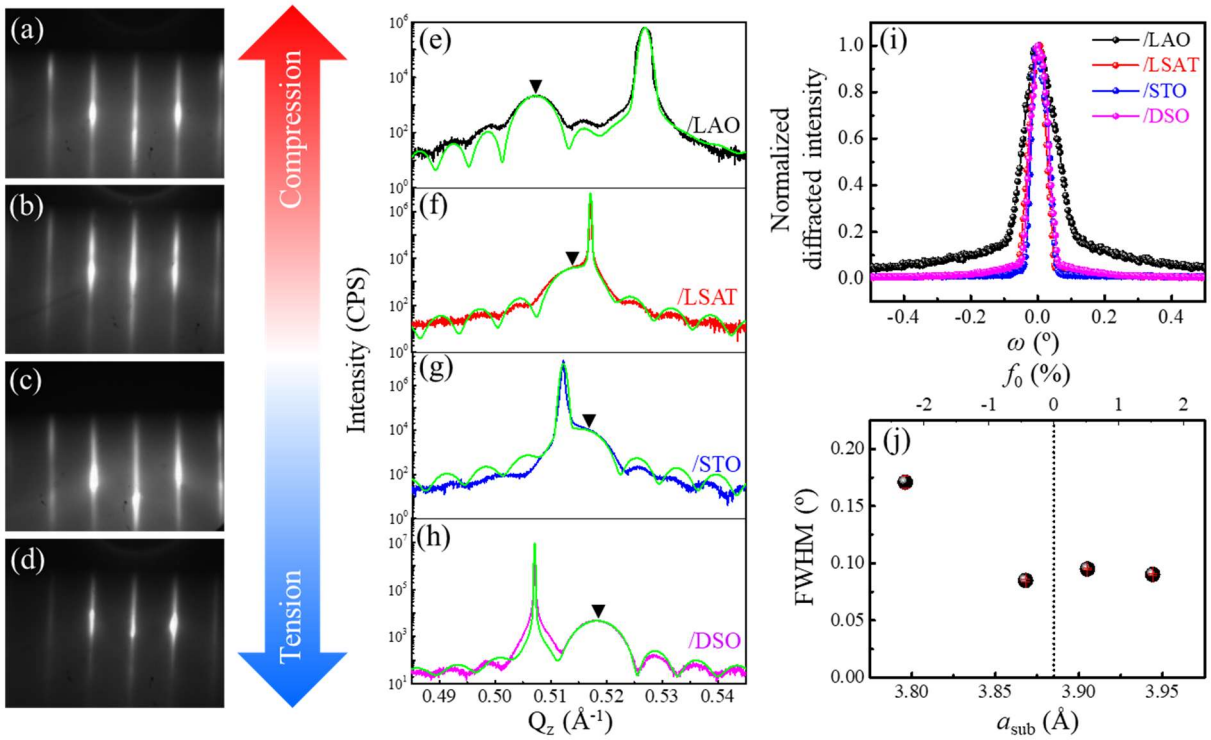

Figure 18 (a-d) Images RHEED le long de l'azimut [100] (prises environ 200 °C, et à $P(O_2) = 1\times10^{-9}$ Torr) après la croissance des films LCO sur les différents substrats (a) LAO, (b) LSAT, (c) STO et (d) DSO. (e-h) scans XRD $2\theta/\omega$ près des réflexions (002) des films et des substrats différents. (i) ω-scans autour de la réflexion (002) pour tous les films, normalisés au film sur STO. (j) Intensité diffractée intégrée normalisée des scans montrés en (i) en fonction de paramètre de maille de substrat.

La Figure 18e-h montre les scans XRD $2\theta/\omega$ autour des réflexions (002) des films LCO et de leurs substrats correspondants. La présence de franges de Pendellösung autour des pics de diffraction des films atteste de leur bonne qualité cristalline et de leurs interfaces (abruptes). Le paramètre de maille hors plan des films est extrait de ces spectres. Le paramètre de maille hors plan des films LCO (c_{LCO}) diminue avec l'augmentation du paramètre de maille du substrat, ce qui est attendu par la loi de Hooke d'élasticité avec un coefficient de Poisson positif [38]. Les valeurs de c_{LCO} sont respectivement de 3,951 Å, 3,891 Å, 3,883 Å et 3,853 Å pour les films LCO sur des substrats LAO, LSAT, STO et DSO.

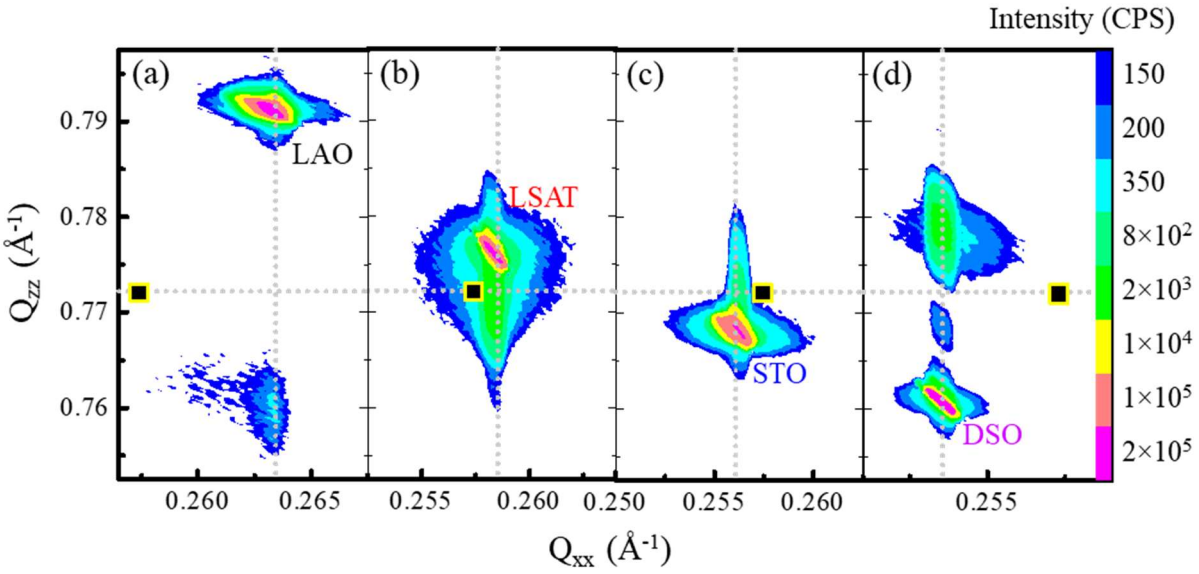

Figure 19 RSM enregistrées autour de la réflexion asymétrique (103) de films minces LCO sur des substrats (a) LAO, (b) LSAT, (c) STO et (d) DSO. Les lignes pointillées verticales indiquent les positions Q_{xx} des substrats. Les carrés sur la ligne pointillée horizontale indiquent les positions du LCO massif (*i.e.* films LCO relaxés).

Les paramètres de maille dans le plan des couches minces LCO (a_{LCO}) sont mesurés par RSM autour des réflexions asymétriques (103) (Figure 19). Pour les substrats LSAT et STO, les nœuds LCO(103) sont complètement alignés verticalement avec celui des substrats, indiquant que a_{LCO} est égal à celui du substrat, et donc que les films sont déformés dans le plan de manière cohérente par les substrats. Pour les films LCO sur substrats LAO et DSO, l'asymétrie des nœuds atteste d'un début de relaxation partielle des contraintes, qui est très probablement due à un décalage de maille plus important sur les substrats (-2,29% pour LAO et 1,52% pour DSO, voir Tableau 6) [39].

La dépendance des paramètres de maille hors plan (c) par rapport au paramètre de maille dans le plan (a) est illustrée pour les films LCO dans la Figure 20. La fonction $c(a)$ est linéaire comme prévu à partir de la déformation élastique du LCO pseudocubique en utilisant l'équation (2) [38] :

$$c = -\frac{2\nu}{1-\nu}a + \frac{1+\nu}{1-\nu}a_{bulk} \qquad (2)$$

Le coefficient de Poisson (ν = 0,24) et la constante de maille du massif de LCO (a_{massif} = 3,888 Å) sont extraits de ce fit. Ils sont très similaires à ceux trouvés dans la littérature (ν = 0,23 et a_{massif} = 3,885 Å) [29, 40], confirmant la validité de notre méthode de mesure.

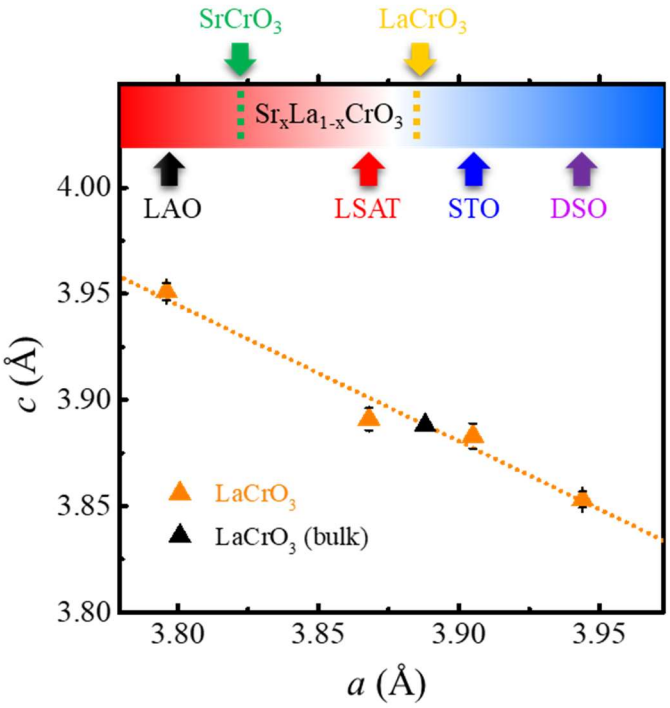

Figure 20 Evolution de *c* (paramètre de maille hors plan) en fonction de *a* (paramètre de maille dans le plan) pour les films épitaxiés LCO (triangles orange) sur les différents substrats. La ligne pointillée représente le fit par régression linéaire. Le triangle noir représente le paramètre de maille du LCO massif dérivé de notre fit.

Tableau 6 Résumé des propriétés structurales et chimiques des couches minces LCO épitaxiées sur les différents substrats.

Substrat	Désaccord de maille (%)	Epaisseur (nm)	[A/(A+B)] (at.%)	*a* (Å)	*c* (Å)	Mosaicité (°)	Rugosité d'interface (nm)	Rugosité de surface (nm)
LAO	-2,29	16,6	54,1	3,796	3,951	0,17	0,15	0,63
LSAT	-0,44	14,5	54,0	3,868	3,891	0,08	0,15	0,61
STO	0,51	13,7	50,0	3,905	3,883	0,10	0,15	0,54
DSO	1,52	13,8	50,8	3,944	3,853	0,09	0,15	0,62

4.3. Propriétés structurales de $La_{0.75}Sr_{0.25}CrO_3$: détermination du coefficient de Poisson et du paramètre de maille massif

Les images RHEED enregistrées à la fin de la croissance des films minces de LSCO sur les quatre substrats différents le long de la direction cristallographique [100] sont montrées dans la Figure 21a-d. Tous les diagrammes, sauf celui correspondant au film sur LAO (Figure 21a), présentent des raies bien contrastées indiquant que les films sont hétéroépitaxiés avec une surface très plane. Les mesures XRR (Tableau 6) et des images AFM (non montré ici) confirment la faible rugosité de surface de ces couches et montrent une rugosité légèrement plus importante sur substrat LAO.

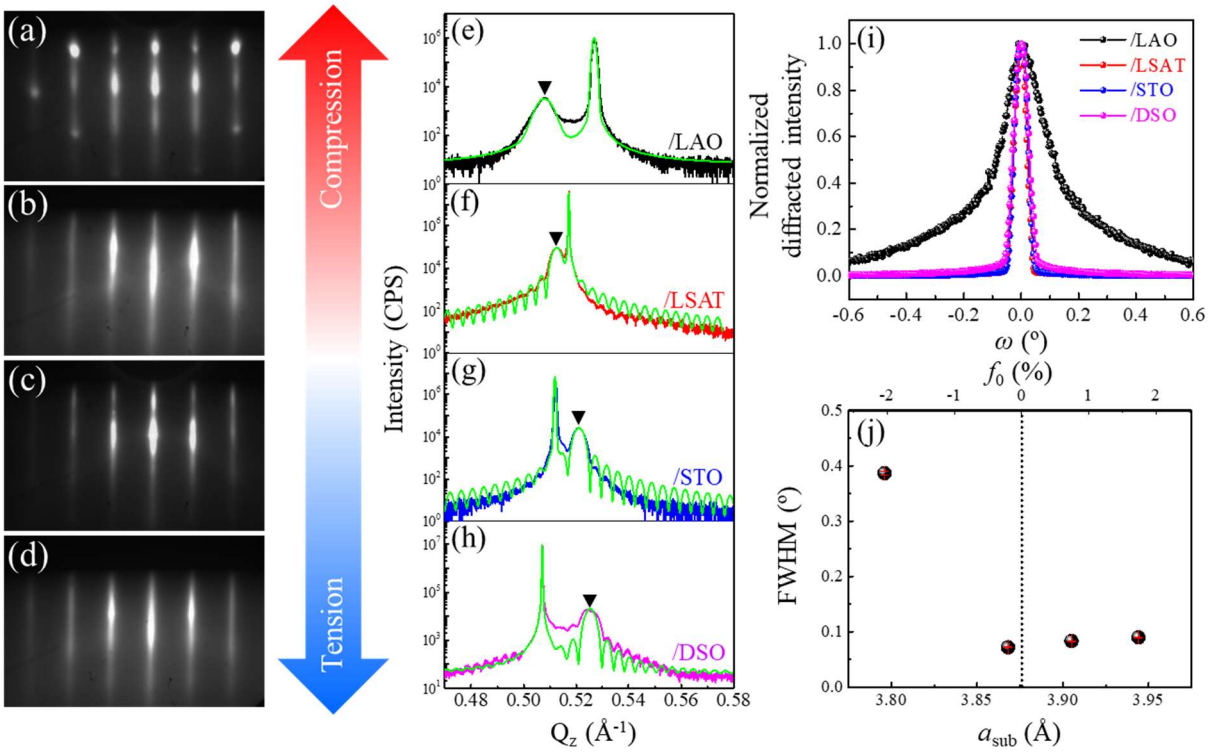

Figure 21 (a-d) Images RHEED le long de l'azimuts [100] (prises environ à 200 °C, et à $P(O_2) = 1\times10^{-9}$ Torr) après la croissance des films LSCO sur les différents substrats (a) LAO, (b) LSAT, (c) STO et (d) DSO. (e-h) scans XRD $2\theta/\omega$ près des réflexions (002) des films et des substrats différents. (i) ω-scans autour de la réflexion (002) pour tous les films, normalisés au film sur STO. (j) Intensité diffractée intégrée normalisée des scans montrés en (i) en fonction de paramètre de maille de substrat.

La Figure 21e-h montre les scans XRD $2\theta/\omega$ autour des réflexions LSCO(002) et leurs substrats correspondants. Le paramètre de maille hors plan des films est extrait de ces spectres. Le paramètre de maille hors plan des films LSCO (c_{LSCO}) diminue également avec

l'augmentation du paramètre de maille du substrat, comme observé pour les films LCO, indiquant que LSCO a un coefficient de Poisson positif également. Les valeurs c_{LSCO} sont de 3,943 Å, 3,904 Å, 3,844 Å et 3,804 Å pour les films LSCO sur des substrats LAO, LSAT, STO et DSO, respectivement. Bien que les films soient d'épaisseur similaire (~30 nm), les pics (002) des films LSCO sur LAO et DSO sont plus larges que ceux des films sur LSAT et STO qui ont un meilleur accord de maille, indiquant une distribution plus large des paramètres de maille hors plan. Très probablement, un début de relaxation des déformations se produit à cette épaisseur pour ces films sur LAO et DSO. Pour le film LSCO sur DSO, deux maxima secondaires semblent être visibles, indiquant la présence de deux paramètres de maille hors plan (3,795 Å et 3,815 Å), mais tous les deux étant bien inférieurs à la valeur mesurée du massif. Un fit unique avec le composant principal conduit à un paramètre de maille hors plan de 3,804 Å (Figure 21h).

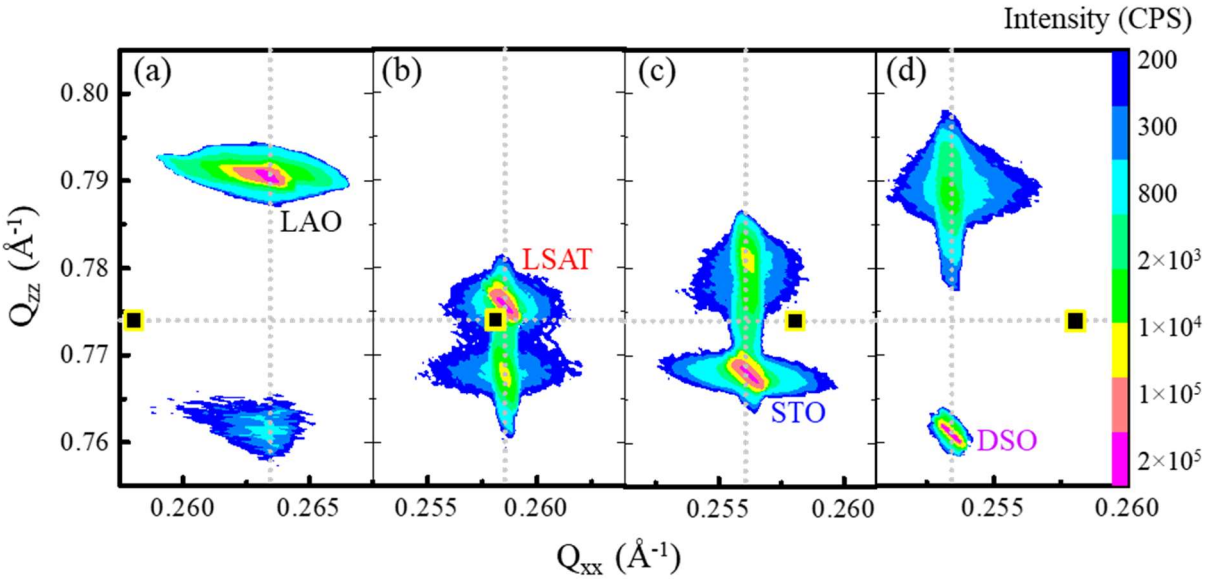

Figure 22 RSM enregistré autour des réflexions asymétriques (103) de films minces LSCO sur (a) LAO, (b) LSAT, (c) STO et (d) DSO substrats. Les lignes pointillées verticales indiquent les positions Q_{xx} des substrats. Les carrés sur la ligne pointillée horizontale indiquent les positions du LSCO massif (*i.e.* films LSCO relaxés) extraites dans ce travail.

Les paramètres de maille dans le plan ont été mesurés par RSM (montrées dans la Figure 22). Pour les substrats DSO, STO et LSAT, les nœuds LSCO(103) sont alignés verticalement avec celui des substrats, indiquant que le paramètre de maille dans le plan du film mince LSCO (a_{LSCO}) et celui du substrat correspondant sont identiques. Pour le film LSCO sur LAO, l'asymétrie des nœuds témoigne également d'une relaxation partielle des contraintes, qui est très probablement due au fort désaccord de paramètre de maille, le plus important (-2,06%) sur ce

substrat [39]. Le même comportement global est observé avec le film mince épitaxié de LCO.

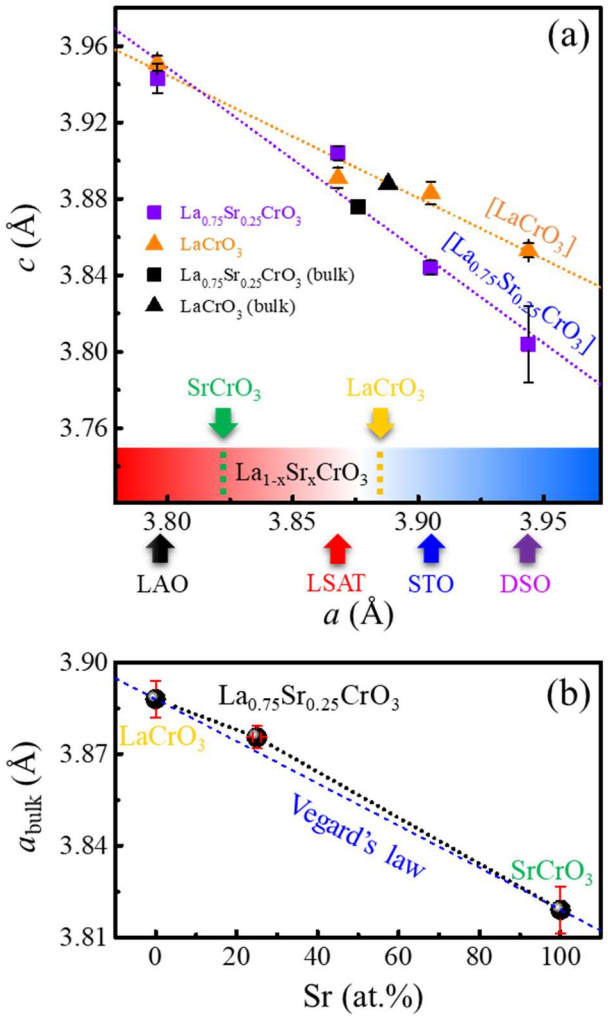

Figure 23 (a) Evolution de c en fonction de a pour les films épitaxiaux LSCO (carrés violets) et LCO (triangles orange) sur les substrats différents. Les lignes pointillées représentent les fits dans les deux cas. Le carré et le triangle noirs représentent les constantes de maille du bulk de LSCO et LCO dérivées de ces ajustements. (b) Variation de paramètre de maille du bulk de $La_{1-x}Sr_xCrO_3$ en fonction de Sr (x).

La dépendance du paramètre de maille hors plan et dans le plan est montrée pour les films LSCO et LCO sur la Figure 23a. La fonction $c(a)$ est linéaire comme prévu à partir de la déformation élastique du LSCO pseudocubique en utilisant également l'équation (2). Le coefficient de Poisson extrait de ces mesures ($\nu = 0{,}32 \pm 0{,}02$), ainsi que le paramètre de maille de l'équivalent massif ($a_{massif} = 3{,}876$ Å) et $C_{12}/C_{11} \approx 0{,}5$ de LSCO, diffèrent notablement de LCO. La substitution de 25% de Sr augmente significativement le ν de plus de 30% par rapport au LCO. Ce changement pourrait également être lié au changement de valence Cr plutôt qu'à la seule substitution Sr. Afin de bien distinguer la cause, d'autres films LSCO avec un état

d'oxydation inférieur devraient être élaborés afin d'obtenir la même valence Cr que dans les films LCO. Figure 23b indique que le paramètre de maille de l'équivalent massif de LSCO ($a_{\text{massif-LSCO}}$ = 3,876 Å) est quasiment linéaire entre celle de LCO ($a_{\text{massif-LCO}}$ = 3,885 Å) et SCO ($a_{\text{massif-SCO}}$ = 3,819 Å) [32, 41], qui est attendu d'une loi de Vegard et en accord avec la littérature [33]. Le $a_{\text{massif-LSCO}}$ est donc intermédiaire entre celui des substrats LSAT et STO (plus proche de LSAT pour lequel le paramètre de maille est de 3,868 Å).

Tableau 7 Résumé des propriétés structurales et compositions chimiques des couches minces LSCO épitaxiées sur les différents substrats.

Substrat	Désaccord de maille (%)	Epaisseur (nm)	[A/(A+B)] (at%)	[Sr] (at%)	*a* (Å)	*c* (Å)	Mosaicité (°)	Rugosité d'interface (nm)	Rugosité de surface (nm)
LAO	-2,06	27,2	49,8	23,8	3,796	3,943	0,38	0,15	0,72
LSAT	-0,21	29,9	56,2	24,8	3,868	3,904	0,07	0,15	0,58
STO	0,75	28,2	54,5	24,5	3,905	3,844	0,08	0,15	0,54
DSO	1,75	29,0	52,9	26,0	3,944	3,804	0,09	0,15	0,49

4.4. Impact des déformations sur les propriétés électroniques et thermoélectriques de $La_{0.75}Sr_{0.25}CrO_3$

Les propriétés électroniques et thermoélectriques des films LSCO mesurées dans le plan à température ambiante sont illustrées à Figure 24 en fonction du désaccord de paramètre de maille (f_0) qui est égal à la déformation dans le plan (ε_{xx}) puisque les couches sont toutes contraintes par le substrat. Sur la base des mesures de l'effet Hall et du coefficient de Seebeck, tous les échantillons présentent une conductivité de type *p*.

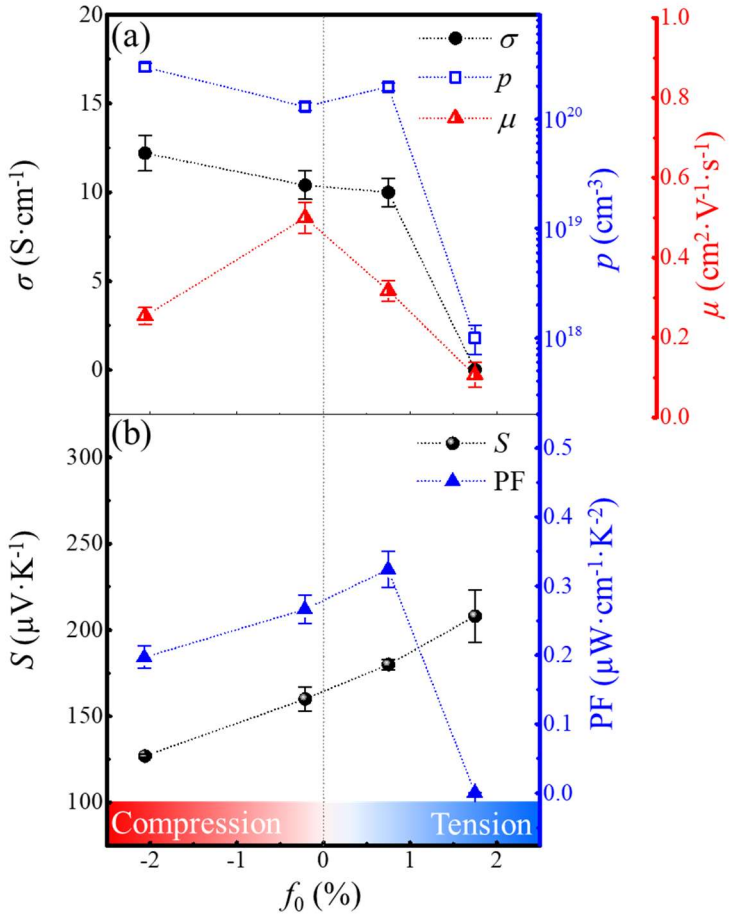

Figure 24 (a) Conductivité électrique σ, concentration p et mobilité μ des porteurs de charge des films LSCO à température ambiante sur différents substrats obtenus à partir de mesures par effet Hall, ainsi que (b) coefficient Seebeck mesuré et le facteur de puissance déduit (PF = $S^2\sigma$) en fonction de la déformation dans le plan.

La Figure 24a présente les mesures de conductivité électrique (σ), de densité (p) et mobilité (μ) des porteurs de charge dans les films LSCO pour les différentes valeurs de déformations épitaxiales. σ diminue avec l'augmentation de la déformation dans le plan (de la compression à la tension). Elle diminue très légèrement de 12,2 S·cm^{-1} à des fortes compressions dans le plan (-2.1%) jusqu'à 12,2 S·cm^{-1} à des faibles valeurs de tension, et chute brutalement de trois ordres de grandeurs jusqu'à 0,02 S·cm^{-1} pour des fortes tensions (+1,8%). Sur substrat STO, la conductivité est autour de 10 S·cm^{-1}, ce qui est en parfait accord avec les résultats du groupe de S. A. Chambers [30]. Des tendances similaires ont pu être observées dans notre oxydes conducteurs tels $SrRuO_3$ et $CaRuO_3$ [42]. Ils ont observé que les films minces sous une grande contrainte de tension dans le plan ont une résistivité plus élevée que leurs homologues moins contraints ou en compression.

La variation de p est cohérente avec l'évolution de σ dans les limites de la résolution

instrumentale. Elle est de l'ordre de quelques 10^{20} cm^{-3} pour les films en compression et légèrement en tension et chute à 10^{18} cm^{-3} pour le film en forte tension. Ces valeurs diffèrent d'un ordre de grandeur de celles estimées par un modèle (et non mesurées) par le groupe de S. A. Chambers [30]. Les raisons probables de telles différences de concentration de trous activés comprend l'autocompensation de charges [43], les compensations électrostatiques aux abords des surfaces et interfaces [44] et la présence de lacunes d'oxygène résiduelles non négligeables qui compense le dopage *p*. De fait, la création de lacunes d'oxygène est liée à la tétragonalité dans les oxydes pérovskites [45, 46, 47] et ces lacunes d'oxygène peuvent s'ordonner en fonction de l'état de contrainte (tension) et ainsi modifier la structure de bande dans la direction considérée.

La mobilité est maximum pour le film qui est le moins contraint, et diminue en fonction de la déformation, quelle que soit le signe (avec une diminution plus importante pour le film en forte tension). Cette tendance est cohérente avec ce qui a été observé pour les films épitaxiés de $SrTiO_3$ dopés au La thermoélectriques de type *n* [48]. La valeur μ se situe entre 0,1 et 0,5 $cm^2 \cdot V^{-1} \cdot s^{-1}$ à température ambiante. Comme mentionné dans la référence [48], les films minces STO dopés La de type *n* avec une contrainte en tension devraient avoir une masse effective (m^*) inférieure à ceux avec une contrainte en compression [49, 50]. La structure de bande peut être modifiée dans les films contraints, conduisant probablement à une modification du m^* [48], qui peut également s'appliquer aux films LSCO de type *p*.

La Figure 24b montre le coefficient Seebeck (*S*) dans le plan et le facteur de puissance (PF) en fonction de f_0 à température ambiante. *S* est positif pour tous les échantillons confirmant que les trous sont les porteurs majoritaires dans ces films. Il est à noter que $S = 180$ $\mu V \cdot K^{-1}$ pour le film LSCO/STO, ce qui est en très bon accord avec le groupe de S. A. Chambers [30]. *S* augmente de façon monotone avec f_0, de 127 $\mu V \cdot K^{-1}$ (en forte compression) à 208 $\mu V \cdot K^{-1}$ (en forte tension), en accord avec d'autres mesures faites sur différents matériaux thermoélectriques sous haute pression [51]. D'autre part, une tendance similaire a été reportée récemment sur des couches minces épitaxiées de $SrRuO_3$ [52].

Le PF thermoélectrique augmente légèrement avec l'augmentation de f_0 jusqu'à atteindre 0,32 $\mu W \cdot cm^{-1} \cdot K^{-2}$ pour une faible tension (sur STO), ce qui est légèrement supérieur à celui des films en faible compression (0,27 $\mu W \cdot cm^{-1} \cdot K^{-2}$ sur LSAT), et chute brutalement à 0,001 $\mu W \cdot cm^{-1} \cdot K^{-2}$ pour une plus forte tension (sur DSO) en raison de la très faible conductivité électrique. Ces mesures indiquent qu'une faible contrainte de tension (+0,75 % ici sur STO) augmente le PF par rapport à un état plus relaxé (ici -0,21 % sur LSAT).

5. Effet de la déviation par rapport à stœchiométrie cationique

Cette section résume le chapitre V de ma thèse portant sur les films de $(La_{0.75}Sr_{0.25})_{1+\delta}CrO_3$ épitaxiés et l'impact de la déviation par rapport à la stœchiométrie cationique ($-0,3 \leq \delta \leq 0,3$) sur leurs propriétés structurales, électroniques et thermoélectriques. Un article est en cours de préparation sur les résultats correspondant à ce chapitre.

5.1. Conditions de croissance

Dans cette étude, des couches minces $(La_{0.75}Sr_{0.25})_{1+\delta}CrO_3$ (LSCO) ont été épitaxiées sur des substrats STO(001) par MBE dans les mêmes conditions de croissance que celles indiquées dans la section 3 correspondant au Chapitre III.

Tableau 8 Résumé de l'épaisseur, de la rugosité (rms), de la densité et des compositions chimiques des films $(La_{0.75}Sr_{0.25})_{1+\delta}CrO_3$.

δ	*t* (nm)	[A/(A+B)] (at.%)	δ_{XPS}	[Sr/La+Sr] (at.%)	Rugosité d'interface (nm)	Rugosité de surface (nm)	Densité ($g \cdot cm^{-3}$)
-0,3	25,0	35,8	-0,44	0,32	0,15	0,68	6,18
-0,15	20,0	43,5	-0,23	0,26	0,15	0,85	6,27
0	28,2	49,9	0	0,25	0,15	0,54	6,35
0,15	40,8	55,8	0,26	0,26	0,15	0,56	6,36
0,3	30,5	60,3	0,52	0,21	0,15	0,72	6,61

D'après les mesures XRR (non montrées ici), la rugosité (rms) de surface de ces films augmente légèrement avec $|\delta|$ (Tableau 8). D'après les mesures XPS, la déviation par rapport à la stœchiométrie cationique mesurée (δ_{XPS}) diffère de celle visée (δ), en particulier pour les films avec $|\delta| = 0,3$. Cependant, ces analyses XPS sur de telles couches d'oxydes complexes comprennent des incertitudes importantes (probablement supérieures à 10%) et la variation de paramètre de maille mesurée par XRD est assez cohérente avec δ (voir plus bas). Le taux de

substitution en Sr (x = 0,25) est quant à lui assez bien respecté dans les limites de résolution de l'instrument ($0,21 \leq x_{XPS} \leq 0,32$).

5.2. Impact sur les propriétés structurales

Les propriétés structurales de cette série ont été mesurées par RHEED, AFM, XRR, XRD, et XPS. Les principaux résultats sont montrés ici.

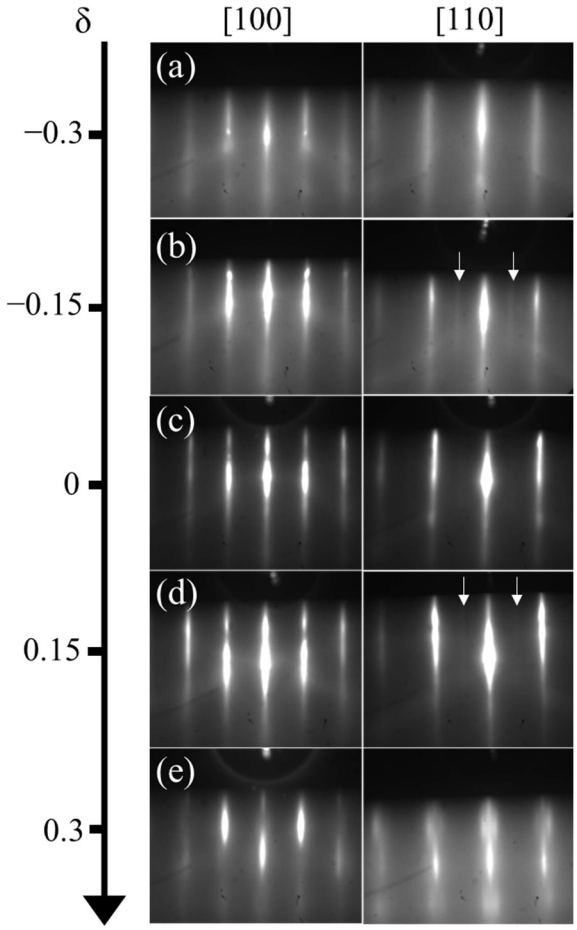

Figure 25 Images RHEED le long des azimuts [100] et [110] (prises à environ 200°C, et $P(O_2) = 1\times10^{-9}$ Torr) après la croissance des films $(La_{0.75}Sr_{0.25})_{1+\delta}CrO_3$ pour (a) δ = -0,3, (b) δ = -0,15, (c) δ = 0, (d) δ = 0,15 et (e) δ = 0,3. Les flèches verticales blanches indiquent des réflexions de 2^{e} ordre démontrant une reconstruction de surface selon l'azimut considéré.

La Figure 26a-e présente les images RHEED le long des directions [100] et [110] de ces films LSCO épitaxiés sur des substrats STO(001) en fonction de δ. Tous les diagrammes présentent des raies, signifiant que tous les films sont hétéroépitaxiaux avec des surfaces planes. Pour $|\delta| \leq 0,15$, les raies sont nettes et bien contrastées le long des deux azimuts, indiquant que les surfaces sont bien cristallisées et ordonnées. Cependant, pour $|\delta| = 0,3$, les raies sont assez

floues (notamment le long de la direction [110]) et le fond devient plus brillant que celui observé pour les échantillons avec un |δ| inférieur, révélant un plus grand désordre cristallin. Pour les deux films avec |δ| = 0,15, on observe une légère réflexion du 2ème ordre le long de la direction [110] (indiquée par des flèches blanches) indiquant une reconstruction de surface 2×1, alors que seule la réflexion du 1er ordre est observée le long de cet azimut à la stœchiométrie (δ = 0). En revanche, lorsque |δ| = 0,3 seules des réflexions du 1er ordre sont visibles indiquant l'absence de reconstruction de surface pour ces films LSCO clairement non stœchiométriques.

La Figure 26a-e montre les scans XRD $2\theta/\omega$ autour des réflexions (002) de tous les films LSCO et de leurs substrats STO(001) dans les unités de l'espace réciproque (Q_z). La position du pic LSCO(002) (marquée par des triangles inversés noirs) diminue avec l'augmentation de |δ|, indiquant une expansion du paramètre de maille hors plan avec |δ| (Figure 26f), comme attendu et comme observé précédemment pour $La_{1+\delta}CrO_3$ et $Sr_{1+\delta}CrO_3$ (voir section 3 correspondant au Chapitre III). La position de $La_{0.75}Sr_{0.25}CrO_3$ stœchiométrique relaxé ($a_{LSCO\text{-}massif}$ = 3,876 Å) est rappelé par une ligne pointillée verticale noire sur la Figure 26a-e. Comme nous l'avons déjà vu, pour le film stœchiométrique (δ = 0), le pic LSCO(002) apparaît à des valeurs Q_z supérieures à la position relaxée, signifiant que cette couche est en tension dans le plan (Fig. 18h). Pour tous les autres films hors stœchiométriques (|δ| > 0), le pic LSCO(002) apparaît à des valeurs Q_z inférieures à la position relaxée, indiquant que ces films ont tous des paramètres de maille massifs correspondants supérieurs à $a_{LSCO\text{-}massif}$ = 3,876 Å. Ces films hors stœchiométriques sont soit en tension dans le plan lorsque $c_{LSCO} < a_{STO}$ (le cas de δ = 0,15), soit en compression lorsque $c_{LSCO} > a_{STO}$ (le cas de |δ| ≥ 0,3). Le film à δ = -0,15 apparaît presque relaxé ($c_{LSCO} \sim a_{STO}$). Pour déterminer proprement les paramètres de maille massif pour chaque compositions hors stœchiométriques (|δ| ≥ 0) et les valeurs de désaccords de paramètres de maille, il faudrait épitaxiés ces films contraints sur différents substrats avec différents états de déformation comme présenté dans la section 4 correspondant au Chapitre IV.

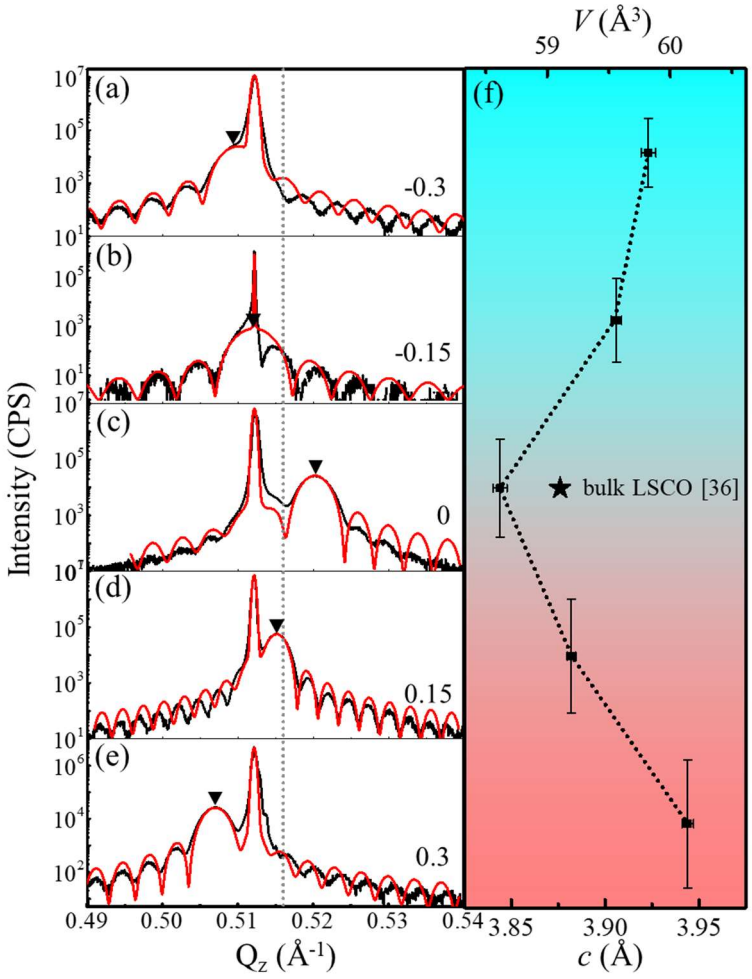

Figure 26 (a-e) Scans XRD $2\theta/\omega$ près des réflexions (002) des films et des substrats pour les différents δ. La position (002) des films est marquée par un triangle inversé noir. La position de $La_{0.75}Sr_{0.25}CrO_3$ stœchiométrique massif (a_{LSCO} = 3,876 Å) est indiquée par une ligne pointillée verticale noire. (f) Paramètres de maille hors plan *c* et volume unitaire *V* de ces films en fonction de δ. Les barres d'erreur horizontales sont liées à *c*.

Pour vérifier que tous ces films LSCO sont complètement contraints par leurs substrats, des RSM autour de la réflexion asymétrique (103) sont mesurées (montrées dans la Figure 27). Les paramètres de maille dans le plan des films LSCO (a_{LSCO}) sont résumés dans le Tableau 9. Le nœud LSCO(103) est aligné verticalement avec le nœud du substrat, indiquant que le a_{LSCO} = 3,905 Å. Comme nous l'avons déjà vu, la déviation par rapport à la stœchiométrie augmente le volume de la maille cristalline à cause de la formation de lacunes ioniques chargées dans le maille pérovskite (défauts ponctuels) ou des fautes d'empilements (défauts planaires s'intercalant entre les mailles pérovskites), tel qu'observé dans d'autres oxydes de structure pérovskite, en particulier STO [25, 26, 27] et même $LaCrO_3$ de nos travaux (voir section 3) [24]. Le volume de la maille du film LSCO stœchiométrique (58,617 $Å^3$) est le plus proche de la valeur

du volume du massif LSCO (58,231 Å^3). Les mosaïcités (FWHM des w-scans, non montrés ici) autour du pic (002) est inférieur à 0,1° pour tous ces films LSCO, indiquant une très bonne qualité cristallline malgré de fortes déviations par rapport à la stœchiométrie et d'une proportion importante de défauts ponctuels et/ou planaires dans le réseau cristallin.

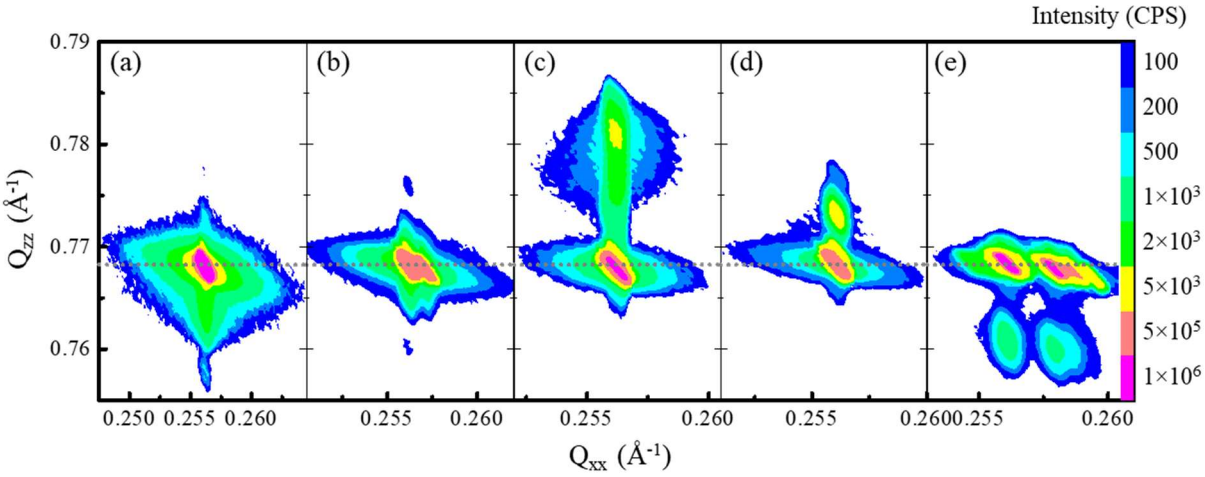

Figure 27 RSM enregistrées autour de la réflexion asymétrique (103) de couches minces LSCO pour (a) δ = -0,3, (b) δ = -0,15, (c) δ = 0, (d) δ = 0,15 et (e) δ = 0,3. La ligne pointillée horizontale indique la position Q_{zz} du substrat STO.

Tableau 9 Résumé des propriétés structurales et des compositions chimiques des films $(La_{0.75}Sr_{0.25})_{1+\delta}CrO_3$.

δ	[Sr]/[La+Sr]	*a* (Å)	*c* (Å)	Contrainte	Mosaicité (°)	Volume (Å^3)
-0,3	0,32	3,905	3,923	compression	0,1	59,823
-0,15	0,26	3,905	3,906	relaxé	0,09	59,547
0	0,25	3,905	3,844	tension	0,07	58,617
0,15	0,26	3,905	3,882	tension	0,07	59,200
0,3	0,21	3,905	3,944	compression	0,09	60,142

5.3. Impact sur les propriétés physiques

Les propriétés électroniques et thermoélectriques de ces films $(La_{0.75}Sr_{0.25})_{1+\delta}CrO_3$ (LSCO) ont été mesurées dans le plan à température ambiante. Les films clairement hors

stœchiométriques à |δ| = 0,3 n'ont pas pu être mesurés, probablement à cause d'une trop grande résistivité électrique. Les mesures des films LSCO avec |δ| ≤ 0,15 sont reportées dans la Figure 28.

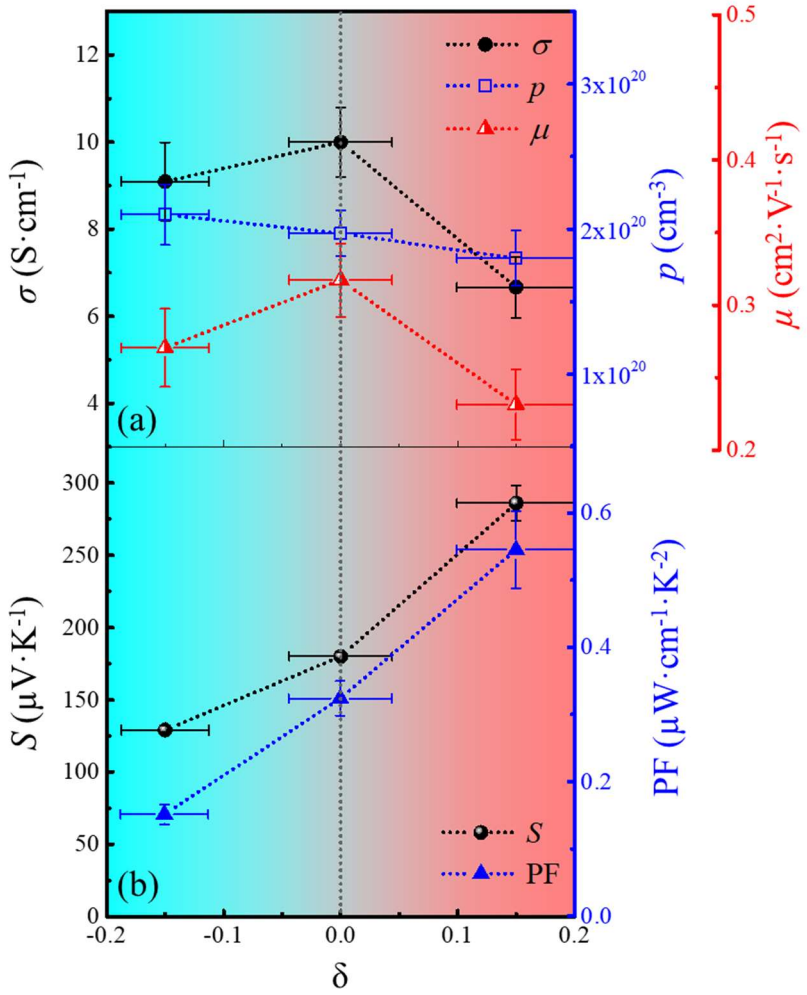

Figure 28 (a) Conductivité électrique σ, concentration p et mobilité μ des porteurs de charge (trous) dans les films $(La_{0.75}Sr_{0.25})_{1+\delta}CrO_3$ à température ambiante obtenus à partir des mesures effet Hall, ainsi que (b) coefficient de Seebeck et facteur de puissance thermoélectrique déduit de ces mesures (PF = $S^2\sigma$) en fonction de δ.

Tous les films présentent une conductivité de type p et une concentration de trous élevée, du même ordre de grandeur que le film stœchiométrique (2×10^{20} cm^{-3}), avec une très légère tendance à la baisse avec l'augmentation de δ (dans les limites des incertitudes de mesures cependant). Le film stœchiométrique LSCO présente la conductivité électrique la plus élevée (σ = 10 $S\cdot cm^{-1}$), ce qui est légèrement supérieure à celle du film déficient en cations A (~9 $S\cdot cm^{-1}$ à δ = -0,15) et clairement supérieure à celle du film déficient en Cr (6,7 $S\cdot cm^{-1}$ à δ = 0,15). La mobilité des trous (μ) diminue légèrement avec |δ|. Elles sont de 0,32 $cm^2\cdot V^{-1}\cdot s^{-1}$ (à δ = 0), 0,27 $cm^2\cdot V^{-1}\cdot s^{-1}$ (à δ = -0,15) et 0,23 $cm^2\cdot V^{-1}\cdot s^{-1}$ (à δ = -0,15). Pour les films non stœchiométriques,

les défauts ponctuels ou planaires induits sont donc certainement une cause de la diminution de la mobilité des trous.

Si la déviation par rapport à la stœchiométrie n'induit que des défauts ponctuels (lacunes cationiques) dans le réseau et pas de défauts planaires (fautes d'empilements) ni de phases secondaires, les différents films LSCO avec δ = -0,15, 0 et 0,15 peuvent être écrits dans leur formule développée comme $La_{0.64}Sr_{0.21}\square_{0.15}CrO_3$, $La_{0.75}Sr_{0.25}CrO_3$ et $La_{0.75}Sr_{0.25}Cr_{0.87}\square_{0.13}O_3$, respectivement. Cependant, de telles déviations dans $SrTiO_3$ par exemple induisent aussi des défauts planaires (fautes d'empilements) [25]. En complément, il est important de noter que les analyses XPS des niveaux de cœurs Cr $2p_{3/2}$ ont montré des contributions de ~25% de Cr^{4+} et ~75% de Cr^{3+} pour toutes les compositions quel que soit δ. Il semble que le degré d'oxydation des éléments est indépendant de δ.

Les mesures thermoélectriques de coefficient Seebeck *S* à température ambiante montrent qu'il est bien positif pour tous les échantillons, confirmant que les trous sont les porteurs majoritaires dans ces films. Les résultats de ces mesures thermoélectriques sont reportées dans la Figure 28b en fonction de δ. Cette figure montre clairement une augmentation significative de *S* avec δ, passant de *S* ~125 $\mu V \cdot K^{-1}$ (à δ = -0,15) à *S* ~280 $\mu V \cdot K^{-1}$ (à δ = 0,15). Nous avons déjà vu que *S* ~180 $\mu V \cdot K^{-1}$ pour le film stœchiométrique, en très bon accord avec les résultats récents du groupe S. A. Chambers [30]. Ces mesures indiquent que un excès en cations A augmentent clairement le coefficient Seebeck de LSCO. Cette tendance est en assez bon accord avec les mesures électroniques qui montraient globalement une tendance à la baisse de la conductivité électrique et de densité de porteurs avec δ dans les limites des incertitudes expérimentales.

Le facteur de puissance thermoélectrique (PF = $S^2\sigma$) déduit de ces mesures montre la même tendance que *S*. Il augmente avec δ passant de ~0,18 $\mu W \cdot cm^{-1} \cdot K^{-2}$ (à δ = -0,15) à ~0,55 $\mu W \cdot cm^{-1} \cdot K^{-2}$ (à δ = 0,15). Comme déjà mentionné auparavant, PF = 0,33 $\mu W \cdot cm^{-1} \cdot K^{-2}$ à δ = 0. Ces mesures indiquent clairement que un excès en cations A dans LSCO augmente le facteur de puissance thermoélectrique d'un facteur ~1,7 par rapport à la stœchiométrie, et d'un facteur ~1,7 par rapport à un excès de Cr. Ces résultats sont d'autant plus intéressants que ces défauts ponctuels ou planaires induits par une telle déviation par rapport à la stœchiométrie permettraient de réduire la conductivité thermique du matériau LSCO et ainsi augmenter d'autant plus son facteur de mérite thermoélectrique global *ZT*.

6. Conclusion et perspectives

6.1. Conclusion

D'intérêt dans le domaine de la thermoélectricité en particulier, ce travail doctoral concerne la croissance et l'étude de films minces épitaxiés $LaCrO_3$ dopé au Sr ($La_{1-x}Sr_xCrO_3$) thermoélectriques de type *p*. Les films minces ont été élaborés par épitaxie par jets moléculaires (MBE) sur substrats (pseudo)cubiques d'oxydes de structure pérovskite. Plusieurs paramètres clés ont été étudiés, tels que *i*) le taux de substitution en Sr (x) (voir section 3, Chapitre III), *ii*) les contraintes d'épitaxie (voir section 4, Chapitre IV), et *iii*) la déviation par rapport à la stœchiométrie cationique (voir section 5, Chapitre V). En particulier, leurs impacts sur les propriétés structurales, électroniques et thermoélectriques ont été bien étudiés.

Dans un premier temps, après des séries de calibrations $La_{1+\delta}CrO_3$ [24] et $Sr_{1+\delta}CrO_3$, des couches minces de la solution solide $La_{1-x}Sr_xCrO_3$ ont été épitaxiées sur substrat de $SrTiO_3$ (001) avec de très faibles mosaïcités (< 0.1°). L'impact du taux de substitution de La^{3+} par Sr^{2+} sur le site A (x) a été étudié. Du point du vue structural, la solution solide obéit à la loi de Végard, en accord avec la littérature [33]. Du point de vue propriétés électroniques et thermoélectriques mesurées à température ambiante dans la gamme $x \leq 0,4$, la densité (p) et mobilité (μ) de porteurs de charge (trous) ainsi que la conductivité électrique (σ) associée augmentent avec x, tandis que le coefficient Seebeck (S) diminue de manière cohérente et en accord avec la littérature [30]. Le facteur de puissance thermoélectrique déduit de ces mesures ($PF = S^2\sigma$) atteint un maximum (0,33 $\mu W \cdot cm^{-1} \cdot K^{-2}$) à x = 0,25 ($La_{0.75}Sr_{0.25}CrO_3$), en accord avec la littérature [30]. Pour cette composition optimale du point de vue thermoélectrique, nos mesures donnent : σ = 10 $S \cdot cm^{-1}$, $p = 2\times10^{20}$ cm^{-3}, μ = 0,3 $cm^2 \cdot V^{-1} \cdot s^{-1}$, et S = 180 $\mu V \cdot K^{-1}$.

Dans un deuxième temps, des couches minces de bonne qualité cristalline de $La_{0.75}Sr_{0.25}CrO_3$ ont été épitaxiées contraintes sur différents substrats d'oxydes (pseudo)cubiques de structure pérovskite afin d'étudier les effets des déformations épitaxiales (de -2,06 % en compression à +1,75 % en tension) sur les propriétés structurales, électroniques et thermoélectriques. De cette étude structurale, le coefficient de Poisson ainsi que le paramètre de maille de l'équivalent massif de cet oxyde prometteur ont été extraits pour la première fois et diffèrent significativement de $LaCrO_3$ (ν_{LSCO} = 0,32 et a_{LSCO} = 3,876 Å). Ces résultats ont été publiés [35]. D'autre part, les déformations épitaxiales ont un large impact sur les propriétés électroniques et thermoélectriques mesurées dans le plan. Une forte contrainte en tension fait

chuter p et σ associée de plusieurs ordres de grandeurs, tandis que S augmente progressivement de 127 $\mu V \cdot K^{-1}$ (forte compression) à 208 $\mu V \cdot K^{-1}$ (forte tension). La mobilité est maximum pour des films les plus proches de l'état relaxé et PF est maximum pour une légère contrainte en tension. Ces résultats sont en cours de publication [36].

Enfin, des couches minces $(La_{0.75}Sr_{0.25})_{1+\delta}CrO_3$ ont été épitaxiées contraintes sur substrat $SrTiO_3(001)$. L'impact de la déviation par rapport à la stœchiométrie cationique (δ) sur les propriétés structurales, électroniques et thermoélectriques a été étudié dans la gamme $-0,3 \leq \delta \leq 0,3$. Du point de vue structural, les couches sont toutes monocristallines avec de faibles mosaïcités ($\leq 0,1°$), et le paramètre de maille hors plan et le volume de la maille augmentent avec $|\delta|$. Ces résultats indiquent que δ induit l'introduction de défauts ponctuels (lacunes cationiques) dans la maille pérovskite ou de défauts planaires (fautes d'empilements qui s'intercalent entre mailles). Les couches clairement hors stœchiométriques à $|\delta| = 0,3$ sont isolantes (en tout cas trop isolantes pour être mesurables avec nos appareils). Concernant les propriétés électroniques et thermoélectriques mesurées à température ambiante, μ et σ sont maximales à la stœchiométrie cationique ($\delta = 0$). Cependant, un excès de Cr ($\delta = -0,15$) a tendance à faire légèrement augmenter p et faire clairement baisser S (de ~30%), tandis que un excès de cations A ($\delta = 0,15$) a tendance à faire légèrement baisser p et faire clairement augmenter S (> 50%). Suivant la tendance de S, par rapport à la stœchiométrie cationique ($\delta = 0$), PF est clairement augmenté (~ +70%) avec un excès de cations A (~15 at.%) et clairement diminué (~ -40%) avec un excès de Cr (~15 at.%). Ces résultats sont très intéressants puisque l'introduction des défauts (ponctuels ou planaires) induits par la déviation par rapport à la stœchiométrie cationique devrait permettre de faire baisser également la conductivité thermique (κ) et donc d'augmenter d'autant plus le facteur de mérite globale thermoélectrique ($ZT = PF/\kappa$).

6.2. Travail en cours et perspectives

Des travaux sont toujours en cours et des perspectives à ce travail sont envisagées. Ils s'intègrent notamment dans le projet ANR MITO et la thèse de M. d'Esperonnat (2019-2022). Notamment, il est important de mesurer les conductivités thermiques afin d'afin d'estimer le facteur de mérite global ZT. Ces mesures sont prévues dans le cadre de la thèse de M. d'Esperonnat, et particulièrement sur la série hors-stœchiométrie cationique où une amélioration du ZT est attendue (voir section 5, Chapitre V). D'autre part, il est important de

mesurer les résistances de contact entre cet oxyde thermoélectrique et un métal conducteur en vue de l'intégration dans un module fonctionnel. Des mesures ont été effectuées par R. Moalla dans le cadre du projet ANR MITO et un article est en préparation sur ces résultats. Ensuite, l'étude de l'intégration monolithique sur silicium est importante pour la fabrication de composants intégrés sur les plateformes de l'industrie microélectronique. Des premières hétéroépitaxies sur $SrTiO_3$/Si(001) ont été réalisées et sont montrées ci-dessous. Enfin, des procédés technologiques sont étudiés pour la microfabrication d'un module à base d'oxydes thermoélectriques intégrés sur silicium, ce qui représente l'objectif ultime du projet ANR MITO.

6.2.1. Conductivité thermique et estimation du *ZT*

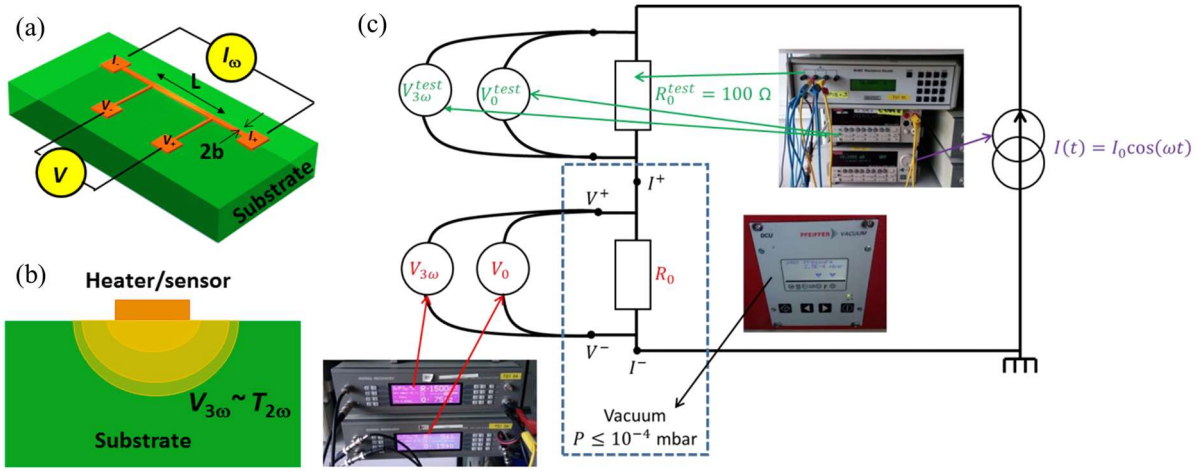

Figure 29 (a) Schéma 3D du dispositif nécessaire à la mesure 3ω (fil métallique déposé sur l'échantillon, servant de chauffage/capteur) et (b) vue en coupe [53, 54]. (c) Schéma de l'appareillage et du circuit électrique nécessaire.

L'estimation du *ZT* nécessite la mesure de la conductivité thermique (κ), assez délicate sur couches minces. Cette mesure de κ est particulièrement intéressante pour la série hors-stœchiométrie cationique pour laquelle une augmentation du *ZT* est attendue. Il est prévu, en collaboration avec le CETHIL (P. O. Chapuis), de mesurer κ par la méthode électrique 3ω, bien adaptée à la mesure sur couches minces [53, 54]. La Figure 29 représente schématiquement les mesures de κ par la méthode 3ω sur films minces ou matériaux massifs.

6.2.2. Mesures des résistances de contact

Dans un module thermoélectrique, les résistances de contact entre les jambes

thermoélectriques et le métal de contact est crucial et doit être le plus faible possible pour un rendement optimal. Par exemple, une résistance de contact supérieur à 10^{-10} $\Omega \cdot m^2$ serait rédhibitoire (limitation ou pas de courant en mode générateur, ou chauffage par effet Joule en mode refroidissement) [55]. Des mesures de résistances de contact ont été effectuées avec différent conducteurs tels que Pt, Ti/Au, Cr/Au, $SrRuO_3$, en utilisant des électrodes supérieures avec des motifs « Transmission Line Model » (TLM) [56]. Ces mesures ont été effectuées par R. Moalla dans le cadre de l'ANR MITO et un article est en cours de préparation.

6.2.3. Intégration monolithique sur silicium

L'intégration monolithique sur silicium par épitaxie est importante pour la fabrication de composants de qualité intégrés sur les plateformes de l'industrie microélectronique. Compte tenu du faible désaccord de paramètre de maille, l'hétéroépitaxie de $La_{1-x}Sr_xCrO_3$ est possible sur les couches de $SrTiO_3$ (STO) hétéroépitaxiées par MBE sur substrats de Si(001), qui sont très utilisées pour l'intégration monolithique de divers oxydes fonctionnels sur silicium [57, 58, 59, 60, 61, 62]. L'INL a ce savoir-faire depuis une quinzaine d'années [61, 63, 64, 65, 66, 67].

Par exemple, la Figure 30a et b montrent les images RHEED, le long des azimuts [100] et [110], d'une couche STO/Si(001) d'environ 37 nm d'épaisseur. Des lignes bien contrastées révèlent une bonne qualité cristalline d'un film ayant une surface plane de faible rugosité. L'absence de reconstruction du 2ème ordre sur deux azimuts prouve la bonne stœchiométrie [68]. Figure 30c indique uniquement les pics de diffraction correspondant aux réflexions {00*l*} du film STO et du substrat. Aucune autre phase orientée que STO(00*l*) n'est présente dans le film épitaxié. Le paramètre de maille hors plan est extrait de la Figure 30d (c_{STO} = 3,925 Å). La mosaïcité du STO(002) est de 0,23° (Figure 30e), ce qui est légèrement supérieur à celui du STO sur des substrats oxydes de structure pérovskite. A noté que la position de la réflexion STO(002) dépend des conditions de croissance (*i.e.* la température, la pression partielle d'oxygène, la stœchiométrie cationique, le désaccord de maille, la relaxation structurale, etc.) [65].

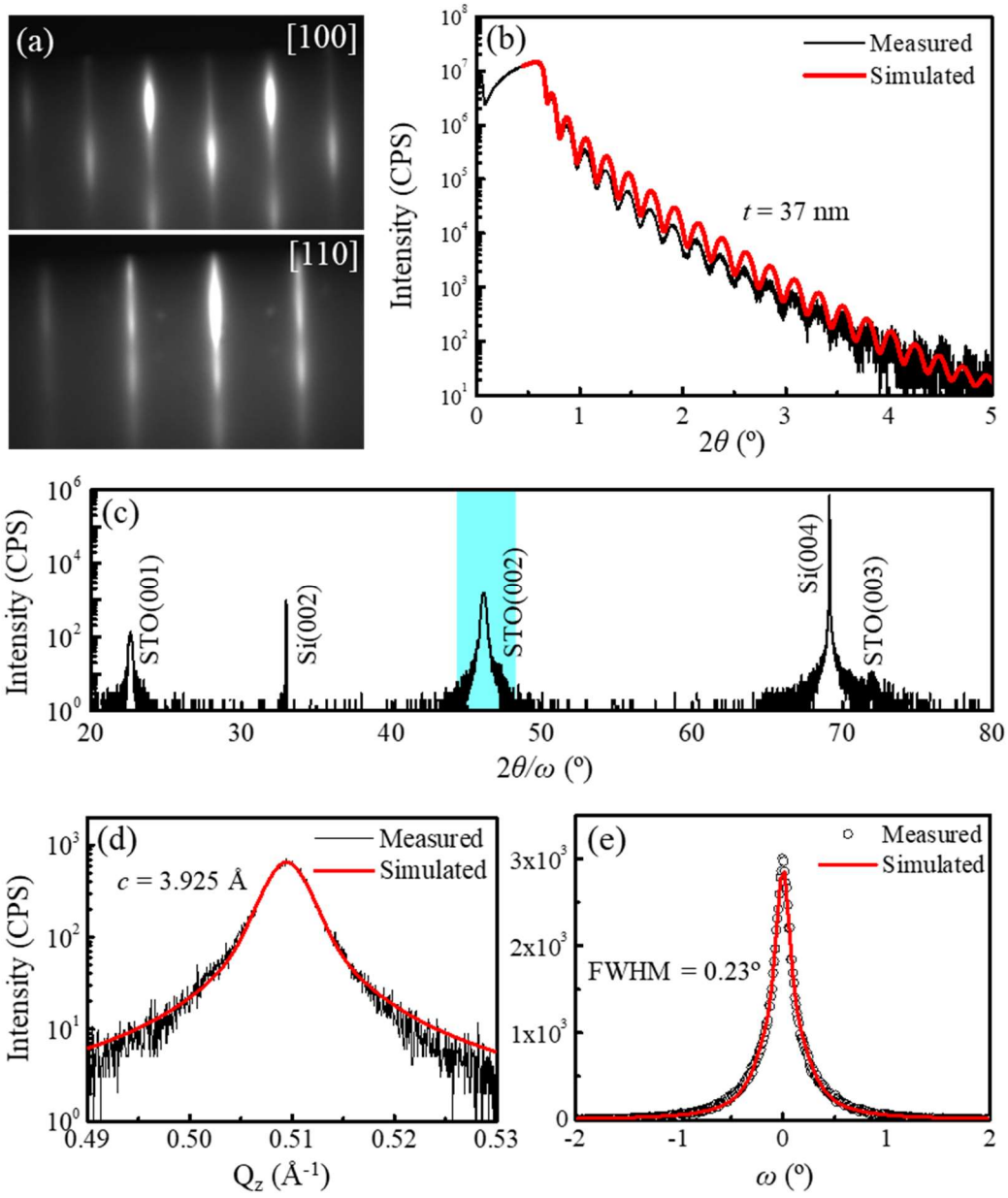

Figure 30 (a) Images RHEED de STO/Si le long des azimuts [100] et [110]. (b) XRR de STO/Si comprenant les données brutes (ligne noire) et le fit (ligne rouge). (c) Scans XRD $2\theta/\omega$ de 20° à 80°. (d) Analyse XRD près de la réflexion STO (002). (e) ω-scan autour de la réflexion STO (002).

Ces couches hétéroépitaxiées de STO/Si(001) servent de pseudo-substrat de bonne qualité pour le dépôt ultérieur d'oxydes fonctionnels de structure pérovskite, comme les oxydes thermoélectriques de type *p* $La_{1-x}Sr_xCrO_3$, ou de type *n* $La_xSr_{1-x}TiO_3$. Par exemple, la Figure 31a montre les images RHEED, le long des azimuts [100] et [110], enregistrés à la fin de la croissance d'un film mince $La_{0.75}Sr_{0.25}CrO_3$ (LSCO) d'environ 28 nm d'épaisseur à 700 °C sous $P(O_2) = 1\times10^{-7}$ Torr (Figure 31a). Des raies avec des surintensités régulières montrent que le

film est en bonne partie épitaxié, mais avec une certaine rugosité. Aussi quelques anneaux (Debye-Scherrer) peuvent être observés indiquant en plus une certaine polycristallinité (orientation aléatoire). Cependant, aucune autre phase ni orientation que celle de LSCO(00*l*) n'est observé sur les scans XRD $2\theta/\omega$ (sur la Figure 31b). Les paramètres de maille hors plan de LSCO et STO sont extraits de Figure 31c (c_{LSCO} = 3,852 Å et c_{STO} = 3,921 Å), et confirmés par la mesure RSM autour de la réflexion asymétrique (103) (Figure 31e). D'après cette RSM, les nœuds (103) des films LSCO et STO sont alignés verticalement indiquant que le film LSCO est contraint cube-sur-cube sur STO/Si.

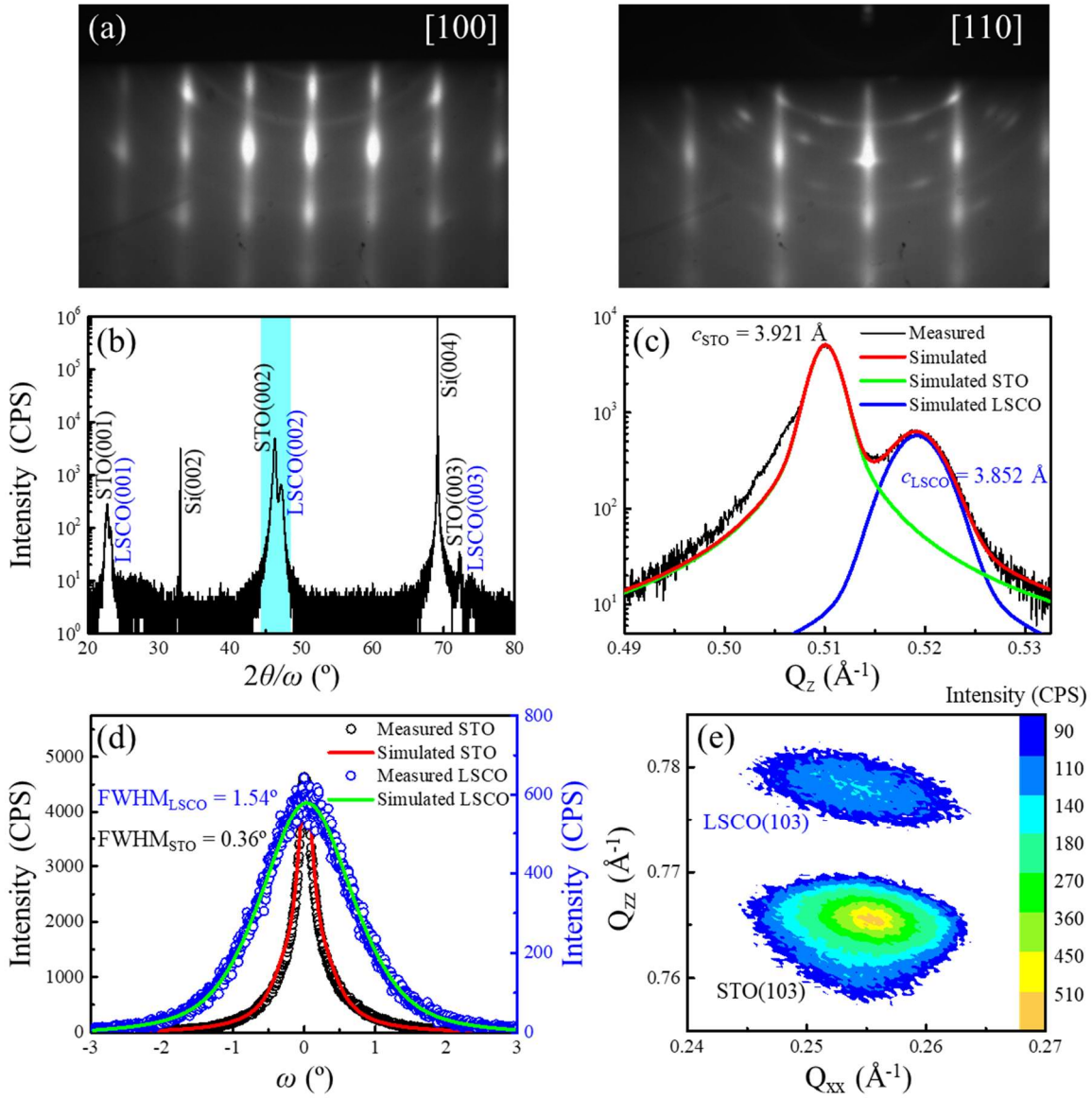

Figure 31 (a) Images RHEED de LSCO/STO/Si le long des azimuts [100] et [110]. (b) Scans XRD $2\theta/\omega$ de 20° à 80°. (c) Analyse XRD près de la réflexion (002). (d) ω-scans autour des réflexions (002). (e) RSM autour de la réflexion asymétrique (103) du film mince LSCO sur STO/Si.

Les ω-scans mesurés autour des réflexions LSCO(002) et STO(002) sont représentés sur Figure 31d. Les mosaïcités sont respectivement de 1,54° et 0,36°. En raison de l'instabilité thermique de STO/Si, la qualité du LSCO sur STO/Si est moins bonne que celles sur les substrats oxydes. Il est à noter que la mosaicité de la couche de STO avant croissance de LSCO montrée sur Figure 30d (0,23°) est légèrement meilleure qu'après croissance de LSCO (0,36°), principalement à cause de la température de croissance de LSCO (700 °C) beaucoup plus élevée que celle de STO (420 °C) sur Si. Cependant, ces premiers essais peuvent être améliorés et les couches STO/Si représentent un excellent moyen d'intégration de couches LSCO épitaxiées sur silicium et la réalisation de composants intégrés.

6.2.4. Micro-fabrication d'un module thermoélectrique d'oxydes

La réalisation d'un micro-module thermoélectrique (µ-TE) intégré représente des défis de fabrication, d'autant plus avec des oxydes épitaxiés sur silicium. Cela nécessite au moins trois croissance localisées successives (jambes *n*, jambes *p* et les contacts). Ces étapes technologiques sont étudiées dans le cadre de l'ANR MITO avec des procédés de l'industrie microélectronique : dépôt d'un masque dur, photolithographie et lift-off. Un schéma du démonstrateur envisagé est présenté dans la Figure 32.

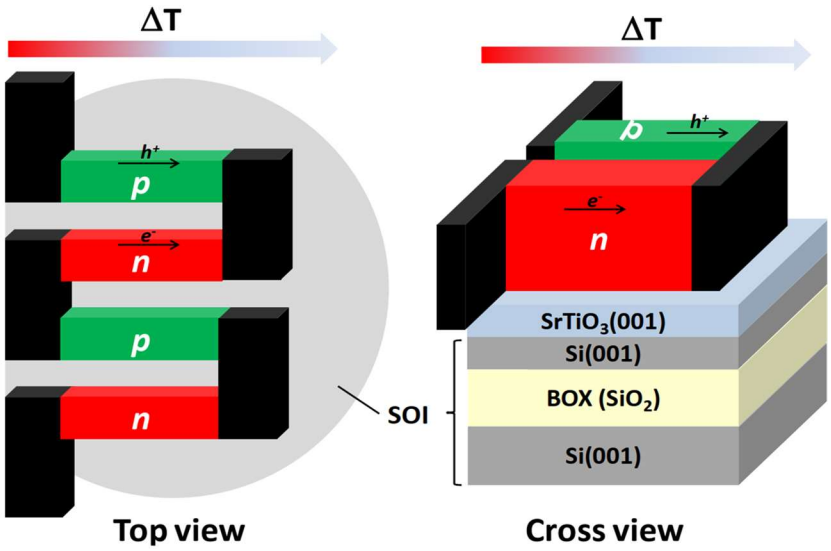

Figure 32 Schéma simplifié d'une architecture planaire de micromodule thermoélectrique en vue de dessus et transversale sur substrat « Silicon-On-Insulator » (SOI).

7. Références

[1] G. J. Snyder and E. S. Toberer. Complex thermoelectric materials. Nature Materials, 2008, 7(2): 105-114.

[2] L. E. Bell. Cooling, heating, generating power, and recovering waste heat with thermoelectric systems. Science, 2008, 321: 1457-1461.

[3] A. J. Minnich, M. S. Dresselhaus, Z. F. Ren and G. Chen. Bulk nanostructured thermoelectric materials: current research and future prospects. Energy & Environmental Science, 2009, 2: 466-479.

[4] C. J. Vineis, A. Shakouri, A. Majumdar and M. G. Kanatzidis. Nanostructured thermoelectrics: big efficiency gains from small features. Advanced Materials, 2010, 22(36): 3970-3980.

[5] L. Yang, Z. Chen, M. S. Dargusch and J. Zou. High performance thermoelectric materials: progress and their applications. Advanced Energy Materials, 2018, 8(6): 1701797.

[6] I. Terasaki, Y. Sasago, and K. Uchinokura. Large thermoelectric power in $NaCo_2O_4$ single crystals. Physical Review B, 1997, 56(20): R12685.

[7] K. Takahata, Y. Iguchi, D. Tanaka, T. Itoh, and I. Terasaki. Low thermal conductivity of the layered oxide (Na, Ca)Co_2O_4: Another example of a phonon glass and an electron crystal. Physical Review B, 2000, 61(19): 12551.

[8] W. Koshibae, K. Tsutsui, and S. Maekawa. Thermopower in cobalt oxides. Physical Review B, 2000, 62(11): 6869.

[9] T. Okuda, K. Nakanishi, S. Miyasaka, and Y. Tokura. Large thermoelectric response of metallic perovskites: $Sr_{1-x}La_xTiO_3$ ($0 < x < 0.1$). Physical Review B, 2001, 63(11): 113104.

[10] Y. Lin, J. Lan, and C. Nan. *Oxide thermoelectric materials: From basic principles to applications*. Wiley-VCH, 2019.

[11] T. Wu and P. Gao. Development of perovskite-type Materials for thermoelectric application. Materials, 2018, 11(6): 999.

[12] B. Poudel, Q. Hao, Y. Ma, Y. C. Lan, A. Minnich, B. Yu, X. Yan, D. Z. Wang, A. Muto, D. Vashaee, X. Y. Chen, J. M. Liu, M. S. Dresselhaus, G. Chen and Z. Ren. High-thermoelectric performance of nanostructured bismuth antimony telluride bulk alloys. Science, 2008, 320(5876): 634-638.

[13] K. F. Hsu, S. Loo, F. Guo, W. Chen, J. S. Dyck, C. Uher, T. Hogan, E. K. Polychroniadis and M. G. Kanatzidis. Cubic $AgPb_mSbTe_{2+m}$: bulk thermoelectric materials with high figure of merit. Science, 2004, 303(5659): 818-821.

[14] B. Yu, M. Zebarjadi, H. Wang, K. Lukas, H. Wang, D. Wang, C. Opeil, M. Dresselhaus, G. Chen and Z. Ren. Enhancement of thermoelectric properties by modulation-doping in silicon germanium alloy nanocomposites. Nano Letters, 2012, 12(4): 2077-2082.

[15] Abstract of the project Premier micro module thermoélectrique à base d'oxydes - MITO. Retrieved from: https://anr.fr/Projet-ANR-17-CE05-0018.

[16] A. Y. Cho. Film deposition by molecular-beam techniques. Journal of Vacuum Science and Technology, 1971, 8(5): S31-S38.

[17] A. Y. Cho and J. R. Arthur. Molecular beam epitaxy. Progress in Solid State Chemistry, 1975, 10: 157.

[18] K. Alavi. in Encyclopedia of Materials: Science and Technology. (edited by K. H. J. Buschow, Amsterdam; New York: Elsevier) 2001.

[19] Hall Effect Measurements. Retrieved from: https://web.archive.org/web/20060615044930/http://www.eeel.nist.gov/812/hall.html.

[20] A method of measuring the resistivity and Hall coefficient on lamellae of arbitrary shape. Retrieved from: http://electron.mit.edu/~gsteele/vanderpauw/vanderpauw.pdf.

[21] J. Ravichandran. Thermal and electrical transport in oxide heterostructures (Thesis). UC Berkeley, California, United States, 2011.

[22] D. M. Rowe. *Handbook of thermoelectrics*. CRC Press, 1995.

[23] D. M. Rowe. *Thermoelectrics handbook: Macro to nano*. CRC Press, 2006.

[24] D. Han, M. Bouras, C. Botella, A. Benamrouche, B. Canut, G. Grenet, G. Saint-Girons and R. Bachelet. Structural properties of strained epitaxial $La_{1+\delta}CrO_3$ thin films. Journal of Vacuum Science & Technology A: Vacuum, Surfaces, and Films, 2019, 37(2): 021512.

[25] C. M. Brooks, L. F. Kourkoutis, T. Heeg, J. Schubert, D. A. Muller and D. G. Schlom. Growth of homoepitaxial $SrTiO_3$ thin films by molecular-beam epitaxy. Applied Physics Letters, 2009, 94(16): 162905.

[26] B. Jalan, R. Engel-Herbert, N. J. Wright and S. Stemmer. Growth of high-quality $SrTiO_3$ films using a hybrid molecular beam epitaxy approach. Journal of Vacuum Science & Technology A: Vacuum, Surfaces, and Films, 2009, 27(3): 461-464.

[27] B. Jalan, P. Moetakef and S. Stemmer. Molecular beam epitaxy of $SrTiO_3$ with a growth window. Applied Physics Letters, 2009, 95(3): 032906.

[28] L. Qiao, K. H. L. Zhang, M. E. Bowden, T. Varga, V. Shutthanandan, R. Colby, Y. Du, B. Kabius, P. V. Sushko, M. D. Biegalski and S. A. Chambers. The impacts of cation stoichiometry and substrate surface quality on nucleation, structure, defect formation, and intermixing in complex oxide heteroepitaxy–$LaCrO_3$ on $SrTiO_3$(001). Advanced Functional Materials, 2013, 23(23): 2953-2963.

[29] L. Qiao, T. C. Droubay, M. E. Bowden, V. Shutthanandan, T. C. Kaspar and S. A. Chambers. $LaCrO_3$ heteroepitaxy on $SrTiO_3$(001) by molecular beam epitaxy. Applied Physics Letters, 2011, 99(6): 061904.

[30] K. H. Zhang, Y. Du, A. Papadogianni, O. Bierwagen, S. Sallis, L. F. Piper, M. E. Bowden, V. Shutthanandan, P. V. Sushko, and S. A. Chambers. Perovskite Sr-doped $LaCrO_3$ as a new p-type transparent conducting oxide. Advanced Materials, 2015, 27(35): 5191-5195.

[31] The relative in-plane epitaxial strain (ε_{xx}) due to the lattice mismatch (f) are defined here as: $\varepsilon_{xx} = (a_{film} - a_{bulk})/a_{bulk}$, and $f = (a_{sub} - a_{bulk})/a_{bulk}$, where a_{film} is the measured in-plane lattice parameter of the film, a_{bulk} the bulk lattice parameter of pseudocubic film, and a_{sub} the lattice parameter of the substrate. Please note that $\varepsilon_{xx} = f$ for fully strained epitaxial films ($a_{film} = a_{sub}$).

[32] K. H. L. Zhang, P. V. Sushko, R. Colby, Y. Du, M. E. Bowden and S. A. Chambers. Reversible nano-structuring of $SrCrO_{3-\delta}$ through oxidation and reduction at low temperature. Nature Communications, 2014, 5(1): 1-7.

[33] K. H. L. Zhang, Y. Du, P. V. Sushko, M. E. Bowden, V. Shutthanandan, S. Sallis, L. F. J. Piper, and S. A. Chambers. Hole-induced insulator-to-metal transition in $La_{1-x}Sr_xCrO_3$ epitaxial films. Physical Review B, 2015, 91(15): 155129.

[34] D. P. Karim and A. T. Aldred. Localized level hopping transport in $La(Sr)CrO_3$. Physical Review B, 1979, 20(6): 2255.

[35] D. Han, M. Bouras, C. Botella, A. Benamrouche, B. Canut, G. Grenet, G. Saint-Girons, and R. Bachelet. Poisson ratio and bulk lattice constant of $(Sr_{0.25}La_{0.75})CrO_3$ from strained epitaxial thin films. Journal of Applied Physics, 2019, 126(8): 085304.

[36] D. Han, M. Bouras, C. Botella, A. Benamrouche, B. Canut, G. Grenet, G. Saint-Girons, and R. Bachelet. Tuning of thermoelectric power factor in *p*-type Sr-doped $LaCrO_3$ thin films by epitaxial strain. Submitted to ACS Applied Electronic Materials, 2020.

[37] D. G. Schlom, L. Q. Chen, X. Pan, A. Schmehl, and M. A. Zurbuchen. A thin film approach to engineering functionality into oxides. Journal of the American Ceramic Society, 2008, 91(8): 2429-2454.

[38] J. Y. Tsao. *Materials fundamentals of molecular beam epitaxy*. Academic Press, London, 1993.

[39] The out-of-plane and in-plane epitaxial strain (ε_{zz} and ε_{xx}, respectively) due to the lattice mismatch $f = (a_{sub} - a_{film})/a_{film}$ are defined here as: $\varepsilon_{zz} = (c_{film} - a_{bulk})/a_{bulk}$ and $\varepsilon_{xx} = (a_{film} - a_{bulk})/a_{bulk}$, where c_{film} and/or a_{film} is the measured out-of-plane/in-plane lattice parameter of the film, a_{bulk} the bulk lattice constant. The relaxation ratio R is defined here as $(a_{film} - a_{sub})/(a_{bulk} - a_{sub})$, where a_{sub} is the in-plane parameter of corresponding substrate.

[40] S. A. Suvorov and A. P. Shevchik. A heating module equipped with lanthanum chromite-based heaters. Refractories and Industrial ceramics, 2004, 45(3): 196-200.

[41] K. H. L. Zhang, K. Xi, M. G. Blamire, and R. G. Egdell. P-type transparent conducting oxides. Journal of Physics: Condensed Matter, 2016, 28(38): 383002.

[42] A. Vailionis, W. Siemons, and Gertjan Koster. Room temperature epitaxial stabilization of a tetragonal phase in $ARuO_3$ (A = Ca and Sr) thin films. Applied Physics Letters, 2008, 93(5): 051909.

[43] N. G. Eror and U. Balachandran. Self-compensation in lanthanum-doped strontium titanate. Journal of Solid State Chemistry, 1981, 40(1): 85-91.

[44] A. Ohtomo and H. Y. Hwang. Surface depletion in doped $SrTiO_3$ thin films. Applied Physics Letters, 2004, 84(10): 1716-1718.

[45] J. Carrasco, F. Illas, N. Lopez, E. A. Kotomin, Yu. F. Zhukovskii, R. A. Evarestov, Yu. A. Mastrikov, S. Piskunov, and J. Maier. First-principles calculations of the atomic and electronic structure of F centers in the bulk and on the (001) surface of $SrTiO_3$. Physical Review B, 2006, 73(6): 064106.

[46] H. Lee, T. Mizoguchi, T.Yamamoto, S. L.Kang, and Y. Ikuhara. First-principles calculation of defect energetics in cubic-$BaTiO_3$ and a comparison with $SrTiO_3$. Acta Materialia, 2007, 55(19): 6535-6540.

[47] T. Tanaka, K. Matsunaga, Y. Ikuhara, and T. Yamamoto. First-principles study on structures and energetics of intrinsic vacancies in $SrTiO_3$. Physical Review B, 2003, 68(20): 205213.

[48] M. Choi, A. B. Posadas, C. A. Rodriguez, A. O'Hara, H. Seinige, A. J. Kellock, M. M. Frank, M. Tsoi, S. Zollner, V. Narayanan, and A. A. Demkov. Structural, optical, and electrical properties of strained La-doped $SrTiO_3$ films. Applied Physics Letters, 2009, 95(11): 112504.

[49] W. Wunderlich, H. Ohta, and K. Koumoto. Enhanced effective mass in doped $SrTiO_3$ and related perovskites. Physica B: Condensed Matter, 2009, 404(16): 2202-2212.

[50] A. Janotti, D. Steiauf, and C. G. Van de Walle. Strain effects on the electronic structure of $SrTiO_3$: Toward high electron mobilities. Physical Review B, 2011, 84(20): 201304.

[51] N. V. Morozova, I. V. Korobeinikov, and S. V. Ovsyannikov. Strategies and challenges of high-pressure methods applied to thermoelectric materials. Journal of Applied Physics, 2019, 125(22): 220901.

[52] D. Kan and Y. Shimakawa. Strain effect on thermoelectric properties of $SrRuO_3$ epitaxial thin films. Applied Physics Letters, 2019, 115(2): 022403.

[53] W. Jaber. Phonon heat conduction probed by means of an electro-thermal method involving deposited micro and nanowires (Thesis). Institut National des Sciences Appliquées de Lyon, Lyon, France, 2016.

[54] A. Pic. Numerical and experimental investigations of self-heating phenomena in 3D Hybrid Bonding imaging technologies (Thesis). Institut National des Sciences Appliquées de Lyon, Lyon, France, 2019.

[55] R. Enright, S. Lei, G. Cunningham, I. Mathews, R. Frizzell, and A. Shen. Integrated thermoelectric cooling for silicon photonics. ECS Journal of Solid State Science and Technology, 2017, 6(3): N3103.

[56] D. K. Schroder. Chapter 3 in *Semiconductor material and device characterization*. John Wiley & Sons, 2006.

[57] J. W. Reiner, A. M. Kolpak, Y. Segal, K. F. Garrity, S. Ismail-Beigi, C. H. Ahn, and F. J. Walker. Crystalline oxides on silicon. Advanced Materials, 2010, 22(26-27): 2919-2938.

[58] A. A. Demkov and A. B. Posadas. *Integration of functional oxides with semiconductors*. Springer, New York, 2014.

[59] S. H. Baek and C. B. Eom. Epitaxial integration of perovskite-based multifunctional oxides on silicon. Acta Materialia, 2013, 61(8): 2734-2750.

[60] R. A. McKee, F. J. Walker, and M. F. Chisholm. Crystalline oxides on silicon: The first five monolayers. Physical Review Letters, 1998, 81(14): 3014.

[61] G. Saint-Girons, R. Bachelet, R. Moalla, B. Meunier, L. Louahadj, B. Canut, A. Carretero -Genevrier, J. Gazquez, P. Regreny, C. Botella, J. Penuelas, M. G. Silly, F. Sirotti, and G. Grenet. Epitaxy of $SrTiO_3$ on silicon: The knitting machine strategy. Chemistry of Materials, 2016, 28(15): 5347-5355.

[62] J. M. Vila-Fungueiriño, R. Bachelet, G. Saint-Girons, M. Gendry, M. Gich, J. Gazquez, E. Ferain, F. Rivadulla, J. Rodriguez-Carvajal, N. Mestres, and A. Carretero-Genevrier. Integration of functional complex oxide nanomaterials on silicon. Frontiers in Physics, 2015, 3: 38.

[63] G. Delhaye, C. Merckling, M. El-Kazzi, G. Saint-Girons, M. Gendry, Y. Robach, G. Hollinger, L. Largeau, and G. Patriarche. Structural properties of epitaxial $SrTiO_3$ thin films grown by molecular beam epitaxy on Si(001). Journal of Applied Physics, 2006, 100(12): 124109.

[64] G. Delhaye, M. El-Kazzi, M. Gendry, G. Hollinger, and Y. Robach. Hetero-epitaxy of $SrTiO_3$ on Si and control of the interface. Thin Solid Films, 2007, 515(16): 6332-6336.

[65] G. Niu. Epitaxy of crystalline oxides for functional materials integration on silicon (Thesis). Institut des Nanotechnologies de Lyon, Ecole Centrale de Lyon, Lyon, France, 2010.

[66] G. Niu, B. Vilquin, J. Penuelas, C. Botella, G. Hollinger, and G. Saint-Girons. Heteroepitaxy of $SrTiO_3$ thin films on Si(001) using different growth strategies: Toward substratelike quality. Journal of Vacuum Science & Technology B, Nanotechnology and Microelectronics: Materials, Processing, Measurement, and Phenomena, 2011, 29(4): 041207.

[67] L. Louahadj. Développement de l'épitaxie par jet moléculaire d'oxydes fonctionnels sur silicium (Thesis). Institut des Nanotechnologies de Lyon, Lyon, France, 2014.

[68] A. P. Kajdos and S. Stemmer. Surface reconstructions in molecular beam epitaxy of $SrTiO_3$. Applied Physics Letters, 2014, 105(19): 191901.

Communication list

Articles published (or submitted) in international peer-reviewed journals:

1. **D. Han**, R. Moalla, V. Giordano, M. d'Esperonnat, C. Botella, R. Debord, S. Pailhès, G. Saint-Girons, and R. Bachelet. *Tuning electronic and thermoelectric properties by epitaxial strain in p-type Sr-doped $LaCrO_3$ transparent thin films*. **ACS Applied Electronic Materials**, 2020 (under revision).

2. **D. Han**, M. Bouras, C. Botella, A. Benamrouche, B. Canut, G. Grenet, G. Saint-Girons, and R. Bachelet. *Poisson ratio and bulk lattice constant of $(Sr_{0.25}La_{0.75})CrO_3$ from strained epitaxial thin films.* **Journal of Applied Physics**, 2019, 126(8): 085304. DOI: 10.1063/1.5101049.

3. M. Bouras, **D. Han**, S. Cueff, R. Bachelet, and G. Saint-Girons. *Perovskite-oxide based hyperbolic metamaterials*. **ACS Photonics**, 2019, 6(7): 1755-1762. DOI: 10.1021/acsphotonics.9b00485.

4. **D. Han**, M. Bouras, C. Botella, A. Benamrouche, B. Canut, G. Grenet, G. Saint-Girons, and R. Bachelet. *Structural properties of strained epitaxial $La_{1+\delta}CrO_3$ thin films.* **Journal of Vacuum Science and Technology A**, 2019, 37(2): 021512. DOI: 10.1116/1.5082185.

Communications in international congresses (the presenting author is underlined):

1. **<u>D. Han</u>**, M. Bouras, R. Moalla, C. Botella, A. Benamrouche, G. Grenet, B. Canut, R. Debord, V. Giordano, S. Pailhès, G. Saint-Girons, and R. Bachelet. "*P-type thermoelectric $LaCrO_3$-based epitaxial thin films grown by MBE*". **European Materials Research Society Spring Meeting (E-MRS Spring 2019)**, Symposium O (Oxides), May 27-31, **2019**, Nice, France (Oral).

2. **<u>D. Han</u>**, M. Bouras, R. Moalla, C. Botella, A. Benamrouche, G. Grenet, B. Canut, R. Debord, V. Giordano, S. Pailhès, G. Saint-Girons, and R. Bachelet. "*Thermoelectric*

perovskite-oxide epitaxial films grown by MBE". **European Materials Research Society Spring Meeting (E-MRS Spring 2019)**, Symposium I (Thermoelectrics), May 27-31, **2019**, Nice, France (Oral).

3. M. Bouras, **D. Han**, S. Cueff, R. Bachelet, and G. Saint-Girons "*Perovskite oxide based hyperbolic epitaxial superlattices grown by oxide molecular beam epitaxy*". **EuroMBE 2019**, February 17-20, **2019**, Lenggries, Germany (Oral).

4. **D. Han**, M. Bouras, R. Moalla, M. Apreutesei, R. Debord, P. Regreny, C. Botella, G. Grenet, J. Gazquez, M. Bugnet, Q. d'Acremont, S. Dilhaire, P. O. Chapuis, S. Pailhès, G. Saint-Girons, and R. Bachelet. "*Decreasing thermal conductivity by atomic engineering in epitaxial oxide films for enhanced integrated thermoelectricity*". **Workshop CNRS GDRe Thermal Nanosciences and NanoEngineering**, October 11-12, 2018, Lyon, France (Oral).

5. G. Saint-Girons, R. Bachelet, M. Bouras, **D. Han**, J. Penuelas, G. Grenet, P. Regreny, S. Cueff, N. Chauvin, and L. Largeau. "*Engineering the properties of functional oxides and integrating them on Si and GaAs thanks to molecular beam epitaxy*". **European Materials Research Society Spring Meeting (E-MRS Spring 2018)**, Symposium V, June 18-22, 2018, Strasbourg, France (Invited talk).

Communications in French national congresses (the presenting author is underlined):

1. R. Moalla, **D. Han**, M. d'Esperonnat, C. Botella, B. Vilquin, N. Baboux, G. Saint-Girons, and R. Bachelet. "*Pyroelectric and thermoelectric epitaxial oxide layers for thermal energy harvesting*". **Journées du GDR CNRS OXYFUN 2020**, March, 2021, Guéthary, France (Oral).

2. M. d'Esperonnat, **D. Han**, R. Moalla, M. Razaghi, C. Botella, B. Canut, N. Baboux, G. Saint-Girons, and R. Bachelet. "*Solid solutions and superlattices of perovskite oxides for enhanced thermoelectricity*". **Journées du GDR CNRS OXYFUN 2020**, March, 2021, Guéthary, France (Poster).

3. M. Razaghi, M. d'Esperonnat, M. Bouras, **D. Han**, S. Cueff, R. Bachelet, and G. Saint-Girons. "*Superlattices and Ruddlesden-Popper phases to engineer the optical properties of*

perovskite oxides". **Journées du GDR CNRS OXYFUN 2020**, March, 2021, Guéthary, France (Poster).

4. **D. Han**, M. d'Esperonnat, M. Bouras, R. Moalla, C. Botella, A. Benamrouche, G. Grenet, B. Canut, R. Debord, V. Giordano, S. Pailhès, G. Saint-Girons, and R. Bachelet. "*P-type thermoelectric $LaCrO_3$-based epitaxial films grown by molecular beam epitaxy*". **Journées Nationales de thermoélectricité 2019 (JNTE 2019) du GIS TE,** January 22-24, 2020, Metz, France (Oral). https://jnte-2019.sciencesconf.org/.

5. R. Moalla, **D. Han**, G. Saint-Girons, J. L. Leclercq, and R. Bachelet. "*Localized oxide MBE growth on Si b yselective etching lift-off for on-chip thermoelectricity*". **Journées Nationales sur les Technochologies Emergentes en micro/nano-fabrication (JNTE 2019),** November 25-27, 2019, Grenoble, France (Oral). https://jnte2019.sciencesconf.org/.

6. M. Bouras, **D. Han**, S. Cueff, R. Bachelet, and G. Saint-Girons. "*Perovskite-oxide based hyperbolic metamaterials*". **Colloque du GDR Oxyfun**, «Couches minces d'oxydes fonctionnels et applications en électronique et photonique», October 1-2, 2019, Caen, France (Oral). https://oxyfun2019caen.sciencesconf.org/.

7. M. Bouras, **D. Han**, S. Cueff, R. Bachelet, and G. Saint-Girons. "*$(La,Sr)TiO_3/SrTiO_3$ superlattices as hyperbolic metamaterials*". **Colloque du GDR Pulse**, July 1-4, 2019, Clermont-Ferrand, France (Oral). https://pulse2019ip.sciencesconf.org/.

8. M. Apreutesei, R. Debord, M. Bouras, **D. Han**, P. Regreny, C. Botella, G. Grenet, Q. d'Acremont, S. Dilhaire, P. O. Chapuis, S. Pailhès, G. Saint-Girons, and R. Bachelet. "*Perovskite oxides grown by MBE for integrated thermoelectricity*". **Journées nationales de thermoélectricité (JNTE 2017)**, December 6-8, 2017, Montpellier, France (Oral).

P-type thermoelectric Sr-doped $LaCrO_3$ epitaxial films

Abstract

The objective of this Ph.D. thesis is to epitaxially grow by molecular beam epitaxy (MBE) *p*-type thermoelectric $La_{1-x}Sr_xCrO_3$ films and study its structural and thermoelectric properties around room temperature as a function of key parameters such as A-site cationic substitution ratio (x), epitaxial strain, and cationic stoichiometry deviation. First, after the stoichiometry calibration series, the effects of the A-site cationic substitution ratio ($0 \leq x \leq 0.4$) on structural, electronic, and thermoelectric properties have been studied at room temperature. In particular, we have shown that films with x = 0.25 yield the largest thermoelectric power factor (0.33 $\mu W \cdot cm^{-1} \cdot K^{-2}$). On this basis, epitaxial strain effects have been studied with high-quality epitaxially-strained $La_{0.75}Sr_{0.25}CrO_3$ (LSCO) thin films grown on different perovskite-oxide substrates, leading to a wide in-plane strain values ($-2.1\% \leq \varepsilon_{xx} \leq +1.8\%$). The investigation of structural properties (in-plane and out-of-plane lattice parameters, unit-cell volume) allowed to extract the Poisson ratio ($\nu = 0.32$) as well as the bulk lattice constant ($a_{LSCO} = 3.876$ Å) for the first time. Besides, we have shown that the electronic and thermoelectric properties of LSCO can be tuned by strain. The slight in-plane tensile strain provides the largest thermoelectric power factor to most relaxed films. Furthermore, the effects of cationic stoichiometry deviation on structural, electronic, and thermoelectric properties were studied at room temperature in epitaxially-strained $(La_{0.75}Sr_{0.25})_{1+\delta}CrO_3$ thin films within a wide off-stoichiometry range ($-0.3 \leq \delta \leq 0.3$). We have shown that electronic and thermoelectric properties can be greatly altered by the cationic stoichiometry deviation alters the properties, and that the slight B-site deficiency ($\delta \sim 0.15$) enhances the thermoelectric power factor by around 70% concerning the stoichiometric film counterpart ($\delta = 0$). Finally, the last part of this work mainly presents the epitaxial integration and structural properties of $La_{0.75}Sr_{0.25}CrO_3$ films on silicon for the first time. These original results are of high interest for engineering various Sr-doped $LaCrO_3$-based devices such as thermal energy harvesters, coolers, transparent diodes, photocatalyzers, etc.

Keywords

Perovskite $La_{1-x}Sr_xCrO_3$ solid solution, P-type semiconductor, Thermoelectricity, Heteroepitaxial film, Molecular beam epitaxy

Films épitaxiés de $LaCrO_3$ dopé au Sr thermoélectriques de type p

Résumé

L'objectif de ce travail de thèse était la croissance épitaxiale par épitaxie par jets moléculaires de films $La_{1-x}Sr_xCrO_3$ de structure pérovskite thermoélectriques de type *p* ainsi que leur étude structurale et thermoélectrique en fonctions de différents paramètres clés tels que le taux de substitution sur le site A (x), les déformations d'épitaxie et la déviation par rapport à la stœchiométrie cationique. Premièrement, après des séries de calibrations stœchiométriques, les effets de taux de substitution ($0 \leq x \leq 0.4$) sur les propriétés structurales, électroniques et thermoélectriques ont été étudiés à température ambiante. En particulier, nous avons montré que les films avec x = 0.25 produisait le plus grand facteur de puissance thermoélectrique (0.33 $\mu W \cdot cm^{-1} \cdot K^{-2}$). Sur cette base, les effets de déformations d'épitaxie ont été étudiés sur des films minces contraints de $La_{0.75}Sr_{0.25}CrO_3$ (LSCO) crus sur différents substrats d'oxydes de structure pérovskite de différents paramètres de maille, induisant une large gamme de déformations dans le plan ($-2.1\% \leq \varepsilon_{xx} \leq +1.8\%$). L'étude des effets structuraux (paramètres de maile dans le plan et hors plan, ainsi que le volume de la maille) a permis d'extraire pour ma première fois le coefficient de Poisson ($\nu = 0.32$) ainsi que le paramètre de maille de son homologue massif ($a_{LSCO} = 3.876$ Å). De plus, nous avons montré que les propriétés électroniques et thermoélectriques de LSCO pouvaient être contrôlées par les déformations structurales. Une légère une déformation en tension dans le plan permet d'obtenir les plus facteurs de puissance thermoélectrique, en comparaison avec les films plus relaxés. Ensuite, les effets de la déviation par rapport à la stœchiométrie cationique sur les propriétés structurales, électroniques et thermoélectriques ont été étudiées pour des films épitaxiés contrains de $(La_{0.75}Sr_{0.25})_{1+\delta}CrO_3$ avec une large gamme de composition ($-0.3 \leq \delta \leq 0.3$). Nous avons montré pour la première fois que les propriétés électroniques et thermoélectriques peuvent être grandement altérées par la déviation par rapport à la stœchiométrie cationique et que des lacunes sur le site B ($\delta \sim 0.15$) augmentent le facteur de puissance thermoélectrique de 70% par rapport à la stœchiométrie ($\delta \sim 0$). Finalement, la dernière partie de manuscrit présente l'intégration monolithique par épitaxie de films LSCO sur silicium ainsi que leur étude structurale. Ces résultats originaux sont de fort intérêt pour de nombreux composants potentiels à base de $LaCrO_3$ dopés au Sr tels que des récupérateurs d'énergie thermique, refroidisseurs, diodes transparentes, photocatalyseurs, etc…

Mots clés

Solution solide de structure pérovskite $La_{1-x}Sr_xCrO_3$, Semiconducteur de type p, Thermoélectricité, Films hétéroépitaxiés, Epitaxie par jets moléculaires

dernière page de la thèse

AUTORISATION DE SOUTENANCE

Vu les dispositions de l'arrêté du 25 mai 2016,

Vu la demande du directeur de thèse

Monsieur G. SAINT-GIRONS

et les rapports de

Mme N. VIART
Professeur - Université de Strasbourg - Institut de Physique et de Chimie des Matériaux (IPCMS) - 23 rue de Loess - BP 43 - 67034 Strasbourg cedex 2

et de

Mme U. LÜDERS
Directrice de Recherche CNRS - ENSICAEN - Laboratoire de Cristallographie et Science des Matériaux (CRISMAT) - 6 bd du Maréchal Juin - CS 45053 - 14050 CAEN cedex 4

Monsieur HAN Dong

est autorisé à soutenir une thèse pour l'obtention du grade de **DOCTEUR**

Ecole doctorale ELECTRONIQUE, ELECTROTECHNIQUE, AUTOMATIQUE

Fait à Ecully, le 3 novembre 2020

P/Le directeur de l'E.C.L.
Le directeur des Etudes

Grégory VIAL
Directeur des Etudes
École Centrale de Lyon

Grégory VIAL